Development of a fault location method based on fault induced transients in distribution networks with wind farm connections

Lout, Kapildev

Award date:
2015

Awarding institution:
University of Bath

DEVELOPMENT OF A FAULT LOCATION METHOD BASED ON FAULT INDUCED TRANSIENTS IN DISTRIBUTION NETWORKS WITH WIND FARM CONNECTIONS

Kapildev V. Lout

A thesis submitted for the degree of Doctor of Philosophy

University of Bath

Department of Electronic and Electrical Engineering

January 2015

Abstract

Electrical transmission and distribution networks are prone to short circuit faults since they span over long distances to deliver the electrical power from generating units to where the energy is required. These faults are usually caused by vegetation growing underneath bare overhead conductors, large birds short circuiting the phases, mechanical failure of pin-type insulators or even insulation failure of cables due to wear and tear, resulting in creepage current.

Short circuit faults are highly undesirable for distribution network companies since they cause interruption of supply, thus affecting the reliability of their network, leading to a loss of revenue for the companies. Therefore, accurate offline fault location is required to quickly tackle the repair of permanent faults on the system so as to improve system reliability. Moreover, it also provides a tool to identify weak spots on the system following transient fault events such that these future potential sources of system failure can be checked during preventive maintenance.

With these aims in mind, a novel fault location technique has been developed to accurately determine the location of short circuit faults in a distribution network consisting of feeders and spurs, using only the phase currents measured at the outgoing end of the feeder in the substation. These phase currents are analysed using the Discrete Wavelet Transform to identify distinct features for each type of fault. To achieve better accuracy and success, the scheme firstly uses these distinct features to train an Artificial Neural Network based algorithm to identify the type of fault on the system. Another Artificial Neural Network based algorithm dedicated to this type of fault then identifies the location of the fault on the feeder or spur. Finally, a series of Artificial Neural Network based algorithms estimate the distance to the point of fault along the feeder or spur.

The impact of wind farm connections consisting of doubly-fed induction generators and permanent magnet synchronous generators on the accuracy of the developed algorithms has also been investigated using detailed models of these wind turbine generator types in Simulink. The results obtained showed that the developed scheme allows the accurate location of the short circuit faults in an active distribution

network. Further sensitivity tests such as the change in fault inception angle, fault impedance, line length, wind farm capacity, network configuration and white noise confirm the robustness of the novel fault location technique in active distribution networks.

Key achievements

- Analysis of short-circuit transients in an overhead distribution network with feeders and spurs using the Discrete Wavelet Transform
- Analysis of the impact of wind turbine types on short-circuit transients with particular interest to the effect on frequency components present in the transients
- Analysis of the impact of wind farm capacity on short-circuit transients
- Development of an Artificial Neural Network (ANN) based algorithm to determine the type of fault on an overhead distribution network with feeders and spurs
- Development of ANN based feeder/spur classification algorithms to detect the faulted section of the distribution network
- Development of ANN based fault location algorithms to evaluate the distance to the point of fault along the feeder or spur
- Critical assessment of the robustness of the proposed approach to changes in system parameters and various other factors that can influence the accuracy of the proposed technique in a real system

Acknowledgements

First and foremost, I would like to express my deepest appreciation and gratitude to my supervisor, Professor Raj Aggarwal, for his guidance and support throughout my studies at the University of Bath. He has generously funded my participation at various conferences during the course of my PhD, thus giving me the opportunity to connect with other people in the power industry and get informative feedback on my research.

I owe particular thanks to Dr Roderick Dunn, Dr Miles Redfern and Dr Simon Le Blond, for being such great company at conferences and for their useful advice on various occasions that have helped me to progress as an individual.

I would like to extend my sincere appreciation to my best friends Dr Tony Zheng and Dr Mehryar Emambaksh, for all the moments of happiness shared together, without which life so far away from home would not have been bearable.

I am forever grateful to my parents and sister for believing in me and supporting me at every step of my life, in particular my parents, who invested all of their life's savings in my education.

And, finally, much love to Elisa.

Table of Contents

Glossary of abbreviations

ABIS	Air Break Isolating Switch
A/D	Analog to Digital
AI	Artificial Intelligence
ANN	Artificial Neural Network
BJT	Bipolar Junction Transistor
CB	Circuit Breaker
DFIG	Doubly-Fed Induction Generator
DFT	Discrete Fourier Transform
DG	Distributed Generation
DMS	Distribution Management System
DWT	Discrete Wavelet Transform
EWEA	European Wind Energy Association
GA	Genetic Algorithm
GD	Gradient Descent
GPS	Global Positioning System
GSC	Grid Side Converter
IGBT	Insulated Gate Bipolar Transistor
LSB	Least Significant Bit

MOSFET	Metal Oxide Semiconductor Field Effect Transistor
PMSG	Permanent Magnet Synchronous Generator
PWM	Pulse Width Modulation
RBFNN	Radial Basis Function Neural Network
ROM	Read Only Memory
RSC	Rotor Side Converter
SAIDI	System Average Interruption Duration Index
SAIFI	System Average Interruption Frequency Index
SCIG	Squirrel Cage Induction Generator
SNR	Signal to Noise Ratio
STFT	Short-Time Fourier Transform
TDR	Time Domain Reflectometry
UKGDS	UK Generic Distribution Network
VSC	Voltage Source Converter
WRIG	Wound Rotor Induction Generator
WRSG	Wound Rotor Synchronous Generator

List of figures

List of symbols

P_W	Power from the wind
$P_{extracted}$	Power extracted from the wind
C_p	Rotor efficiency
$\propto_{critical}$	Critical angle of attack
X_d	Synchronous generator reactance
X'_d	Synchronous generator transient reactance
X''_d	Synchronous generator subtransient reactance
R0	Zero sequence resistance
L0	Zero sequence inductance
C0	Zero sequence capacitance
R1	Positive sequence resistance
L1	Positive sequence inductance
C1	Positive sequence capacitance
V_{LL}	Line to line voltage
m_a	Modulation index
Θ	Fault inception angle
Rf	Fault impedance

List of tables

Chapter 1: Introduction

1.1 Importance of fault location

An electrical power system is a complex system comprising a large number of interconnected electrical components with the sole global aim of allowing the electrical power produced at various locations to reach the customers. Any electrical power system can be simplified into three main stages, namely, generation, transmission and distribution. Power system components in each of these three sections are all prone to failure but the vast majority of disturbances that cause the power system to operate outside normal conditions occur in the transmission and distribution sides of the network.

The prime reason that explains why transmission and distribution networks experience more disturbances than other network components is because they expand over long distances and the long conductors are directly exposed to harsh climate conditions and external contacts. Faults that generally occur in transmission and distribution networks are short circuit transients caused predominantly by vegetation, animal and weather effects such as tree contact, large birds short circuiting phases, creepage current through path created by rain or moisture and the build up of contaminants. These faults can be classified into four main categories namely single line to ground faults (AG, BG and CG), line to line faults (AB, AC, BC), double line to ground faults (ABG, ACG and BCG) and three phase faults (ABC).

Fault location techniques in transmission and distribution networks have been developed for decades and their importance is mainly linked to power quality. The deregulation of the electricity market has incentivised utilities to offer a competitive service to consumers based on continuity of supply and reduced outage frequency and duration. Power utilities measure the reliability of their networks using the System Average Interruption Duration Index (SAIDI) and the System Average Interruption Frequency Index (SAIFI). Fault location techniques have the task of finding the exact point of occurrence of a fault on a line which is usually given in terms of distance of the point of fault from the measuring end inside a substation. In the event of a permanent fault on a network, fault location allows the maintenance

personnel to quickly locate, repair and restore supply to the system, thus reducing outage time and maintaining good values for system reliability indices.

Moreover, transient faults which are usually cleared by de-energising and re-energising the line, can cause minor damages on electrical networks which can later turn into permanent faults when line loading increases. Fault location, in this case, allows the network operator to identify weak points caused by transient faults on the network and deploy maintenance personnel to reinforce the system during routine preventive maintenance. Therefore, fault location improves power system reliability by reducing the outage time on the network and also mitigates the occurrence of faults in the future.

1.2 Conventional fault location methods

Fault location in distribution networks have long been performed in a primitive manner. The first line of defence against faults in an overhead distribution networks is usually autoreclosers. An autorecloser is a device which will de-energise a line and attempt to re-energise the line after a predefined dead time. For a transient fault, this operation is sufficient to clear the line of the fault and restore the network back to normal operation. In a situation where the fault persists after the first autoreclosing attempt, the autorecloser will perform the same operation a couple of times (usually three in all) before it goes into the lockout mode if it failed all attempts.

Once in the lockout mode, remote operation of the autorecloser is impossible and a maintenance crew has to be dispatched to the site to perform manual operation. For a network not fitted with fault indicators, the maintenance crew will proceed to locate the fault by trial and error method. The air break isolating switches (ABIS) at the beginning of each spur will be opened and the main feeder re-energised. The ABIS of each spur will then be closed one at a time and until the faulted section is located. The maintenance crew will then need to patrol the faulted section and visually identify the point of fault.

For networks fitted with fault indicators, the faulty section can easily be identified visually from the fault indicator such as flashing lights or a mechanical red flag. However, the exact point of fault is still not determined and the maintenance crew

still needs to patrol the line to find the point of fault. The fault indicator is usually a device which can easily sense the voltage and current levels on a line through sensors without any direct contact. The current level is picked up from the magnetic field while the voltage level is obtained from the electric field. The voltage and current levels are then compared to a threshold level to determine whether a given phase is faulty. The main advantage of this type of fault indicator is that it is easy to install on an existing network but one drawback is that it is not good in detecting faults involving a path to the ground since the small value of the zero sequence component may not be picked up by the magnetic sensor. A solution is to use fault indicators with iron core current transformers instead to measure the current levels. Another pitfall of fault indicators is that they have to be installed one pole after the T-point (point of connection) with the main feeder which leaves one span of line without fault indication[1].

Sometimes, system restoration can be achieved rapidly when faults are reported by power consumers themselves. There are numerous circumstances when phone calls from consumers have alerted the utilities of the location of a fault since sparks are often seen around a faulted section before the line is de-energised. Sparks can sometimes be difficult to observe in daylight and easier seen at night but faults occurring at night are seldom reported as there are fewer people on the streets at night.

1.3 Challenges of fault location in distribution networks

Extensive research has been carried out in developing modern fault location techniques in transmission lines since they are responsible for the bulk transfer of electrical power to consumers and any outage in transmission lines implies a larger amount of consumers will be affected as compared to service interruption in distribution networks. Fault location techniques in transmission lines can be broadly classified into impedances based methods, travelling wave methods and knowledge based approaches. Many have tried to apply the same techniques to distribution networks but these methods have encountered difficulties due to the nature of distribution networks. The characteristics of distribution networks as defined in [2] are their topology, the unbalanced loads and their heterogeneity.

The topology of distribution networks is different from that of transmission systems. Distribution networks are often radial systems with the source on one side and the loads on the other with the main feeders containing numerous load tap laterals/spurs. These spurs make fault location by existing transmission line fault location techniques difficult since transmission lines do not normally have spurs. Also, due to the short length of distribution network feeders and spurs, impedance based fault location methods often yield multiple solutions and hence prove to be inappropriate.

Distribution networks are also non-homogeneous since the cross-sectional area of conductors may vary on the network as opposed to transmission lines where the cross-section of the conductor is similar throughout the line. Distribution systems also often comprise of overhead conductors and underground cables. The higher capacitance in underground cables may lead to inaccuracies in fault location.

The types of load connected to distribution systems vary from single phase to three phase loads which cause the system to be unbalanced. Finally, the fault impedance in distribution networks is often higher than that in transmission lines. The high fault impedances cause damping of high frequency transients such that for high fault impedance values, the fault current level and load current level may look similar.

1.4 Renewable energy integration into electrical networks

The integration of renewable energy plants at distribution voltage level changes the system to an active network and this further justifies the need of fast response to outages in distribution networks. In the last few years, substantial effort has been made to use more renewable energy sources for electricity generation and cleaner alternatives for transportation. In the UK, these changes have been driven by the agreement of the UK government to meet the European Commission target of having at least one fifth of the total energies from the European countries to come from renewable energy sources by 2020 [3] and the Climate Change Act target of reducing the carbon footprint of the UK by 80 percent by 2050 [4].

Wind energy is, nowadays, a dominant alternative to electricity generation. Wind energy has been the mostly installed type of renewable energy technology in 2013 with a 10.5 GW of installed capacity available in UK only at the end of 2013.

According to the European Wind Energy Association (EWEA), the total installed capacity of wind energy across Europe represents around 8% of the European electricity consumption [5]. In 2012, onshore wind energy reached a milestone of 5 GW [6] with a further increase of 1.3 GW of installed onshore wind farm capacity by the end of 2013. The growth of onshore wind farm installations in the UK shows no sign of loss of momentum with around 1.6 GW of onshore wind farms in construction and another 7 GW in planning by the end of 2013 [7]. On the 17th of August 2014, wind farms across the UK produced 22% of the electricity consumption needs of the country, with contribution from coal and nuclear power being only 13% and 24% respectively on that particular day [8].

The increase in onshore wind energy integration can also be explained by the need for a balanced energy mix to ensure system security. Nuclear power plants can sometimes be shut down due to some problems and electricity generation from other sources need to compensate for the short supply. An example is the contribution from wind farms when Sizewell B nuclear plant was not producing electricity for a period of seven months in 2010 [9].

1.5 Aims of thesis

The aims of this work are to:

1. Investigate appropriate signal processing techniques for feature extraction from measured currents at the substation end for accurate fault classification and location in an active distribution network. Current signals are usually recorded on microprocessor based relays in the substation during fault conditions and these recorded waveforms can be used to locate faults in distribution networks. Current transformers for instrumentation and metering purposes are always present at the substation end whereas voltage transformers are often omitted as they are expensive devices.

2. Develop an accurate model of a 33 kV distribution network test system with a reasonable number of feeders, spurs and dynamic loads in ATP/EMTP and Simulink. Validate the test system by verifying the voltage and current waveforms obtained during normal and fault conditions. Simulate different

types of faults (single phase to ground, line to line, double line to ground and three phase faults) at various locations on the feeder and spurs to build a database of faults. The fault inception angles and fault impedances have to be varied so that the information can be later analysed to identify distinct signatures from each fault type.

3. Develop Artificial Neural Network (ANN) based algorithms for accurate fault classification and fault location in the active distribution network using only the distinct signatures extracted from the current waveforms by supervised learning. The algorithms need to clearly differentiate between faults on the feeder and spurs, and estimate the distance to the point of fault along the feeder or spur.

4. Investigate the impact of Type 3 (doubly fed induction generator) and Type 4 (permanent magnet synchronous generator) wind turbine systems on the extracted features from fault current waveforms by firstly identifying appropriate models of wind turbine systems for short circuit studies. Use these models to study the influence of these types of wind turbine configurations on the robustness of the developed fault classification and location algorithms.

5. Test the robustness of the developed algorithms by changing system parameters such as the fault inception angle, fault impedance and capacity of wind farms connected to the system. Further tests include the change in network configuration, change in line length, a change in source capacity, composite networks and the influence of white noise on the fault current signals.

Chapter 2: Fault location methods in distribution networks

2.1 Introduction

Over the past thirty years, researchers and power system engineers have mainly focussed their efforts in locating faults in transmission lines. There are several reasons that justify this choice. Firstly, any outage in transmission lines affects a larger number of consumers. Secondly, the structure of transmission line towers and the terrain where they are located often make it impossible to perform visual inspection on the lines from ground level. Nowadays, with a deregulated power system, there is a need to ensure reliability and quality of supply to consumers. The fierce competition between distribution network operators to provide better service to their customers has been one of the driving forces for fault location in distribution networks. Accurate and fast fault location reduces the outage time of the system thus improving the reliability of the system and reduces loss of revenue for the distribution network companies. The increase in interest in fault location techniques in these medium voltage networks also arises from an increasing number of distributed generation plants being connected into the system.

Most of the proposed methods for fault location in distribution networks have been adapted from that used in transmission lines and these can be classified as knowledge based methods, impedance methods, travelling wave techniques, signal injection method and computational intelligence methods. The methods had to be adjusted to cope with the different topology of distribution networks. In this chapter, a summary of the different techniques for fault location in distribution networks is given along with their advantages and limitations.

2.2 Knowledge based methods

The idea of a knowledge based method for fault location was introduced around twenty years ago with the objective of assisting operators to make an informed decision about the location of faults in distribution networks. In 1992, Eickhoff et al. [10] presented such an approach. The aim was to create a database of different types of faults at various locations while also taking into consideration the influence of external parameters such as environmental conditions. This database would then be

used alongside system information obtained from the SCADA system which will allow the network operator to make a more accurate decision on the actual fault location. One such method was proposed by Jarventausta et al. [11] in 1994 where the fuzzy sets were used to build an information database that can assist the operator to locate the fault on the network.

A distribution management system (DMS) is a similar knowledge based method for fault location in distribution networks. The underlying principle is to compare measured system parameters such as voltage and current signals during a fault to calculated values such that the fault can be located. A distribution management system requires adequate system information to accurately model an existing distribution network from which a database of various faults can be created. The main advantage of a DMS is that the system parameters are obtained from devices that are already installed on the network. Microprocessor relays at the substation are often able to record voltage and current signals which can easily be utilized by the DMS. This is appealing from an industrial perspective since no extra costs are necessary for the installation of new devices for measurement and recording. The other advantages of a distribution management system is that it can give further information such as the terrain where the fault occurred and the weather condition so as the maintenance crews are better prepared to restore system supply. Other additional features such as sending a warning signal to flag a fault, assistance in fault restoration and generating reports after the event of a fault make the system attractive to industrial application. The main disadvantage of a DMS is that the system only applies to locating short circuit faults in distribution networks [12].

Fault location using a knowledge based approach requires modelling of the distribution system to obtain information about different types of faults at various nodes on the network. Mora et al. [13] proposed using ATP and MATLAB to create a database from their simulation models. In addition to the recorded voltage and current waveforms at the substation, the voltage sag, type of load, frequency and time duration of transients, and Clark transform coefficients are required for accurate fault location. Chen-Fu et al. [14] proposed a different knowledge based approach for fault location in an underground distribution network. The method does not compute the distance to the point of fault but instead it identifies faults in specific components

of the distribution network such as fuses, transformers, cable joints or cable sections based on historical data and a Bayesian Network. A Bayesian Network is simply a probabilistic graphical model relating inputs to outputs based on a certain probability. For example, relating symptoms to diseases based on probability obtained from historical data. The developed fault location method was tested in Taiwan Power Company but it is unable to pinpoint fault position in a cable section.

Other different approaches for fault location in distribution networks were tested with the aim to improve the robustness of knowledge based methods [15-17]. One such method [17] combines the use of information collected at the substation end by disturbance recorders, relays or power-quality analysers with known system topology and electrical parameters to estimate the distance to the fault. Digital signal processing techniques are used to identify the faulted phases on the system and a three phase power flow calculation enables the determination of the prefault load power so as to reduce errors in fault location. The technique yields multiple solutions which are ranked in order of highest likelihood and a major drawback is that it does not operate for fault resistance values above 20Ω. A search algorithm has been developed in [15] to deal with the multiple possible fault positions by analysing which protective device operated on the system and the sequence of operation of each protective device. Another method that utilises voltage sag measurements and additional protective devices information on the system has also been proposed [16]. It is limited to single phase to ground faults and is largely affected by distributed generation (DG) connection since the voltage sag effect is cancelled by DG connection, hence resulting in higher fault location errors.

2.3 Impedance methods

Fault location using impedance methods have been mostly applied to transmission lines [18]. Impedance based methods are often referred to as fundamental frequency methods since they use the measured voltage and current signal to estimate the distance to the fault by computing the impedance during a fault. The impedance based methods can be further classified into one-ended techniques and two-ended techniques. In one-ended techniques, the voltage and current waveforms during a fault condition are measured from one end of the line only. Examples of such

methods are the simple reactance method, the Takagi method, the modified Takagi method and the Eriksson method. In the simple reactance method, the distance to the fault is computed by estimating the reactance of the line to the point of fault by assuming that the line is homogeneous and that the fault current measured at one end of the line is in phase with the fault current at the point of fault. The Takagi method is an improvement over the simple reactance method since it compensates for the load current thus reducing the fault location errors. The modified Takagi method further improves the accuracy of the impedance method by using the zero sequence network components to compensate for the load current and the non-homogeneous nature of the system [19]. Two-ended methods are usually more accurate than one-ended methods in computing the distance to the point of fault since the reactance can be estimated from both sides.

Reactance relays have been utilized in Austria and Germany for the purpose of fault location. This has been performed by dividing the line into much smaller segments, usually around 50 to 500 metres in length, and then short circuit analysis is carried out to determine the reactance at each segment. The different reactance values are stored in a database such that in the event of a fault in the network, the measured reactance is run through the database to find a match which then gives an indication of the corresponding segment where the fault is actually located. The accuracy of impedance based methods is sensitive to load currents, fault impedance, line impedance and errors in measurement devices [20, 21].

Vahamaki et al. [20] proposed a reactance based fault location method in distribution networks that is more accurate than other methods by compensating for the load current. The loading of the line affects the accuracy of the reactance methods because of the reactive component of the load current that can be present in the network. The reactance method is in itself better than the impedance method since the fault impedance is usually an unknown. The authors proposed compensating for the load current by estimating its magnitude from pre-fault, fault and post-fault information. The reactance is then computed to estimate the distance to the point of fault. A 20 kV distribution network test system with three feeders was set up in the EMTP/ATP software and the voltage and current waveforms were recorded on the primary side of the transformer in the substation. Although the authors claim that the

proposed fault location method is accurate, further sensitivity tests have to be carried out to determine the true potential of that method. One evident drawback of such a method is that laterals have not been considered on the feeder. Hence the overall performance of such a system is questionable.

A recent study [22] suggested that the bus impedance matrix can be a promising method in locating faults in active distribution networks with laterals. The authors developed separate algorithms for a radial distribution network and for an active distribution network. The measured voltage and current signals at the substation end are processed using the Discrete Fourier Transform (DFT) to obtain their frequency phasor components which are then fed into the fault location algorithms. The use of the phasor elements eliminates the sensitivity of the fault location algorithms to unbalanced systems. One major drawback of this approach is that information about the distribution network parameters and the system topology has to be known. The robustness of the proposed algorithms were tested by investigating the impact of changing load conditions, fault impedance and instrument transformer errors on the accuracy of fault location. The results showed that in some cases, multiple candidate solutions for the fault position were obtained and load current compensation has to be performed for accurate fault location.

Many studies have been carried out to make impedance based fault location methods more accurate. Some of the techniques proposed modelling of the load from load flow studies and accounting for losses and capacitive coupling by using a distributed parameter model [23] instead of a lumped model for improved accuracy. Others have studied the characteristics of fault currents for different types of system grounding [24], high impedance faults [25] and intermittent faults [26] to gain a better insight of improving fault location. Some researchers have derived complex equations using circuit analysis [27] for fault location but have encountered inaccuracies introduced by various system parameters. Impedance based fault location in underground networks are mainly affected by the capacitive currents in underground cables thus resulting in capacitive current compensation [28] studies. Finally, some researchers have dealt with the multiple solutions problem by combining an impedance based method with a travelling wave method [29] or by acquiring further information from intelligent devices connected to the system for an improved search algorithm [30].

2.4 Travelling wave methods

Travelling waves is a very common approach to fault location in transmission lines and its application to distribution networks have also been investigated in the past. The concept of travelling waves for fault location was first introduced by Dommel and Michels in 1978 [31].

A fault that occurs in a line generates high frequency transients which propagate along the line on both sides of the fault. These travelling waves are reflected back along the line when they encounter an impedance/discontinuity. The discontinuity can be anything from a busbar, the junction between a spur and a feeder and a point of fault. It should be noted that only part of the travelling wave is reflected back and this is often determined by the reflection coefficient. The reflection coefficient may be a function of the surge impedance of the line, the impedance of the power system elements connected to the line and last but not the least, the resistance of the fault [32]. Travelling wave methods can be classified into two main categories namely one ended methods and two ended methods. The one ended methods make use of the analysis of the high frequency components present in the transient signals and their travelling time to determine the fault location [33-35] whereas the two ended methods rely on the time tagging of the measurement signals at each end of the line to calculate the fault location [36, 37]. Therefore, for accurate fault location using the two ended methods, the travelling wave recorders at each end of the line have to be synchronised. This is not an issue nowadays since global positioning system (GPS) technologies are readily available for time based referencing.

A recent study [38] proposed using two travelling wave recorders at each end of a distribution network for accurate fault location. The test system was set up in the EMTP/ATP software and different faults were simulated on the network. The recorded voltage and current signals were then processed using the Wavelet Transform in MATLAB to obtain the time difference between the fault initiated transient wave and the reflected wave. The distance to the point of fault can then be calculated separately at the two ends of the line. The depth search method is then applied to eliminate multiple candidate solutions that can be obtained for a distribution network with laterals. The robustness of the proposed system was further

tested on the IEEE 34 bus test feeder network. This technique correctly identifies the faulted section of the network but it is not clear which distance to take from the point of observation as there are two of them and only one is correct. The other drawback is that the developed scheme has not been tested for changes in system parameters such as changes in fault impedance, distributed generation connection or even a change in network topology by simply disconnecting a lateral. It is also not very clear about how the author determined the location of the second travelling wave recorder on the IEEE 34 bus system since it could have also been placed at node 848.

Magnago F.H. and Abur A. [39] investigated the use of the Wavelet Transform for the decomposition of high frequency signals in recorded measurement signals for fault location in distribution networks. The authors had previously used the wavelet transform for fault location in transmission lines and have adapted that method to finding faults in distribution networks [36]. The recorded voltage waveform at the point of observation is first broken down into its modal components which are then analysed using the Wavelet Transform. The sum of the wavelet transform coefficients for the scale of 12-25 kHz are used to locate the faulted segment by comparing the recorded value to simulated values from a database. The distance to the point of fault is then evaluated mathematically whereby the laterals are replaced by the equivalent impedances. The authors also investigated the impact of the fault impedance on the accuracy of the proposed technique and found out that the fault impedance did not affect the sum of the wavelet transform coefficients for the range of 12-25 kHz [39].

Borghetti A. et al. [32] suggested the use of the Continuous Wavelet Transform to identify specific frequencies which can be related to the location of faults in distribution networks. The novelty of the study is that the authors defined their own mother wavelet from the fault generated voltage transient waveform that was recorded during a fault. The results of fault location were compared to those obtained using the conventional Morlet mother wavelet. The authors tested the proposed scheme on the IEEE 34 bus test system and concluded that the results obtained showed some positive features of the method but it had to be further developed. In a later paper, Borghetti A. et al. [35] used the time frequency resolution of the Wavelet Transform decomposition instead of only the frequency resolution to refine the

estimation of the distance to the point of fault. They used the same defined mother wavelet from their previous paper to perform the wavelet decomposition and fault distance results were slightly improved by using the time stamps of the fault transients to locate the fault.

Prony analysis has also been used to extract the frequencies from fault generated transients. The point of observation was located at the low voltage side of the distribution transformer and the characteristic frequencies were extracted from the voltage signal. A distribution network was set up in PSCAD/EMTDC to simulate different types of faults from which a database containing the various characteristic frequencies at the different locations was created. The measured voltage signal would then be processed using Prony analysis and the features compared to the database to find the closest match [40]. The proposed method was tested on a passive distribution network of very short length, which makes the conclusion of the authors that the adopted technique is practical and reliable system questionable. Tang J. et al. [41] also investigated the use of wavelet packet analysis for fault location in distribution networks. The proposed scheme is very similar to the one in [40] apart from the fact that Prony analysis was replaced by Wavelet Transform decomposition. The work again showed a lack of detailed investigation as only a passive distribution network was considered and general sensitivity tests that determine the robustness of the proposed method have not been performed.

2.5 Signal injection method

The signal injection method is the same technique that is currently used to locate faults in cables in distribution networks. The type of signal used in this method can be an ac signal of non-fundamental frequency, a dc signal or a pulse depending on the type of the network. The signal injection technique has to comply with the EN 50160 regulation which stipulates that the injected current should not cause the overvoltage level to exceed 10% of the rated voltage level. Signals can be injected on to the system in different ways namely by using the primary winding of a transformer or by interfacing it through an arc suppression coil. Current injection is usually more suitable for compensated networks, isolated grounded systems and high impedance grounded networks. The type of signal to be injected for fault location has

to be correctly determined since the accuracy of the technique is sensitive to the length of the line. A dc signal injection is preferred in most cases since the accuracy of the technique is not affected by line inductances and capacitances. The injected signal is easily detected by the use of Hall sensor handheld devices [42].

After sending a pulse into an underground cable, the reflected waveforms are recorded using a Time Domain Reflectometry (TDR) instrument. These waveforms are then analysed by experienced engineers to determine the location of the fault in the distribution network and it is often a daunting task. Navaneethan et al. [43] proposed an automated process to locate faults in distribution networks based on the TDR measurements. They developed a set of rules to analyse the TDR measurements and the results showed that the developed process was able to locate the faults with an acceptable accuracy.

2.6 Hybrid methods

In this section, methods that use a combination of techniques for fault location will be discussed. Hybrid methods often use feature extraction methods such as the Discrete Fourier Transform (DFT) or the Discrete Wavelet Transform (DWT) to obtain different characteristics from the measured voltage and current signals that can clearly define fault types at various locations. These characteristics are then used as inputs to Artificial Intelligence (AI) algorithms such as Artificial Neural Networks (ANN) or Genetic Algorithms (GA) which are trained to give the distance to the point of fault location as output. Hybrid methods have been widely employed for fault location in transmission lines [44-47] but their applications to distribution networks [48-51] have been minimal due to the complexity and technical differences of the latter when compared to transmission lines.

Thukaram D. et al. [52] proposed two schemes for the location of faults in distribution networks using Artificial Neural Networks. The first scheme is valid for short lines with a few laterals while the second scheme can be applied to longer lines with more laterals connected to the feeders. The distribution network has been modelled as a three phase four wire system and further tests were performed on the IEEE 34 bus test system to validate the proposed schemes. The schemes require pre-fault and fault information to estimate the distance to the point of fault and this is

done by using load flow analysis and short circuit analysis. The major drawback of the proposed approach is that measurements are not taken at only the substation. Fault location in the laterals is done by using radial basis function neural networks with the currents at the start of the lateral as the inputs.

Distribution networks often comprise of overhead conductors and underground cables. Fault location in medium voltage cables has been investigated in [53] using a combination of the Discrete Fourier Transform and the Artificial Neural Network. A section of a 33kV distribution system made up of a cable of length 80 km was modelled in the EMTDC software. The Bergeron model was chosen to represent the cable. The simulated signals were passed through a second order Butterworth anti-aliasing filter with a cut-off frequency of 400 Hz and further pre-processing of the signals were performed so as to reduce the number of input data to the Artificial Neural Networks thus reducing the size of the neural networks and improve training performances. The Discrete Fourier Transform was used as a feature extraction tool and the chosen patterns were fed to the neural networks as inputs. The hybrid methods are often a twofold process whereby fault classification is first obtained using one neural network algorithm and then the appropriate neural network is chosen for fault location. The fault classifier was constructed as a multilayer perceptron neural network with four inputs namely the phase current of each phase and the neutral line current. The network had four neurons in the output layer to identify which phases were faulty and whether ground was involved in the fault. Once the fault type was identified, the corresponding fault location algorithm was selected to estimate the distance to the fault. The sensitivity tests showed a good overall response of the fault location algorithms except for faults located close to the source. One major drawback of the proposed scheme is that it has not been tested on a more realistic distribution network with spurs.

The increase in the number of distributed generation connected to distribution networks has led to the investigation of the impact of these systems on hybrid based fault location methods. Javadian et al. [54] suggested the use of the measured current signals at the substation end along with the current contribution of each distributed generation unit for fault location in distribution networks. According to the authors, this method does not involve any extra cost for installing monitoring devices at the

distributed generation end since the IEEE 1547 standard already specifies that the monitoring of the output current of distributed generation is an obligation prior to connection. The test system was set up in the DIgSILENT software and simulations for different types of faults were carried out at every 100 metres on the distribution network. The fault resistance was also varied from 0 to 150 Ω in steps of 50 Ω. Four multilayer perceptron neural networks were built to determine the fault location for each category of fault namely single phase to ground, line to line, double line to ground and three phase faults. The main drawback of the work is that an inadequate number of sensitivity tests were performed on the proposed scheme and the distributed generation was simply represented by a voltage source. In a later work [55], the same scheme was proposed but the multilayer perceptron networks were replaced by radial basis function neural networks (RBFNN). The only addition to the scheme was that the distance to the fault was estimated by the appropriate radial basis function neural network and then a second neural network would identify the segment where the fault occurred. A comparison study [56] also showed that the radial basis function had a slightly much better performance than the multilayer perceptron for fault location.

2.7 Summary

It has been seen that fault location methods in distribution networks can be broadly classified into five categories, namely knowledge based methods, impedance based methods, travelling wave methods, signal injection method and hybrid methods. Table 2.1 summarises the applicability and practicalities of the various fault location methods. Knowledge based methods can have a low cost of implementation but they require accurate modelling of the network with additional information from protection relays or power quality analysers to determine the location of a fault in distribution networks. These methods are sometimes restricted to single phase to ground faults only and their accuracies are influenced by fault impedances.

Impedance based methods use only the fundamental frequency component of voltage and current to calculate the impedance to the point of fault so as to determine its location. As such, the high frequency transients that can contain essential information about a particular type of fault are discarded. It is also assumed that the network is

homogeneous. Impedance based methods are affected by the phase angle between the voltage and current waveforms and due to the short lengths of distribution networks and the presence of spurs, these techniques yield multiple possible fault locations.

Fault location technique	**Applicability**	**Pros**	**Cons**
Knowledge based	Transmission and distribution network	Low cost and good accuracy in transmission lines	Requires accurate modelling, extensive fault simulations, additional data from fault indicators and power quality analysers
Impedance	Transmission and distribution network	Low cost and good accuracy in transmission lines	Multiple fault positions in distribution networks, assume homogeneous network, errors due to load currents, fault impedance etc.
Travelling wave	Transmission and distribution network	Good accuracy in transmission lines	Expensive, multiple fault positions in distribution network
Signal injection	Distribution network only	Good to locate faults in underground cables	Performance depends on signal type and line length, cumbersome
Hybrid	Transmission and distribution network	Good accuracy in transmission lines, low cost, algorithm can be neatly integrated in a digital relay	Multiple solutions in a distribution network, AI training issues

Table 2.1: Practicalities of fault location techniques

Travelling wave methods can be expensive to implement as the accuracy of the method requires accurate time tagging of the signals. In a distribution network, reflections of the surge propagating along the line after the inception of a fault can cause difficulties in identifying the reflection from the fault. Hence, travelling wave methods require the deployment of travelling wave recorders across the network to achieve higher fault location accuracy and as such are not economically viable. Also, choosing the ideal location of the travelling wave recorders on the network is challenging.

The signal injection method has also been employed for fault location in underground cable sections but in general this method is tedious and cumbersome as it requires the deployment of the maintenance crew. Moreover, the accuracy of the method relies on the type of signal injected, the length of the line and the interpretation of the recorded signals. Hybrid methods are more promising as they analyse the information contained in the fault voltage and current signals using advanced signal processing tools so as to obtain distinct features about different types of faults. These features are then used to train Artificial Intelligence algorithms to estimate the distance to the fault. These algorithms can be neatly integrated into digital relays and therefore have a low cost of implementation. Hybrid methods require detailed models of electrical networks but are better at dealing with the non-linear relationship better various system parameters and the distance to the fault.

In general, it has been observed that the fault location methods yield multiple fault positions when applied to a distribution network. The algorithms are not able to differentiate between a fault on a feeder and a spur. Moreover, general sensitivity tests such as a change in load, network topology or source capacity that investigate the impact of non-algorithmic errors on the accuracy of the proposed techniques are rarely performed. This questions the practicality of the fault location methods and it is therefore difficult to ascertain their robustness in a real distribution network. Hence, my proposed method will have to address the above mentioned short-comings of the previous methods and be able to operate in a real environment.

Chapter 3: Electricity from Wind

3.1 Introduction

Wind energy integration in transmission and distribution networks in the UK, has escalated over the past few years. The increase in wind energy penetration is mainly driven by the agreement of the UK government to ensure that fifteen percent of all the country's energy requirements (electricity, heating and transport) will be provided from renewable energy sources by 2020 [57].

In 2009, the Renewable Energy Strategy presented to the Parliament, stated that this target can be achieved by different renewable energy contributions from various sectors namely thirty percent from electricity production, fifteen percent from heating requirements and ten percent from the transportation sector. At the end of 2013, around fifteen percent of UK's electricity generation came from renewable energy sources with 63% supplied from coal and gas combined as shown in Figure 3.1 [58].

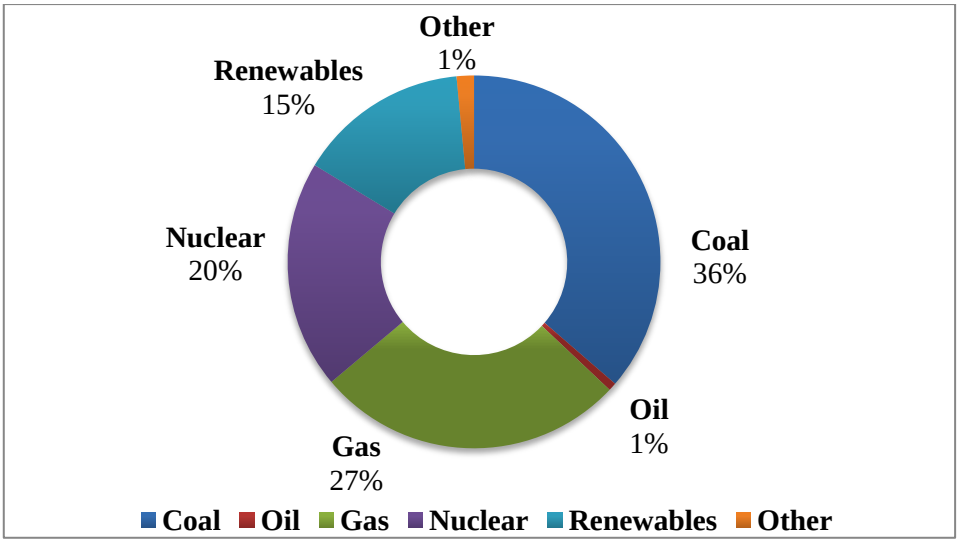

Figure 3.1: UK electricity generation mix 2013

Onshore and offshore wind turbines produced around 40% of the electricity supplied from renewable energy sources, with 24% supplied by biomass. Figure 3.2 shows the share of electricity generated from various sources of renewable energy for the second quarter of 2014 [59].

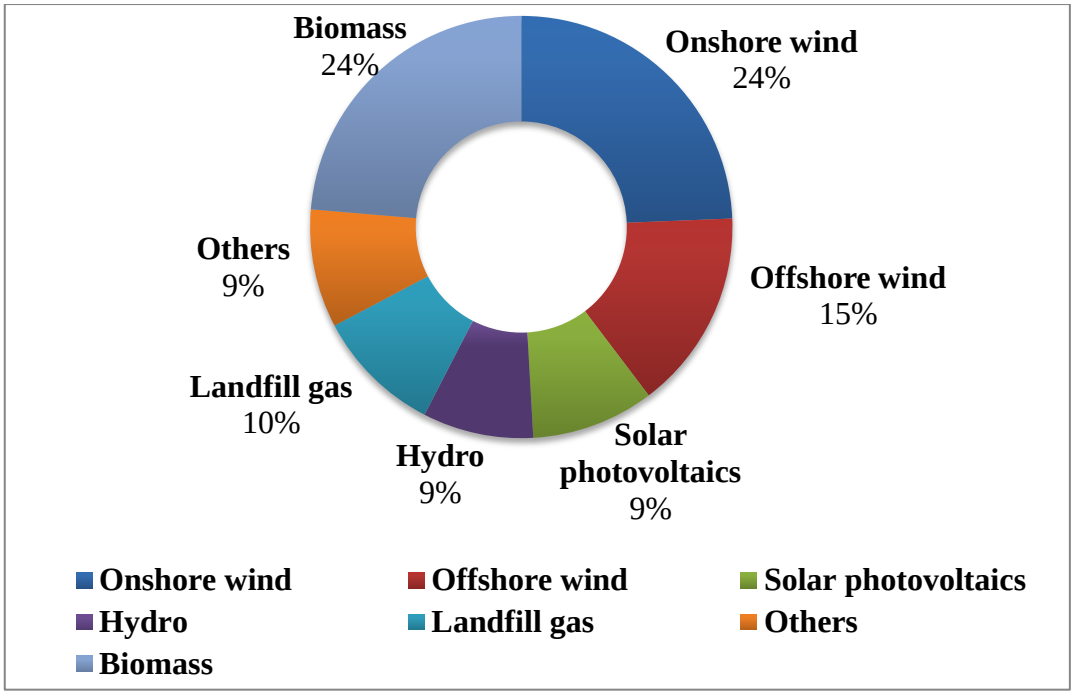

Figure 3.2: Electricity produced from renewable energy mid 2014

In June 2013, statistics showed that around 6.4 GW of power were available from onshore wind farms, representing nearly twice the amount available from offshore wind farms in the same time period (Figure 3.3).

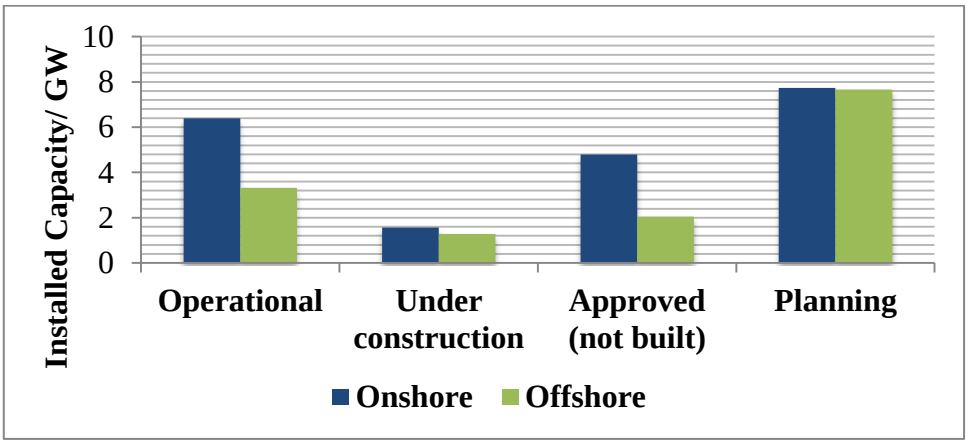

Figure 3.3: UK onshore and offshore wind turbine statistics [60]

Onshore and offshore wind projects in the planning phase accounted for nearly 15 GW of future installed capacity, showing a keen interest in wind turbine technology in the coming years.

3.2 Basics of wind energy

Wind energy has been harvested for a long time for different uses ranging from basic applications such as sailing, to converting the energy to potential energy to pump water for storage and also most importantly to produce electricity. The first electricity generating wind turbine was built by Professor James Blyth in Glasgow in 1887 [61] to charge accumulators to power lighting but the work of Poul la Cour, a Danish scientist, was probably more interesting since he was using the electricity to electrolyse water to produce hydrogen gas [62].

The power in the wind is directly proportional to the cube of the wind speed. The power also depends on the density of the air and the area covered by the device capturing the wind. The air density itself is dependent on altitude and temperature and in the case of a wind turbine with a blade, the area is dependent of the length of the blade. Equation 3.1 shows the relationship between wind power, air density, swept area of a blade and the wind speed.

$$P_W = \frac{1}{2}\rho A v^3 \qquad \text{Equation 3.1}$$

where ρ is the air density in kg/m^3

A is the swept area in m^2

and v is the wind speed in m/s

The power that can be harvested from the wind is only a fraction of the power contained in the wind. German physicist Albert Betz, demonstrated that the power that can be extracted from the wind is dependent upon the ratio of downward wind speed to upward wind speed as shown in Figure 3.4. The power extracted from the wind by the wind turbine blades can therefore be expressed as in Equation 3.2.

$$P_{extracted} = \frac{1}{2}\rho A v^3 . \left[\frac{1}{2}(1 + \lambda)(1 + \lambda^2)\right] \qquad \text{Equation 3.2}$$

where λ is the ratio of the downward wind speed to the upward wind speed i.e. $\lambda = \left(\frac{v_d}{v}\right)$.

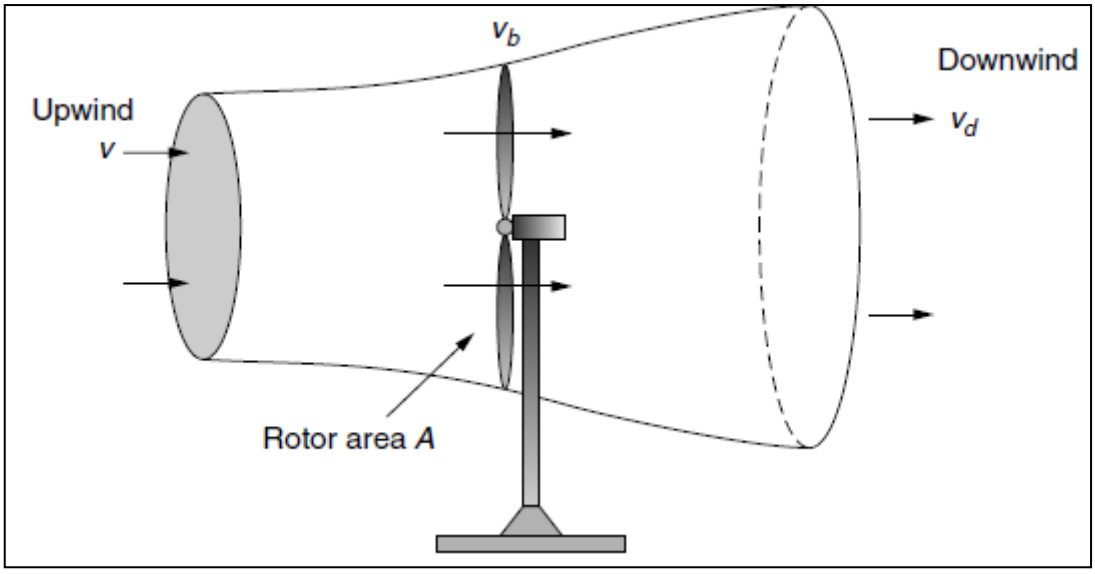

Figure 3.4: Power extracted from wind [62]

The additional term to the power extracted equation is referred to as the rotor efficiency C_p given in Equation 3.3. The maximum theoretical rotor efficiency can be calculated by equating the first derivative of the equation to zero, i.e. $\frac{dC_p}{d\lambda} = 0$.

$$C_p = \left[\frac{1}{2}(1 + \lambda)(1 + \lambda^2)\right] \qquad \text{Equation 3.3}$$

This gives a value of maximum rotor efficiency of around 59.3% indicating that two fifth of the power in the wind is not captured by the blades. In order to operate at maximum efficiency, the rotor blades should turn at a reasonable speed since if the blades turn too slowly, not enough power is captured from the wind. On the other hand, if the blades turn too fast, then the turbulence created by each blade negatively affects the performance of the other. The speed of the blade with respect to the wind speed is given by the tip-speed ratio and is expressed as in Equation 3.4.

$$Tip - speed\ ratio = \frac{Rotor\ tip\ speed}{Wind\ speed} = \frac{rotor\ rpm\ \times\ \pi D}{v} \qquad \text{Equation 3.4}$$

where D is the rotor diameter.

A plot of rotor efficiency against tip-speed ratio is given in Figure 3.5. It shows a comparison of the efficiency of different types of wind turbine systems to the ideal case i.e. the Betz efficiency. As it can be seen, the tip-speed ratio for maximum efficiency is higher for systems with fewer blades (around 0.8 for a multi-blade system as compared to around 4 for a modern wind turbine with 3 blades) and the maximum efficiency of all of the existing wind turbine systems are much lower than the ideal maximum rotor efficiency of Betz. In fact, horizontal axis 3 blade wind turbines can only reach around 80% of the Betz limit.

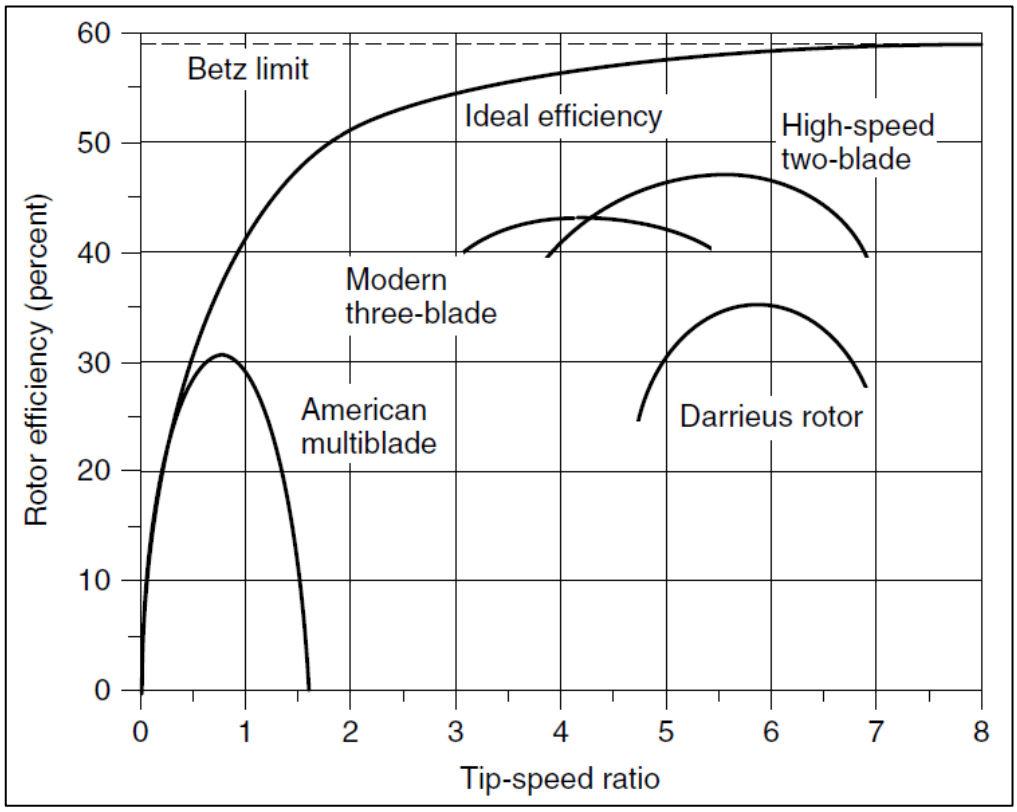

Figure 3.5: Rotor efficiency versus tip-speed ratio for various wind turbine systems [62]

3.3 Wind turbine technologies

3.3.1 Fixed-speed wind turbine

All wind turbines that were first introduced for electricity generation around two decades ago were fixed speed systems. As the name suggest, the rotor speed remains fixed irrespective of the wind speed. This is done by adjusting the mechanical power output of the wind turbine at different wind speeds using a pitch controller (as explained in Section 3.4).

Figure 3.6 shows a Type A, fixed speed wind turbine speed, coupled to a squirrel cage induction generator (SCIG) to export electrical power directly to the grid through a transformer. The generators that can be used for fixed speed wind turbines are either squirrel cage induction generators or wound rotor induction generators (WRIG) that are directly coupled to the grid. Induction generators tend to absorb reactive power from the system thus capacitor banks for reactive power compensation are connected to the generators. Moreover, a soft-starter is required to limit the inrush current which can cause voltage disturbances on the grid. Two winding sets are often used to obtain maximum efficiency for such configurations, a low speed winding with 8 poles and a high speed winding with 4 to 6 poles.

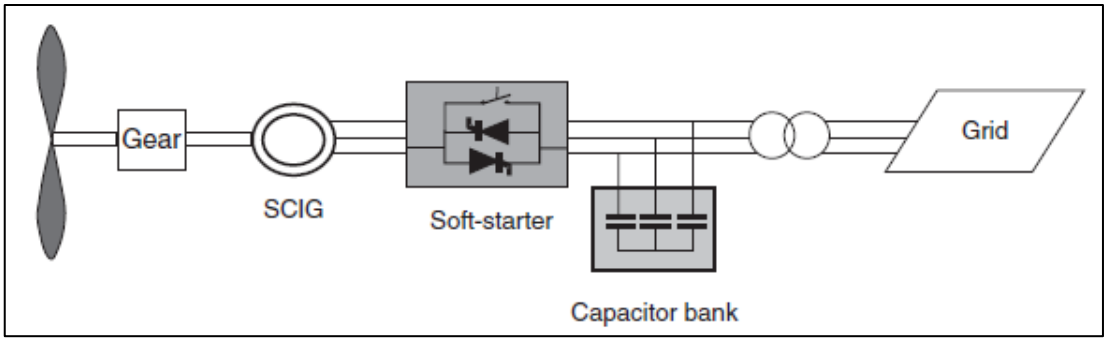

Figure 3.6: Type A wind turbine configuration [63]

The advantages of fixed speed wind turbines are that they are simple, sturdy and low cost. Their major disadvantages are that power quality control is very limited and power fluctuations on the rotor side are easily conveyed to the grid thus resulting in power losses.

3.3.2 Variable speed wind turbine

Variable speed wind turbines allow the generator torque to be maintained at a near constant value by keeping the tip-speed ratio constant. This allows maximum efficiency to be obtained over a range of wind speeds. Figure 3.7 shows a Type B wind turbine configuration, also referred to as a limited variable speed system. This configuration has been used by Vestas. The variable resistance allows the slip of the rotor to be controlled thus allowing power output control of the wind turbine. The wound rotor induction generator (WRIG) is interfaced to the grid through a transformer and capacitor banks provide reactive power compensation of the system.

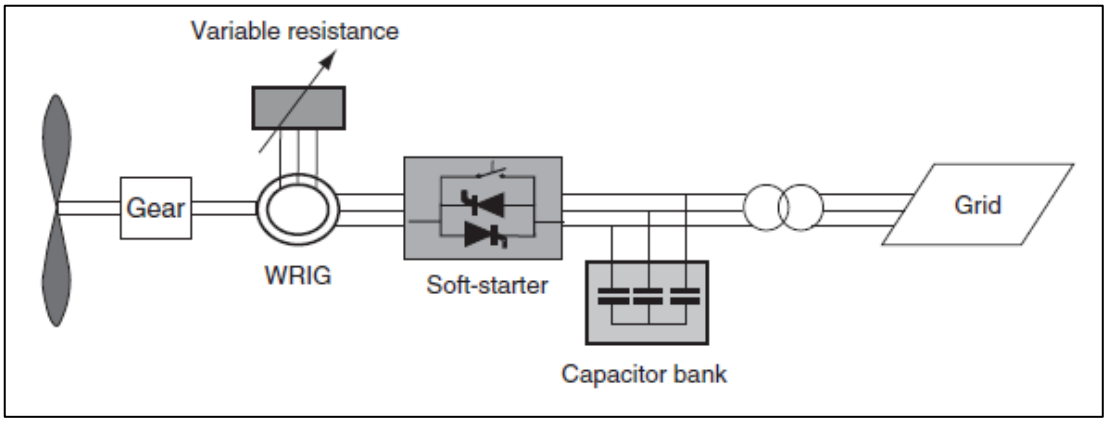

Figure 3.7: Type B wind turbine configuration [63]

Variable speed wind turbines may also be interfaced to the grid through power electronic converters. Figure 3.8 shows a Type C wind turbine configuration, also commonly referred to as the doubly fed induction generator (DFIG), as the rotor circuit of the wound rotor induction generator is partially fed by a frequency converter. The role of the frequency converter is to perform reactive power compensation and better grid connection.

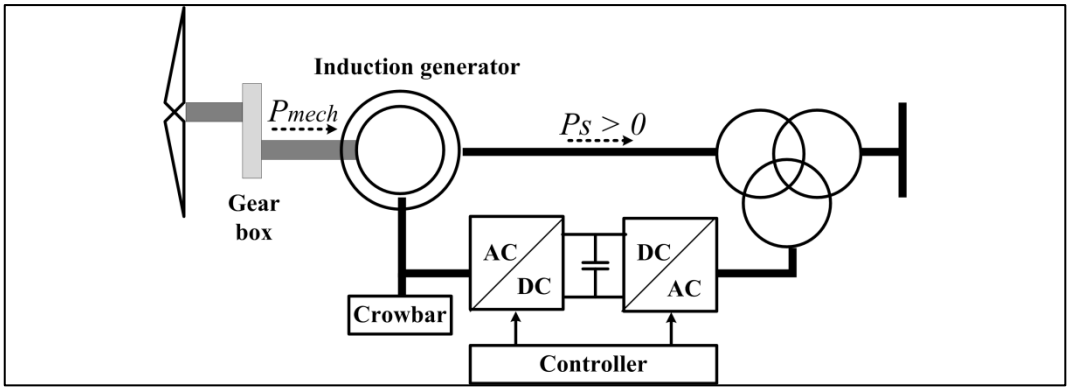

Figure 3.8: Type C wind turbine configuration

Type D configuration (Figure 3.9) has the generator connected to the grid through a full scale frequency converter that performs reactive power compensation. The generator can be a wound rotor induction generator (WRIG), a wound rotor synchronous generator (WRSG) or a permanent magnet synchronous generator (PMSG). The gear box is shown in dotted lines because in some systems such as the Enercon wind turbines, the gear box is omitted and a direct driven multiple pole generator is used [63].

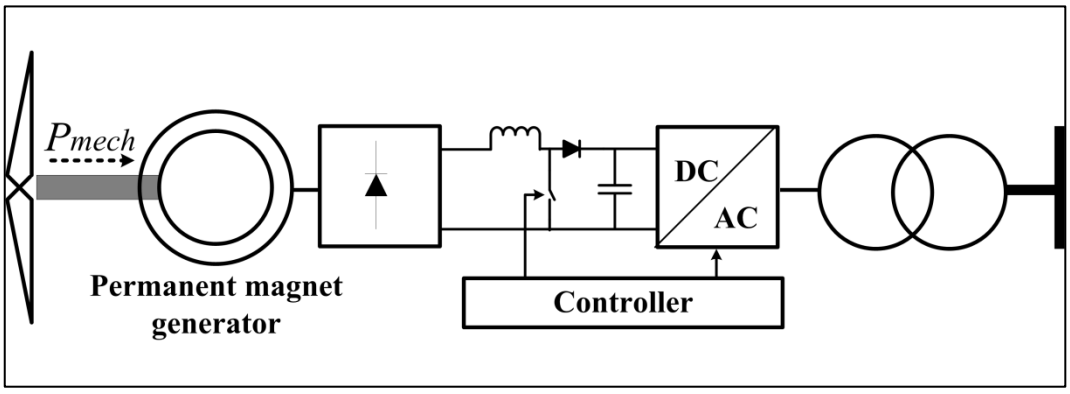

Figure 3.9: Type D wind turbine configuration

The advantages of variable speed wind turbines are that more energy can be harvested from the wind and the power electronic converter allows the power fluctuations to be controlled. The main disadvantage is the added cost due to the power electronic devices.

3.4 Power control strategy

The power curve of a wind turbine provides useful information when choosing a wind turbine for a particular application. The power curve illustrates the output power of the generator versus the wind speed and is provided in the manufacturer's datasheet. A typical power curve for a wind turbine generator is shown in Figure 3.10.

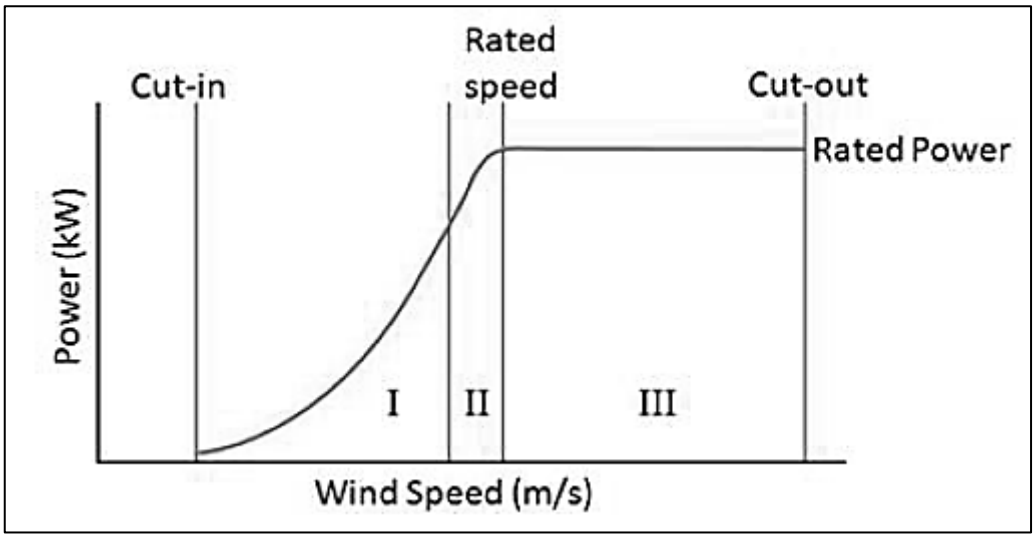

Figure 3.10: Power curve of a wind turbine

The cut-in wind speed is the minimum wind speed for the generation of electrical power i.e. no power is generated below the cut-in speed. The cut-out wind speed defines the limit beyond which the turbine stops generation to protect it from high wind speeds. Within the operating region (i.e. between cut-in and cut-off speeds), the output power varies at approximately the cube of the wind speed above the cut-in speed until it reaches the rated wind speed. The output power is at the rated power of the generator when operating at the rated wind speed. Above the rated wind speed, some mechanism has to be activated to shed the excess power produced by the wind to prevent any damage to the blades and/or generator. This can be done by pitch control, stall control and active-stall control.

3.4.1 Pitch control

Pitch control is carried out by varying the angle of attack, $\alpha_{A,}$ of the blade, i.e. by turning the blades either in or out of the wind, to control the aerodynamic forces acting upon the blades. When the angle of attack is increased (by mechanical action) to its critical angle $\alpha_{critical}$ at high wind speeds, laminar flow over the blade is no longer possible, thus creating turbulences that have a braking effect on the blades (stall effect) [64]. This offers good control and maintains the output power close to the rated value at high wind speeds. In Figure 3.11, the angle of attack of the blade is reduced at high wind speeds so as to reduce the force acting on the blades. This operation is referred to as 'pitch to feather'.

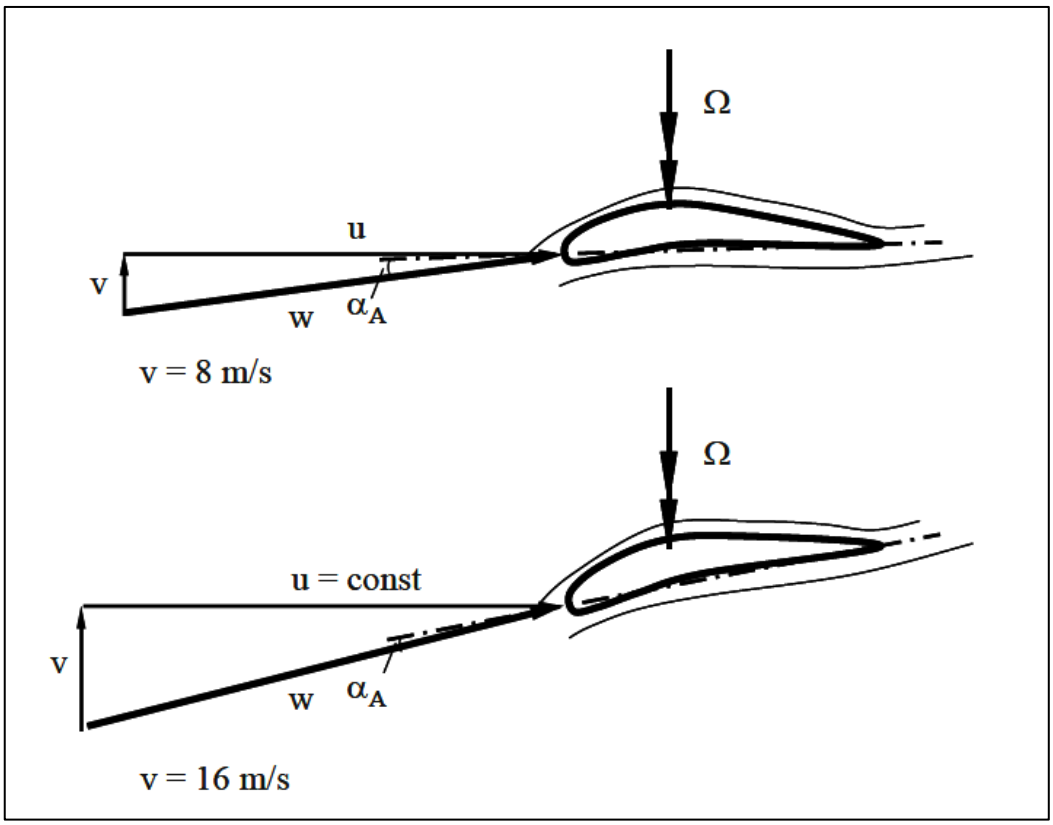

Figure 3.11: Pitch control of blade [64]

3.4.2 Stall control

In stall control (passive control), the stall effect is created by the aerodynamic design of the blade itself and the blades are not moved in any way. At high wind speeds,

turbulences created over the blade reduce the power captured from the wind. Figure 3.12 illustrates stall control at high wind speeds.

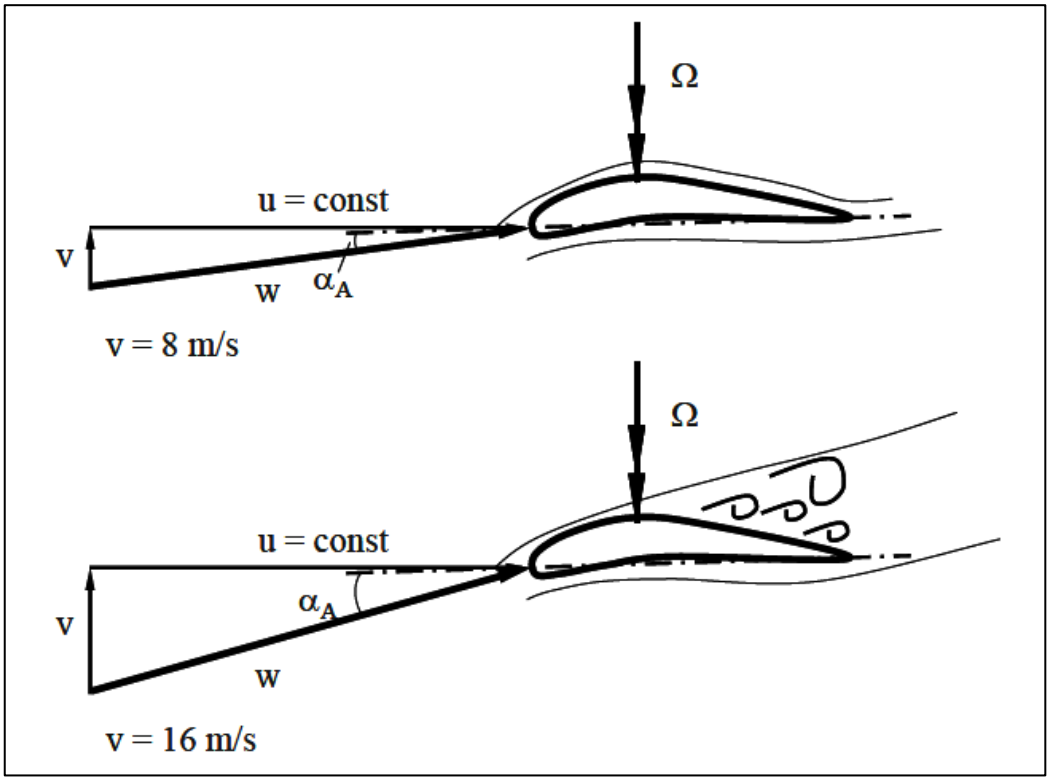

Figure 3.12: Stall control at high wind speeds [64]

3.4.3 Active stall control

Active stall control is a combination of pitch control and stall control. It allows a smooth power control by pitching the blades at low wind speeds and using stall control at high wind speeds.

3.5 Short circuit contribution of wind turbine generators

As seen in Section 3.3, wind turbine technologies employ various types of electrical generators to export electricity to the grid namely squirrel cage induction generators, wound rotor induction generators, doubly fed induction generators and permanent magnet synchronous generators. The doubly fed induction generator and the permanent magnet synchronous generator export power to the grid through a power electronic converter and as such, the short circuit behaviour of these types of wind turbine generators are not similar to a conventional synchronous generator. In fact, not only do the various types of wind turbine generators have dissimilar short circuit contribution to a fault but variations within a particular type of wind turbine generator design can also produce a different response to a fault [65-68].

Figure 3.13 typifies the short circuit current variation with time according to BS EN 60909-0:2001 for a short circuit fault located close to a synchronous generator. A near-to-generator short circuit fault is usually defined by the fact that the short circuit contribution from one synchronous generator is more than twice its rated current [69]. The initial stage of the short circuit current, i.e. the subtransient component, occurs for a few cycles after the fault inception and is defined by the subtransient reactance X_d''(impedance between the stator winding and the damping winding).

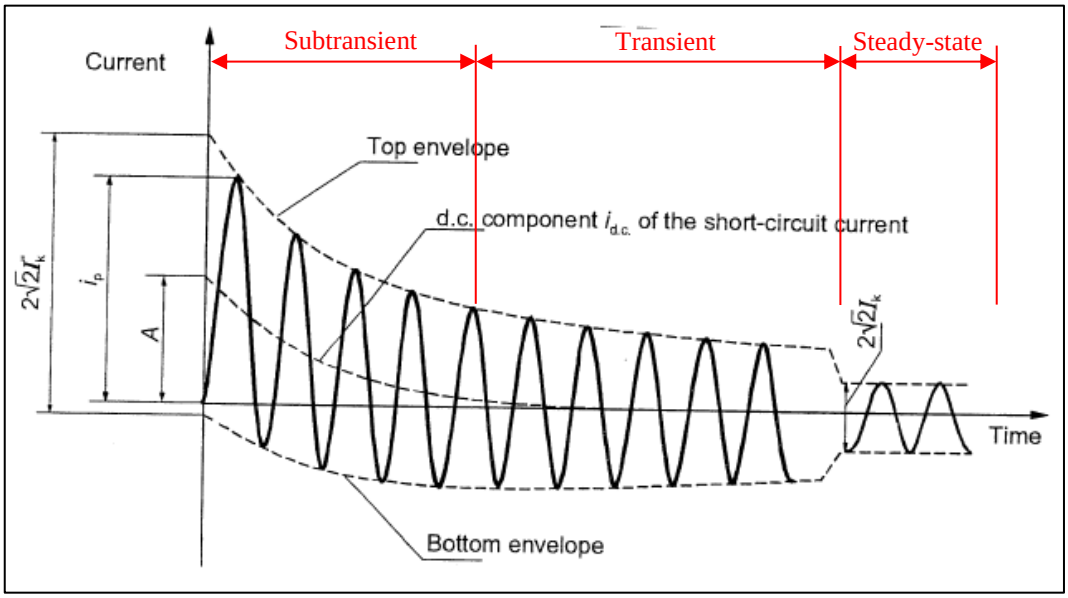

Figure 3.13: Short circuit current for a fault near to a generator [69]

The transient period may last for several cycles depending on the size of the synchronous generator and is defined by the transient reactance, X'_d, which is the reactance between the stator winding and the exciter windings. Finally, the short circuit current in the steady-state period is given by the synchronous reactance X_d of the synchronous generator [69].

In this section, the short circuit contribution from Type A, Type B, Type C and Type D [63] wind turbine configurations will be presented. (Note: These wind turbines configurations are sometimes also referred to as Type 1, Type 2, Type 3 and Type 4 systems [65])

3.5.1 Type A wind turbine

The Type A wind turbine is a fixed speed wind turbine with the squirrel cage induction generator directly connected to the grid. The blades of the wind turbine are coupled to the rotor and at speeds above the synchronous speed, the generator exports power to the grid as shown in Figure 3.14.

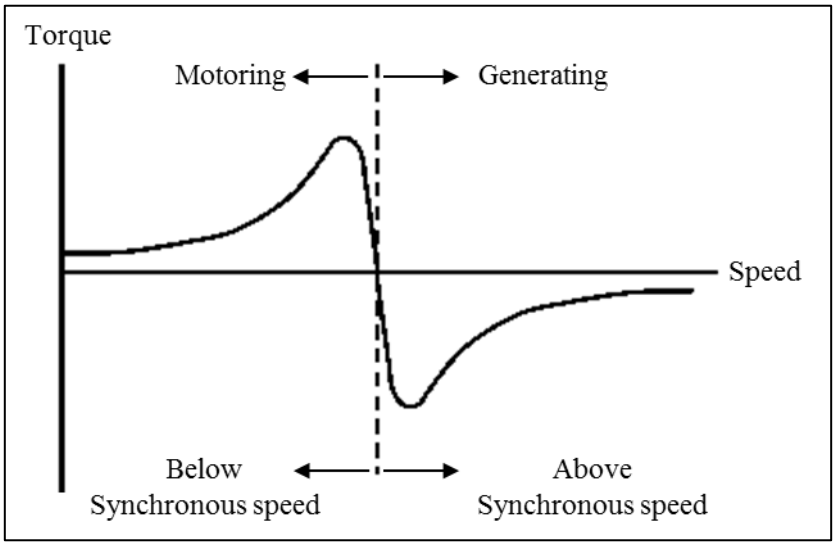

Figure 3.14: Torque-speed characteristic for an induction machine

The induction generator requires reactive power from the grid for proper operation and some form of reactive power compensation is always present for Type A wind turbine systems. Also, during a fault, a large amount of reactive power can be drawn from the grid which may lead to collapse of system voltage if no reactive power

compensation is present. This hinders the low voltage ride through capability function of Type A wind turbine systems in the absence of dynamic reactive power compensation [65].

The short circuit behaviour of a Type A wind turbine configuration can be represented as a voltage source in series with a subtransient reactance as in the case of a synchronous generator [70]. For unbalanced faults, the positive sequence and negative sequence impedances can be represented by the substransient reactance [65].

3.5.2 Type B wind turbine

A Type B wind turbine configuration provides a limited variable speed capability and is made up of a wound rotor induction generator with an external controllable resistance connected to the rotor windings. The external resistance enables the torque-speed characteristics of the machine to be controlled, hence allowing operation over a range of wind speeds. Type B wind turbine systems also require reactive power compensation and have issues to cope with low voltage ride through capability requirement for grid connection [65].

The short circuit contribution of a Type B wind turbine configuration is similar to a Type A system and can also be represented by a voltage source behind a subtransient reactance [65, 71].

3.5.3 Type C wind turbine

In the Type C wind turbine configuration, the wind turbine generator is a doubly fed induction generator. The rotor current is supplied through an ac-dc-ac power electronic converter connected to the grid and therefore, both the magnitude and phase of the rotor current can be controlled to operate over a variable wind speed range. Usually, output power can be exported to the grid at power frequency (50 Hz or 60 Hz) for a range of speed of ± 33% of synchronous speed.

At speeds below the synchronous speed, real power flows into the rotor of the doubly fed induction generator whereas at speeds over the synchronous speed, real power is generated in both the rotor windings and stator windings and the combined power

exported to the grid. At synchronous speed, dc excitation is provided to the rotor and thus the power flow into the rotor is only to compensate for the copper losses in the rotor winding. The power electronic converter allows control of reactive power (given by the magnitude of rotor flux) and active power (given by the phase of rotor flux) into the electrical machine or into the grid and the power electronic switches (IGBTs) enable fast response of the electrical machine thus making the Type C wind turbine configuration suitable for the low voltage ride through requirement of the grid [65].

The short circuit behaviour of a Type C system depends on the operation of the crowbar circuit. A fault that occurs on the network can induce currents of high amplitudes in the rotor circuit due to the magnetic coupling between the stator windings and the rotor windings and thus damage the rotor windings. It can also cause an overvoltage in the DC link and damage the power electronic converter. The doubly fed induction generator operates as a controlled current source for faults below a certain degree of severity. The level of severity of the fault is determined by the voltage level at the generator terminals during a fault. For severe faults on the network, a crowbar protection is used to limit the magnitude of the currents flowing in the rotor circuit [72-74].

The crowbar schemes used in wind turbine systems can be classified as a passive scheme or an active scheme. In the passive scheme, the crowbar is activated by monitoring the magnitude of the rotor current and the DC link voltage. Once triggered, the crowbar stays on until the generator is disconnected from the network. In order to comply with the low voltage ride through requirement, an active crowbar scheme is used instead. The crowbar stays connected for a few cycles until the magnitude of the current in the rotor and the DC link voltage have been limited to a certain value after which the crowbar is disconnected from the rotor circuit [75]. The short circuit behaviour of a Type C wind turbine configuration is similar to an induction generator when the crowbar protection is activated and behaves more like a controlled current source when the crowbar is deactivated. This implies that for unbalanced faults on the network, the positive sequence and negative sequence components are coupled as opposed to in the case of a synchronous generator [72].

Therefore, using a voltage source behind a subtransient reactance is not an accurate representation of a Type C wind turbine.

3.5.4 Type D wind turbine

In this type of wind turbine configuration, the wind turbine generator can be a synchronous generator with wound rotor, a permanent magnet synchronous generator or an induction generator but all the power is exported to the grid through an ac-dc-ac power electronic converter. The output current of this type of wind turbine configuration is controlled through the firing of IGBTs in the power electronic converters. These devices are very sensitive to the current flowing through them and the voltage across their terminals. A control mechanism protects the IGBTs from failure due to high fault currents and therefore, their contribution to short circuit currents on the network during a fault is very limited. Hence, their short circuit behaviour is dissimilar to that of a voltage source behind a subtransient reactance and is mainly defined by the inverter characteristics [65, 72, 76].

3.6 Market trends

This section aims at identifying the main manufacturers of wind turbines for onshore wind connections and also to identify the most dominant designs currently on the market. This enables accurate mathematical models of these wind turbine configurations to be integrated in the implementation part of this thesis and their short circuit behaviour studied. Figure 3.15 shows that Siemens is the dominant choice of manufacturer of onshore wind turbines, based on the amount of wind turbines commissioned in the UK from 2012 to 2013 (29 %). Vestas follows closely with 25% of the market share.

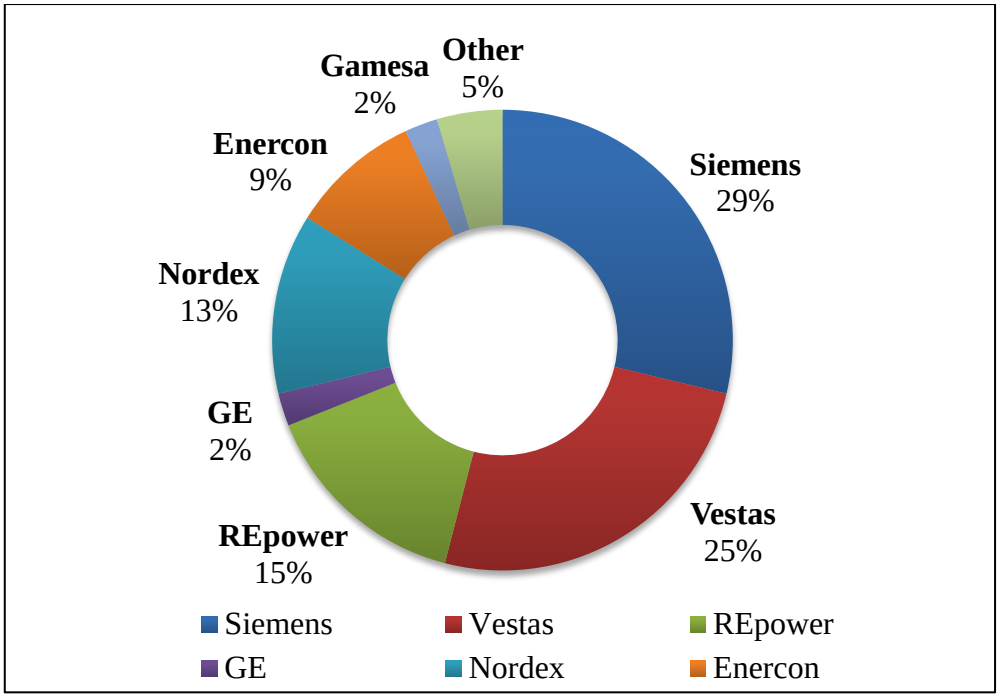

Figure 3.15: Onshore wind turbine manufacturers UK market share 2012-2013 [60]

In terms of wind turbine configurations, Type D wind turbines became increasingly popular from 2000 to 2009 while Type C wind turbines are the dominant designs on the market. Type A and Type B systems have been phased out by wind turbine manufacturers [77]. According to Reference [77], a gearless wind turbine is more attractive to companies since it is becoming more complex to interface Type C wind turbines to the grid due to rigid grid code regulations and, in offshore applications no gearbox implies easier maintenance of wind turbines.

Table 3.1 gives the types of configurations designed by the top wind turbine manufacturers which are currently available on the market for onshore wind farm solutions. Firstly, it can be seen that a pitch control mechanism is widely used to control the rotational speed of the wind turbine blades. Secondly, the generators employed are either doubly fed asynchronous generators (Type C) or permanent magnet synchronous generators (Type D).

Manufacturer	Model	Power regulation	Generator type
Siemens	SWT-2.3-101	Pitch control	Type C
	SWT-2.3-108	Pitch control	Type C
	SWT-3.0-101	Pitch control	Type D
	SWT-3.2-108	Pitch control	Type D
Vestas	V110-2.0	Pitch control	Type C
	V105-3.3	Pitch control	Type D
Nordex	N100/3300	Pitch control	Type C
	N117/3000	Pitch control	Type C
	N131/3000	Pitch control	Type C

Table 3.1: Survey of modern wind turbine configurations [78-80]

3.7 Summary

It has been seen that the power contained in the wind is proportional to the cube of its velocity but only around 59 % (Betz maximum efficiency) of the power can be harvested by the blades of a wind turbine in an ideal situation. To prevent damage to the blades of the wind turbine at high wind speeds, power control strategies such as pitch control, stall control and active-stall control are often employed to prevent mechanical damage of the blades.

A survey of current wind turbine technologies has showed that Type C (doubly-fed induction generator) and Type D (permanent magnet synchronous generator) variable speed wind turbine systems are the dominant designs on the market for onshore wind turbine solutions and therefore the impact of only these two types of wind turbine configurations on the accuracy of the developed fault classification and location algorithms in distribution networks will be investigated.

It has also been found that Type C and Type D systems cannot be modelled as a voltage source behind a subtransient reactance as the short circuit behaviour of Type C wind turbine configurations depend on the crowbar protection and that of Type D wind turbine configurations depend on the characteristics of the power electronic converters.

Chapter 4: System modelling and simulation

4.1 Introduction

This chapter is focussed on developing an accurate typical 33 kV active distribution network. Firstly, an accurate model of a 33 kV distribution network is set up in Simulink comprising of feeders and spurs. The spurs have loads connected to them through distribution transformers. Then, details on the wind turbine models used in Simulink are given. The wind turbine configurations are validated by observing their power contributions during normal operation and also by simulating their short circuit behaviour during fault conditions, to ensure that their voltage and current signatures match that of the manufacturer's technical specifications. Different types of short circuit faults are then simulated on the developed 33 kV distribution network. The simulated voltage and current signals enable the validation of the accuracy of the developed network for fault location studies.

4.2 Implementation of a typical 33 kV distribution network

The selection of an appropriate test system was a tedious task as the test system had to be simple but accurate so as various experiments could be carried out on it. The first test system to be considered was the UK Generic Distribution System (UKGDS) developed by the University of Strathclyde. The various distribution networks were thoroughly analysed but they were not deemed as appropriate since the models in ATP/EMTP were not flexible enough to place faults at various locations. The line parameters and transformer configurations given could not be used directly in ATP/EMTP since other information were required to model them in ATP. The IEEE 34 bus distribution network test system was also considered but it was observed that sections of the line were single phase circuits. Furthermore, no suitable full representations of Type C and Type D wind turbine configurations were available and there is a limitation to the number of electrical machines that can be connected in parallel in ATP/EMTP.

Finally, a typical 33 kV overhead distribution network was developed and implemented in Simulink based on practical electrical parameters of distribution lines and transformers obtained from UK power utilities reports [81, 82]. Figure 4.1

illustrates the developed typical 33 kV active distribution network. The network was validated by performing a simplified short-circuit calculation on the system which provides a good approximation to understand the physical phenomena during a fault (Appendix A).

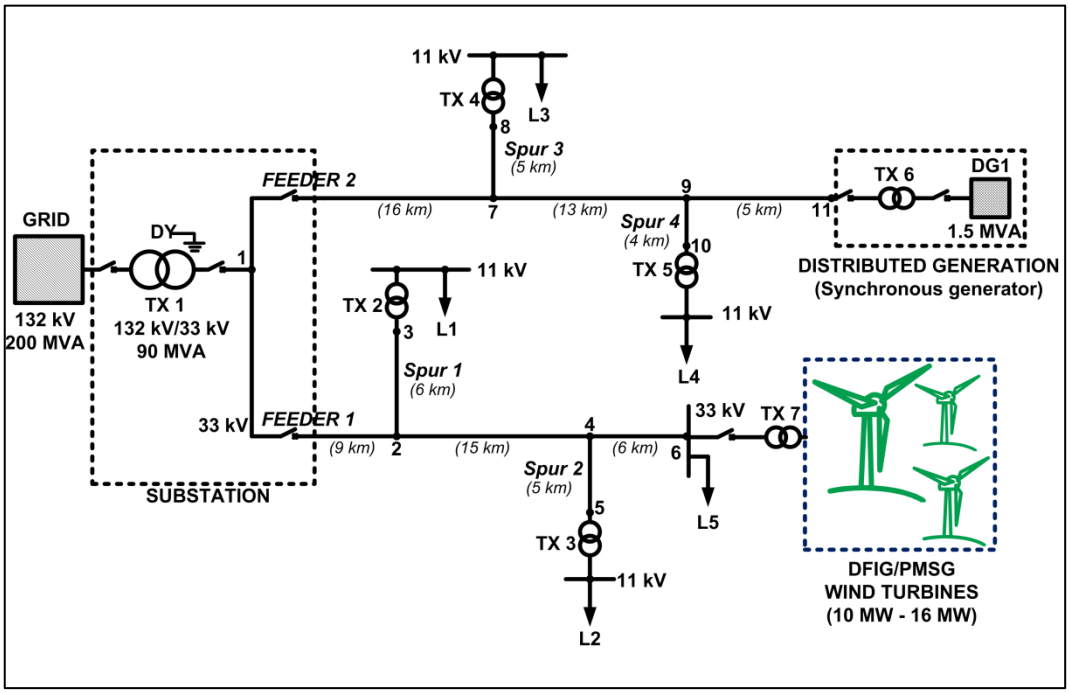

Figure 4.1: Typical 33 kV active distribution network

The distribution network is made up of two feeders going out of a substation with two spurs on each feeder. A small distributed generator (DG1) of 1.5 MVA is connected at the end of Feeder 2 through transformer TX 6 to represent a remote infeed. Single phase loads and three phase loads are connected on the spurs at locations L1, L2, L3 and L4. At the end of Feeder 1, a wind farm consisting of either a set of doubly fed induction generator wind turbines or permanent magnet synchronous generator wind turbines can be connected to the distribution network to investigate the integration of wind farm connection to the system.

4.2.1 Generator parameters

The 132 kV GRID is supplied by synchronous generators and as such, it can be represented by a voltage source in series with a subtransient reactance (X_d'') since the subtransient reactance determines the contribution of the generator to a short circuit

fault and it contributes to the initial peak fault current. The generator parameters are given in Table 4.1.

132 kV GRID	
Source capacity/ MVA	200
X/R ratio	13
Line to line voltage/ kV	132

Table 4.1: Generator parameters

4.2.2 Line parameters

The overhead line sections are rated at 33 kV with the positive sequence resistance R1, inductance L1 and capacitance C1 set at 0.1152 Ω/km, 1.24 mH/km and 1.133 nF/km respectively. The zero sequence resistance R0, inductance L0 and capacitance C0 were taken as 0.413 Ω/km, 3.32 mH/km and 5 nF/km respectively. These values are within the range of values for typical 33 kV overhead lines used by distribution network companies [81, 82]. The lengths of the various line sections are given in Table 4.2 below.

Line section	**Length/km**
1-2	9
2-3	6
2-4	15
4-5	5
4-6	6
1-7	16
7-8	5
7-9	13
9-10	4
9-11	5

Table 4.2: Line lengths for various sections of the distribution network

4.2.3 Load settings

Loads connected to the network are a combination of unbalanced single phase loads and balanced three phase loads such as induction motors which are usually present at industrial customers connected on the 33 kV network. The loads are connected at various positions on the distribution network as given in Table 4.3.

Load	Description
L1	10 induction motors + 2 3ϕ Y connected balanced loads, total= 2.4 MVA
L2	unbalanced Y connected 3ϕ load, total = 1.8 MVA
L3	single phase loads on B phase and C phase, total= 925 kVA
L4	balanced Y connected 3ϕ load, total=807 kVA
L5	balanced Y connected 3ϕ load, total=20 MVA

Table 4.3: Load settings

4.2.4 Transformer parameters

Tx1 is a power transformer supplying both feeders with a capacity of 90 MVA and stepping down the voltage at the substation from 132 kV to 33 kV. Tx2 to Tx6 are distribution transformers of 2.5 MVA, usually mounted at the customers' premises in a small substation to supply the loads connected to their installations. Tx7 is rated at 24 MVA and exports all the power produced by the wind turbines to the 33 kV distribution network. Table 4.4 summarises the transformer parameters used to implement the typical 33 kV distribution network.

Transformer	Rating/ MVA	HV/ kV	LV/ kV	Vector group
Tx1	90	132	33	Dyn1
Tx2-Tx5	2.5	33	11	Dyn1
Tx6	2.5	33	11	Ydn1
Tx7	24	33	0.575	Dyn11

Table 4.4: Transformer electrical parameters

4.3 DFIG model

The SimpowerSystems library does not offer a complete model of a DFIG wind turbine. The only available detailed model is a SimPowerSystems example developed by Richard Gagnon from Hydro-Quebec [83]. The model consists of a wound rotor induction generator with the rotor side converter and the grid side converter implemented using Insulated Gate Bipolar Transistors (IGBTs). As seen in Figure 4.2, the rotor is partially fed through the ac-dc-ac power electronic converter.

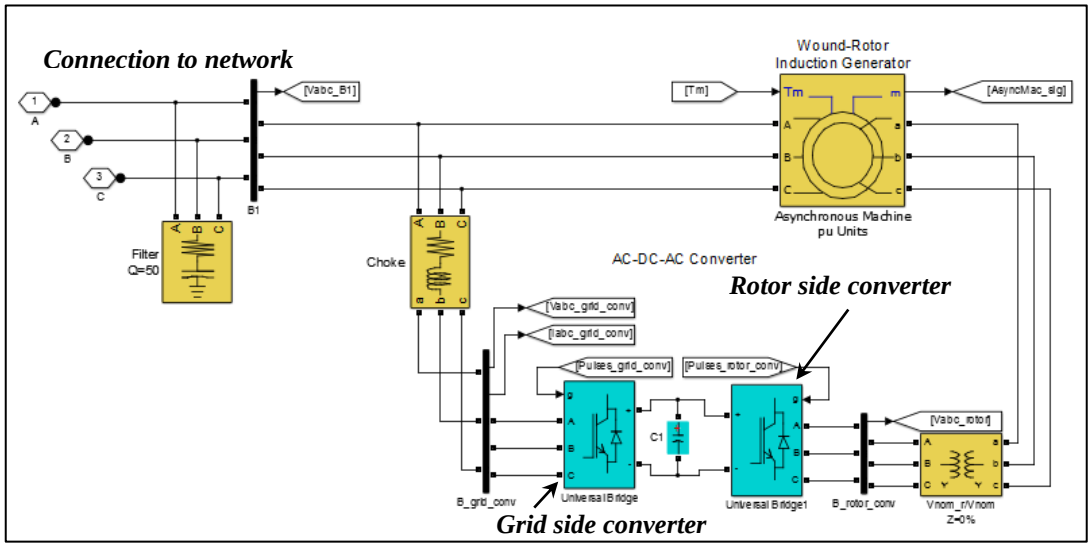

Figure 4.2: Doubly fed induction generator Simulink model

An IGBT is suitable for medium/high voltage and power applications. It has a low collector to emitter voltage drop in the on state and a switching speed similar to a Bipolar Junction Transistor (BJT). Moreover, another attribute is its high impedance voltage operated gate similar to a Metal Oxide Semiconductor Field Effect Transistor (MOSFET). This enables the IGBT to be switched on and off with ease with a relatively low power loss.

Each wind turbine generator is rated at 1.5 MW and the firing of the IGBTs has been modelled upon the same type of control applied in the GE 1.5 MW DFIG wind turbine. Figure 4.3 shows the various control blocks in Simulink with the speed of the turbine controlled by the pitch control block, the firing of the grid side converter controlled by a PWM generator linked to its control block and finally the control of the rotor side converter is carried out in a separate block.

The simulation is run with a time step of 5μs, thus enabling the observation of the dynamic performance of the power electronic converters and harmonics for short time periods (in the range of milliseconds to seconds).

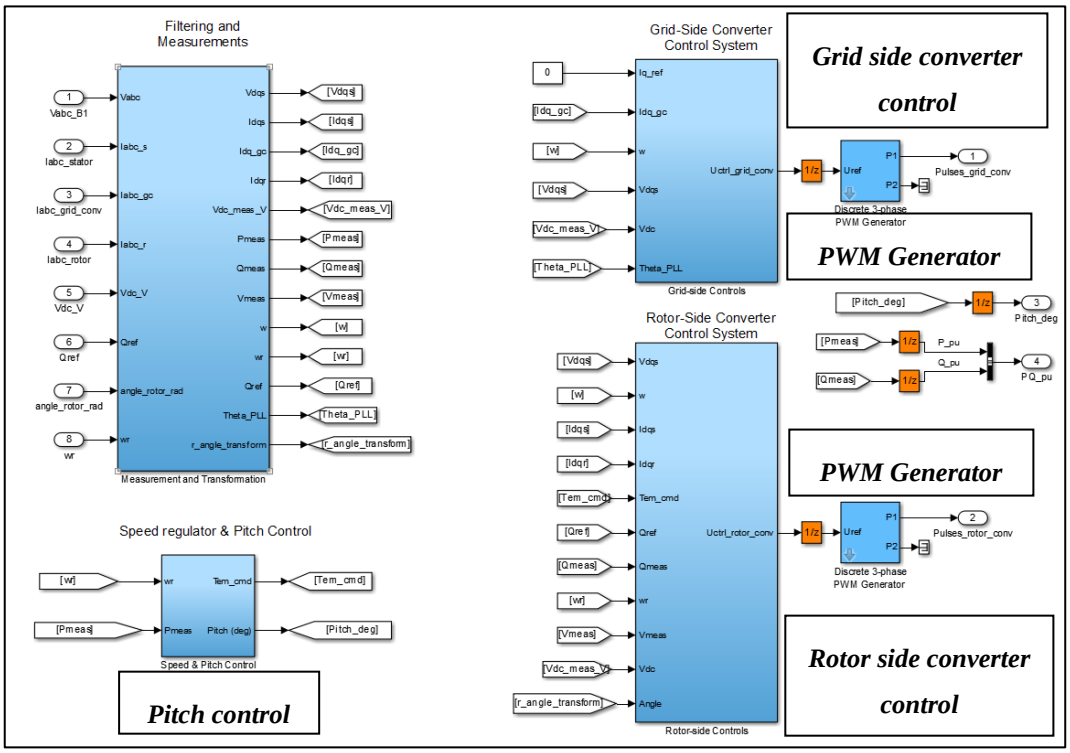

Figure 4.3: Simulink control blocks for the wind turbine

The rated wind speed of the turbine is at 11 m/s and during each simulation, the input wind speed is kept at a constant value of 15 m/s to ensure that the power output delivered by the wind turbine is at its rated power.

4.3.1 Power converter operation

The rotor circuit is fed with ac excitation from the grid through the ac-dc-ac converter (also referred to as a back-to-back converter). The back-to-back converter consists of two voltage source converters linked to each other through the dc link capacitor. The voltage source converters are capable of bi-directional power flow and can therefore operate as both a rectifier and an inverter depending on the speed of operation of the wind turbine. Since the power output is a function of wind speed (variable voltage and variable frequency), the ac-dc-ac converter ensures that a fixed

voltage and a fixed frequency is delivered at the point of connection to meet the grid requirements.

As mentioned before, the ac-dc-ac converter is made up of the grid side converter and the rotor side converter. The function of the grid side converter is mainly to maintain the dc link voltage, V_{dc}, at the correct level irrespective of the direction of power flow in the converter and also to provide some voltage support to the grid. The grid side converter is a two-level three phase voltage source converter with six IGBTs as shown in Figure 4.4.

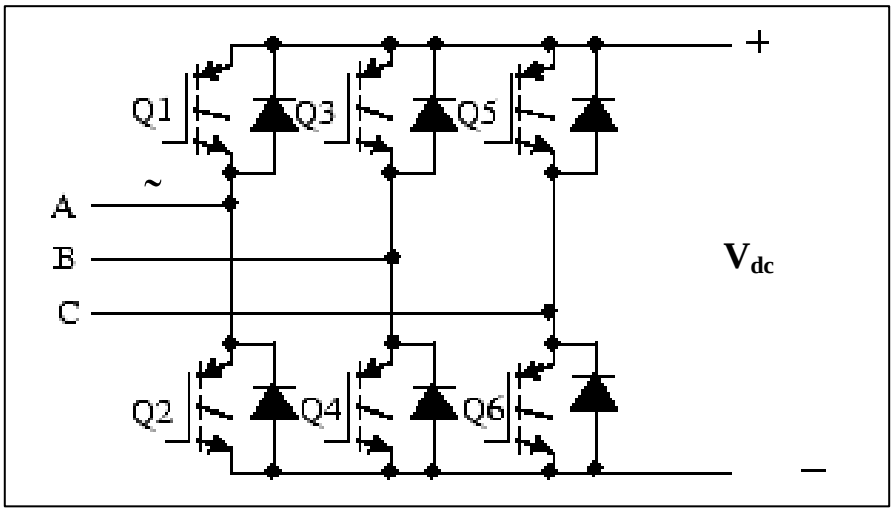

Figure 4.4: Three phase, two level IGBT bridge converter [84]

The output voltage is controlled by switching on and off the IGBTs in a sequence using pulse width modulation (PWM). The pulse width modulated voltage control signal is synthesised by comparing the modulated signal (low frequency) with the carrier signal as depicted in Figure 4.5. The output voltage of the three phase bridge converter is therefore a function of the dc link voltage V_{dc} and the modulation index, m_a (or duty cycle) i.e. the ratio of the on time of the switch (t_{on}) and the switch period (T_{sw}).

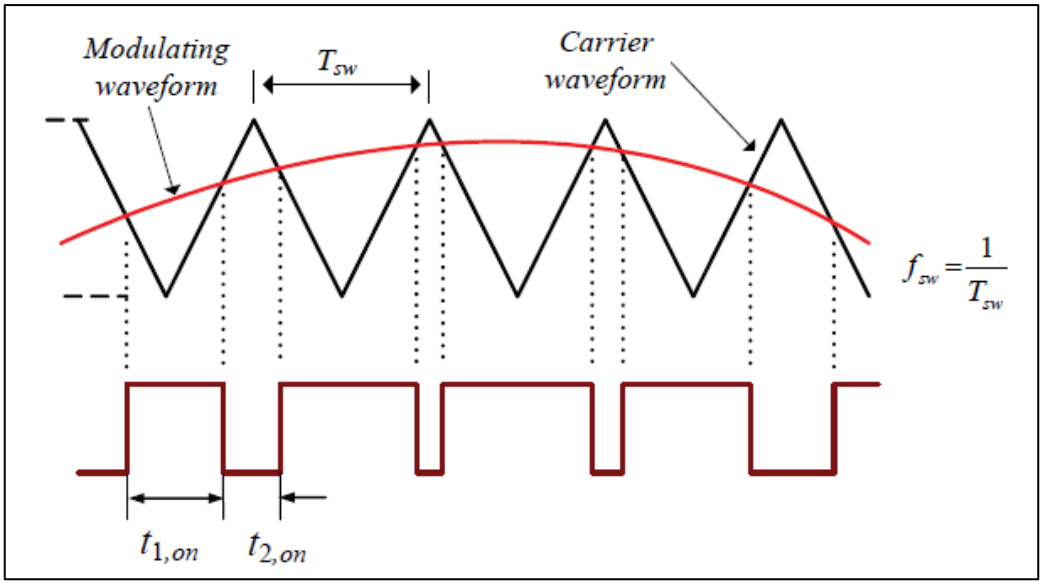

Figure 4.5: PWM control signal from a voltage comparator [85]

Figure 4.6 shows the relationship between the rms output phase to phase voltage with modulation index m_a. In the linear region, i.e. $0 \leq m_a \leq 1$, the rms output voltage varies linearly with m_a but the maximum value does not exceed $0.354V_{dc}$. The output voltage can be increased when operating with a modulation index $m_a > 1$, i.e. overmodulation. For $m_a > 3.24$ (square wave operation), the output voltage cannot exceed $0.45V_{dc}$.

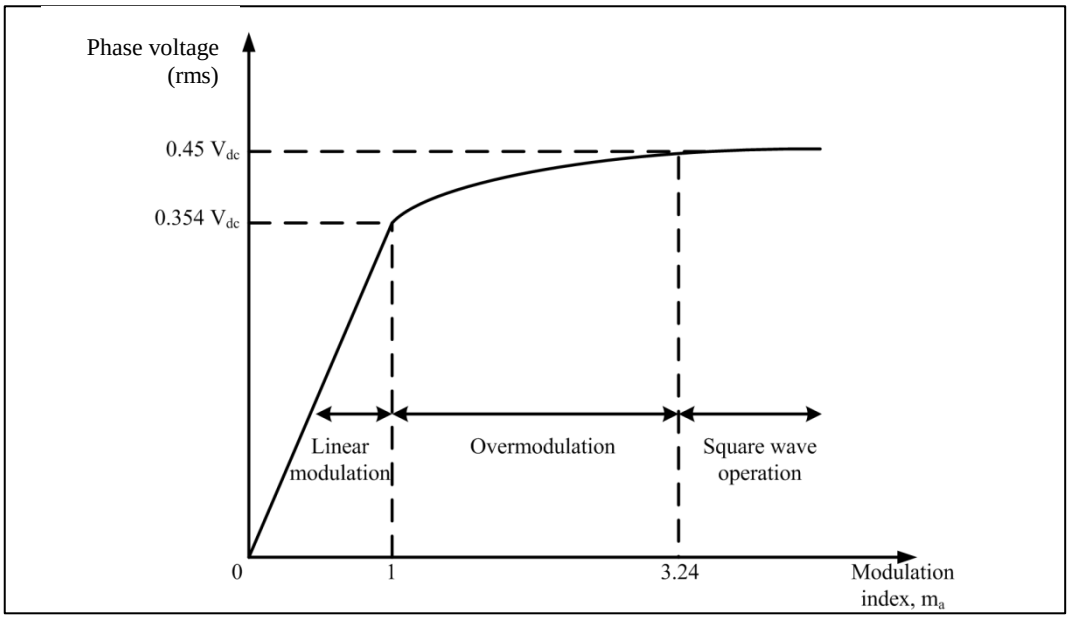

Figure 4.6: Output voltage of three phase inverter with modulation index

The function of the rotor side converter is to excite the rotor windings, control the torque on the rotor and provide reactive power control. The controllers for both the rotor side converter and the grid side converter have been modelled in Simulink using d-q axis transformations. Further information on the detailed modelling of the controllers can be found in Reference [86].

4.3.2 Crowbar implementation

One major drawback of the DFIG model in Simulink is the absence of a crowbar. Without a crowbar, the short circuit behaviour of the model is inaccurate and not representative of the actual behaviour of a real machine when a fault occurs on the grid. Therefore, the actual Simulink model has been improved by implementing a crowbar circuit between the rotor windings and the rotor side converter (Figure 4.7). Circuit breaker CB1 closes when the rotor currents are high and dissipates the energy through the resistors. At the same time, circuit breaker CB2 opens, thus disconnecting the rotor side converter from the rotor circuit.

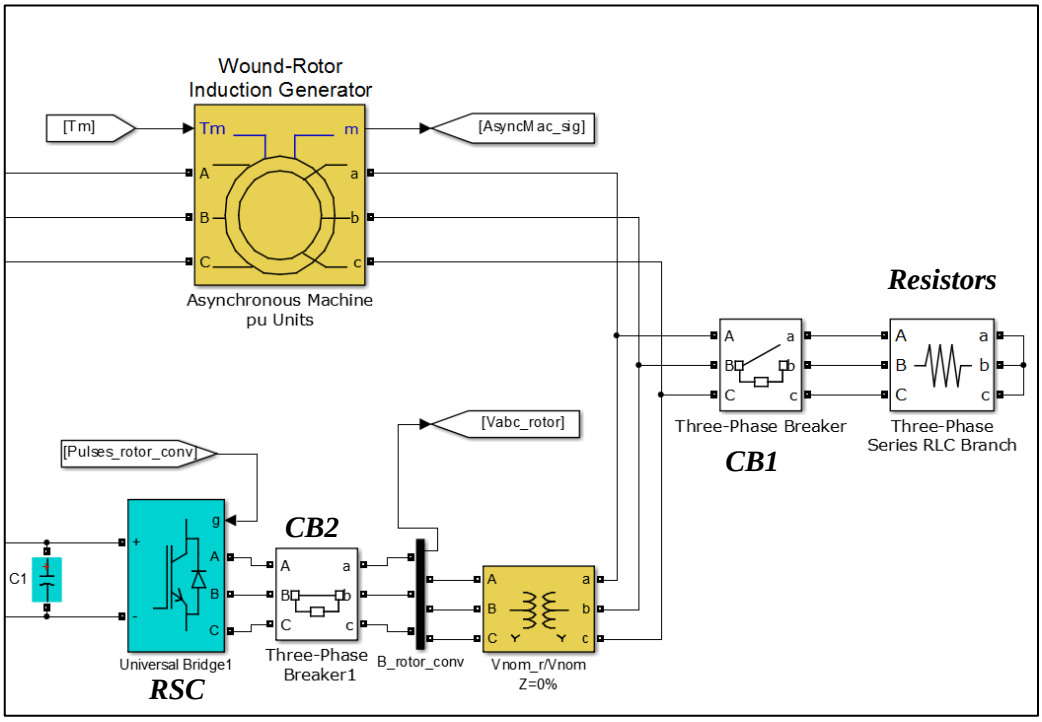

Figure 4.7: Crowbar circuit implementation in Simulink

4.3.3 Simulation of DFIG model

A three phase fault is placed at the DFIG terminals to verify its short circuit behaviour during fault conditions. Without the crowbar protection (Figure 4.8), the response of the DFIG model is inaccurate. A three phase fault occurs at time t=0.04s at the DFIG terminals when it is supplying 9 MW of power to the grid. The active power rapidly decreases to zero after the fault.

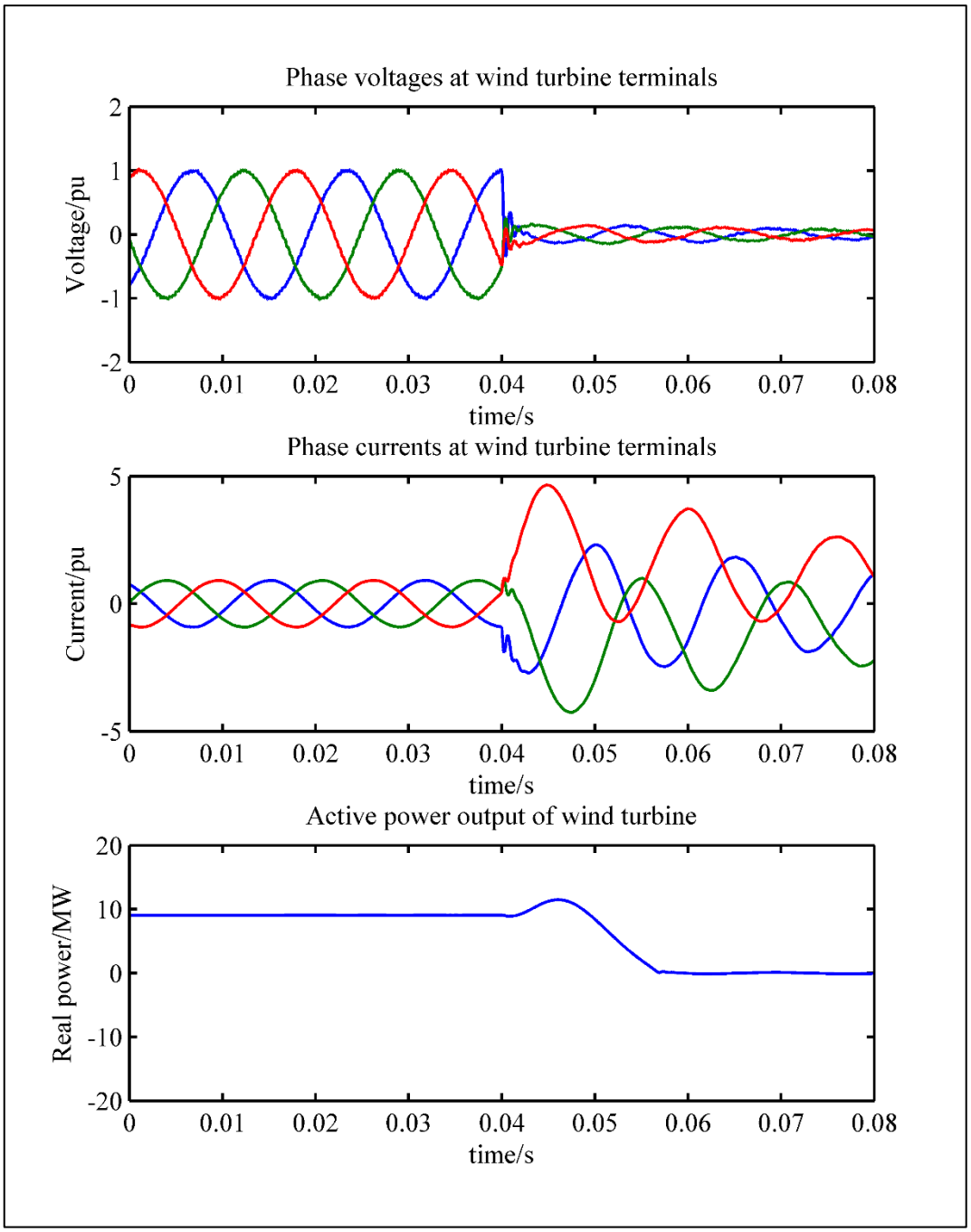

Figure 4.8: Short circuit behaviour of DFIG model without crowbar protection

However, the phase currents do not exhibit similar behaviour to a real DFIG wind turbine [72] as it can be clearly observed that the phase currents have zero crossings soon after the occurrence of the fault. With implementation of the crowbar circuit (Figure 4.9), the short circuit behaviour of the DFIG model is more representative of a real system since it can be seen that the phase currents do not have any zero crossings for a few cycles after the fault inception.

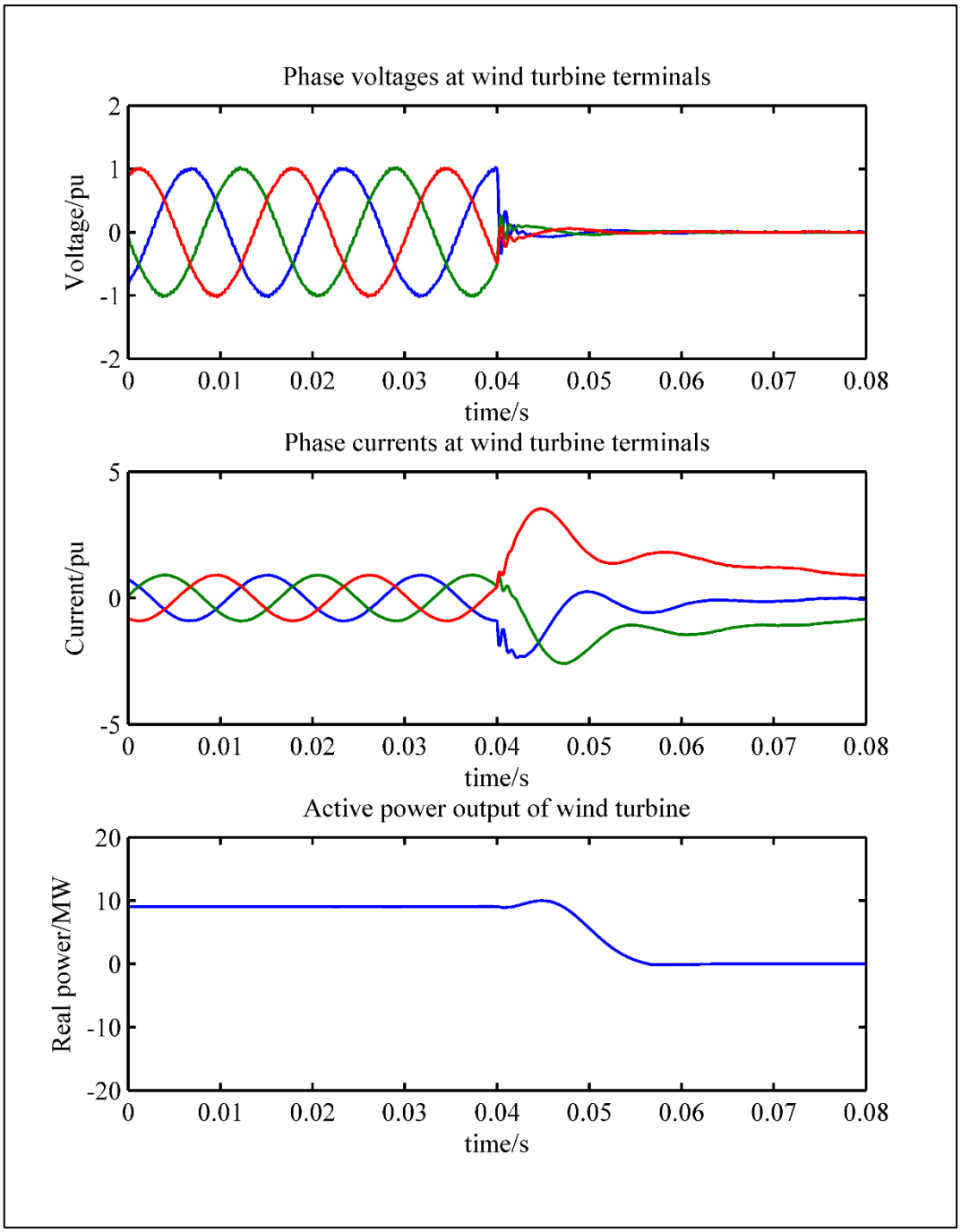

Figure 4.9: Short circuit behaviour of DFIG model with crowbar protection

4.4 PMSG model

The detailed model of a PMSG wind turbine system in Simulink was developed by Richard Gagnon and Jacques Brochu from Hydro-Quebec [87]. Each permanent magnet synchronous generator machine is rated at 2 MW and maximum power is delivered at a rated wind speed of 11 m/s. The synchronous generator exports power to the grid through a diode rectifier, a dc-dc boost converter and a three phase voltage source inverter as depicted in Figure 4.10. The operation of the power electronic components will be explored in the next section. The rotor of the synchronous generator is driven by the wind turbine blades for a wind speed of 15 m/s and a blade pitch angle of 8.8°. The high switching frequency (around 2 kHz to 3 kHz) of the IGBTs for the three phase inverter is suitable to investigate the contribution of the power electronic converter to short circuit currents during fault transients on the network.

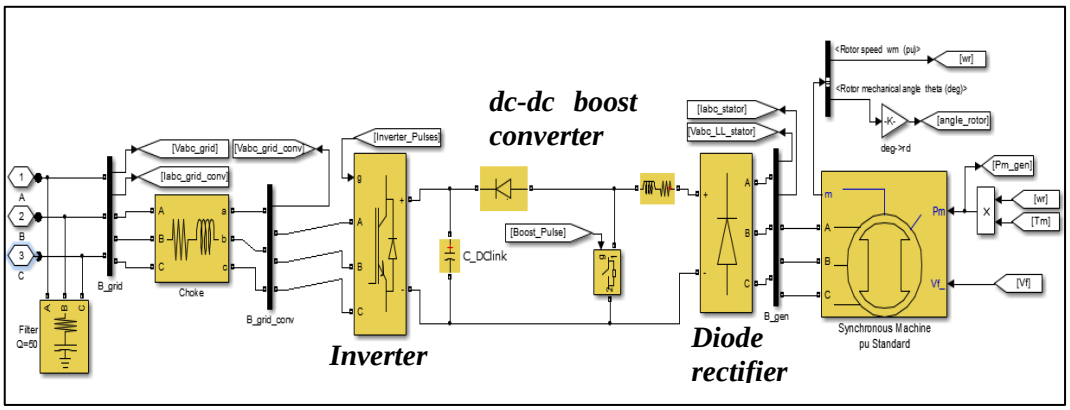

Figure 4.10: PMSG wind turbine model in Simulink

4.4.1 Power converter operation

In contrast to the DFIG wind turbine configuration which uses a back-to-back converter to export power to the grid, the PMSG model exports all its power through a fully rated power converter consisting of a diode rectifier, a dc-dc boost converter and a three phase voltage source inverter. Due to the passive diode rectifier, power flow is unidirectional but overall, the PMSG wind turbine configuration offers a simpler and more cost effective solution since PWM control is required only for the inverter.

The three phase diode bridge rectifier (Figure 4.11) converts the variable amplitude output voltage of the synchronous generator (due to varying wind speeds) to a variable dc voltage.

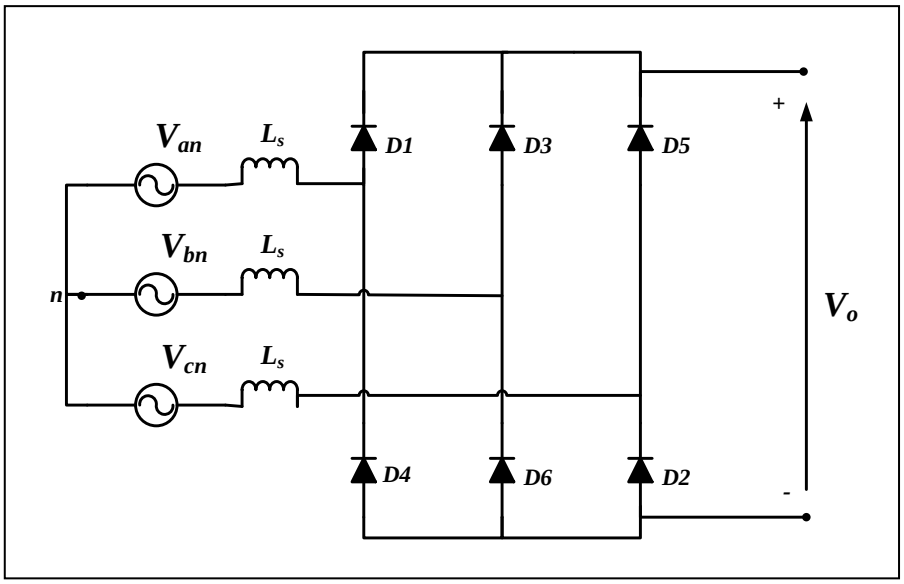

Figure 4.11: Three phase full wave diode rectifier

Assuming L_s is zero, the line to line voltages are fully rectified, with each diode conducting for 120˚, giving an instantaneous output voltage waveform consisting of 6 segments per cycle (Figure 4.12). Each segment is 60˚ or π/3 wide and the average dc output voltage, V_0, can be calculated by integrating the instantaneous output voltage waveform from –π/6 to π/6.

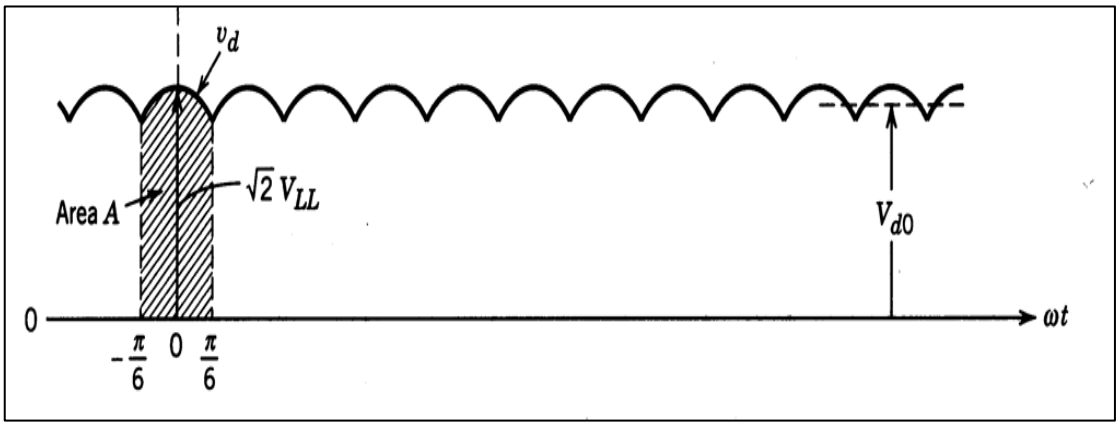

Figure 4.12: Instantaneous output voltage waveform of 6 pulse rectifier [88]

The average dc output voltage is:

$$V_0 = \frac{1}{\pi/3}\int_{-\pi/6}^{\pi/6}\sqrt{2}V_{LL}\cos\omega t\ d(\omega t) = \frac{3}{\pi}\sqrt{2}V_{LL} \qquad \text{Equation 4.1}$$

At low wind speeds, the dc output voltage of the three phase diode bridge rectifier may be insufficient for proper operation of the three phase PWM inverter i.e. the inverter may be unable to export power to the grid due to insufficient dc input voltage. Therefore, the dc output voltage of the diode rectifier has to be controllable to achieve proper operation of the three phase PWM inverter. Hence a dc-dc boost converter is used to convert the variable diode rectifier output dc voltage to a controllable dc output voltage that can be fed to the three phase voltage source PWM inverter.

The output voltage of the dc-dc boost converter is controlled by operating switch S (Figure 4.13). When switch S is closed, energy is stored in the inductor as the diode is reversed biased and when switch S is opened, the energy is transferred to the output side.

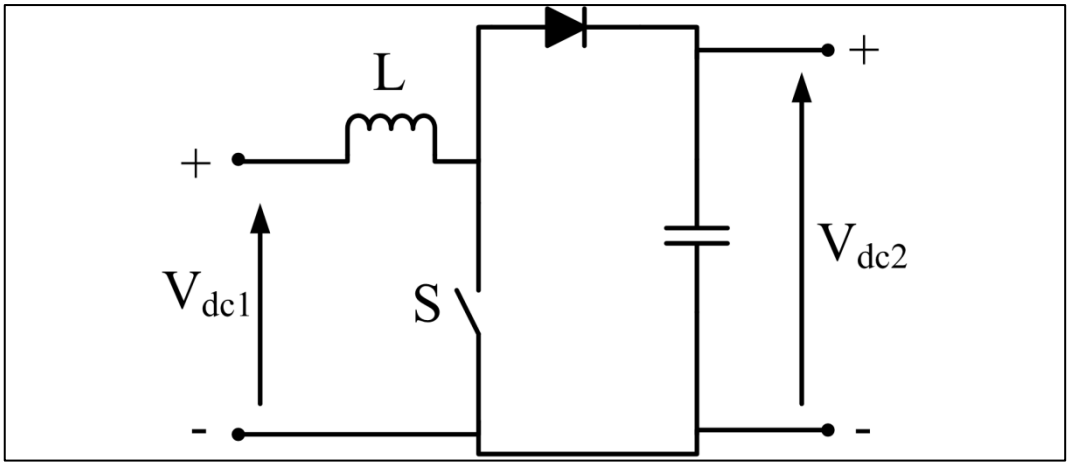

Figure 4.13: dc-dc boost converter

The relationship between the input voltage V_{dc1} and output voltage V_{dc2} in the continuous conduction mode (i.e. $i_L(t) > 0$) is as follows:

$$V_{dc1}t_{on} + (V_{dc1} - V_{dc2})t_{off} = 0 \qquad \text{Equation 4.2}$$

Re-arranging:

$$V_{dc1}(t_{on} + t_{off}) = V_{dc2}t_{off} \quad \text{Equation 4.3}$$

$$\frac{V_{dc2}}{V_{dc1}} = \frac{t_{on} + t_{off}}{t_{off}} \quad \text{Equation 4.4}$$

Replacing $T_S = t_{on} + t_{off}$,

and duty cycle $D = \frac{t_{on}}{t_{off}}$

$$\frac{V_{dc2}}{V_{dc1}} = \frac{1}{1 - D} \quad \text{Equation 4.5}$$

The relationship of V_{dc2} with respect to V_{dc1} and D is illustrated in Figure 4.14. It clearly shows that the output dc voltage V_{dc2} of the dc-dc boost converter is always greater or equal to the input voltage V_{dc1}.

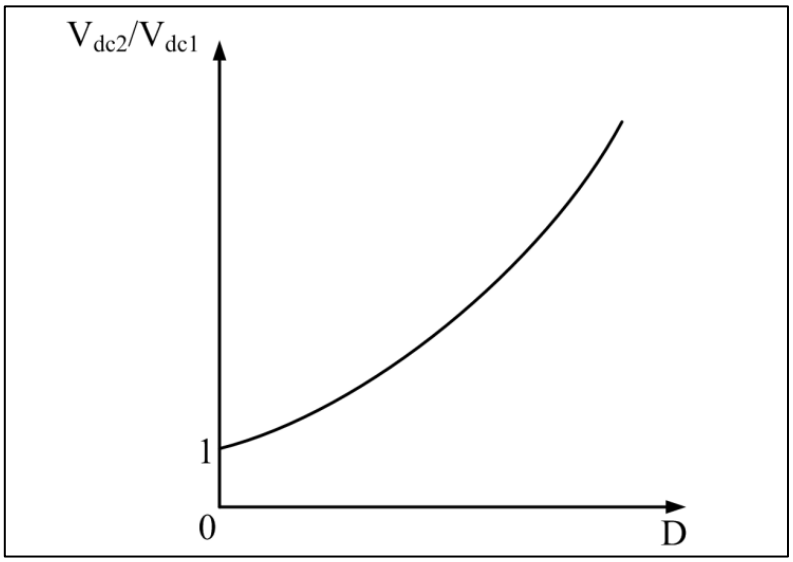

Figure 4.14: Output voltage of dc-dc boost converter with duty cycle

4.4.2 Simulation of PMSG model

In the case of unidirectional power flow (no wind farm connection) along Feeder 1 from the substation to the load, the current flowing in Feeder 1 can be seen to be around 500 A peak phase current (Figure 4.15).

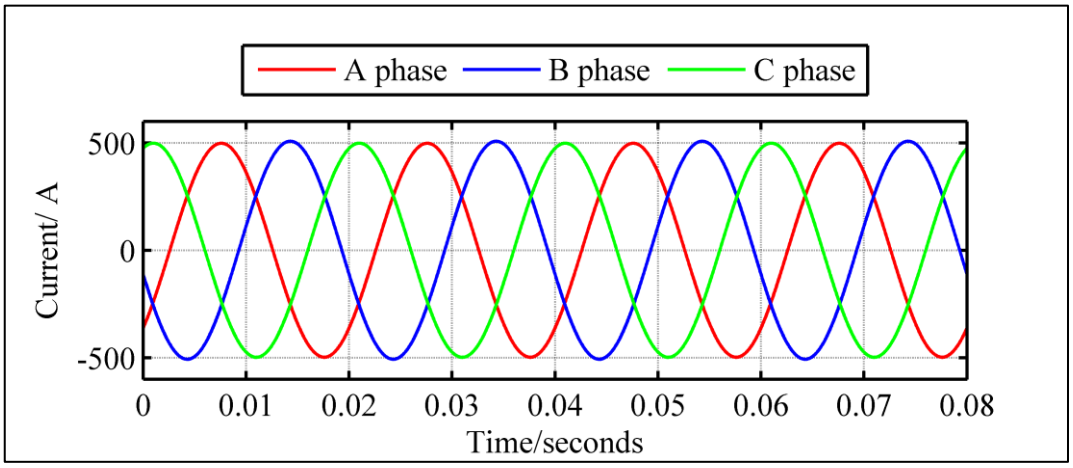

Figure 4.15: Phase currents in Feeder 1 without wind farm connection

With the connection of a wind farm of 10 MW capacity consisting of 5 permanent magnet synchronous generator wind turbine, each of 2 MW capacity, there is bidirectional power flow along Feeder 1 and the load is now supplied by both the power flow from the substation and power from the wind farm. This is confirmed by a decrease in peak phase current to around 250 A, measured at the substation end of Feeder 1 (Figure 4.16).

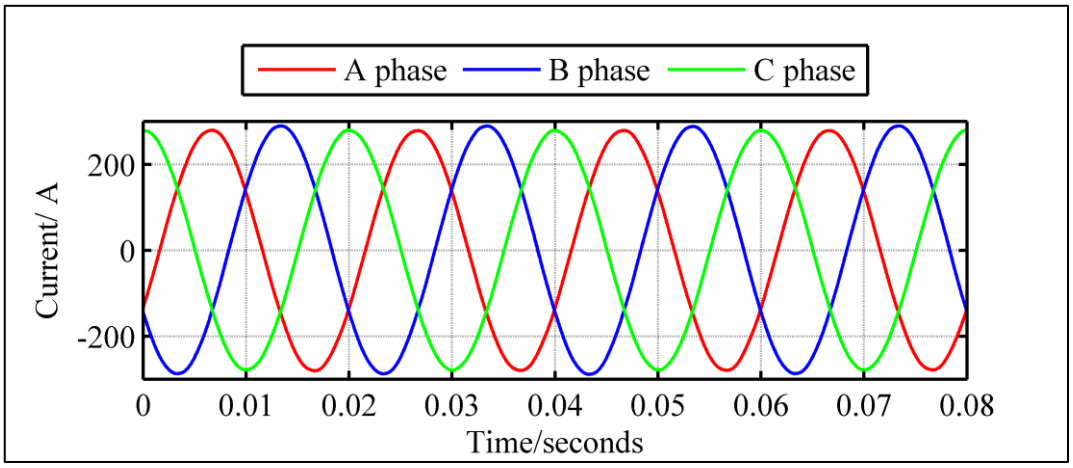

Figure 4.16: Phase currents with 10 MW PMSG wind farm connection

4.5 Simulation of short circuit faults

In this section, the voltage and current waveforms of single phase to ground (AG, BG and CG), phase to phase (AB, BC and AC), double phase to ground (ABG, BCG and ACG) and three phase (ABC) faults obtained through simulation from the typical 33 kV distribution network are presented. These fault types were simulated at various locations on the distribution network, with fault positions changed in steps of 3 km on Feeder 1 and those on spurs changed in steps of 1 km. The faults occurring at voltage minimum (i.e. fault inception angle $\theta=0°$) and voltage maximum (i.e. fault inception angle $\theta=90°$) were also considered with the fault impedance for ground faults taken as 0Ω, 25Ω and 50Ω. The sampling frequency was set to 100 kHz, i.e. 2000 samples per 50 Hz cycle, to capture the high frequency transients produced during a fault. The frequency was then downsampled in MATLAB to 25 kHz to reduce the size of the input data.

The voltage and current waveforms obtained for each type of fault with wind farm integration are also presented. The wind farm considered is either a configuration of seven, 1.5 MW DFIG wind turbines (i.e. total capacity of 10.5 MW), or a configuration of five, 2 MW PMSG wind turbines, yielding a total capacity of 10 MW.

4.5.1 Single phase to ground faults

Figure 4.17 (a) and (b) show the voltage and current signals for an A phase to ground fault at 1 km on Feeder 1 with a fault inception angle, $\theta=0°$, and a fault impedance of 0Ω. As can be seen, the fault caused a voltage drop on the A phase while the voltage level on the healthy phases (B and C phases) remained almost unchanged. The amplitude of the current on the A phase also rises to a much higher value.

With the same fault occurring at voltage maximum (Figure 4.18 (a) and (b)), it can be noticed that there is no dc offset in the fault current waveform of the A phase. The amplitude of the fault current on the A phase is also much lower than that at a fault inception angle of 0°.

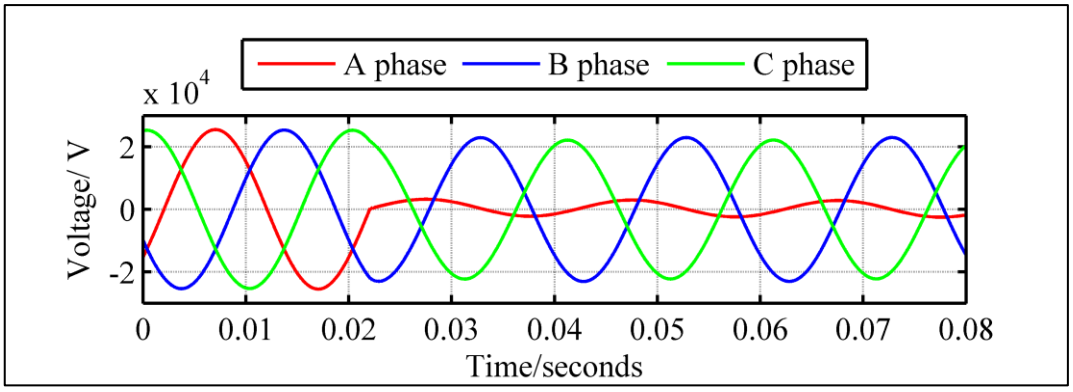

Figure 4.17 (a): Voltage waveforms for an A phase to ground fault with fault impedance Rf=0Ω and fault inception angle θ=0° at L=1 km on Feeder 1

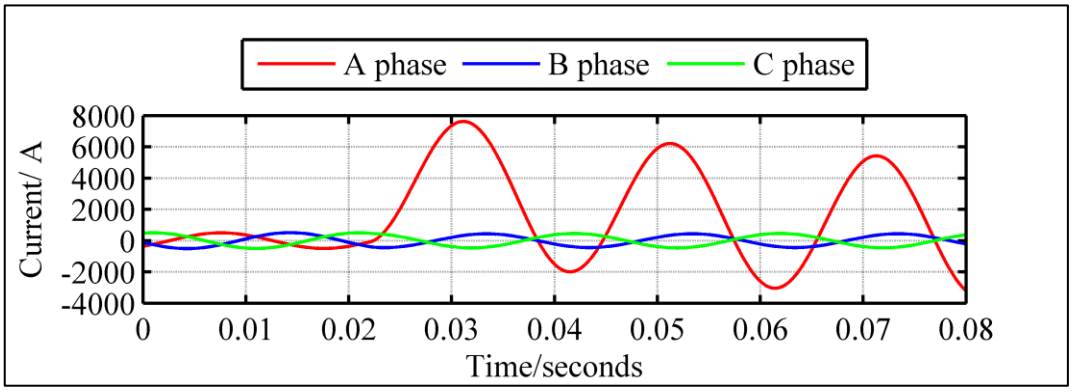

Figure 4.17 (b): Current waveforms for an A phase to ground fault with fault impedance Rf=0Ω and fault inception angle θ=0° at L=1 km on Feeder 1

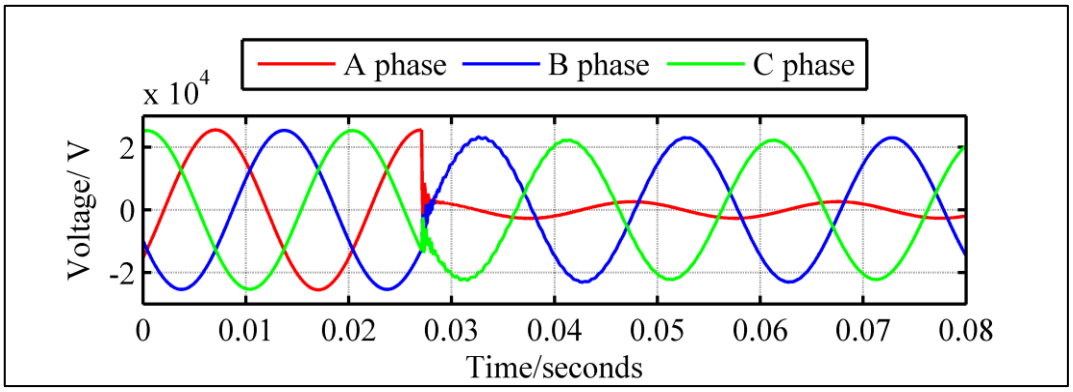

Figure 4.18 (a): Voltage waveforms for an A phase to ground fault with fault impedance Rf=0Ω and fault inception angle θ=90° at L=1 km on Feeder 1

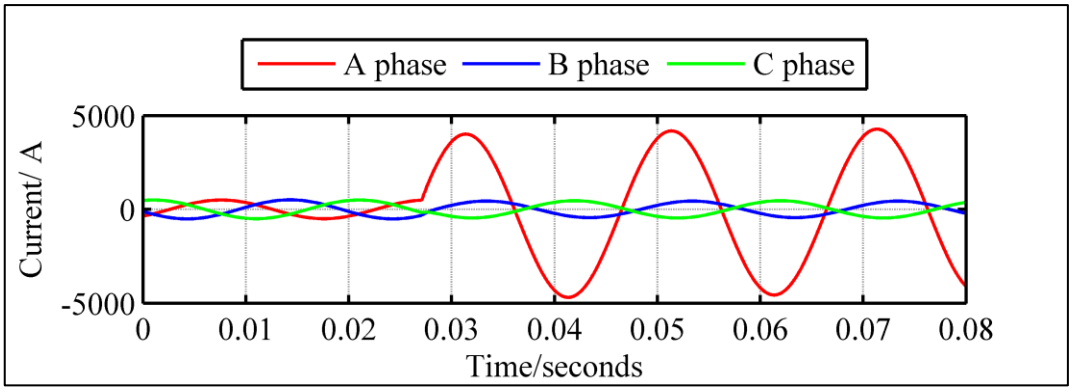

Figure 4.18 (b): Current waveforms for an A phase to ground fault with fault impedance Rf=0Ω and fault inception angle θ=90° at L=1 km on Feeder 1

With the connection of a 10.5 MW DFIG wind farm at the end of Feeder 1, the voltage and current waveforms are as depicted in Figure 4.19 (a) and (b). It can be noticed that for the A phase to ground fault occurring at 1 km on Feeder 1 with a fault impedance of 0Ω and a fault inception angle of 90°, the voltage level on the A phase drops while the voltage level on the healthy phases are almost unchanged.

As discussed earlier, the phase currents before the fault are much lower than for a network configuration without the connection of the wind farm since the load is shared by both sources. When the fault occurs, the fault current on the A phase is slightly higher than without the wind farm connection.

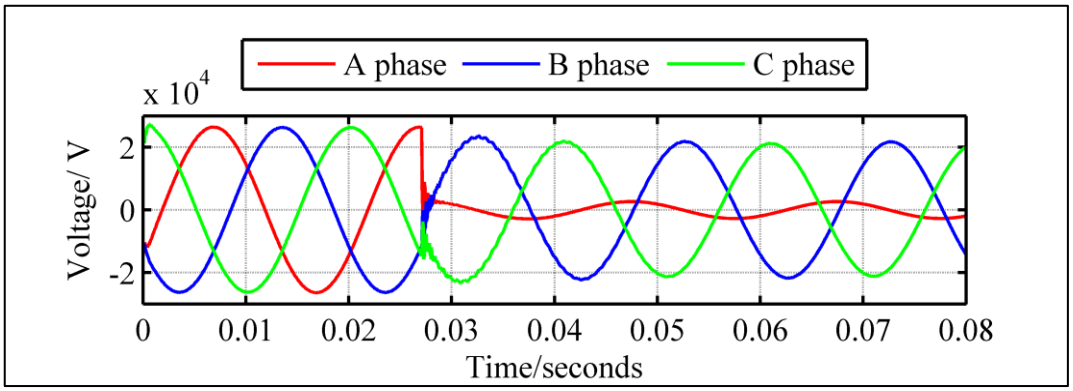

Figure 4.19 (a): Voltage waveforms for an A phase to ground fault with fault impedance Rf=0Ω and fault inception angle θ=90° at L=1 km on Feeder 1 with 10.5 MW DFIG wind farm connection

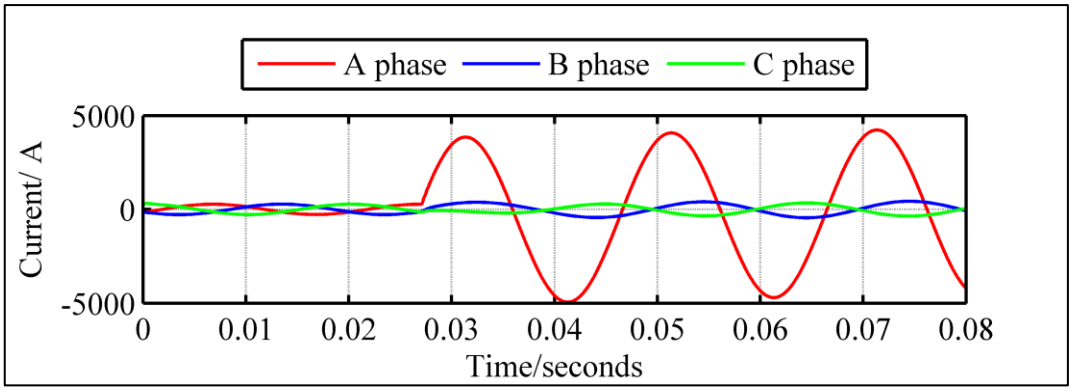

Figure 4.19 (b): Current waveforms for an A phase to ground fault with fault impedance Rf=0Ω and fault inception angle θ=90° at L=1 km on Feeder 1 with 10.5 MW DFIG wind farm connection

When a 10 MW PMSG wind farm is connected to the end of Feeder 1 and an A phase to ground fault with fault inception angle of 90° and fault impedance of 0Ω is simulated at 1 km on Feeder 1, the voltages and current waveforms are as shown in Figure 4.20 (a) and (b).

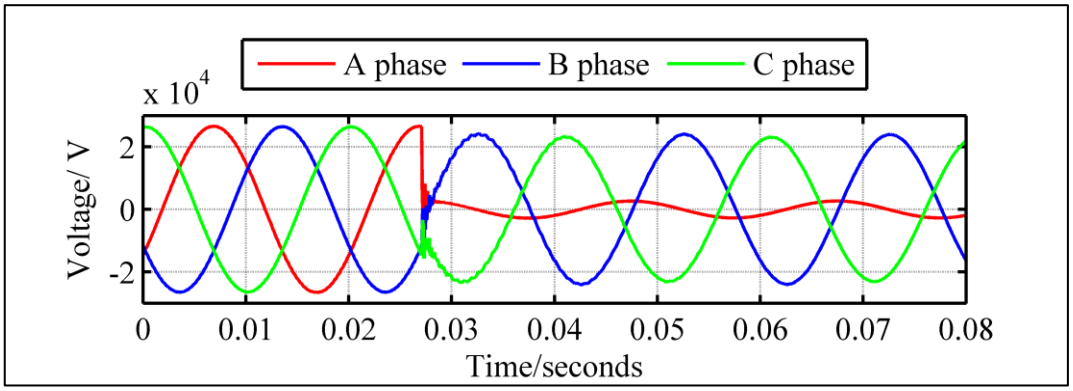

Figure 4.20 (a): Voltage waveforms for an A phase to ground fault with fault impedance Rf=0Ω and fault inception angle θ=90° at L=1 km on Feeder 1 with 10 MW PMSG wind farm connection

The fault current on the A phase (Figure 4.20 (b)) is also slightly higher than without a wind farm connection. The behaviour is as expected since the wind turbines are interfaced to the distribution network through power electronic converters which limit the fault current.

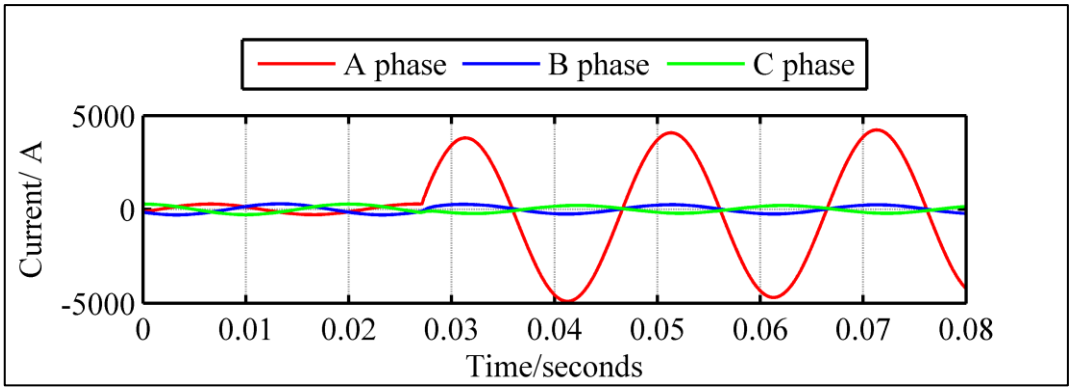

Figure 4.20 (b): Current waveforms for an A phase to ground fault with fault impedance Rf=0Ω and fault inception angle θ=90° at L=1 km on Feeder 1 with 10 MW PMSG wind farm connection

4.5.2 Phase to phase faults

The voltage and current waveforms for an A phase to B phase fault (AB) occurring at voltage maximum at 1 km on Feeder 1 are given in Figure 4.21 (a) and (b). The first observation is that there is an equal voltage drop in the faulted phases after the occurrence of the fault while the voltage level on the healthy phase remains unchanged.

This characteristic of phase to phase faults can be further verified by observing the voltage waveforms for a B phase to C phase fault at 15 km on Feeder 1 (Figure 4.22 (a)). Here again, the voltage drop on the faulted phases are equal.

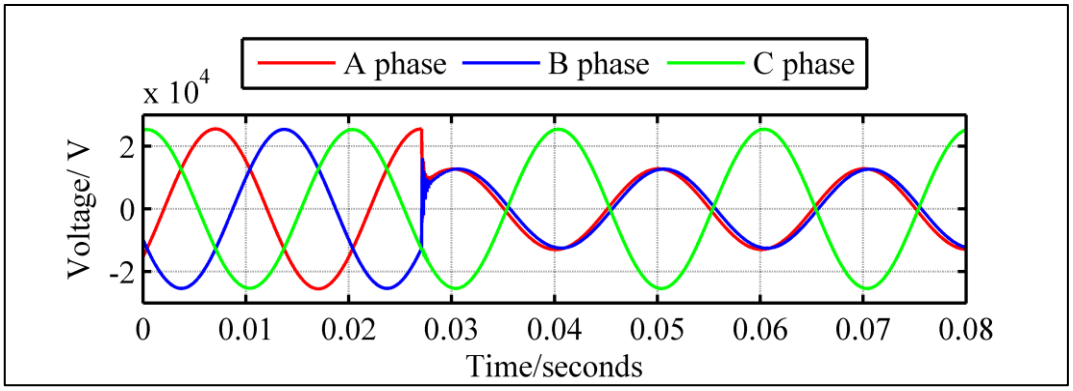

Figure 4.21 (a): Voltage waveforms for an AB phase to phase fault at L=1 km on Feeder 1

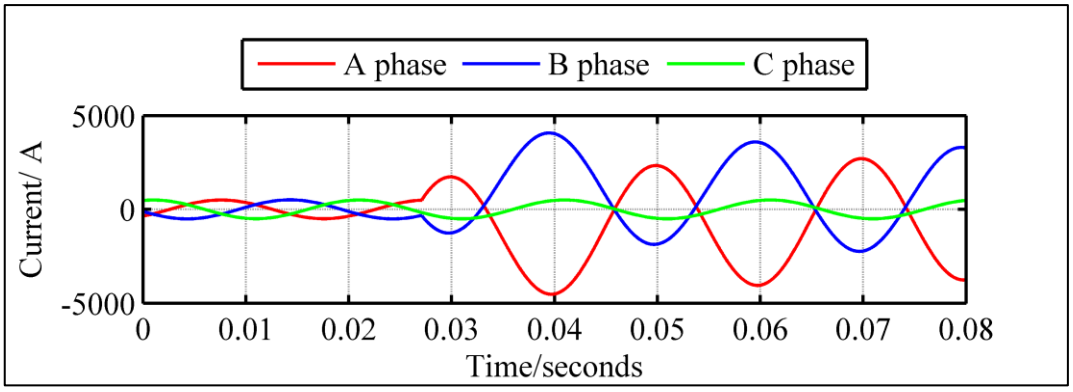

Figure 4.21 (b): Current waveforms for an AB phase to phase fault at L=1 km on Feeder 1

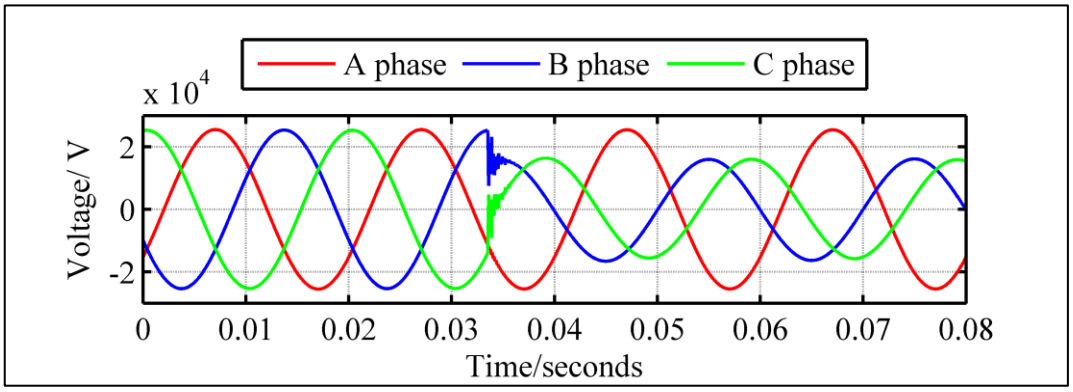

Figure 4.22 (a): Voltage waveforms for a BC phase to phase fault at L=15 km on Feeder 1

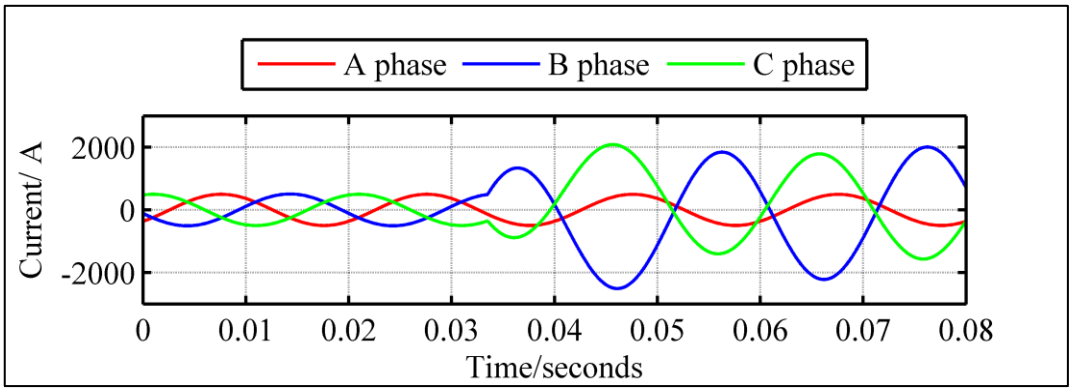

Figure 4.22 (b): Current waveforms for a BC phase to phase fault at L=15 km on Feeder 1

It can also be observed that there is an increase in current in the faulted phases after the fault (Figure 4.21 (b) and Figure 4.22 (b)), and there is a phase shift of 180° between the faulted phase currents.

The phase currents on the faulted phases after the fault are slightly increased with the wind farm connection (Figure 4.23 (b) and Figure 4.24 (b)). The phase voltages on the faulted phases suffer from an equal voltage drop irrespective of the fault inception angle, as can be seen in Figure 4.24 (a).

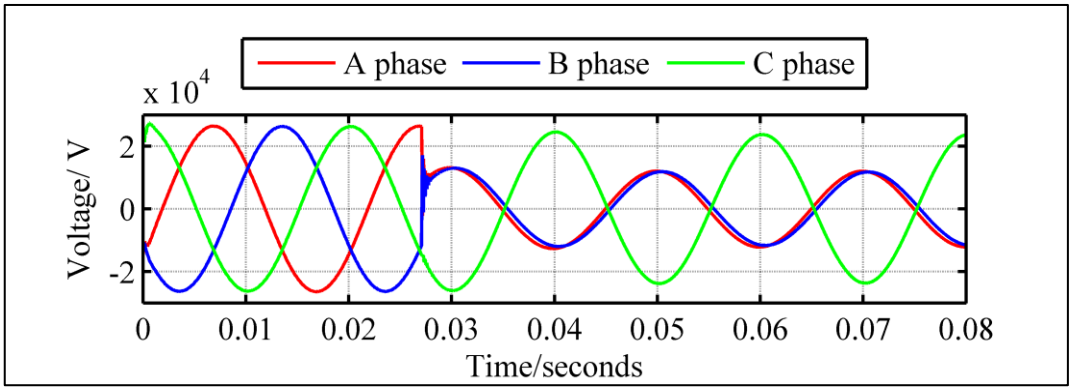

Figure 4.23 (a): Voltage waveforms for an AB phase to phase fault at L=1 km on Feeder 1 with 10.5 MW DFIG connection

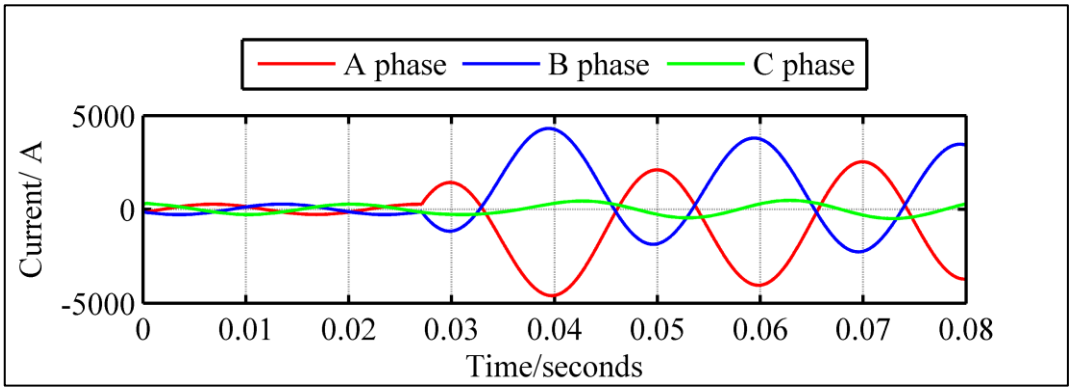

Figure 4.23 (b): Current waveforms for an AB phase to phase fault at L=1 km on Feeder 1 with 10.5 MW DFIG connection

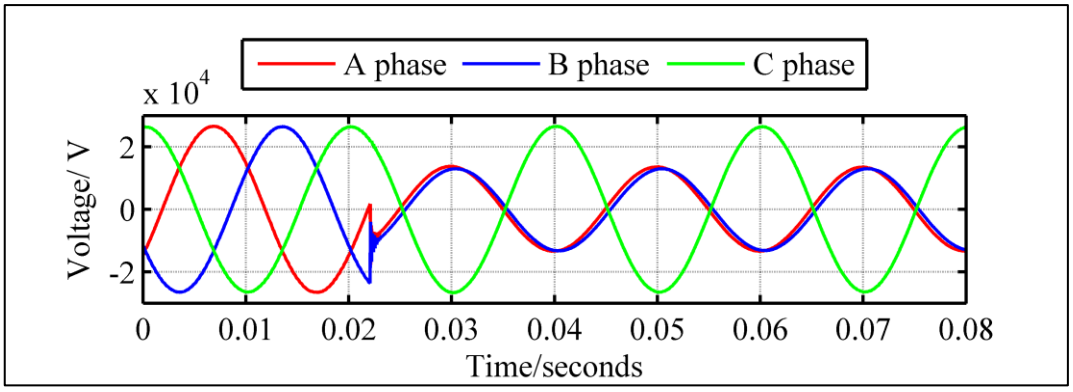

Figure 4.24 (a): Voltage waveforms for an AB phase to phase fault at L=1 km on Feeder 1 with 10 MW PMSG connection

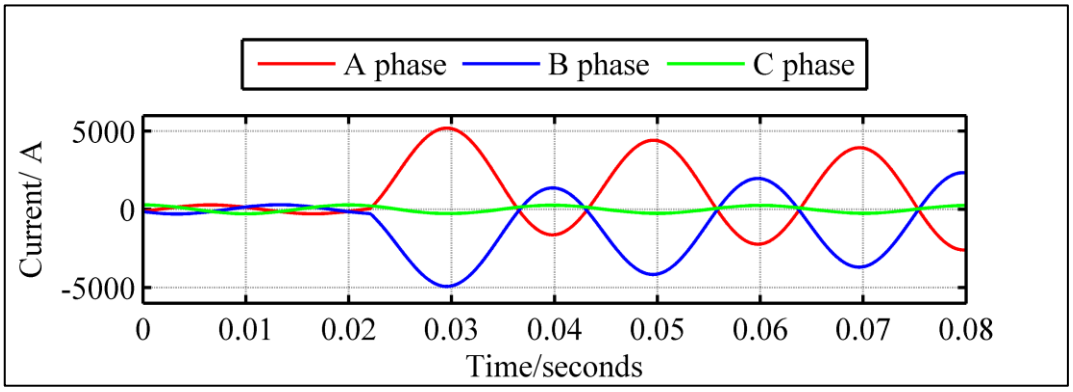

Figure 4.24 (b): Current waveforms for an AB phase to phase fault at L=1 km on Feeder 1 with 10 MW PMSG connection

4.5.3 Double phase to ground faults

The voltage and current waveforms of double phase to ground faults without wind farm connection are given in Figures 4.25 and 4.26. When a double phase to ground fault occurs on the network, the faulted phases are affected by an equal voltage drop whereas the voltage level in the healthy phase remains almost unchanged. The same observation can be made irrespective of the fault inception angle.

With the integration of the 10.5 MW DFIG wind farm (Figure 4.27) and 10 MW PMSG wind farm (Figure 4.28), a slight increase of the phase current in the faulted phases can be noted.

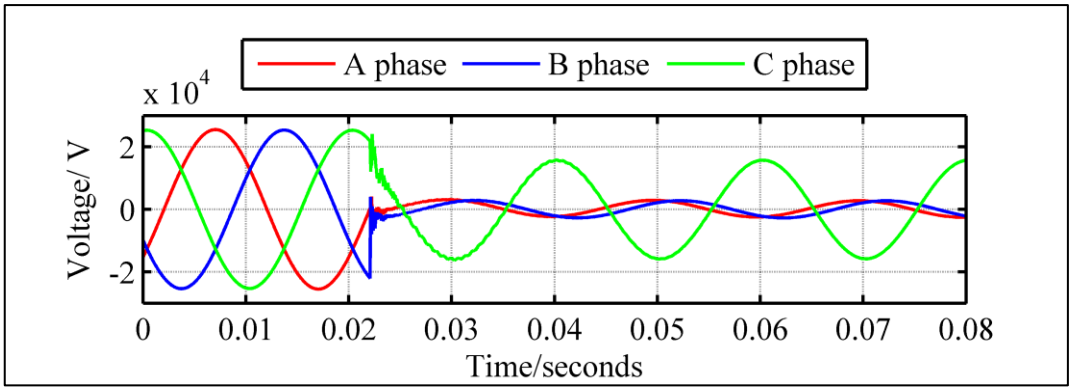

Figure 4.25 (a): Voltage waveforms for an ABG double phase to ground fault at L=1 km on Feeder 1 and Rf=0Ω

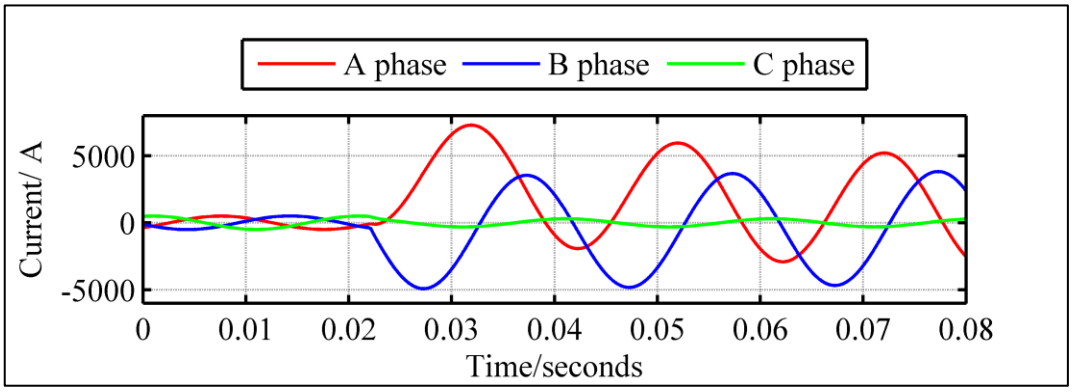

Figure 4.25 (b): Current waveforms for an ABG double phase to ground fault at L=1 km on Feeder 1 and Rf=0Ω

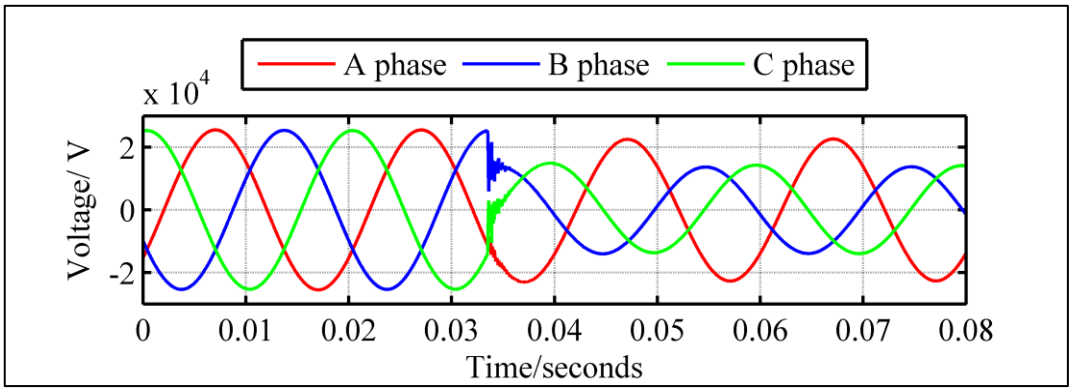

Figure 4.26 (a): Voltage waveforms for a BCG double phase to ground fault at L=15 km on Feeder 1 and Rf=0Ω

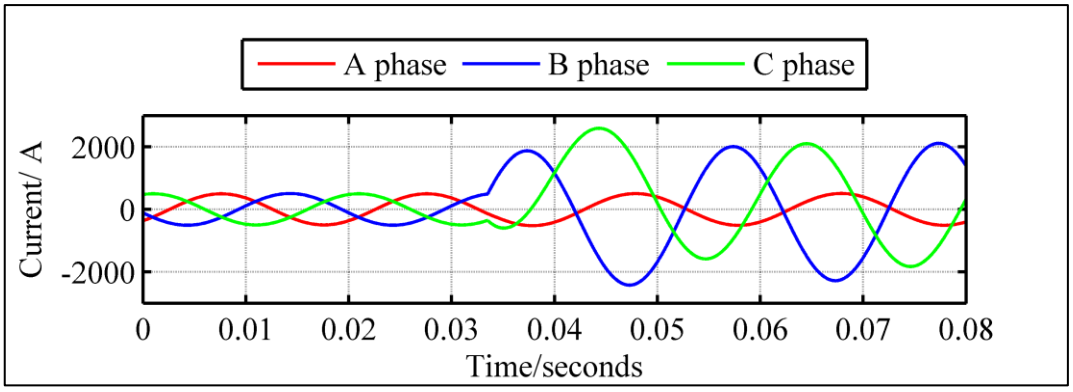

Figure 4.26 (b): Current waveforms for a BCG double phase to ground fault at L=15 km on Feeder 1 and Rf=0Ω

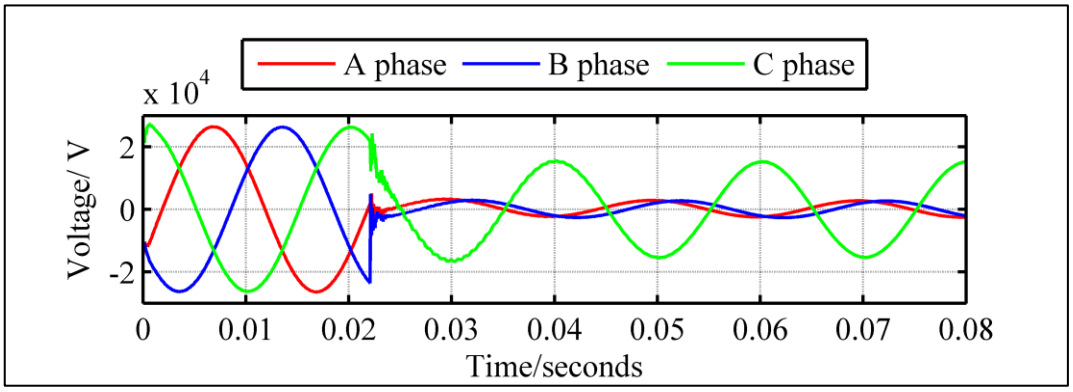

Figure 4.27 (a): Voltage waveforms for an ABG double phase to ground fault at L=1 km on Feeder 1 and Rf=0Ω with 10.5 MW DFIG wind farm connection

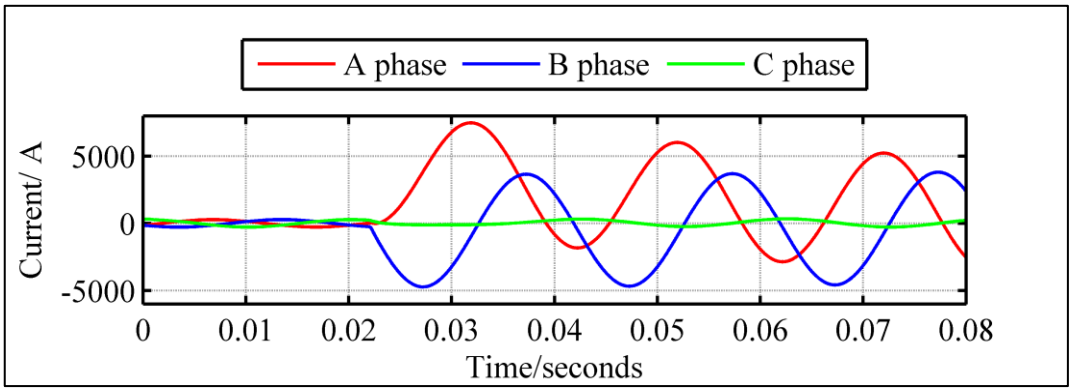

Figure 4.27 (b): Current waveforms for an ABG double phase to ground fault at L=1 km on Feeder 1 and Rf=0Ω with 10.5 MW DFIG wind farm connection

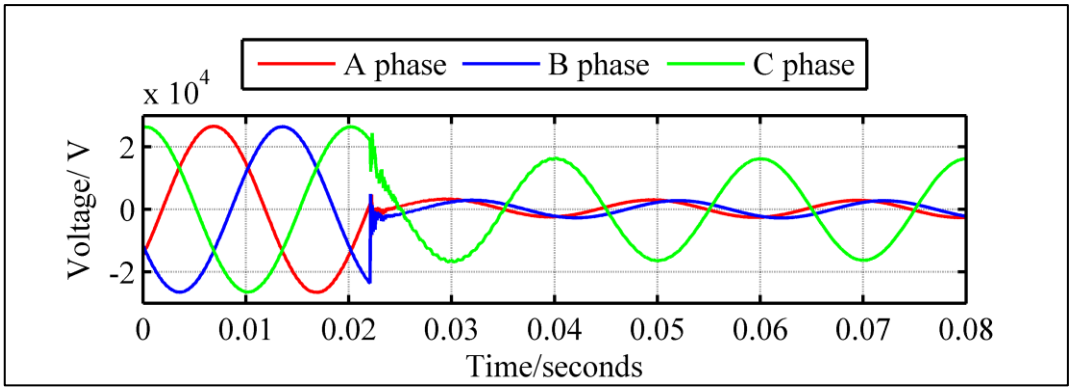

Figure 4.28 (a): Voltage waveforms for an ABG double phase to ground fault at L=1 km on Feeder 1 and Rf=0Ω with 10 MW PMSG wind farm connection

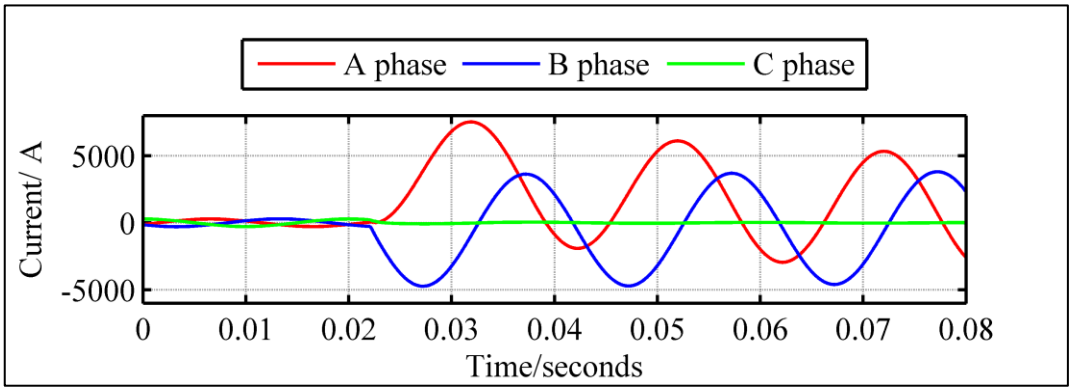

Figure 4.28 (b): Current waveforms for an ABG double phase to ground fault at L=1 km on Feeder 1 and Rf=0Ω with 10 MW PMSG wind farm connection

4.5.4 Three phase faults

For a three phase fault occurring on the network, the voltage drop in all three phases are equal, as shown in Figure 4.29 (a). There is an increase in the phase current amplitude of all three phases after the fault and a dc offset is also present soon after the fault (Figure 4.29 (b)).

The integration of a 10.5 MW DFIG wind farm (Figure 4.30) and a 10 MW PMSG wind farm (Figure 4.31) at the end of Feeder 1 reduces the current flowing from the substation during normal operation. After a fault, the phase currents are slightly increased but the effect is better observed after signal processing (discussed in Chapter 5).

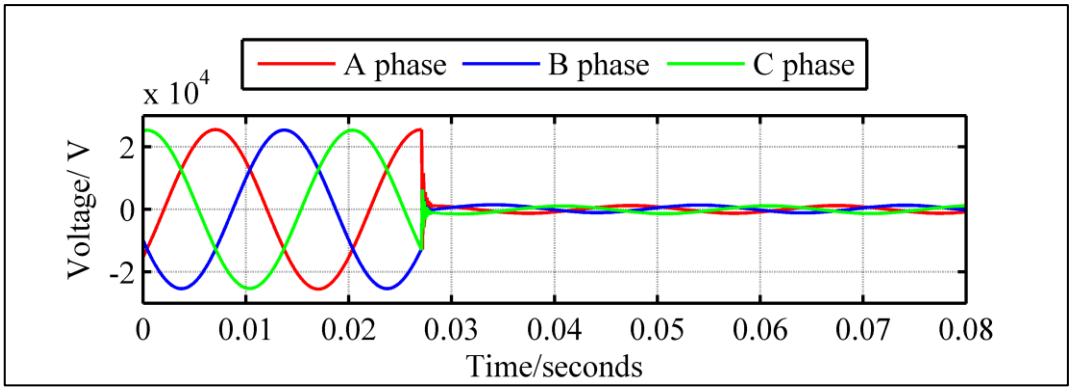

Figure 4.29 (a): Voltage waveforms for an ABC three phase fault at L=1 km on Feeder 1

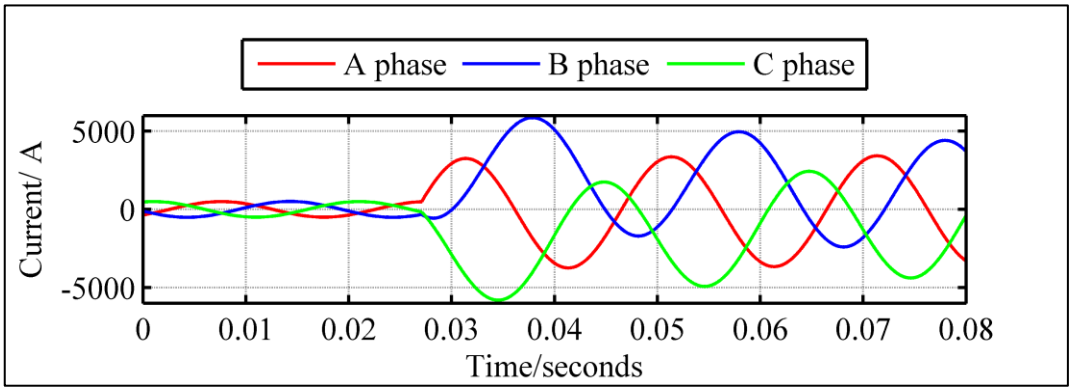

Figure 4.29 (b): Current waveforms for an ABC three phase fault at L=1 km on Feeder 1

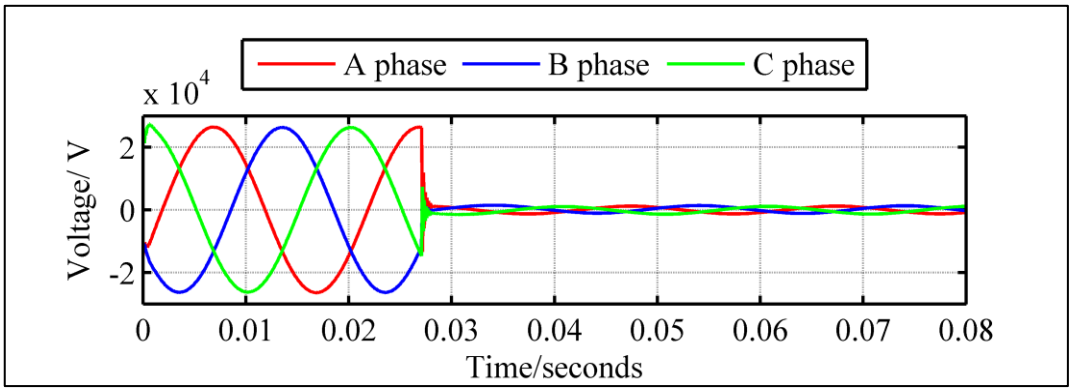

Figure 4.30 (a): Voltage waveforms for an ABC three phase fault at L=1 km on Feeder 1 with 10.5 MW DFIG wind farm connection

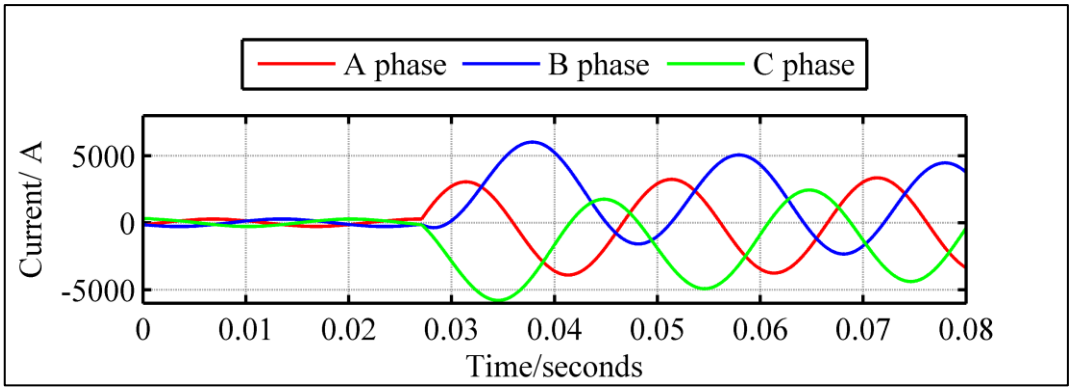

Figure 4.30 (b): Current waveforms for an ABC three phase fault at L=1 km on Feeder 1 with 10.5 MW DFIG wind farm connection

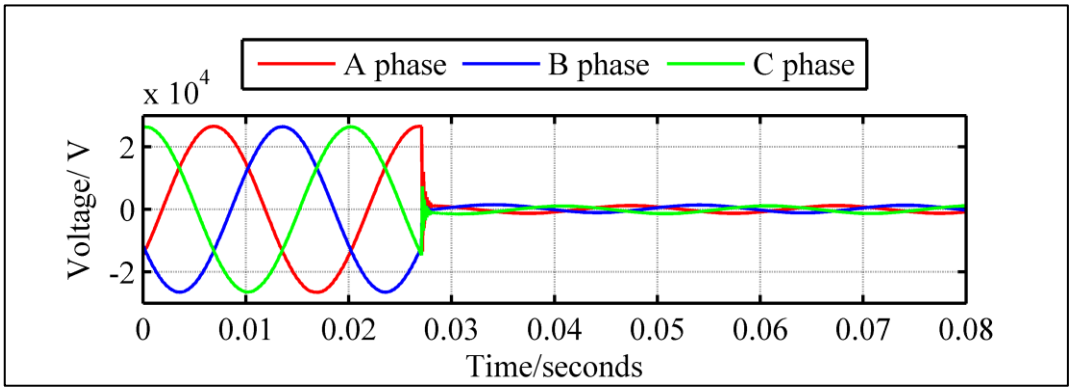

Figure 4.31 (a): Voltage waveforms for an ABC three phase fault at L=1 km on Feeder 1 with 10 MW PMSG wind farm connection

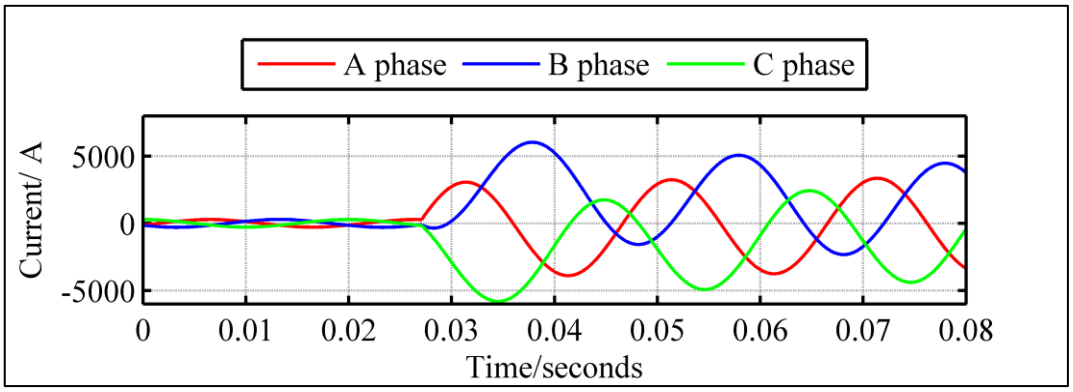

Figure 4.31 (b): Current waveforms for an ABC three phase fault at L=1 km on Feeder 1 with 10 MW PMSG wind farm connection

4.6 Signal conditioning

In real world applications, the continuous time analogue voltage and current signals (usually in the order of a few kV and kA) measured by instrument transformers on the power system, have to be conditioned in a certain way before they can be used by a microprocessor relay. Figure 4.32 shows the main stages involved to generate a command signal to perform a specific task such as closing or opening of a circuit breaker on the power system network.

The continuous time signals are acquired and processed to a suitable voltage level in the analogue input subsystem and analogue interface blocks. The status of the circuit breaker is fed to the microprocessor via the digital input subsystem. The relay settings are stored in the Read Only Memory (ROM) and all the information is processed by the relay algorithm in the microprocessor. The output command is then sent to the circuit breaker through the digital output subsystem.

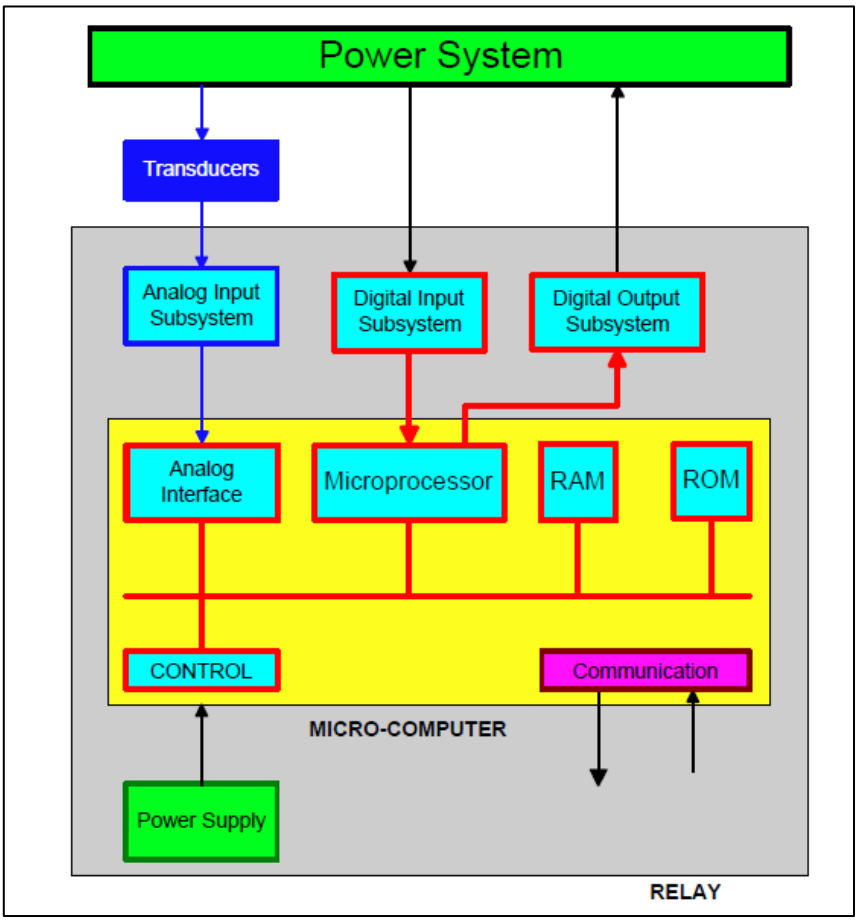

Figure 4.32: Typical microprocessor based relay [89]

The transducers, i.e. voltage transformers and current transformers, step down the measured voltage and current signals before feeding them to the analogue input subsystem. In this subsystem, the voltage levels are further reduced and the currents are converted to their equivalent voltage levels using precision resistors since the analogue to digital (A/D) converter in the analogue interface block can only manipulate voltages.

Another function of the analogue input subsystem block is to filter out some high frequency components from the input signals to prevent aliasing [90] when the voltage and current signals are sampled by the A/D converter. Aliasing occurs when the sampling time interval of the continuous time signals is not small enough to reconstruct the original signals from the discrete time samples. Mathematically, sampling is the multiplication of the continuous time signal, $g_c(t)$, by a periodic impulse train signal $i_p(t)$ (impulses uniformly spaced at t=nT). The result is a discrete time impulse train signal $g_p(t)$. The equation relating to the sampling process is as follows:

$$g_p(t) = g_c(t)i_p(t) = \sum_{n=-\infty}^{\infty} g_c(nT)\delta(t - nT) \qquad \text{Equation 4.6}$$

To avoid aliasing, the required sampling rate is given by the Nyquist criterion, which states that the minimum sampling frequency that must be used to fully reconstruct the continuous time signal from its discrete time signal is at least twice the frequency of the highest frequency component (Nyquist frequency, f_n) present in the continuous time signal i.e.

$$Minimum\ sampling\ frequency, f_s \geq 2f_n \qquad \text{Equation 4.7}$$

Figure 4.33 shows a 300 Hz signal superimposed onto a 60 Hz signal for five cycles. When that signal is sampled at a frequency of 960 Hz (above minimum sampling frequency) and reconstructed from the discrete sample values, the reconstructed waveform (Figure 4.34) is similar to the original waveform. However, if the signal is sampled at 480 Hz, the reconstructed waveform is not a faithful representation of the original signal due to aliasing (Figure 4.35).

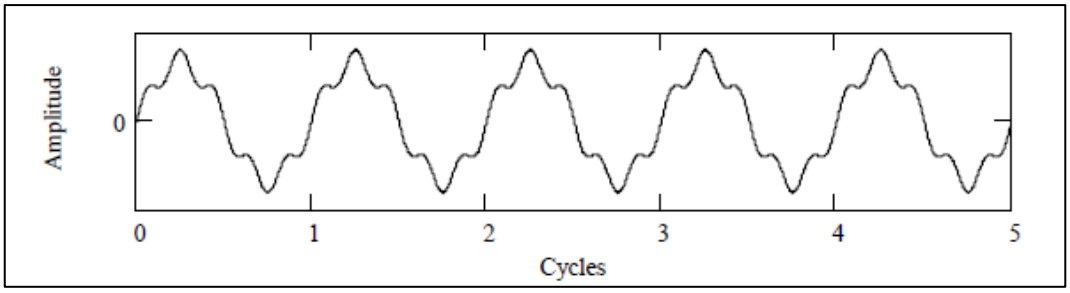

Figure 4.33: Original signal with 300 Hz component superimposed onto 60 Hz signal [89]

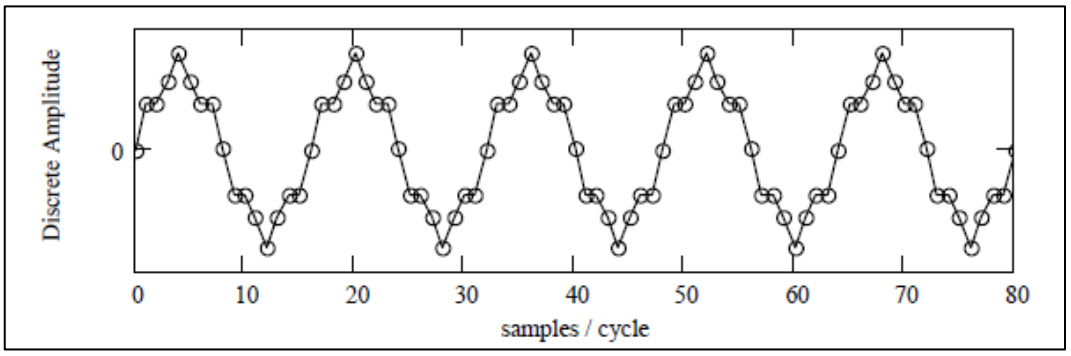

Figure 4.34: Reconstructed signal with a sampling frequency of 960 Hz [89]

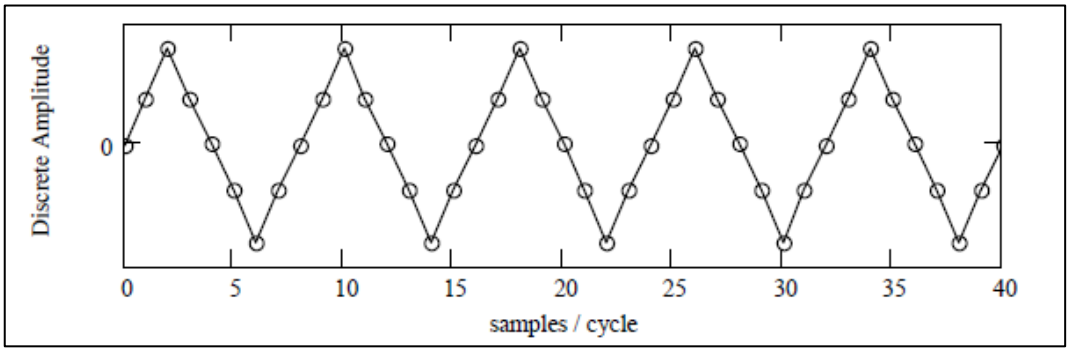

Figure 4.35: Aliasing due to sampling frequency of 480 Hz [89]

Sometimes, it is not possible to choose an appropriate sampling frequency and the signals are filtered using a lowpass filter before sampling. The A/D converter in the analogue interface block then converts the discrete amplitude of the sampled signals into binary outputs to be used by the microprocessor. It is therefore important to consider these signal conditioning stages in the fault simulations so that the

algorithms to be developed at a later stage are representative of a real world application.

4.6.1 Anti-aliasing filtering

The simulated current signals have been converted to their equivalent voltage levels in the range of ± 10 V. These signals are then passed through a lowpass anti-aliasing filter to remove some of the high frequency components in the signals [91, 92]. The filtering is performed by implementing a Butterworth filter of order 3 in MATLAB with a cut-off frequency at 10 kHz.

4.6.2 Quantization

Quantization is performed in the analog to digital conversion process of an analogue signal by giving it discrete amplitude levels. A 16-bit A/D converter has been implemented which represents 10 volts with the binary value of 1111111111111111 and -10 volts with the binary value 0000000000000000. Therefore, this represents 65536 (2^{16}) discrete levels. Thus, the least significant bit (LSB) of the converter is approximately 0.3 mV (i.e. $20/2^{16}$). Quantization has been implemented in MATLAB with the floor function which is used for uniform mid-rise quantization.

The signal to noise ratio (SNR) of the uniform quantizer is given by [91]:

$$SNR(dB) = 6n + 4.77 - 20\log_{10}\left(\frac{X_{max}}{\sigma_X}\right) \qquad \text{Equation 4.8}$$

$$SNR = 98\ dB$$

where, n=number of bits in A/D converter = 16

X_{max} = peak to peak voltage/2

and σ_x = RMS value of input = 10/√2

4.7 Summary

In this chapter, the implementation of a typical 33 kV overhead active distribution network in Simulink has been thoroughly discussed. The network consists of feeders and spurs from which different types of short circuit faults can be simulated at various locations in the network.

The full-scale model of a DFIG wind turbine configuration in Simulink has been presented together with modifications involving the implementation of a crowbar protection scheme. The general operating principle of the grid-side converter and the rotor-side converter has been explained to better understand the operation of the DFIG model. Similarly, the various components of the PMSG model namely the inverter, the dc-dc boost converter and the diode rectifier have been explained.

The simulation of different types of short circuit faults on the network allowed the validation of the developed 33 kV active distribution network by observing the voltage and current signals obtained during these faults. Finally, the signal conditioning stage showed how analog signals captured in the outside environment are processed into a digital form that can be easily manipulated by a microprocessor relay. The various stages involve anti-aliasing filtering and analog to digital conversion. The simulated fault current signals have been put through the above mentioned signal conditioning stages in order to cater for errors that can be introduced by these stages in real applications.

Chapter 5: Extraction of fault current signatures

5.1 Introduction

Feature extraction is the first and most important step for accurate fault classification and location using ANN based methods. Faults induce electromagnetic transients onto the power frequency signals and feature extraction is a tool used to determine the frequency composition of a voltage or current signal which can help to characterise a particular type of fault or pinpoint the source of the fault. Several digital signal processing algorithms such as the Discrete Fourier Transform (DFT), the Short-Time Fourier Transform (STFT) and the Discrete Wavelet Transform (DWT) have been widely employed to extract distinct features to characterise fault transients, switching transients and lightning transients in power systems. Therefore, the basic principles of the above mentioned digital signal processing algorithms are explained in this section and their applications to fault induced transients are also demonstrated.

5.2 Discrete Fourier Transform

A continuous-time signal $x(t)$ can be mapped to the frequency domain, $X(j\omega)$, by performing the Fourier Transform given by:

$$X(j\omega) = \int_{-\infty}^{\infty} x(t)\, e^{-j\omega t} dt \qquad \text{Equation 5.1}$$

In polar form,

$$X(j\omega) = |X(j\omega)| e^{j\theta(\omega)} \qquad \text{Equation 5.2}$$

The amplitude spectrum and phase spectrum of the continuous-time signal can thus be obtained by performing the Fourier Transform. The original signal $x(t)$ can be reconstructed by performing the Inverse Fourier Transform as follows:

$$x(t) = \frac{1}{2\pi} \int_{-\infty}^{\infty} X(j\omega)\, e^{j\omega t} d\omega \qquad \text{Equation 5.3}$$

The continuous-time signal $x(t)$ can be sampled at discrete time intervals to form a discrete time signal $x[n]$ sampled at every T_s seconds for N samples i.e.

$$x[n] = x(nT_s) \; n = 0,1,2,\dots,N-1 \qquad \text{Equation 5.4}$$

and the Discrete Fourier Transform of the digital signal can be represented as [93]:

$$X[k] = \sum_{n=0}^{N-1} x[n]\, e^{-j\frac{2\pi kn}{N}} \qquad \text{Equation 5.5}$$

An application of the Discrete Fourier Transform to a typical capacitor switching transient signal is depicted in Figure 5.1. The digital signal has a 900 Hz component superimposed onto the 60 Hz component and the magnitude spectrum of the signal is obtained by applying the Discrete Fourier Transform.

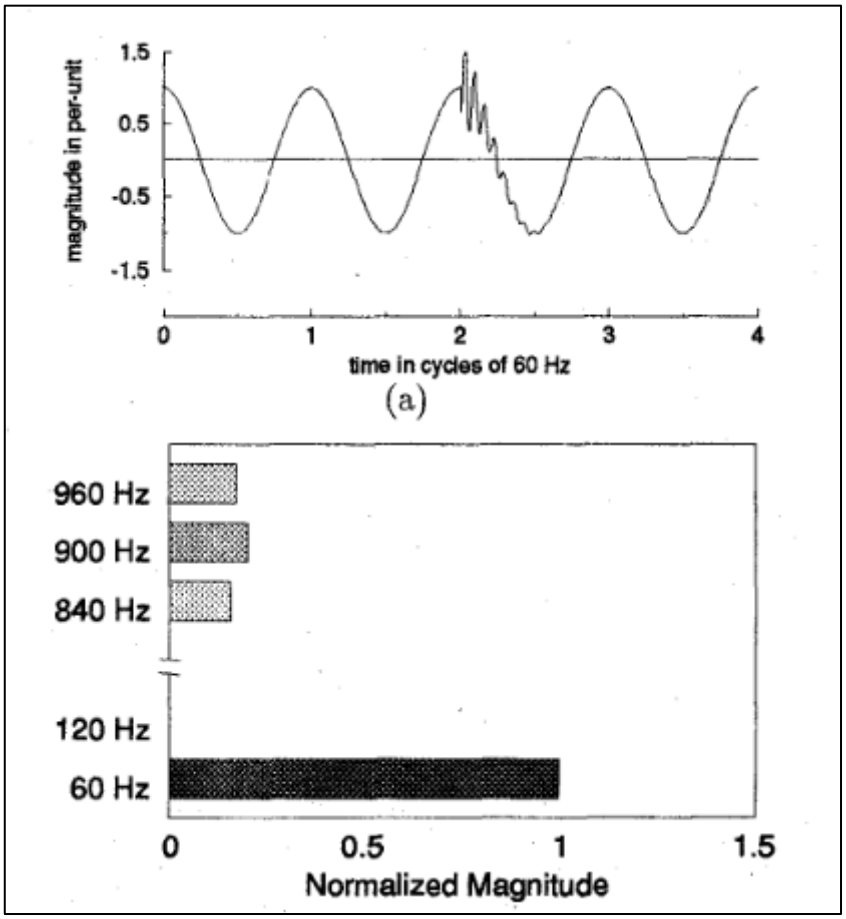

Figure 5.1: Magnitude spectrum of a capacitor switching transient signal using the Discrete Fourier Transform [94]

The Discrete Fourier Transform assumes that the signal is periodic in nature. However, power system transients are non-periodic signals with high frequency and low frequency components superimposed onto the fundamental frequency signal. This results in more energy present in the sidebands which may significantly corrupt useful information to accurately detect the source or cause of the transient. The Discrete Fourier Transform therefore requires a high sampling rate to deal with wide-band signals associated with power system transients [94]. Another drawback is that as can be seen from the magnitude spectrum of Figure 5.1, there is no record of when in time the transient occurred. In order to minimise the effect of the non-periodic signal and to achieve a better time resolution, the Short-Time Fourier Transform can be adopted.

5.3 Short-Time Fourier Transform

The Short-Time Fourier Transform is an attempt to reduce the effect of the non-periodic nature of the power system transients and also yield a better time resolution. This is done by performing the Fourier Transform for a specific window which represents only part of the whole length of the input signal. For a discrete-time signal, the Windowed Discrete Fourier Transform (WDFT) is given by [93, 95]:

$$WDFT\ (k,m) = \sum_{n} x[n]\, w[n-m] e^{-j\frac{2\pi kn}{N}} \qquad \text{Equation 5.6}$$

The function $w[n-m]$ is a rectangular window function given by:

$$w[n-m] = \begin{cases} 1 & if\ 0 \leq [n-m] \leq N-1 \\ 0 & otherwise \end{cases} \qquad \text{Equation 5.7}$$

The WDFT is applied to the same signal of capacitor switching transient and the results are depicted in Figure 5.2. As it can be observed in Figure 5.2 (b), the window size is one cycle and it is now possible to observe the various frequencies present in the signal at various time intervals. For the first two cycles, only the fundamental frequency (60 Hz) is present in the waveform. When the transient occurs (third cycle), it can be seen that higher frequency components are detected in the waveform.

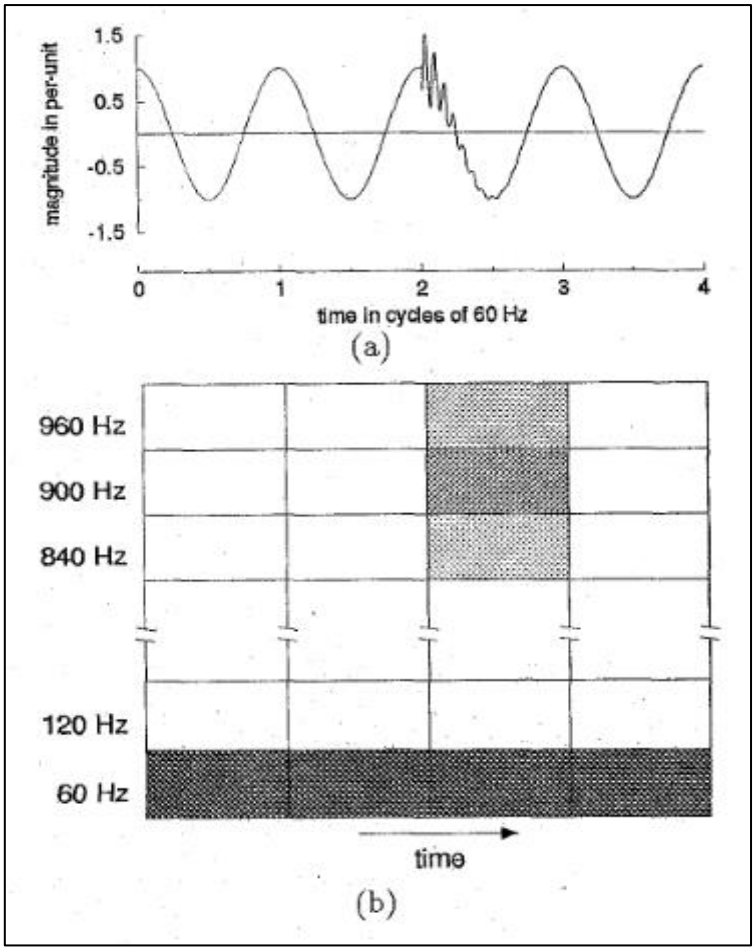

Figure 5.2: Windowed Discrete Fourier Transform with once cycle window size [94]

When the window size is reduced to a quarter of a cycle, better time resolution is achieved as can be seen in Figure 5.3. However, frequency resolution is decreased as can be observed by the appearance of the 60 Hz component in the 240 Hz components.

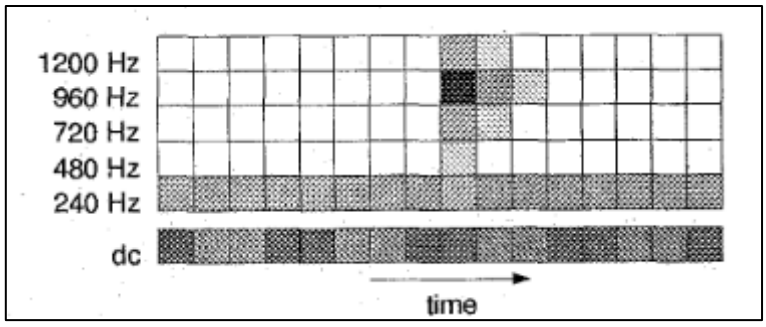

Figure 5.3: Windowed Discrete Fourier Transform with quarter cycle window size [94]

It has been observed that the Short-Time Fourier Transform allows only a fixed window size to be applied to the input signal. The width of the window has an impact on the frequency and time resolution. A small window size allows a good time resolution but affects the frequency resolution whereas a wide window enables good frequency resolution but also gives poor time resolution.

5.4 Discrete Wavelet Transform

The Discrete Wavelet Transform is another digital signal processing tool for the analysis of signals by comparing the actual signal with a base wavelet (mother wavelet) in order to identify the different frequency components present in the signal. The mother wavelet or windowing function has zero mean and decays rapidly at both ends. Figure 5.4 shows various types of mother wavelets developed over the years.

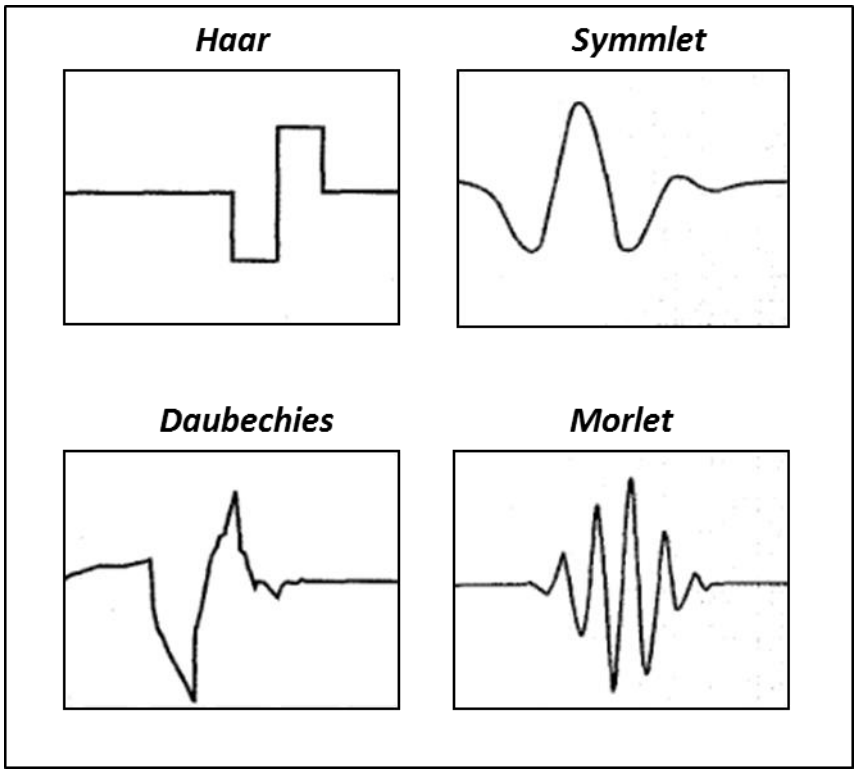

Figure 5.4: Mother wavelets

The initial concept of the Wavelet Transform was developed by Alfred Haar in 1909 with a rectangular function as a base wavelet. Further advancements made by Jean Morlet in the 1970's resulted in a varying window width analysis by scaling or time shifting the base wavelet [95]. This overcame the limitation of the fixed window size

of the Short-Time Fourier Transform by enabling the application of a short wavelet to analyse high frequency components and the application of a long wavelet to analyse low frequency components, thus resulting in both good time and frequency resolution.

For a continuous-time signal, $x(t)$ and a mother wavelet $g(t)$, the Wavelet Transform is given by [93, 94]:

$$WT(a,b) = \frac{1}{\sqrt{a}} \int_{-\infty}^{\infty} x(t) g\left(\frac{t-b}{a}\right) dt \qquad \text{Equation 5.8}$$

Where a and b are the scaling factor and translation factor respectively. The value of a, expands or contracts the mother wavelet $g(t)$ in time i.e. for $a > 1$, the width of $g(t)$ increases in time but the frequency of oscillations decreases while for $a < 1$, the width of the mother wavelet decreases in time and thus the frequency of oscillations in the mother wavelet increases.

Therefore, by varying the a and b parameters, a family of wavelets also called daughter wavelets can be generated from the mother wavelet. For example, Figure 5.5 illustrates the Daubechies (db) family of wavelets of order 1 to 10.

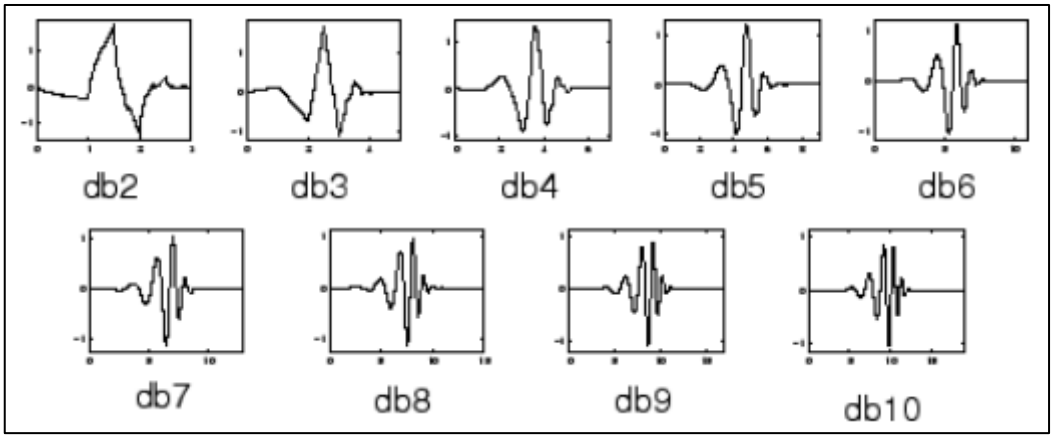

Figure 5.5: Daubechies daughter wavelets [96]

The Discrete Wavelet Transform of a digital signal is given by [93]:

$$DWT(m,k) = \frac{1}{\sqrt{a_0^m}} \sum_n x(n) g\left(\frac{k - nb_0 a_0^m}{a_0^m}\right) \qquad \text{Equation 5.9}$$

It can be implemented using a set of lowpass and highpass filters as shown in Figure 5.6. The Discrete Wavelet Transform decomposes an original signal into an approximation coefficient using a lowpass filter $g(n)$ (mother wavelet) and a detailed component using a highpass filter $h(n)$ (dual of $g(n)$). For a sampling frequency Fs of the original signal, the first detail component (D1) contains frequencies in the range of Fs/4 to Fs/2. The approximation component is then decomposed into another set of detail (D2) and approximation components by a dilated wavelet of factor 2 resulting from the downsampling at the output of the lowpass filter. The detail component contains frequencies in the range of Fs/8 to Fs/4. The process is repeated a number of times until the desired level of decomposition of the signal is achieved [97].

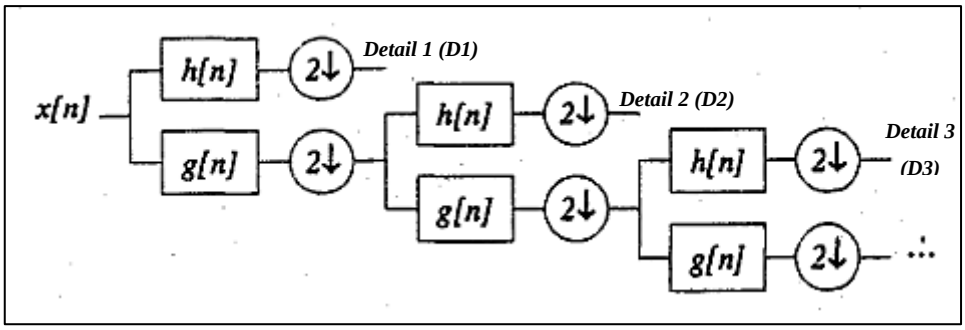

Figure 5.6: Multi-stage filter DWT implementation [94]

The application of the Discrete Wavelet Transform to a typical capacitor switching transient waveform is illustrated in Figure 5.7. It can be seen that there is a varying window width at different frequencies in the signal. At high frequencies (960 Hz), the window width is small whereas at low frequencies (60 Hz), the window width is large. This allows multi-resolution analysis of the signal and yields both a good time and frequency resolution. The high frequency component (960 Hz) gives a precise indication of the occurrence of the transient in the time domain.

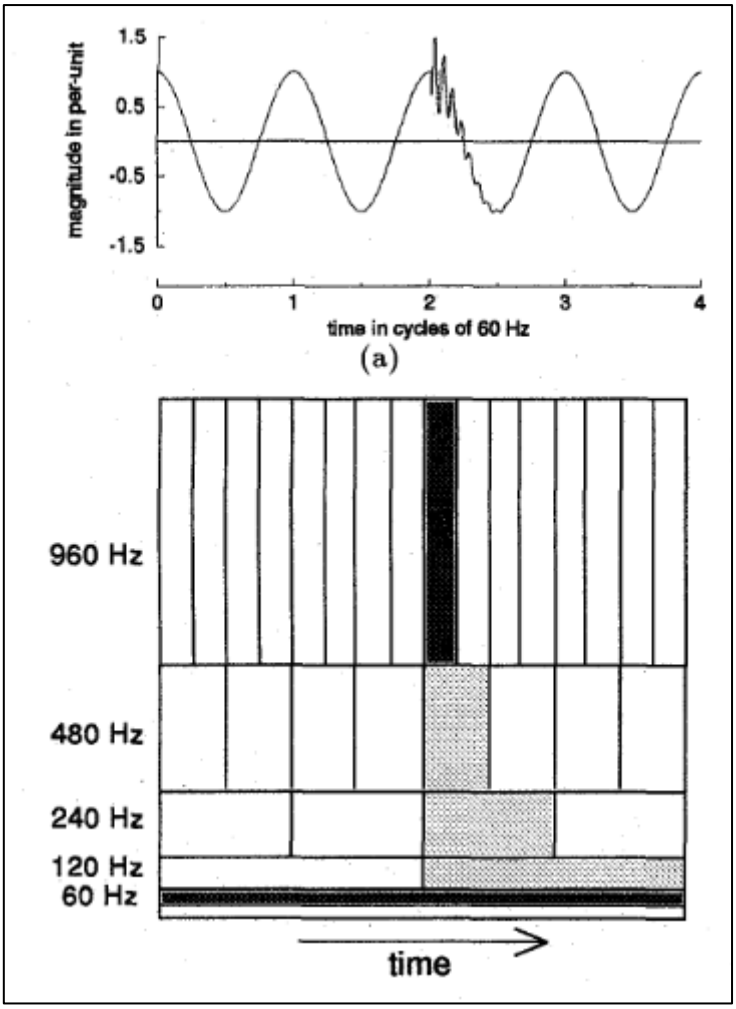

Figure 5.7: Multi-resolution analysis with the Discrete Wavelet Transform [94]

5.5 DWT analysis of short-circuit current signals

As discussed in the previous sections, the Discrete Fourier Transform has a poor time resolution and the Windowed Fourier Transform gives a better time resolution but at the detriment of the frequency resolution due to the fixed window length. The Discrete Wavelet Transform gives a better resolution in both time and frequency and therefore it has been chosen as the desired signal processing tool to extract the features from fault current signals.

The Discrete Wavelet Transform enables the identification of the distinct features present in the short-circuit transients for accurate fault classification and fault location using the Artificial Neural Network based algorithms. The Discrete Wavelet Transform is applied to a data window of 1 cycle pre-fault and 2 cycles post fault to

enable the training of the Artificial Neural Network algorithms to differentiate between a normal and a fault condition.

According to Hwan Kim and Aggarwal [93, 97], the Daubechies mother wavelet is more suitable for the analysis of fast decaying oscillating signals superimposed on the fundamental frequency component in power systems. Hence the Daubechies mother wavelet at level 4 (db4) has been utilised for feature extraction. The range of frequencies of detail 1 to detail 10 components for a sampling frequency of 25 kHz is given in Table 5.1.

Detail component	**Frequency range**
Detail 1	6.25 kHz – 12.5 kHz
Detail 2	3.125 kHz – 6.25 kHz
Detail 3	1.56 kHz – 3.125 kHz
Detail 4	781 Hz – 1.56 kHz
Detail 5	390 Hz – 781 Hz
Detail 6	195 Hz – 390 Hz
Detail 7	97.5 Hz – 195 Hz
Detail 8	48.75 Hz – 97.5 Hz
Detail 9	24.38 Hz – 48.75 Hz
Detail 10	12.19 Hz – 24.38 Hz

Table 5.1: Frequency decomposition with DWT successive filtering

The spectral energy of each detail component is obtained by calculating the energy of the wavelet coefficient over a small window. The window size is 20 samples and the energy is calculated by the equation:

$$Energy = \sum_{n=1}^{20} (magnitude\ of\ wavelet\ coefficient)^2 \qquad \text{Equation 5.10}$$

Using Equation 5.10, the spectral energies of the A phase, B phase and C phase can be obtained for different types of faults at various locations on the typical 33 kV distribution network.

5.5.1 Single phase to ground faults

Figure 5.8 to Figure 5.13 show the Discrete Wavelet Transform analysis of the fault current waveforms for A phase to ground faults at various locations on Feeder 1 for fault inception angles of 0° and 90° and fault impedances of 0 Ω, 25 Ω and 50Ω.

In Figure 5.8, it can be seen that the A phase to ground fault occurs at sample number 26. Before the occurrence of the fault, the energies of the high frequency components (781 Hz to 12.5 kHz) for all three phases are approximately zero. When the fault occurs on the A phase, this results in a spike being produced on the A phase waveforms for the high frequency components. However, the energies of the healthy B and C phases remain close to zero.

The waveforms of the low frequency detail components (12.19 Hz to 781 Hz) show an oscillatory behaviour on the A phase after the occurrence of the fault. The amplitudes of the low frequency detail components are much higher than the amplitudes of the spikes for the high frequency components but the amplitudes of the healthy B and C phases remain close to zero before and after the fault.

Figure 5.9 shows the A phase to ground fault occurring at 15 km on Feeder 1 with a fault inception angle of 0° and a fault impedance of 0Ω. It can be observed that the fault produces a spike for the high frequency components of the A phase and oscillatory waveforms of higher amplitudes for the low frequency components. The energies of the healthy B and C phases for the low frequency components (12.19 Hz to 781 Hz) are close to zero but for the high frequency components, some spikes can be detected for certain frequencies. This can be explained by the electromagnetic coupling between the phases due to the ground return path.

Figure 5.10 and Figure 5.11 show the effect of increasing the fault impedance on the fault current signatures. Higher fault impedances of 25Ω and 50Ω decrease the amplitudes of the energy waveforms of the faulted phase for components in the range of 12.19 Hz to 195 Hz.

Finally, Figure 5.12 and Figure 5.13 demonstrate that changing the fault inception angle yield similar results as explained above for the various frequency components.

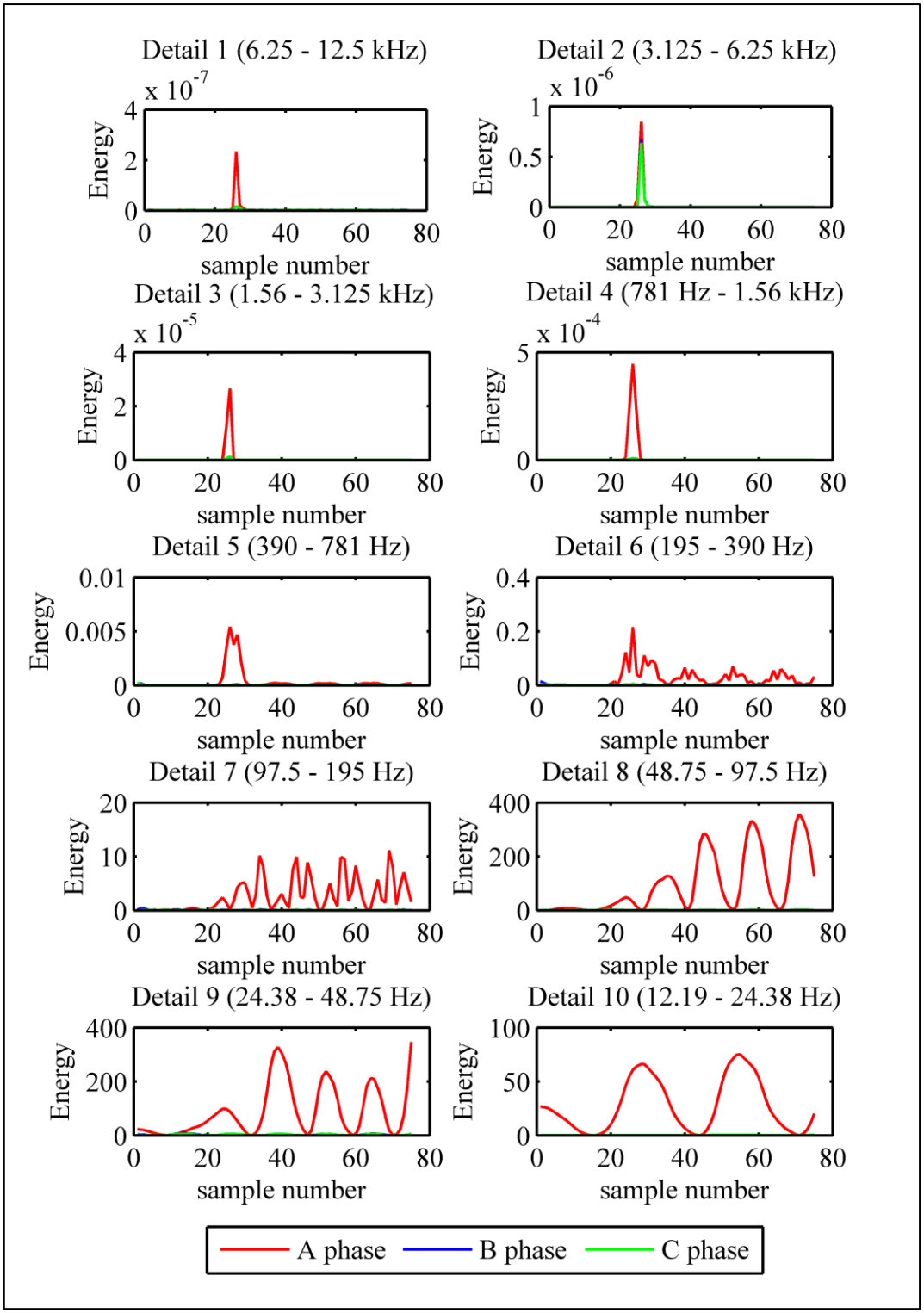

Figure 5.8: DWT of current waveforms for an A phase to ground fault with fault impedance Rf=0Ω and fault inception angle θ=0° at L=1 km on Feeder 1

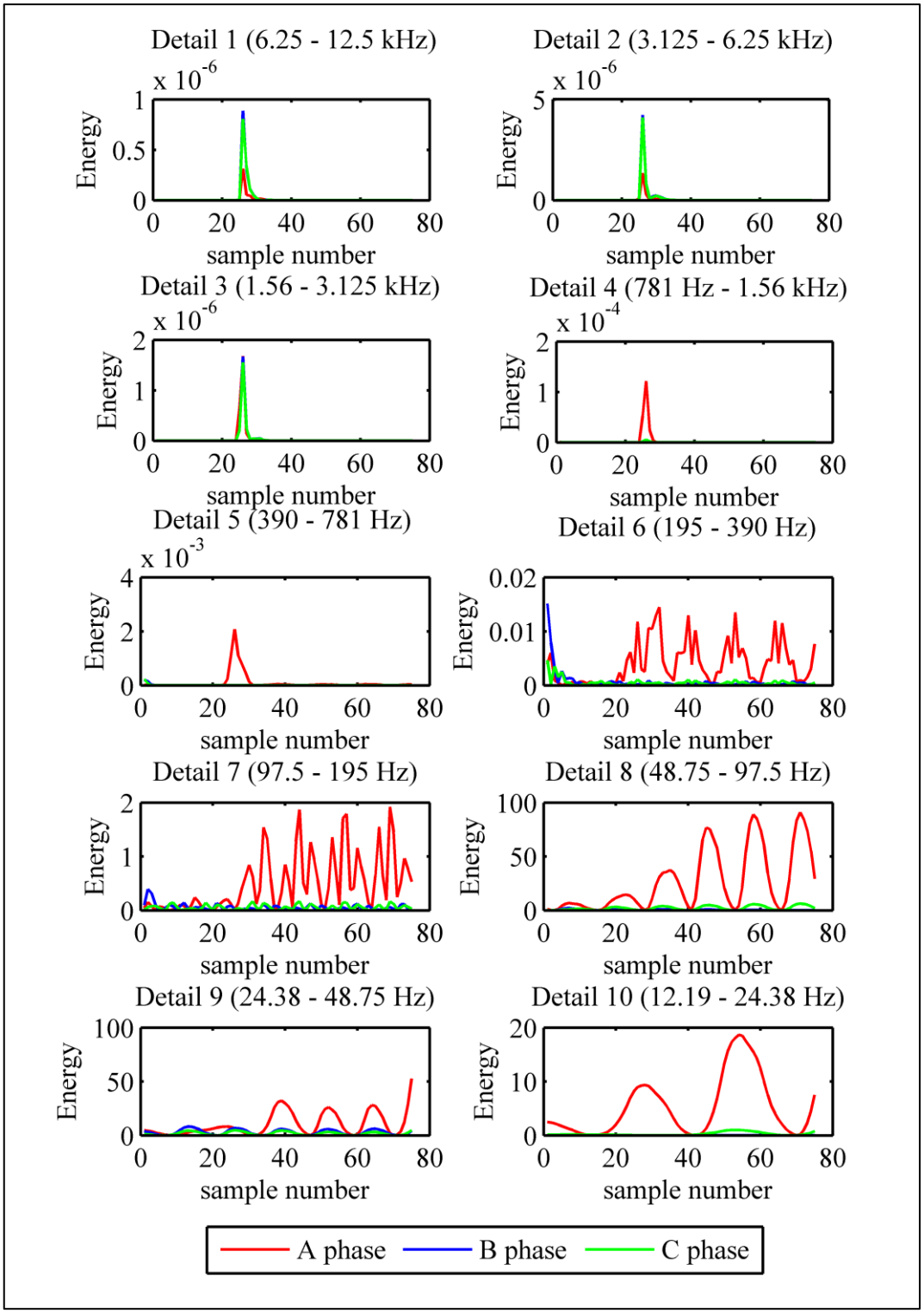

Figure 5.9: DWT of current waveforms for an A phase to ground fault with fault impedance Rf=0Ω and fault inception angle θ=0° at L=15 km on Feeder 1

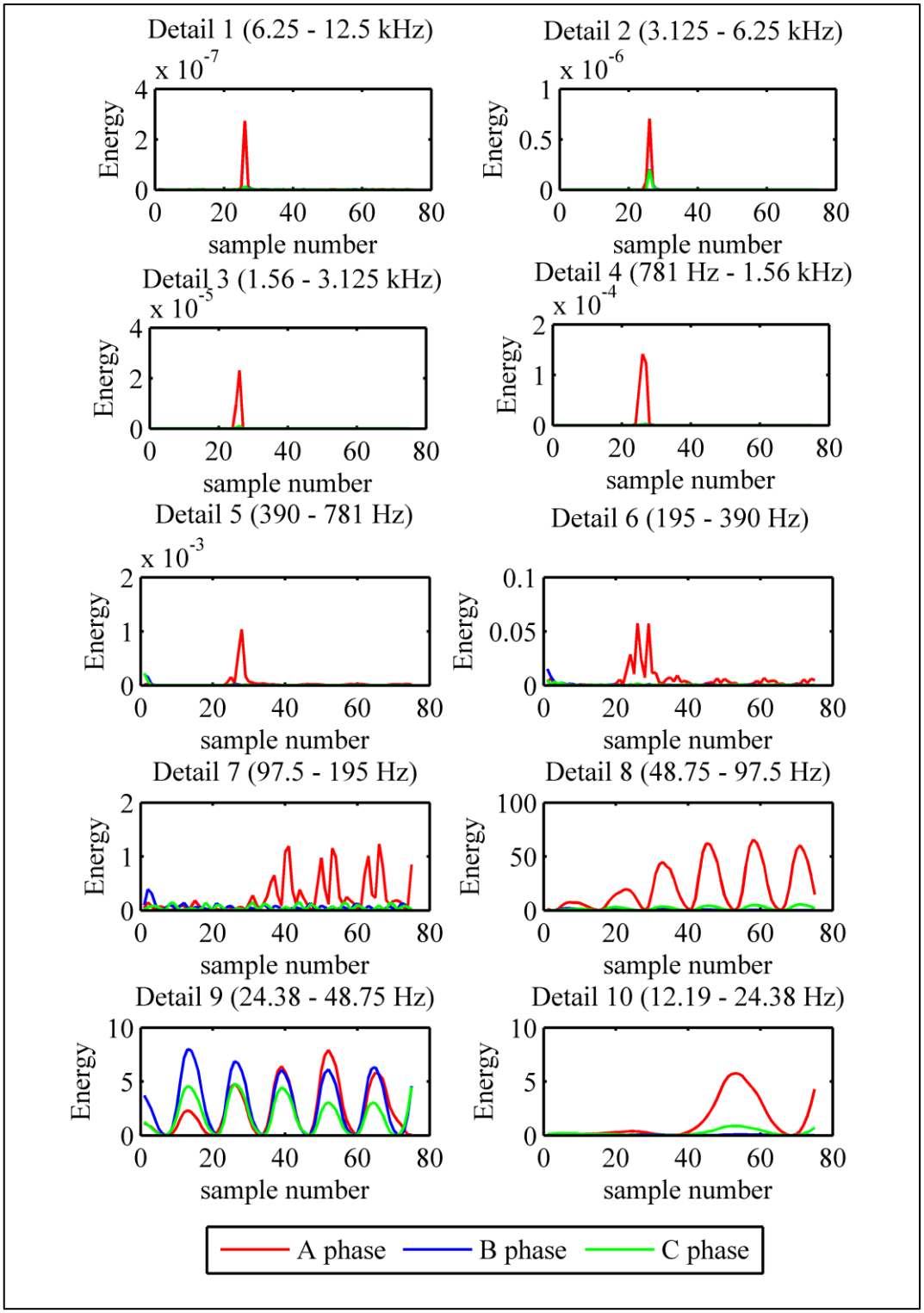

Figure 5.10: DWT of current waveforms for an A phase to ground fault with fault impedance Rf=25Ω and fault inception angle θ=0° at L=1 km on Feeder 1

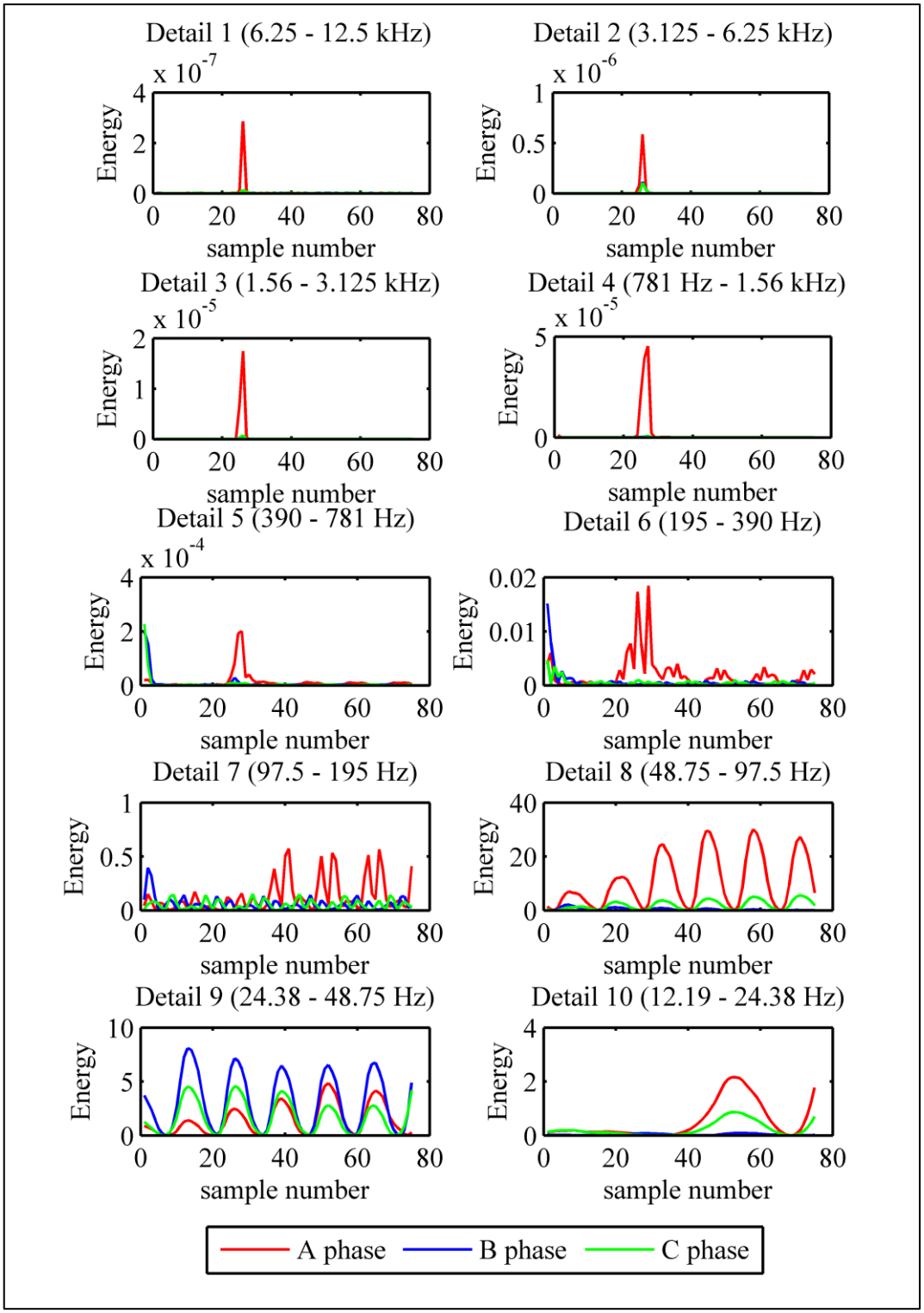

Figure 5.11: DWT of current waveforms for an A phase to ground fault with fault impedance Rf=50Ω and fault inception angle θ=0° at L=1 km on Feeder 1

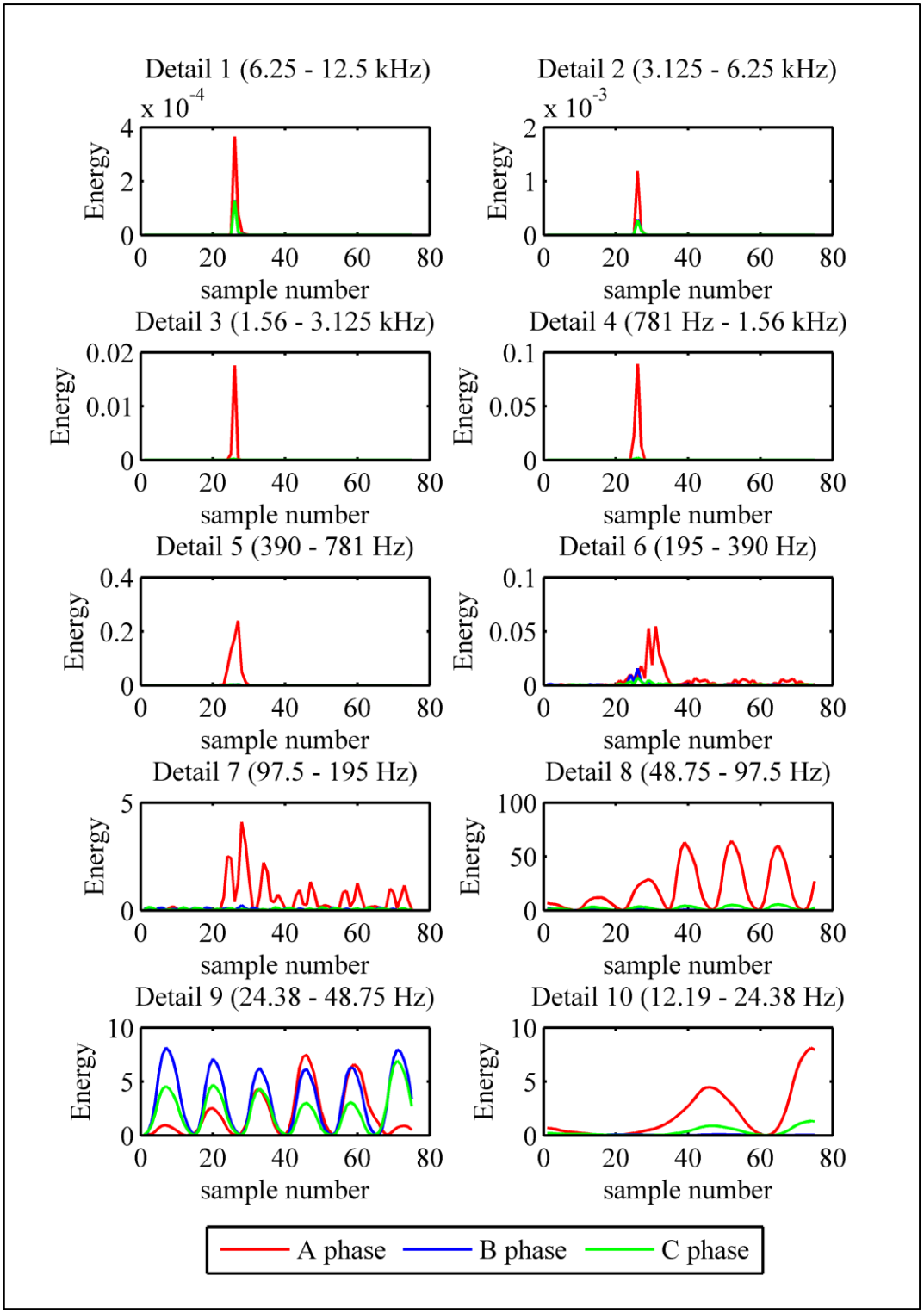

Figure 5.12: DWT of current waveforms for an A phase to ground fault with fault impedance Rf=25Ω and fault inception angle θ=90° at L=1 km on Feeder 1

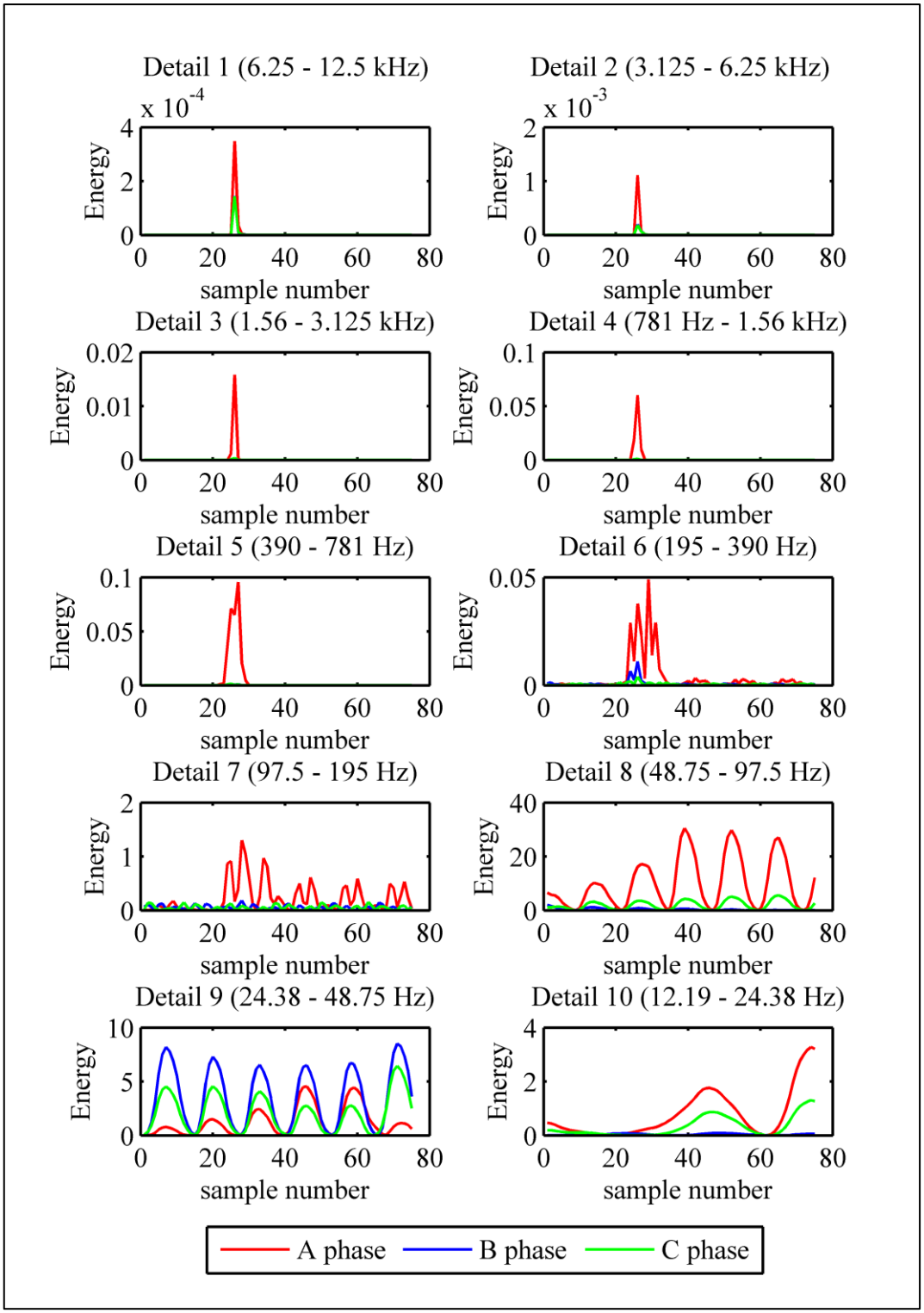

Figure 5.13: DWT of current waveforms for an A phase to ground fault with fault impedance Rf=50Ω and fault inception angle θ=90° at L=1 km on Feeder 1

5.5.2 Phase to phase faults

Figure 5.14 to Figure 5.16 depict the Discrete Wavelet Transform analysis of the phase current waveforms for an AB, phase to phase fault, occurring on Feeder 1. A spike can be detected after the fault occurrence for the faulted A phase and B phase for the high frequency detail components whereas oscillatory waveforms are obtained for the low frequency components. The energy waveforms of detail components of the C phase stay at zero level for both before and during the fault.

It can also be noticed that for detail 1 to detail 6 components, the energy waveform of the A phase has the same amplitude and same phase angle as the B phase. The same observation can be made even when changing the fault location to 15 km on Feeder 1 (Figure 5.15) and also when changing the fault inception angle of the fault (Figure 5.16).

It can also be noted that as compared to single phase to ground faults, phase to phase faults do not give rise to a spike in the high frequency components for the healthy C phase since there is no ground return path and hence less electromagnetic coupling between phases.

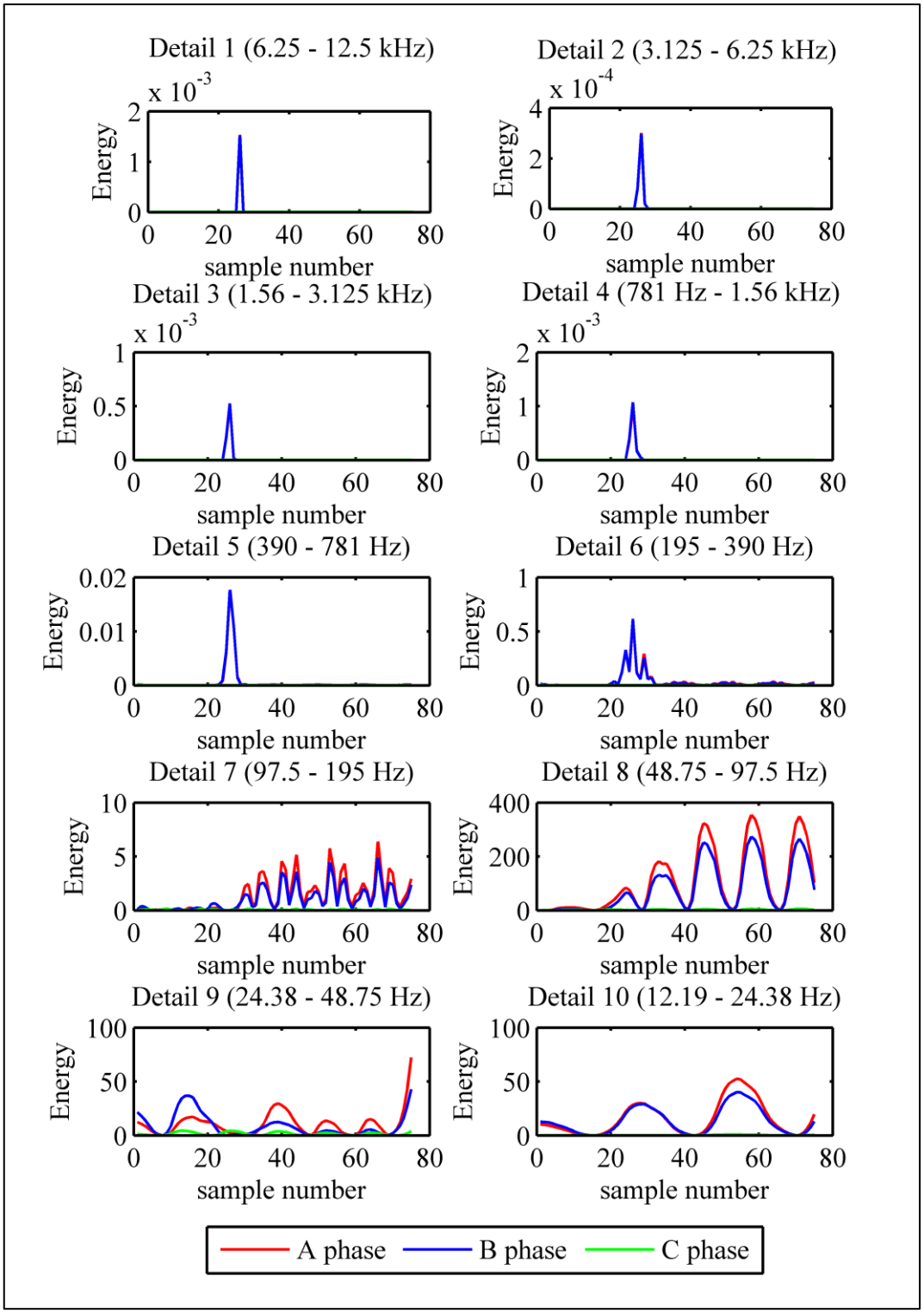

Figure 5.14: DWT of current waveforms for an A phase to B phase fault with fault inception angle θ=0° on the A phase at L=1 km on Feeder 1

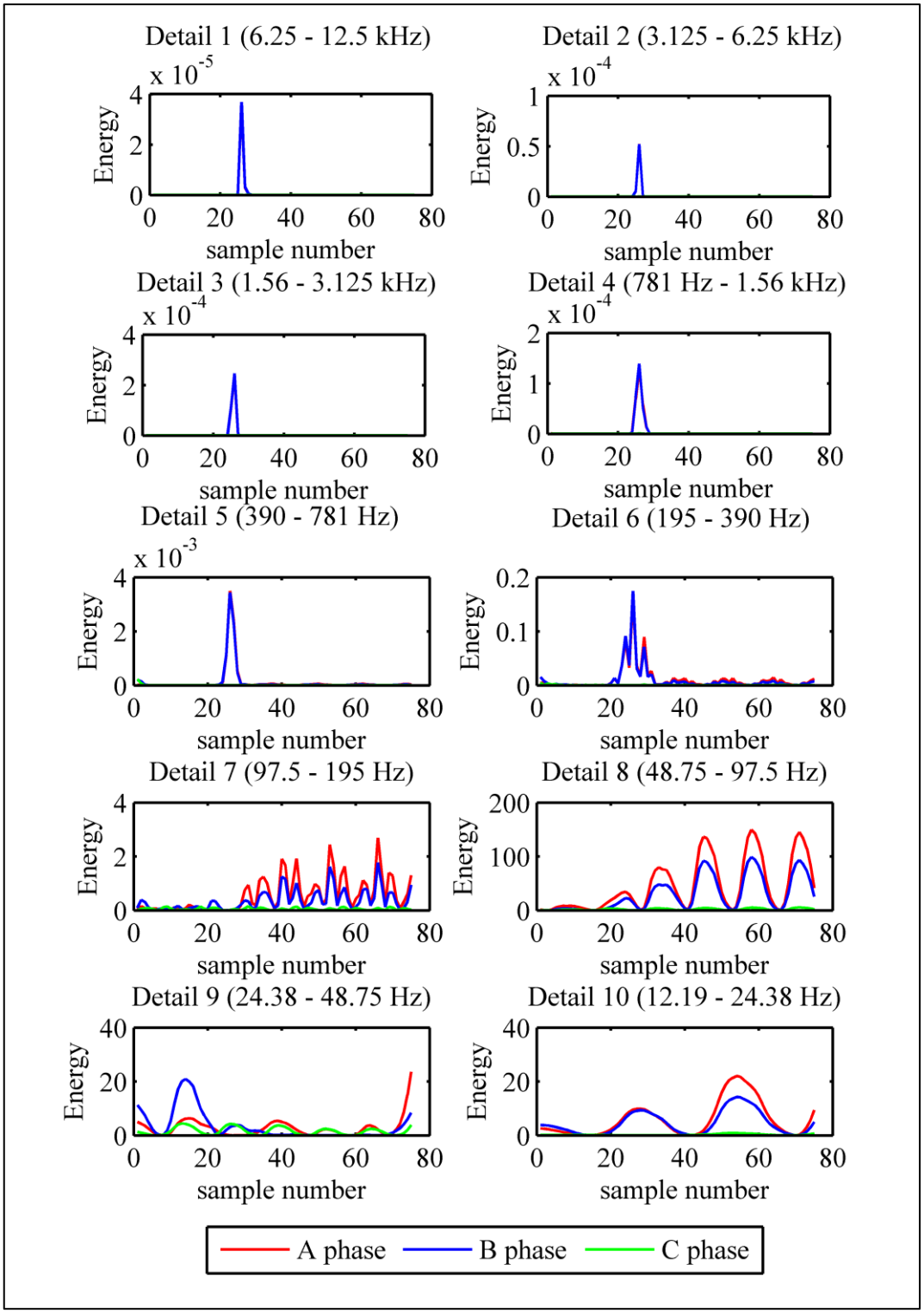

Figure 5.15: DWT of current waveforms for an A phase to B phase fault with fault inception angle θ=0° on the A phase at L=15 km on Feeder 1

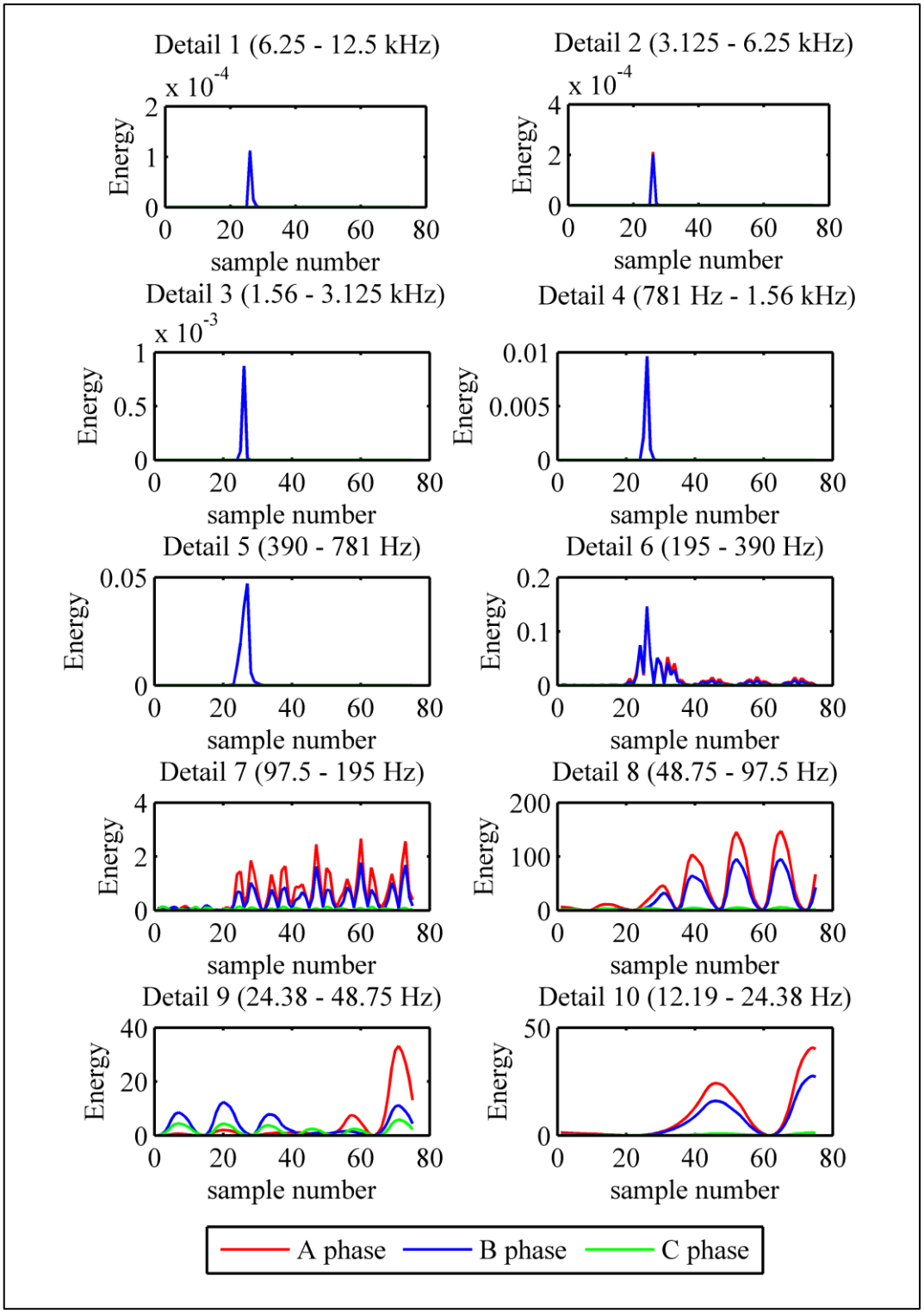

Figure 5.16: DWT of current waveforms for an A phase to B phase fault with fault inception angle θ=90° on the A phase at L=15 km on Feeder 1

5.5.3 Double phase to ground faults

In this section, the Discrete Wavelet Transform analysis of phase current waveforms for a double phase to ground fault on Feeder 1 are discussed. Figure 5.17 to Figure 5.19 show that before the occurrence of the fault, the energies of all three phases are at zero for the high frequency detail components. When the fault occurs on the feeder (sample number 26), a spike can be observed for the faulted A phase and B phase whereas the energy of the healthy C phase remains zero. For the low frequency components, oscillatory waveforms can be observed for the faulted phases after the occurrence of the fault on Feeder 1.

The faulted A phase and B phase waveforms for low frequency components are in phase but differ slightly in amplitudes. The location of the fault on the feeder (Figure 5.18) does not influence the pattern observed for the high frequency and low frequency components i.e. spikes on the faulted phases for high frequency components and oscillatory waveforms for the low frequency components.

The increase in fault impedance (Figure 5.19) dampens the amplitudes of the low frequency components.

In Figure 5.18, it can be seen that the ABG fault produces spikes on the healthy C phase for high frequency components in the range of 3.125 kHz to 12.5 kHz due to the electromagnetic coupling between phases.

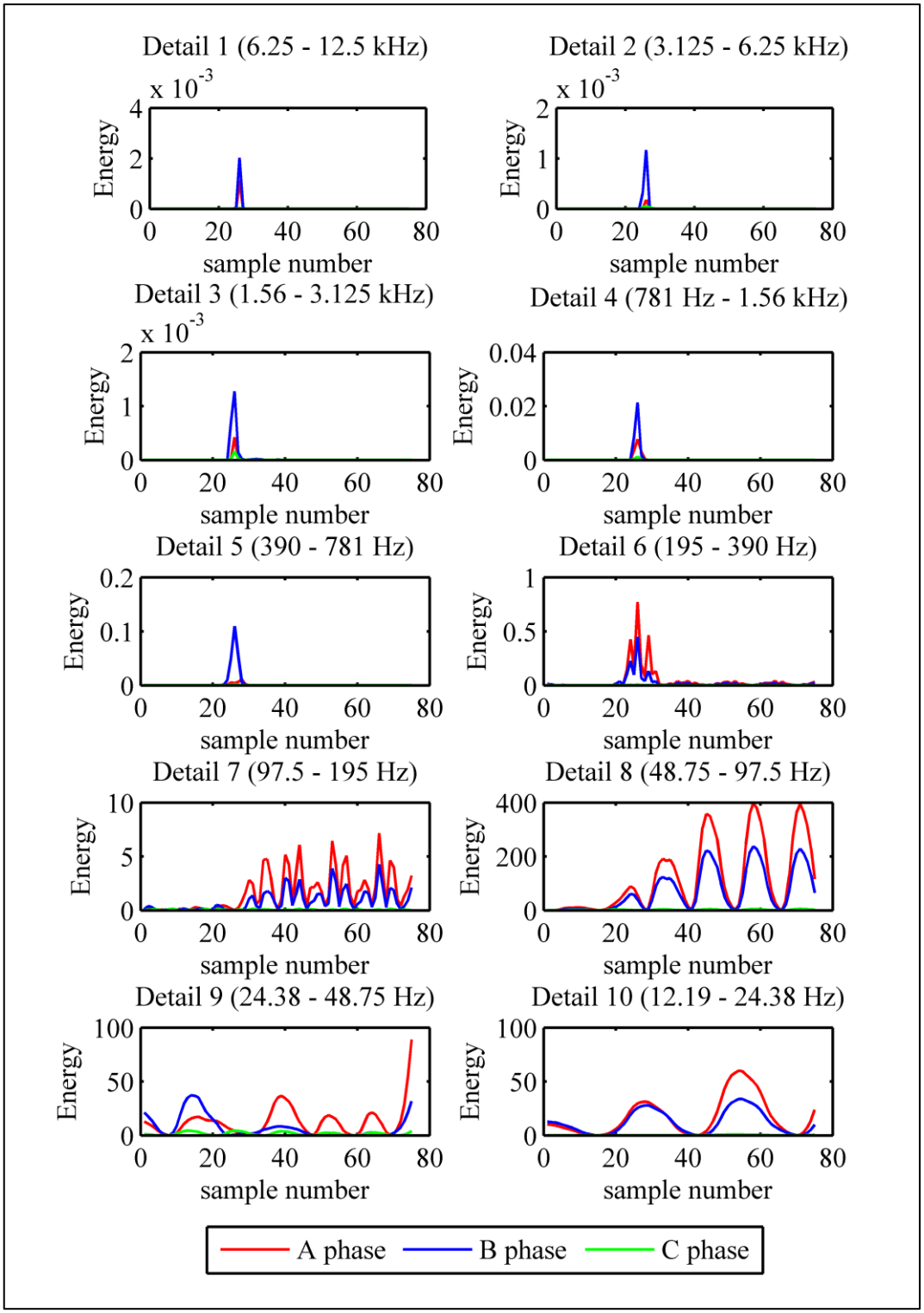

Figure 5.17: DWT of current waveforms for an ABG fault with fault impedance Rf=25Ω at L=1 km on Feeder 1

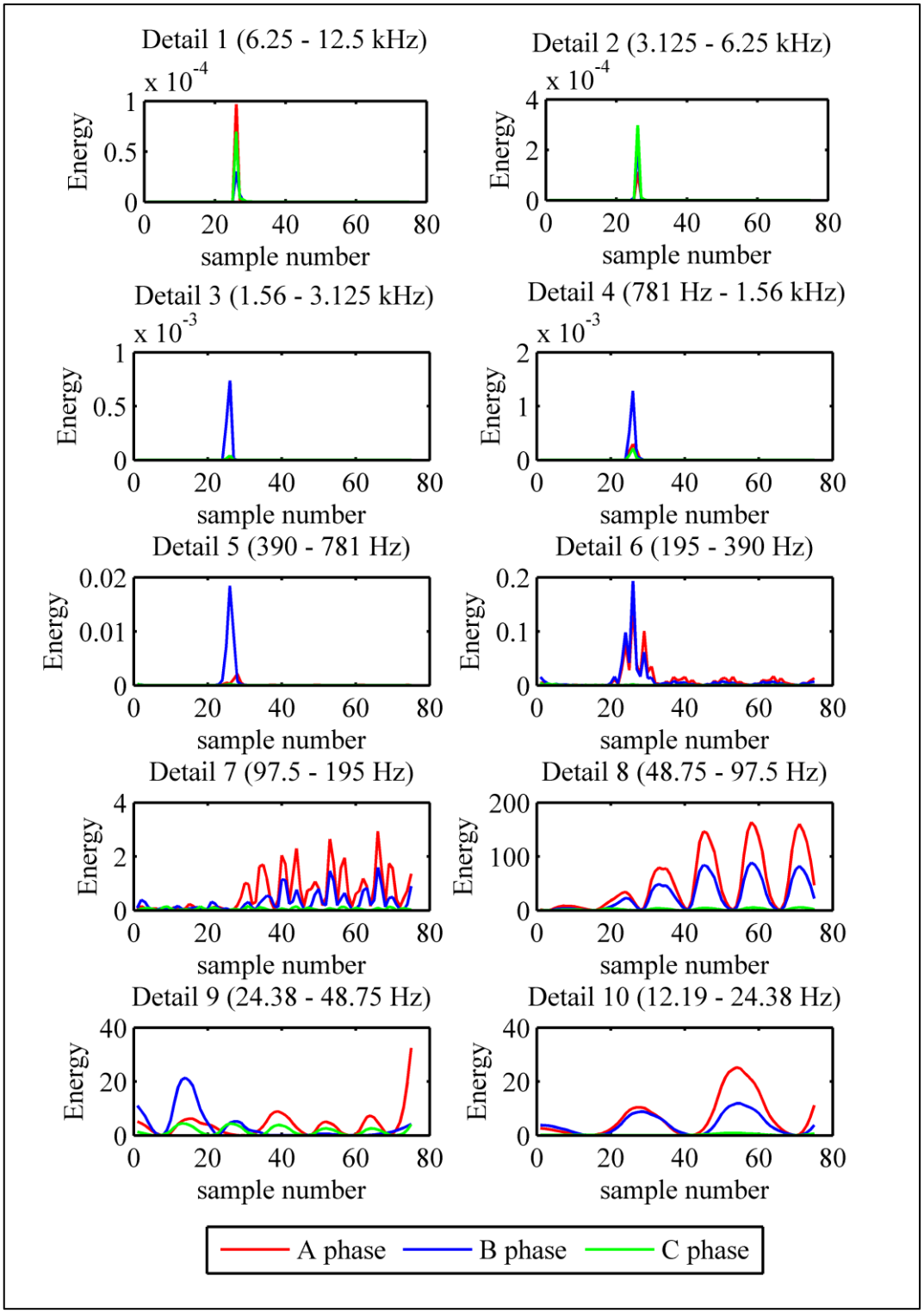

Figure 5.18: DWT of current waveforms for an ABG fault with fault impedance Rf=25Ω at L=15 km on Feeder 1

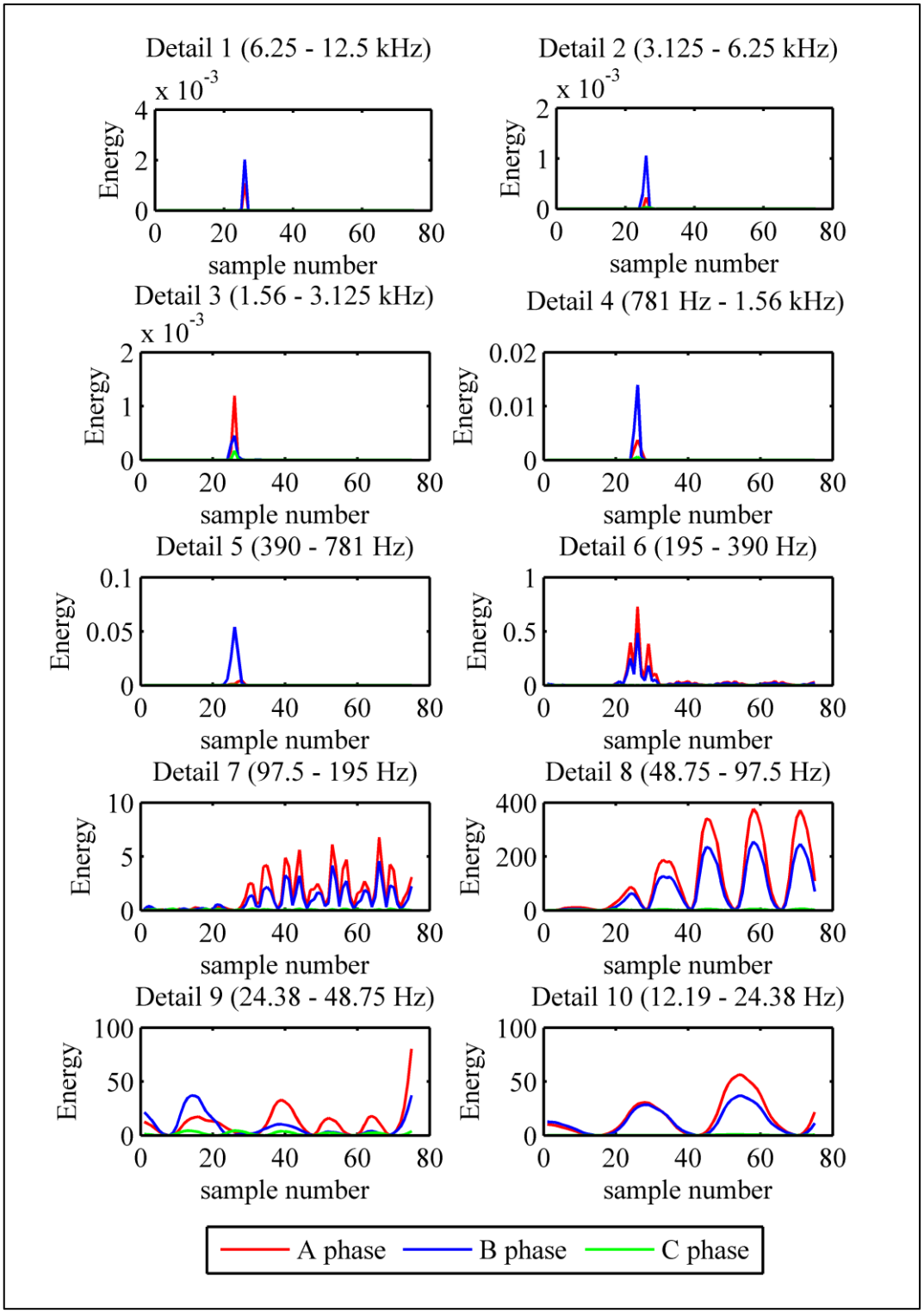

Figure 5.19: DWT of current waveforms for an ABG fault with fault impedance Rf=50Ω at L=1 km on Feeder 1

5.5.4 Three phase faults

For three phase faults, it can be observed that some energy is present in the waveforms of all three phases after the occurrence of the fault. A spike is obtained for the high frequency components and an oscillatory behaviour is observed for the low frequency components.

The energy waveforms of the A phase, B phase and C phase for the high frequency components, tend to have the same amplitude and phase angle (Figure 5.20). However, the waveforms have different amplitudes for the low frequency components. The same observation can be made for a three phase fault at a different location on Feeder 1 (Figure 5.21).

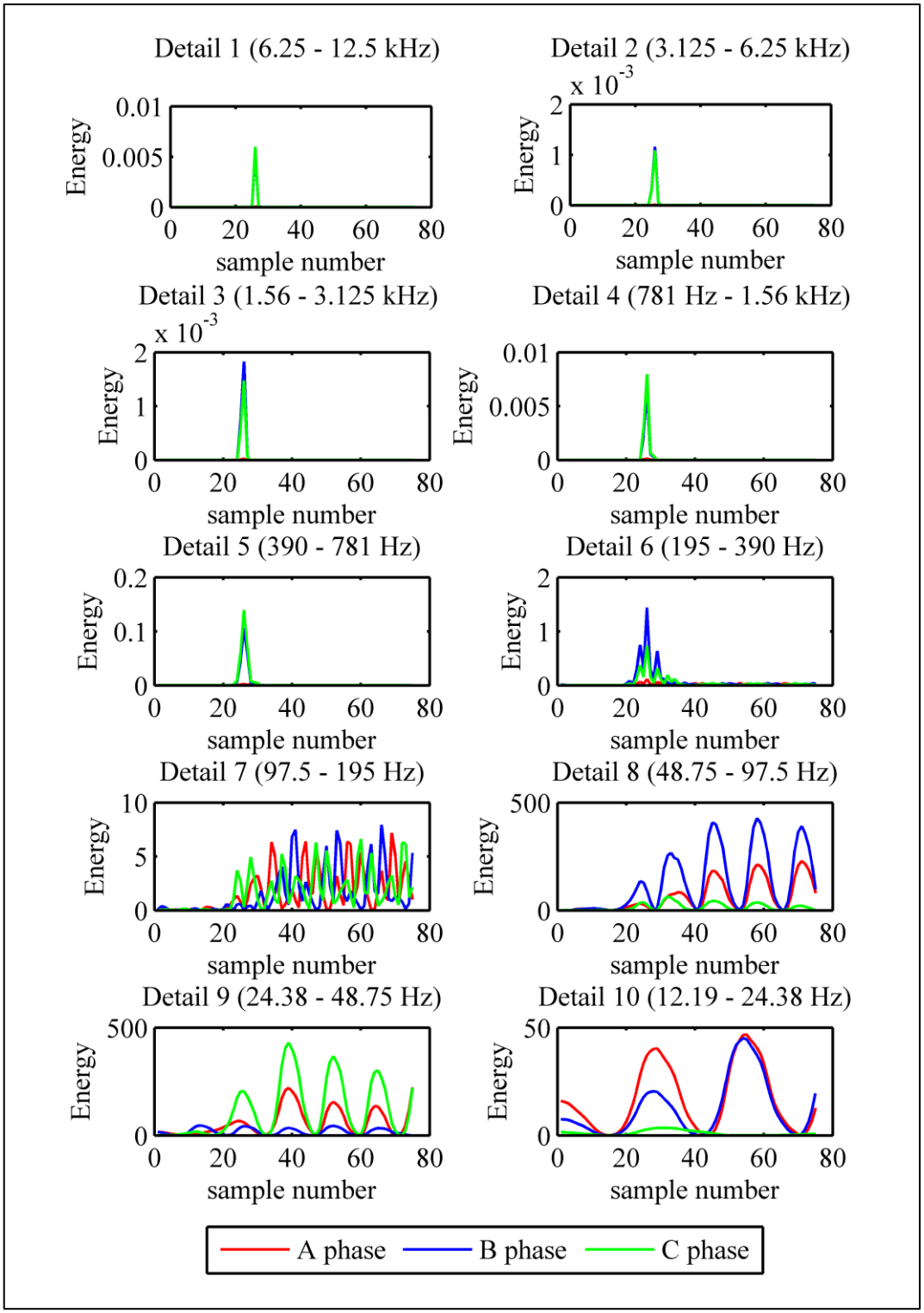

Figure 5.20: DWT of current waveforms for an ABC fault at L=1 km on Feeder 1

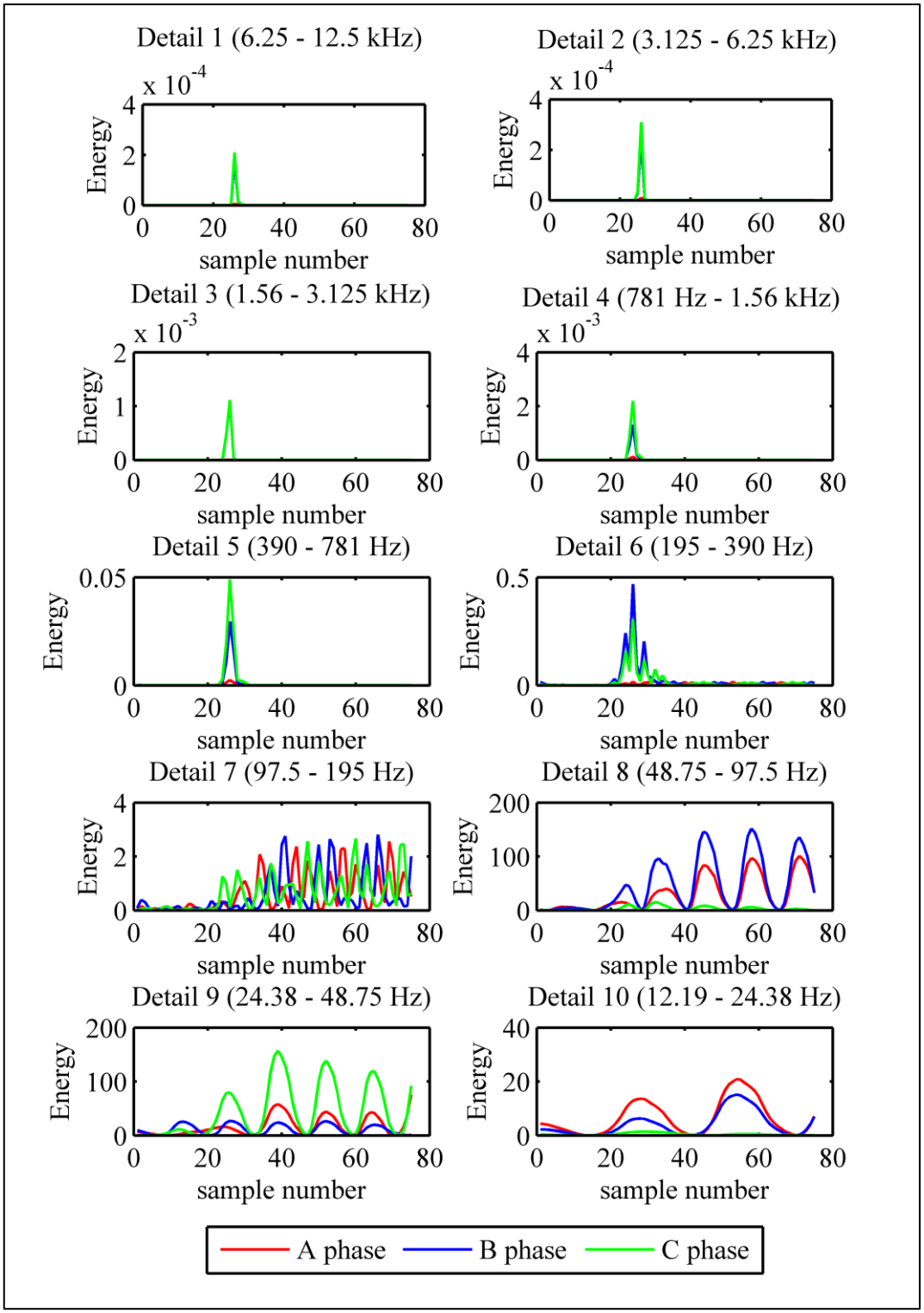

Figure 5.21: DWT of current waveforms for an ABC fault at L=15 km on Feeder 1

5.6 Summary

The Discrete Fourier Transform, the Short-Time Fourier Transform and the Discrete Wavelet Transform are common advanced signal processing tools used to extract distinct features from short-circuit current signals for various types of faults. However, it has been seen that the Discrete Wavelet Transform is most suited to the non-periodic nature of power system transient signals and it gives better resolution in both the frequency and time domain.

A 10 level decomposition of the short-circuit current signals using the Discrete Wavelet Transform showed that each level contains useful information about the fault. For the faulted phase, a spike is observed for the high frequency detail components present in the fault current waveform whereas an oscillatory behaviour is observed in the low frequency components just after the inception of the fault. For the healthy phases, the energies of both the high and low frequency components remain close to zero thus making it easy to identify the faulted phase from the healthy phase/s.

The same observations have been made for various types of short-circuit faults and changes in fault location, fault inception angle and fault impedance only affect the amplitudes of the detail components. It has also been observed that there is some coupling between phases for ground faults due to the return path of the ground connection.

Chapter 6: Development and performance analysis of ANN based fault classification and location algorithms

6.1 Introduction

Accurate fault classification and fault location in a distribution network is a very complicated task due to the nature of electrical distribution networks. As mentioned earlier, the short lengths of the feeders and spurs make the use of the relationship between impedance and distance an unreliable way to accurately locate the fault on the system. The presence of feeders and spurs gives rise to multiple possible fault positions using impedance based methods. The fault inception angle can also produce a dc offset on the fault current waveforms which can induce further errors in the determination of the correct fault location. Moreover, the fault impedance in single phase to ground and double phase to ground faults dampens the amplitude of the fault current. Therefore, a mathematical equation to evaluate the fault location is too complex and may result in unsatisfactory results since some types of faults involve various system parameters that are not readily available to solve the mathematical equation.

In this chapter, an Artificial Neural Network based technique for accurate fault classification and fault location using only current signals measured at the substation end is presented. The Artificial Neural Network has been selected since it is very good at mapping complex problems and producing good generalisation characteristics. The ANN based algorithm is tolerant to changes in system parameters and can perform in a noisy environment. The developed Artificial Neural Network algorithms are also computationally fast to run and can be readily integrated in a microprocessor relay. Mathematical methods use fundamental frequency voltage and current measurements to compute the fault location but in so doing, they discard a lot of important high frequency information associated with fault transients. Artificial Neural Network based methods, on the other hand, allow the use of the high frequency components induced during faults to improve fault location accuracy, particularly when ambitiously using only the fault current signals measured at the substation end.

6.2 Neural Networks

Artificial Neural Networks are part of Artificial Intelligence techniques inspired by nature, developed to solve real world problems. The Artificial Neural Networks attempt to replicate the human thinking process. Nerve cells present in the brain are referred to as biological neurons and each biological neuron is like a processing unit. These biological neurons are interconnected with other neurons to form a biological neural network capable of demonstrating intelligence, thinking and memory functions. The Artificial Neural Networks emulate the biological neural network but have limited functionality since the exact working of the brain is not fully understood [98].

The first developments in Artificial Neural Networks date back to 1943 with the invention of a simple binary threshold logic neural network by McCulloch and Pitts. Analogous to the biological neural network, the Artificial Neural Network also learns by examples. In 1949, Hebb developed a rule for training which was later used to derive most of the modern training rules for Artificial Neural Networks. One major contribution was the invention of the Perceptron by Rosenblatt in 1950 and further works in the 1960's led to the development of various Artificial Neural Networks architectures and training algorithms [99].

The Artificial Neural Networks are suitable for solving problems that have a high complexity and take a long computational time to be solved such as unit commitment and contingency analysis problems often encountered in power systems. Also, Artificial Neural Networks are more suitable for problems that have statistical inputs such as load forecasting and fault location. Once trained properly, Artificial Neural Networks are robust and are not affected by noisy or inconsistent data. They provide fast computing due to their parallel operation and the algorithms are compact, hence commercially attractive [100].

6.2.1 Biological neuron

The structure of a biological neuron is shown in Figure 6.1. The biological neuron can be considered as a processing element. It accepts various input signals from other interconnected neurons through the dendrites.

An output signal is generated through the axon when the inputs signals are strong enough to activate the neuron. Before reaching the nucleus, each input signal goes through a synaptic junction which is filled with a neurotransmitter fluid. The neurotransmitter fluid decides whether to accelerate or slow down the flow of electrical charges to the nucleus.

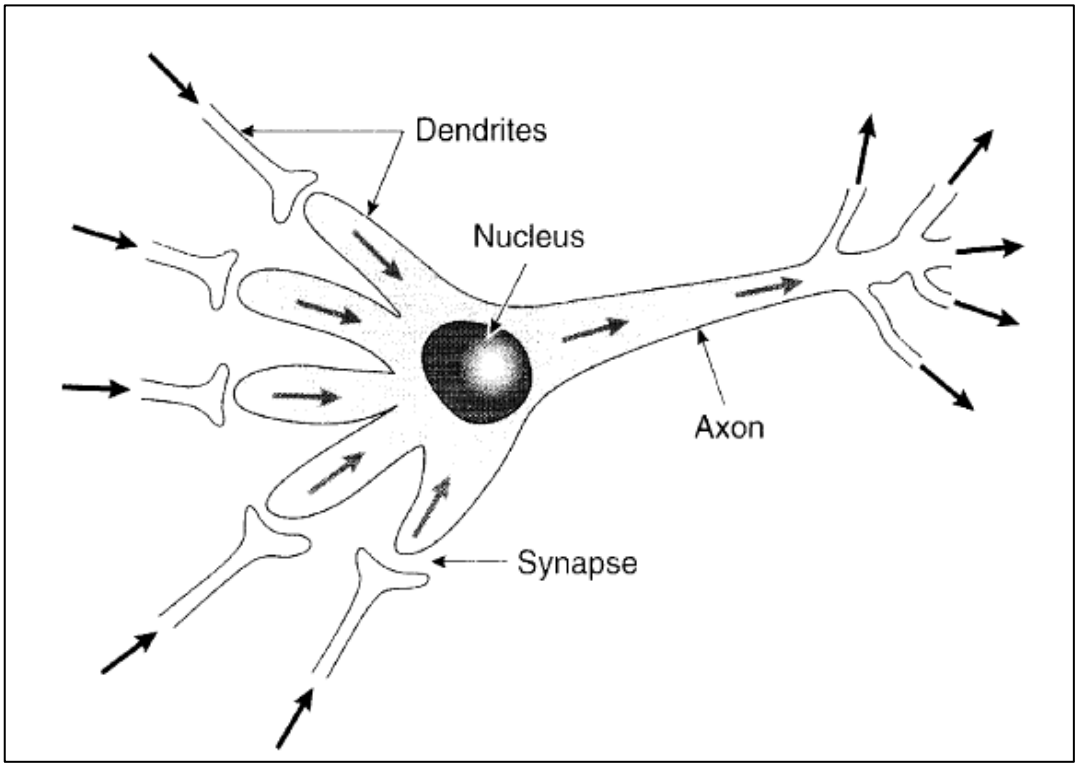

Figure 6.1: Structure of a biological neuron [99]

6.2.2 Artificial neuron

Similarly to the biological neuron, the artificial neuron has a series of input signals X_1, X_2, X_3,…, X_N that can be continuous or discrete variables. As shown in Figure 6.2, each input signal is multiplied by a synaptic weight which can either be a positive or a negative value. A positive value corresponds to an acceleration of the flow of electrical charges in a biological neuron while a negative value slows down

the flow of electrical charges. All of the weighted inputs are then added in a summing junction together with the bias signal b.

The relationship between the inputs and the output is determined by the activation function, also referred to as the transfer function. The output function is as follows [99]:

$$Y = F(S) = F\left[\sum_{K=1}^{N} X_K W_K + b\right] \qquad \text{Equation 6.1}$$

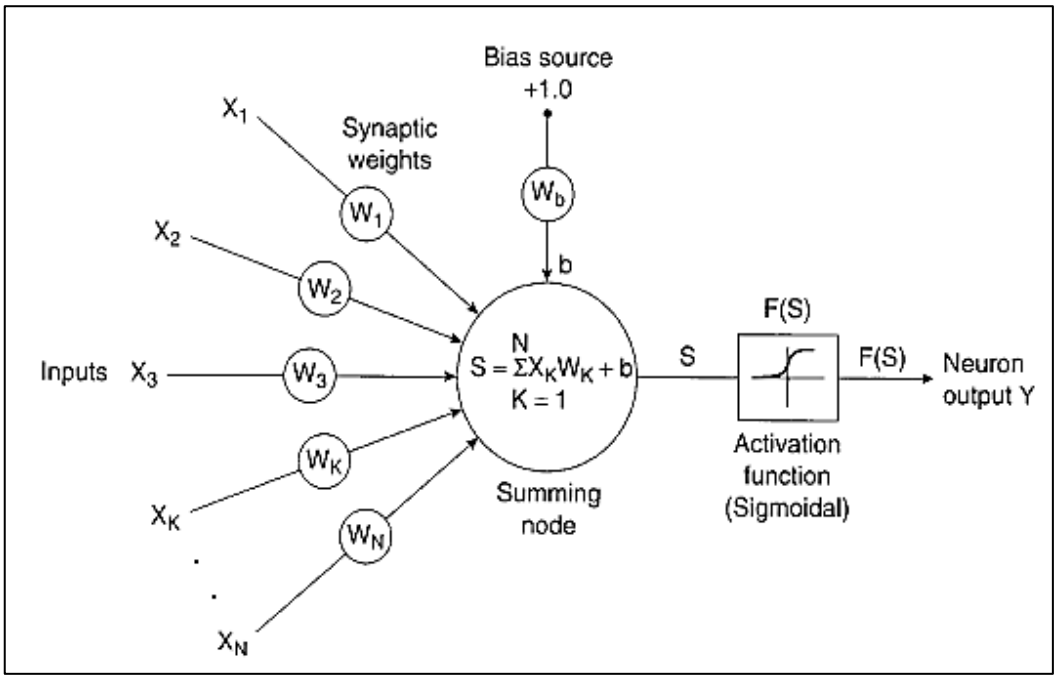

Figure 6.2: Artificial neuron structure [99]

6.2.3 Activation functions

The inputs are mapped onto the output using an activation function, also commonly known as a transfer function. Figure 6.3 illustrate the various transfer functions that can be used to map the inputs to the output.

In Figure 6.3 (a), the output F(S) varies linearly with input S until the magnitude of the input S saturates the output to ± 1. For a step transfer function (Figure 6.3 (b)), the output is at logic 0 if S < 0 or it is at logic 1 if the input S > 0. If there is a bias b, then the output is 1 for S > b, otherwise the output is 0 for S < b.

Figure 6.3 (d) shows the non-linear sigmoidal activation function. It is often referred to as the log-sigmoid and the output varies non-linearly between 0 and +1 with input S. Figure 6.3 (e) shows the non-linear hyperbolic tan transfer function (also referred to as the tan-sigmoid) with the output varying from -1 to +1.

The gain coefficient α adjusts the sensitivity of the function. For example, when α=2, the output changes more rapidly with input whereas when α=0.5, the output changes less rapidly with input S.

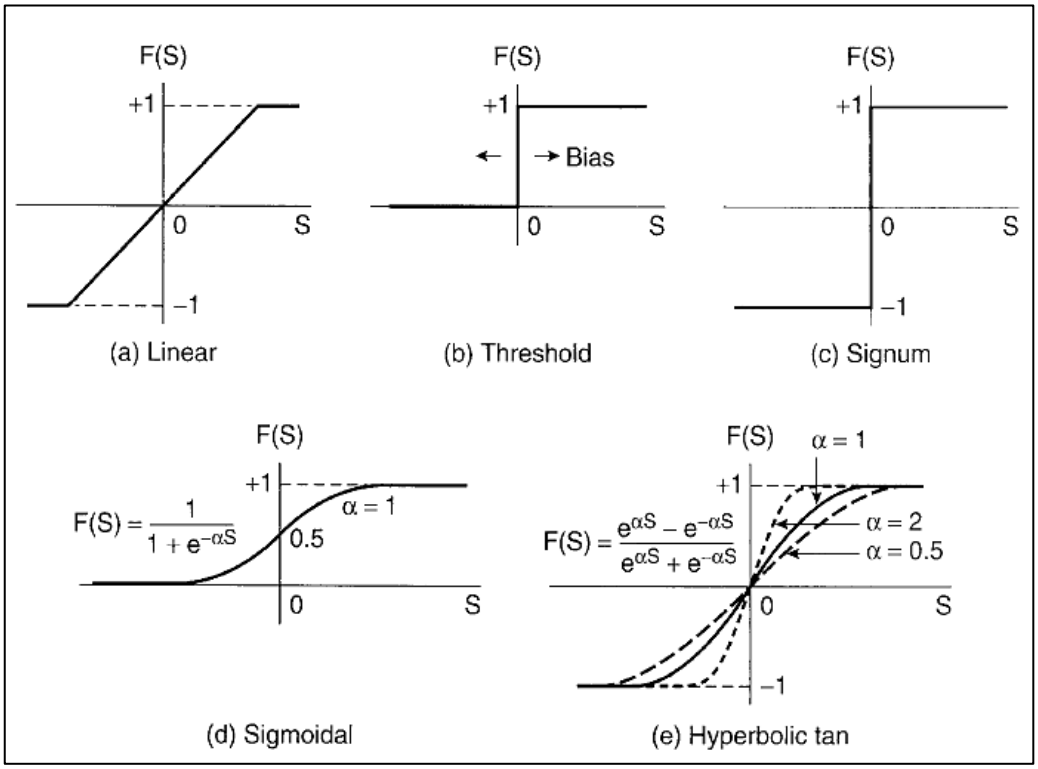

Figure 6.3: Types of activation functions [99]

6.2.4 The Perceptron

The Perceptron (Figure 6.4) is a single neuron with a threshold activation function that functions as a linear classifier. The output is restricted between 0 and 1 and takes a value of 1 only when the sum of all inputs is greater than the threshold value b.

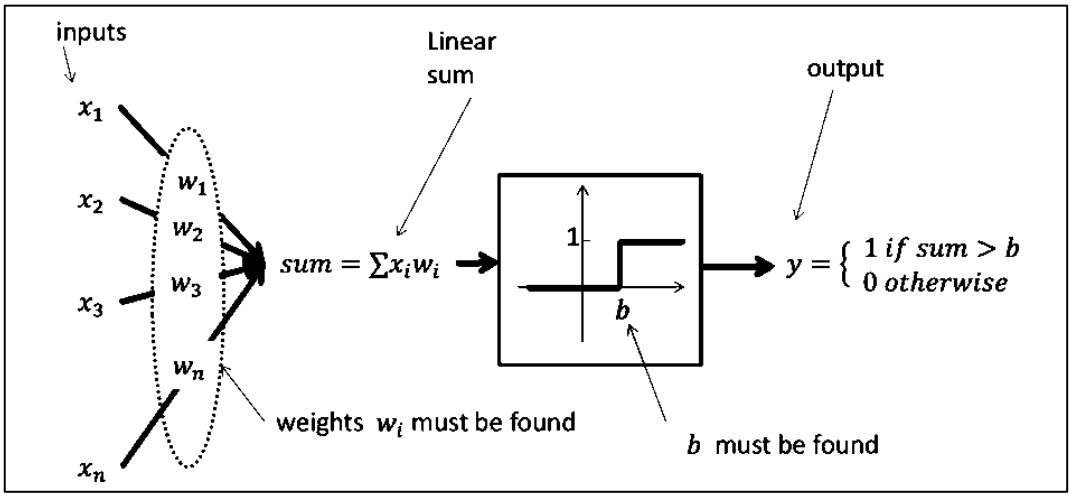

Figure 6.4: The Perceptron [101]

6.3 Multi-layer Perceptron network

An Artificial Neural Network can be formed by arranging neurons in layers and connecting several layers together to form a network [102]. The number of neurons and layers in a network depends on the complexity of the problem to be solved. The simplest multi-layer Perceptron network architecture is the Feedforward Neural Network as shown in Figure 6.5. Feedforward indicates that the signal flow between neurons is in the forward direction only. The Feedforward Neural Network is made up of 3 layers namely an input layer, a hidden layer and an output layer.

The number of neurons in the input layer depends on the number of input signals for a particular problem. Similarly, the number of neurons in the output layer is pre-determined by the number of desired outputs from the Artificial Neural Network. However, the number of neurons in the hidden layer has to be chosen arbitrarily and sometimes re-adjusted to provide better performance.

In Figure 6.5, the parallel input and parallel output configuration of the Feedforward Neural Network, which provides fast computing, can be easily observed. The

training process of the Feedforward Neural Network using backpropagation is also illustrated. The training process adjusts the synaptic weights in the network to minimise the error between the actual output signal and the desired output signal.

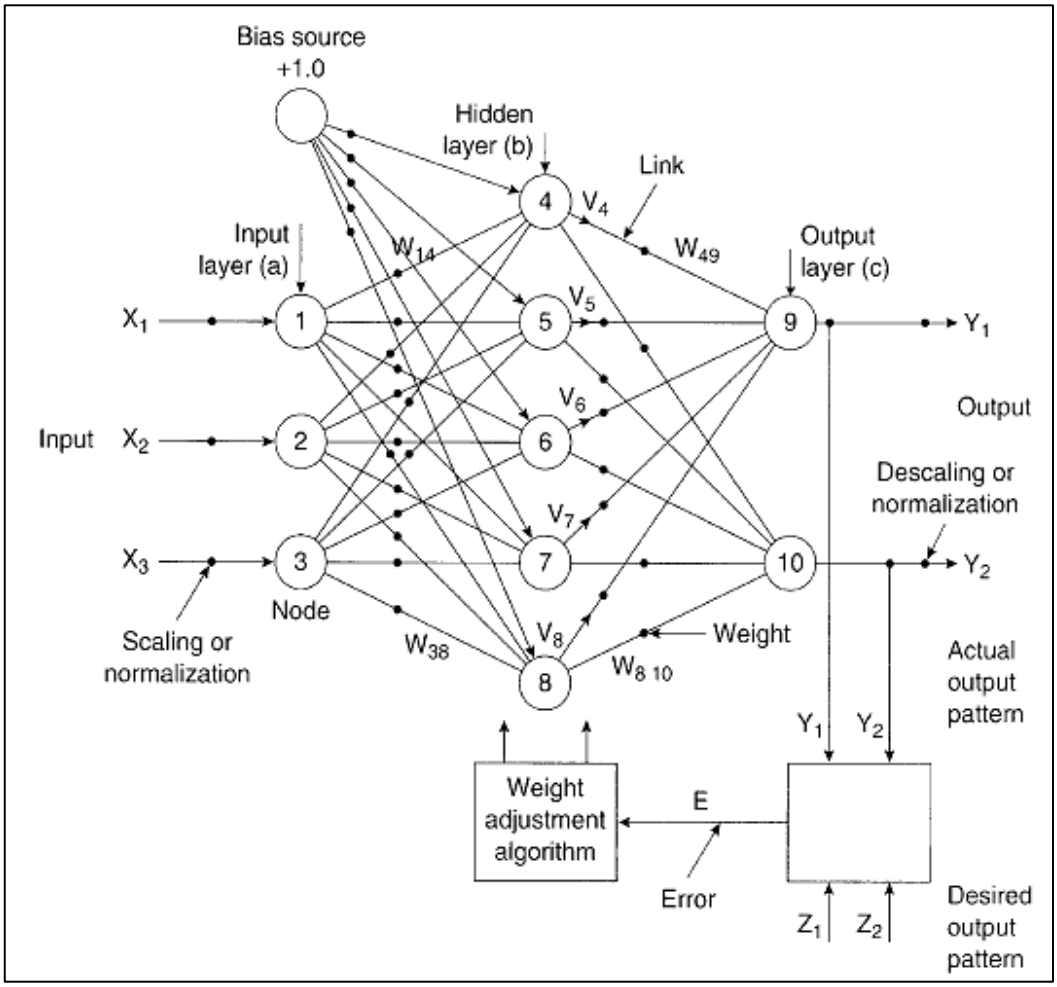

Figure 6.5: Feedforward Neural Network [99]

6.4 Training

Training is the process of adjusting the weights of the Artificial Neural Network such that the desired output can be obtained from the set of inputs. The three main types of training are [103]:

- **Supervised learning**: The input data and the target output are presented to the Artificial Neural Network. The error between the actual output and the target output is then minimised by adjusting the weights in the network.
- **Unsupervised learning**: Patterns are discovered in the input data by the Artificial Neural Network and sometimes input data sharing the same properties are clustered.
- **Reinforcement learning**: Neurons in the network are rewarded for a good performance and penalised for a poor performance.

The Feedforward Neural Network is trained using supervised learning. The gradient descent (GD) learning rule is generally used to minimise the error between the actual output and the target outputs. The error, ε, is the sum of the squared of the difference between the target output and the actual output i.e.

$$\varepsilon = \sum_{p=1}^{P_T} (t_p - o_p)^2 \qquad \text{Equation 6.2}$$

where P_T is the total number of input-target vector pair.

The weights are adjusted such that the error, ε, is minimised. As seen in Figure 6.6, the gradient of ε is calculated and the weight is adjusted by moving down the slope until the minimum value of ε is reached.

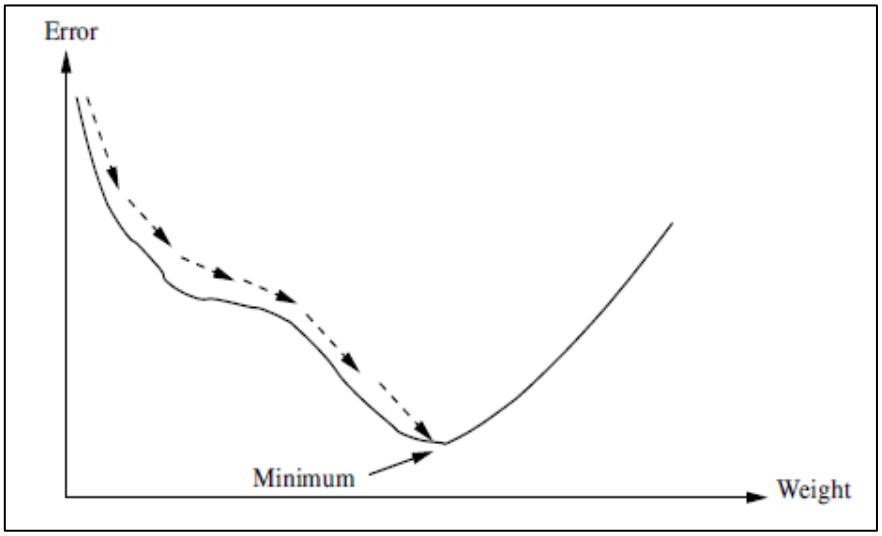

Figure 6.6: Gradient descent training rule [103]

Backpropagation training uses the gradient descent rule to minimise the error between the target output and the actual output but the weights are adjusted starting from the output layer and working towards the input layer.

The following factors can affect good training of the Artificial Neural Network:

- **Network size**: The number of layers and the number of neurons in each layer can affect the performance of a network. A large number of neurons can increase the time for training an Artificial Neural Network. On the other hand, an insufficient number of neurons may lead to poor network performance for a problem of high complexity.

- **Input/output data**: A good training performance can only be achieved if the network is presented with enough information for it to learn and map a problem. The input data is also usually normalised between -1 and 1 to achieve better training performance. This can be done in MATLAB using the *mapminmax* function. The output data or target output has to be carefully chosen and usually binary outputs work best.

- **Stopping condition**: The Artificial Neural Network is trained to enable good generalisation and not memorisation. Generalisation refers to the ability of the Artificial Neural Network to correctly classify data not found in the training set. This can be achieved when the training is stopped at the right moment to prevent overfitting as shown in Figure 6.7.

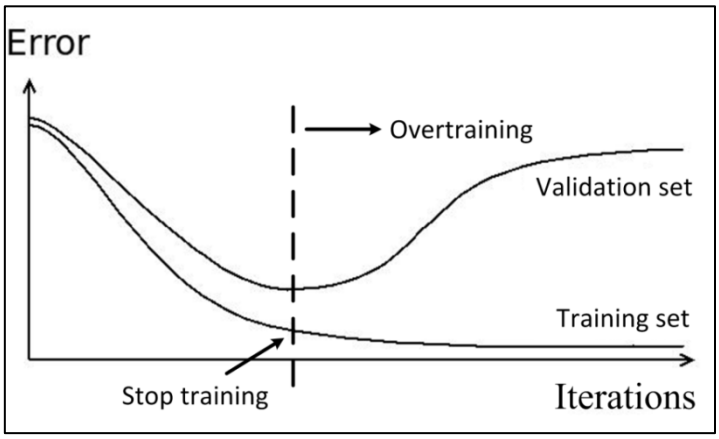

Figure 6.7: Stopping condition for good generalisation [104]

6.5 ANN fault classification architecture

Fault location in a distribution network with feeders and spurs using only current measurements at the substation end is a complicated task. The problem has to be divided into various stages in order to find a feasible and practical solution. The first stage is therefore to identify the type of short-circuit fault occurring on the network irrespective of its position in the distribution network.

From the developed typical 33 kV UK distribution network, different types of short-circuit faults have been simulated at various locations on Feeder 1, Spur 1 and Spur 2. The faults have been simulated at every 3 km on Feeder 1 (starting with 1 km, 3 km, 6 km,..., 30 km) and at every 1 km on the spurs due to their short lengths. The fault inception angle has been taken as 0˚ and 90˚ and the fault impedances taken as 0Ω, 25Ω and 50Ω. Distinct features have then been extracted using the Discrete Wavelet Transform.

Detail 1 to Detail 5 (390 Hz to 12.5 kHz) components of the A phase, B phase and C phase currents have been used as inputs to the Artificial Neural Network mainly because a spike is obtained on the faulted phase whenever a fault occurs on the network and the energy of the healthy phases remain close to zero. This implies that 15 neurons are present in the input layer of the Artificial Neural Network due to the 15 input signals. Four outputs have been chosen for the fault classifier with each of the outputs representing the status of the A phase, B phase, C phase and ground G respectively. Table 6.1 gives the target outputs of the fault classifier for single phase to ground faults (AG, BG, CG), phase to phase faults (AB, BC, AC), double phase to ground faults (ABG, BCG, ACG) and three phase faults (ABC) on the 33 kV distribution network. For a no fault condition, the outputs of the fault classifier are all at logic 0.

A Feedforward Artificial Neural Network has been chosen for the fault classifier and 22 neurons in the hidden layer have showed good training performance. The simplest way to configure and train the Feedforward Artificial Neural Network in MATLAB is by using the *nntool* function but codes can also be written in a MATLAB script *M-file* to allow more control over the training parameters. The magnitudes of the inputs are small numbers and a logarithmic scale has been used to normalize them. The

tansig activation function has been used in both the hidden layer and the output layer and the Levenberg-Marquardt backpropagation function has been employed for training. The error function is the *mse* MATLAB function which calculates the mean squared error between the target and actual output during training.

Fault type	**Fault classifier target outputs**			
	A	**B**	**C**	**G**
No fault	0	0	0	0
AG	1	0	0	1
BG	0	1	0	1
CG	0	0	1	1
AB	1	1	0	0
BC	0	1	1	0
AC	1	0	1	0
ABG	1	1	0	1
BCG	0	1	1	1
ACG	1	0	1	1
ABC	1	1	1	0

Table 6.1: Fault classifier target outputs

Figure 6.8 shows the architecture of the trained Feedforward Artificial Neural Network for fault classification implemented in MATLAB.

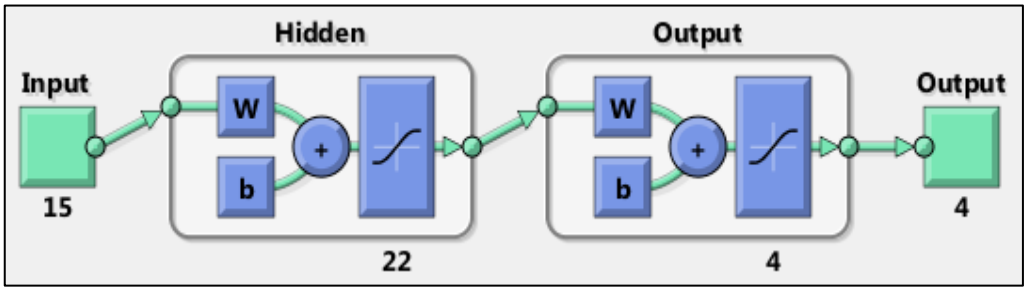

Figure 6.8: ANN based fault classifier architecture

The training performance of the fault classification algorithm is shown in Figure 6.9. As it can be seen, the training performance converges to a minimum closely followed by the test curve which is here used to validate the training performance of the Artificial Neural Network.

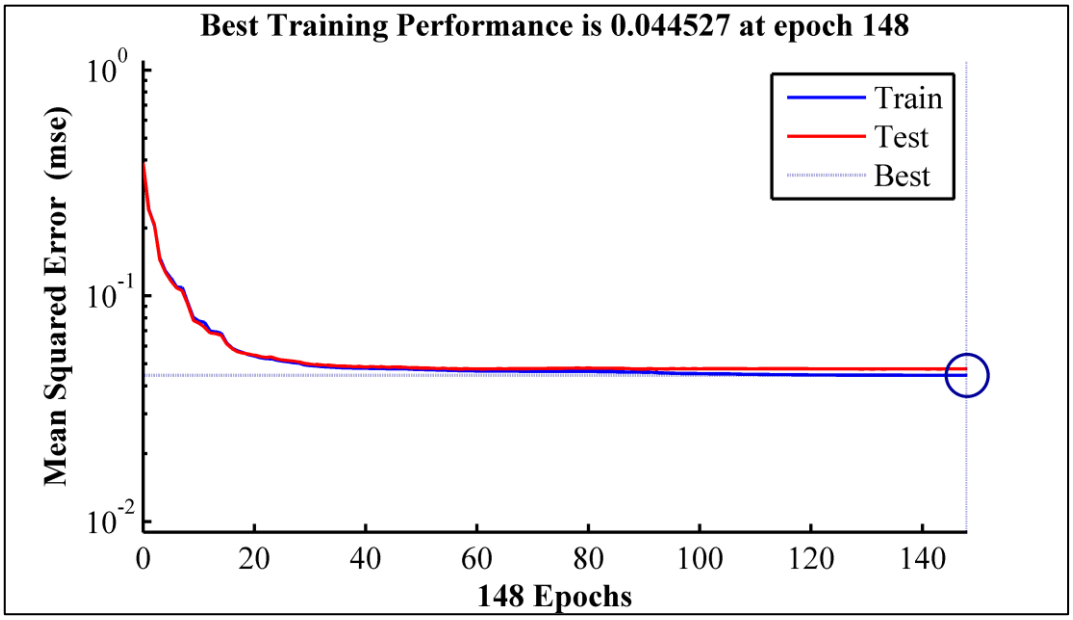

Figure 6.9: Training performance of fault classifier

6.6 ANN feeder/spur classification architecture

The next stage after determining the type of fault on the network is to identify whether the fault occurred on Feeder 1, Spur 1 or Spur 2. Therefore, an ANN based feeder/spur classification algorithm has to be developed for each type of fault, thus yielding 10 different ANN based algorithms as shown in Figure 6.10. Each ANN based algorithm has three outputs (i.e. 3 neurons in the output layer) each representing the status of Feeder 1, Spur 1 and Spur 2. The inputs to each ANN based algorithm are the detail 1 to detail 10 components of each phase current so as sufficient information is available to correctly identify the faulted section even for varying distribution network parameters and configuration such as the connection of wind farms to the end of Feeder 1.

By training one ANN algorithm for each type of fault firstly ensures that the ANN network size is minimised, hence improving the training time. Secondly, by pre-

identifying the faulted section of the distribution network i.e. Feeder 1, Spur 1 or Spur 2, it is then possible to eliminate the risk of obtaining multiple fault positions on the distribution network and to ensure that an accurate estimation of the distance to the point of fault can be evaluated.

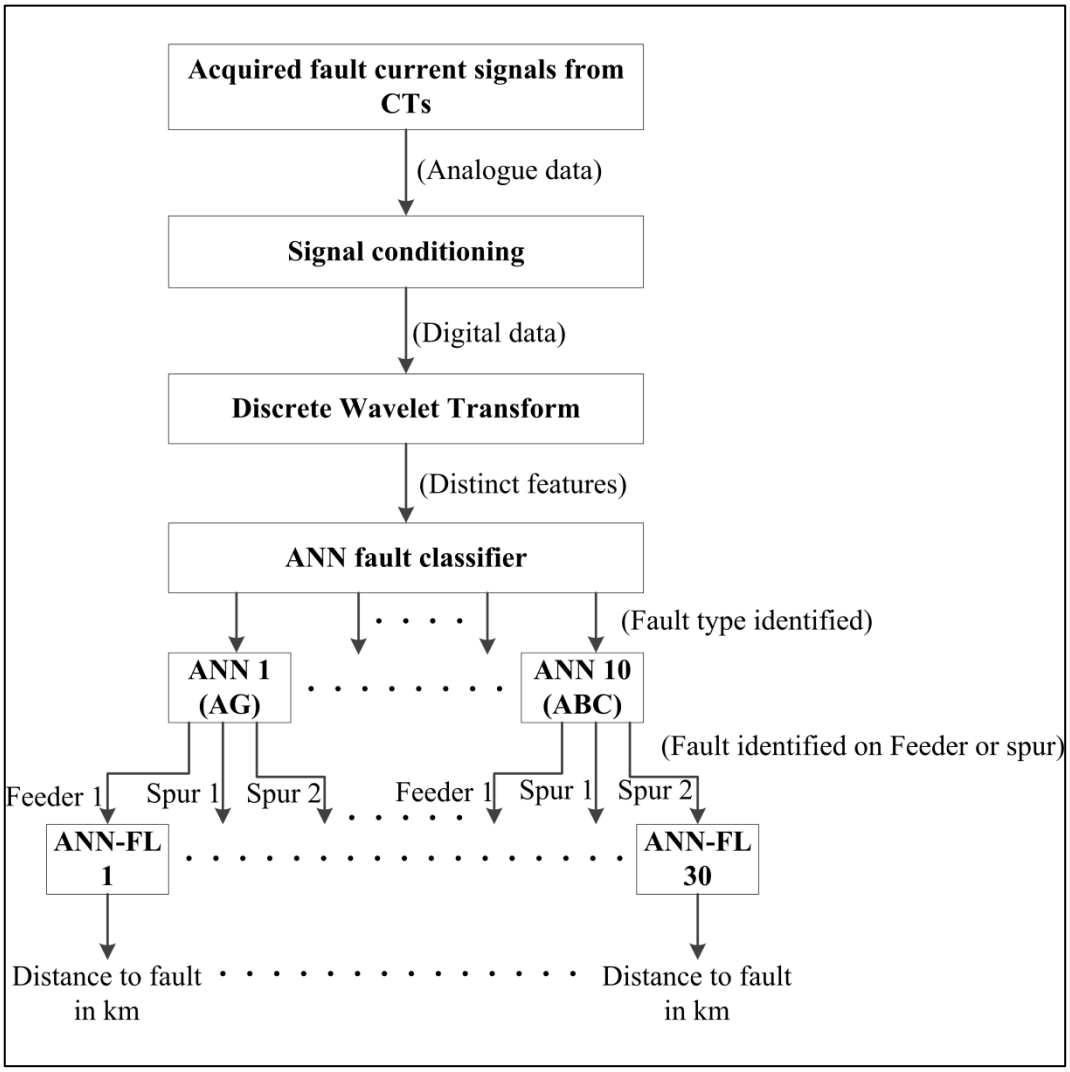

Figure 6.10: Stages to ANN based fault location

Table 6.2 shows the target outputs of each ANN based feeder/spur classification algorithm. For a no fault condition, the outputs Feeder 1, Spur 1 and Spur 2 are chosen to be at logic 0, indicating that they are not faulty. For a fault on Feeder 1, the Feeder 1 output goes to logic 1 whilst the other two outputs Spur 1 and Spur 2 stay at logic 0. The same principle applies for a fault on Spur 1 and Spur 2.

Fault condition	Feeder/spur classification algorithms outputs		
	Feeder 1	Spur 1	Spur 2
No fault	0	0	0
Feeder 1 fault	1	0	0
Spur 1 fault	0	1	0
Spur 2 fault	0	0	1

Table 6.2: Target outputs of feeder/spur classification algorithms

The architecture of an ANN based feeder/spur classification algorithm set up in MATLAB for A phase to ground faults is illustrated in Figure 6.11. The Artificial Neural Network consists of 30 neurons in the input layer resulting from selecting detail 1 to detail 10 components for each phase current. The size of the input data has been reduced by further summing the energies in each detail component over a window length of 5 samples and scaled using a logarithmic function. The hidden layer consists of 15 neurons and the *tansig* activation function has been used in both the hidden layer and the output layer. Training is performed using the Levenberg-Marquardt backpropagation function and the weights are adjusted after evaluating the error using the *mse* function.

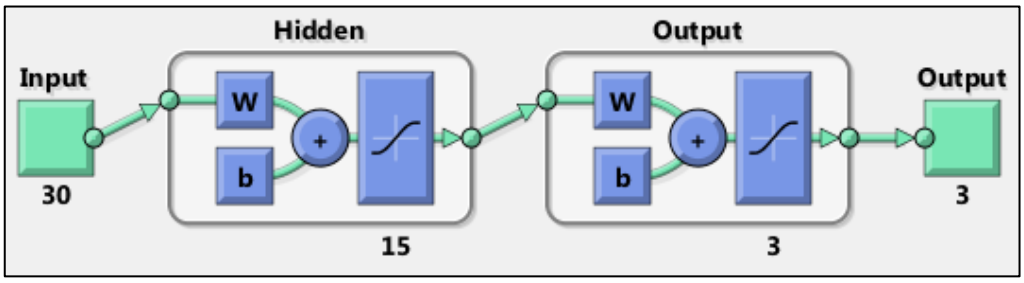

Figure 6.11: ANN based feeder/spur classification algorithm for AG faults

The feeder/spur classification algorithm for AB phase to phase faults is shown in Figure 6.12. The number of neurons in the input and output layer are the same for all the feeder/spur classification algorithms since they all have the same input signals and output signals. However, in this case, the number of neurons in the hidden layer is 10 due to the fact that the size of the input data set for phase to phase faults is much less than that of single phase to ground faults.

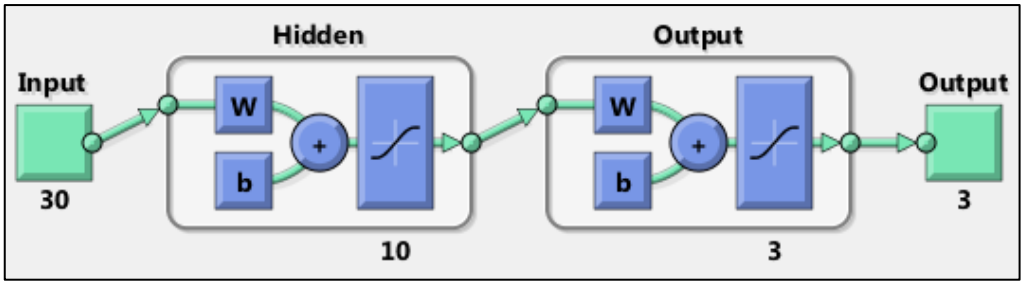

Figure 6.12: ANN based feeder/spur classification algorithm for AB faults

The architecture of ANN based feeder/spur classification algorithms for ABG double phase to ground faults and three phase ABC faults are shown in Figure 6.13 and Figure 6.14 respectively.

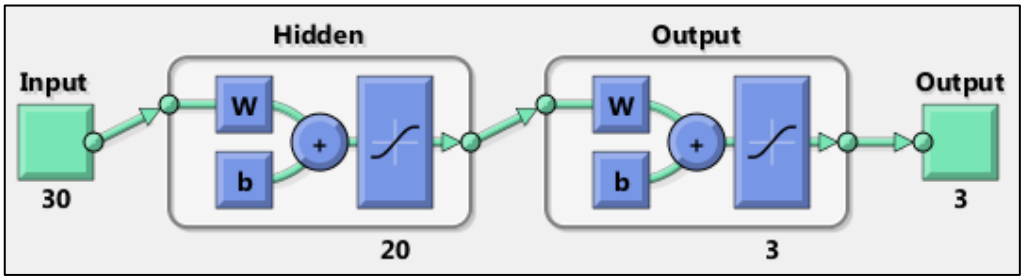

Figure 6.13: ANN based feeder/spur classification algorithm for ABG faults

All the ANN based feeder/spur classification algorithms trained in MATLAB use the *tansig* transfer function in the hidden layer and the output layer. The error between the target output and the actual output has been evaluated using the *mse* function and the *trainlm* function has been used for learning.

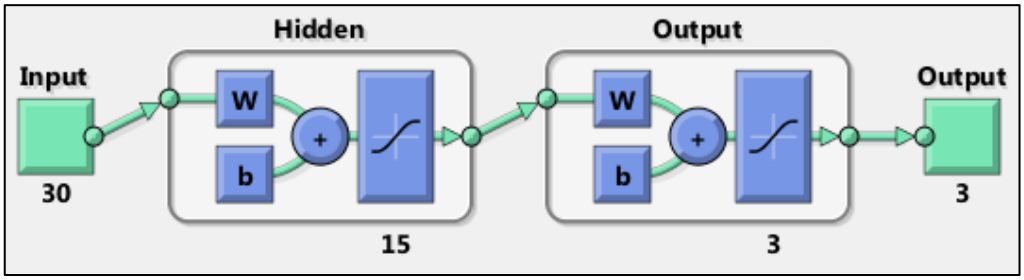

Figure 6.14: ANN based feeder/spur classification algorithm for ABC faults

6.7 ANN fault location architecture

The fault location algorithms estimate the distance to the point of fault along Feeder 1, Spur 1 and Spur 2. Therefore, for each type of fault, 3 ANN based fault location algorithms have to be developed. This implies that a total of 30 ANN based fault location algorithms have to be trained to accurately calculate the distance to the point of fault. The input layer of all the 30 ANN based fault location algorithms have 30 neurons since detail 1 to detail 10 components of the A phase, B phase and C phase currents are used as the input signals. The size of the input data has been reduced by summing the energies over a window length of 5 samples as in the case of feeder/spur classification. The Discrete Wavelet Transform of these signals also revealed that the low frequency detail components have much higher amplitudes than the high frequency components. Therefore, the input signals have been scaled using a logarithmic function to ensure that the training is not biased by the low frequency components.

There is only 1 neuron in the output layer of each ANN based fault location algorithm since the only required output is the distance to the point of fault in kilometres. The target outputs have been scaled in the range of 0 to 1 by dividing the target distance by the length of the line section under consideration i.e. depending whether it is for Feeder 1, Spur 1 or Spur 2.

Feedforward Artificial Neural Networks have been trained in MATLAB to perform fault location on the feeder and the spurs. Figure 6.15 shows the fault location algorithm for AG faults on Feeder 1. The hidden layer consists of 16 neurons and the *tansig* transfer function has been used in both the hidden layer and the output layer.

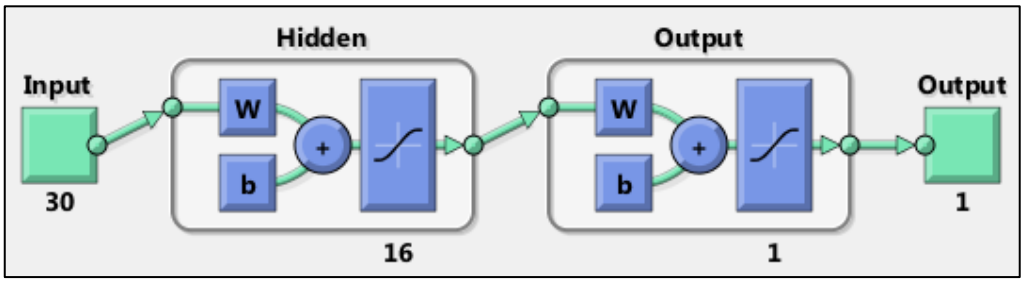

Figure 6.15: ANN based fault location algorithm for AG fault on Feeder 1

The ANN based fault location algorithm for AG faults on Spur 1 has 20 neurons in the hidden layer as shown in Figure 6.16. For all of the 30 ANN based fault location algorithms, the *tansig* transfer function has been employed in the hidden layer and the output layer. The Levenberg-Marquardt backpropagation training method has also been utilised to adjust the weights in the network after the error has been evaluated using the *mse* function.

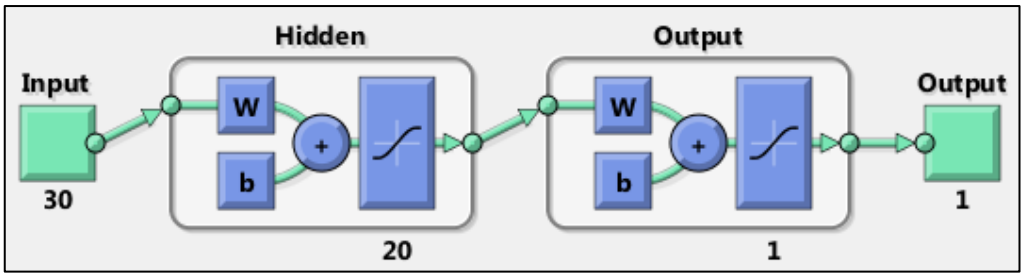

Figure 6.16: ANN based fault location algorithm for AG fault on Spur 1

Since it is lengthy to cover the configuration of all 30 ANN based fault location algorithms, comments henceforth will be restricted to only Feeder 1 and Spur 1 fault location algorithms for AG faults, ABG faults, AB faults and ABC faults.

For ABG faults, the ANN based fault location algorithm has 14 neurons in the hidden layer for Feeder 1 (ABG-Feeder 1 30-14-1) and that of Spur 1 has 20 neurons (ABG-Spur 1 30-20-1).

For AB faults, the fault location algorithm of Feeder 1 has 14 neurons in the hidden layer (AB-Feeder 1 30-14-1) and that of Spur 1 has 15 neurons (AB-Spur 1 30-15-1).

And finally, for ABC faults, good training performance has been achieved for 20 neurons in the hidden layer for Feeder 1 (ABC-Feeder 1 30-20-1) and 15 neurons on the hidden layer of Spur 1 (ABC-Spur 1 30-15-1).

6.8 Performance analysis of developed algorithms

The ANN based fault type classification, feeder/spur classification and fault location algorithms have been developed for a passive (conventional) distribution network with feeders and spurs. A short-circuit fault can occur at any location and at any time on the sinusoidal voltage/current waveform. In Chapter 5, it was observed that the location of the fault, the fault inception angle and the fault impedance affect the peak amplitude of the short-circuit transient and thus directly influence the energies of detail components present in the fault current waveforms. It is therefore important to test the performance of the developed algorithms for such changes in system parameters. Different types of faults were simulated at various locations in the distribution network as shown in Figure 6.17. The fault positions on Feeder 1 were at 0.5 km, 16.5 km and 28.5 km, and the faults on Spur 1 were at 2.5 km

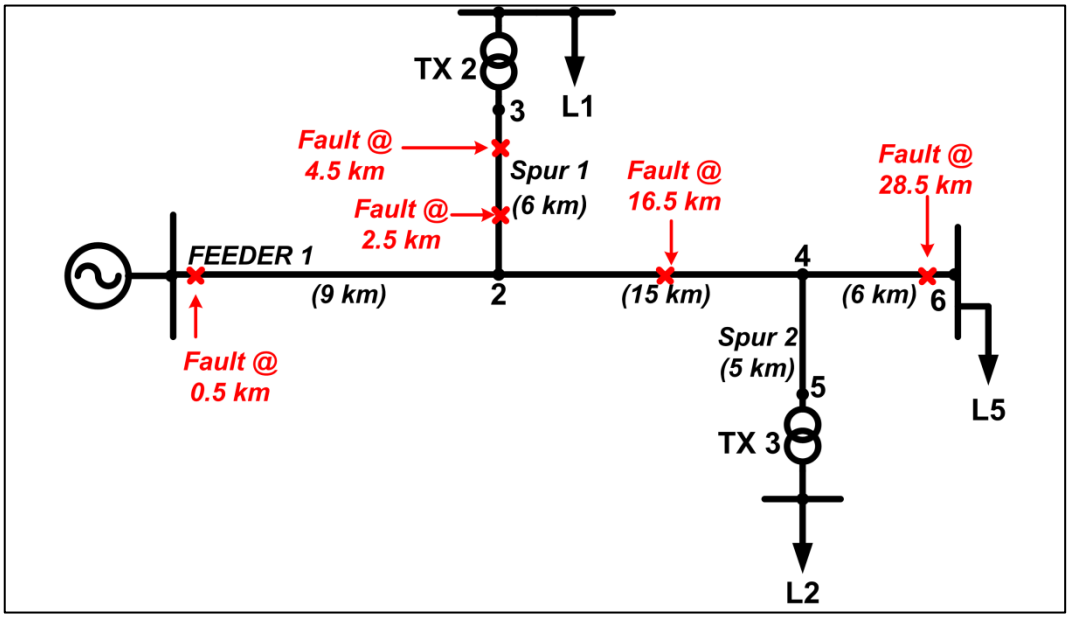

Figure 6.17: Simplified 33 kV distribution network

Figure 6.18 shows the output of the fault classifier for an AG fault at 16.5 km on Feeder 1 with a fault inception angle of 45° and a fault impedance of 10Ω.

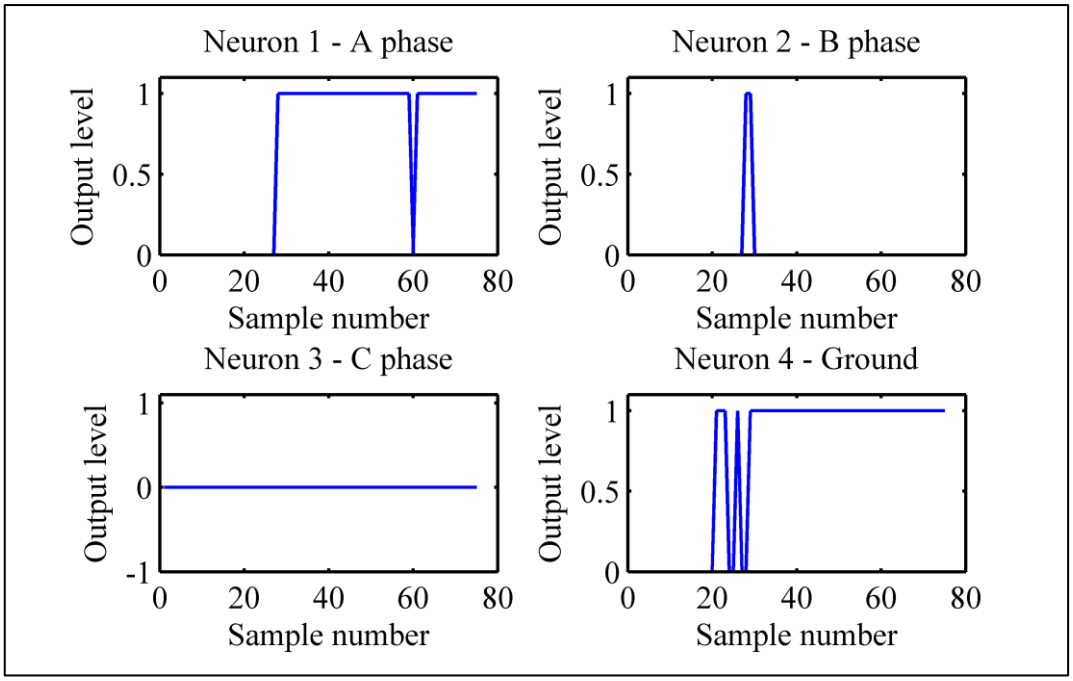

Figure 6.18: Output of the fault classification algorithm for an AG fault at 16.5 km on Feeder 1 with a fault inception angle θ=45° and fault impedance Rf=10Ω

As it can be seen, all the outputs are at level 0 before the inception of the fault i.e. before sample number 26. When the AG fault occurs on the feeder, the output level of the A phase and the ground jump to level 1 and stay at level 1 for 2 cycles post-fault. The actual output of the ANN fault classifier is a real number between 0 and 1. A threshold detector has been implemented to set all output levels greater and equal to 0.7 to level 1 and those below 0.7 have been set to level 0 (see Appendix B).

A decision logic algorithm has also been implemented to interpret the output of the fault classifier by evaluating the area under the graph of each output (see Appendix B). From Figure 6.18, it is clear that the area under the A phase and ground are much higher than that of the B phase and C phase. Therefore, the decision logic algorithm will flag the fault as an AG fault to the power system engineer or operator. The glitches in the outputs are due to noise and training errors but the decision logic algorithm ensures that the correct type of fault is identified.

Figure 6.19 illustrates the output of the fault classifier for a double phase to ground BCG fault at 16.5 km on Feeder 1 with a fault inception angle of 45° (on the B phase) and a fault impedance of 10Ω.

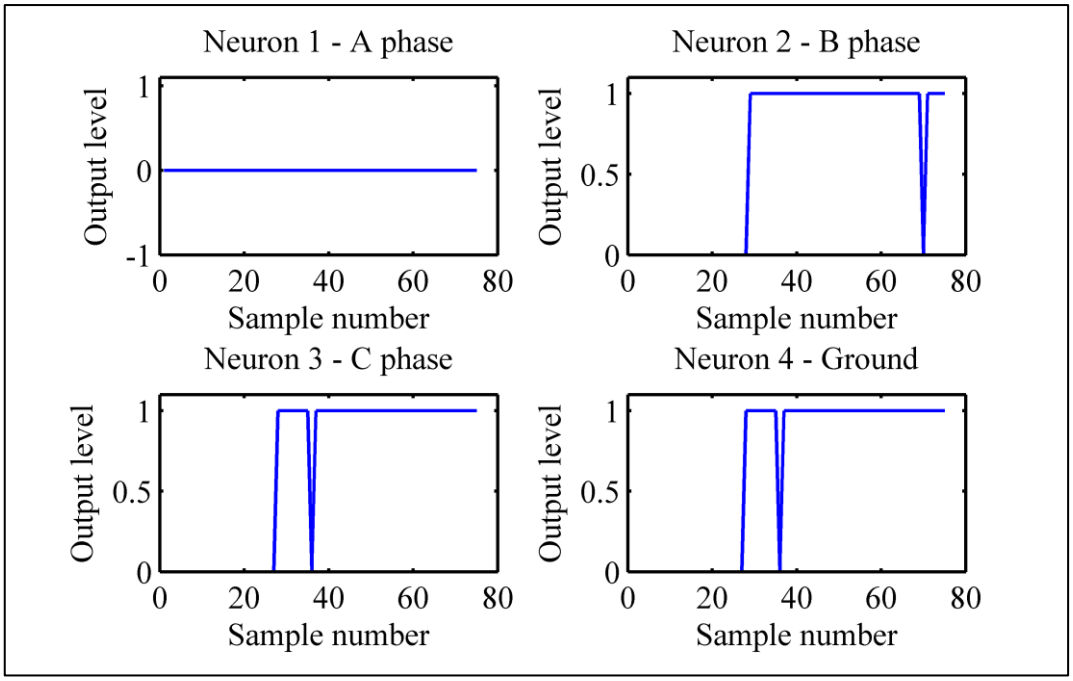

Figure 6.19: Output of the fault classification algorithm for a BCG fault at 16.5 km on Feeder 1 with a fault impedance Rf=10Ω

Similarly, Figure 6.20 shows the output of the fault classifier for a BC, phase to phase fault at 4.5 km on Spur 1. Since the output of the B phase and C phase are at level 1 after the fault inception and the area under these two graphs are much higher than that for the A phase and ground, it implies that the fault classifier has accurately detected the fault type.

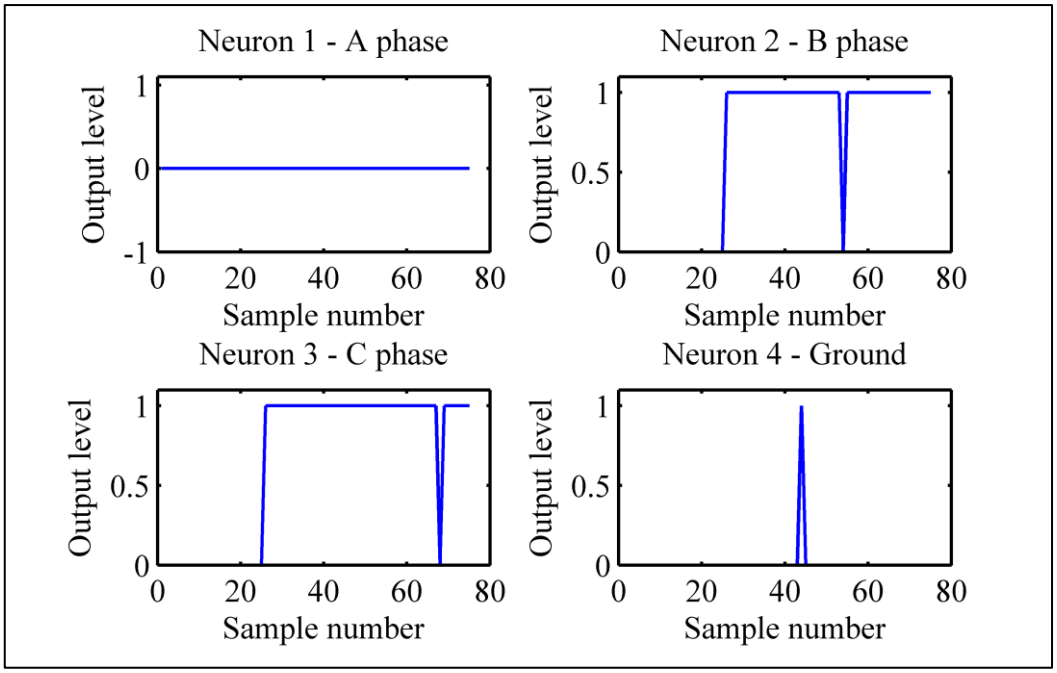

Figure 6.20: Output of the fault classification algorithm for a BC fault at 4.5 km on Spur 1

The fault classification algorithm has been extensively tested for all types of faults at various locations on the feeder and spurs with a fault inception angle of 45° and fault impedances of 10Ω and 35Ω (not part of the training set). The results obtained showed that the outputs of the fault classifier remained accurate for changes in fault inception angles and fault impedances.

The feeder/spur classification algorithms have also been tested for different types of faults for changes in fault inception angle and fault impedances. Figure 6.21 shows the outputs of the feeder/spur classification algorithm for an AG fault at 16.5 km on Feeder1 with a fault inception angle of 45° and a fault impedance of 35Ω. For a no fault condition (i.e. before sample number 6), the Feeder 1, Spur 1 and Spur 2 outputs are all at level 0. When the fault occurs on Feeder 1, the Feeder 1 output level jumps to 1 and remains at level 1, thus indicating that the fault lies on Feeder 1. Spur 1 and Spur 2 outputs remain at level 0.

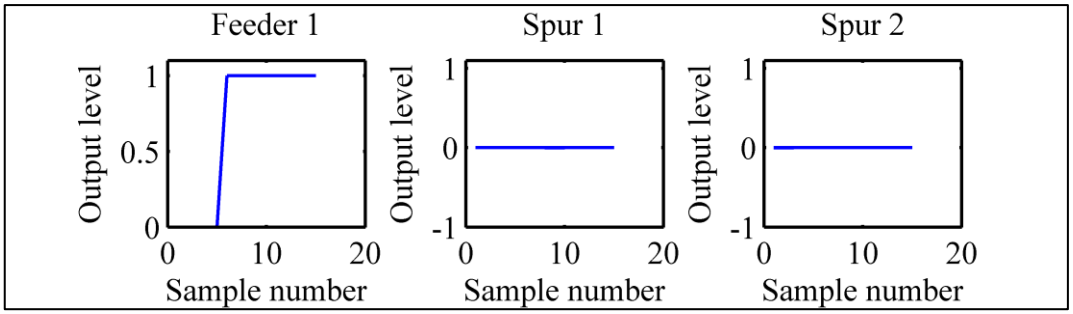

Figure 6.21: Feeder/spur classification algorithm for an AG fault at 16.5 km on Feeder 1 with a fault inception angle θ =45° and a fault impedance Rf=35Ω.

For an AG fault at 2.5 km on Spur 1 (Figure 6.22), the Spur 1 output level jumps to 1 and remains at level 1 after the occurrence of the fault.

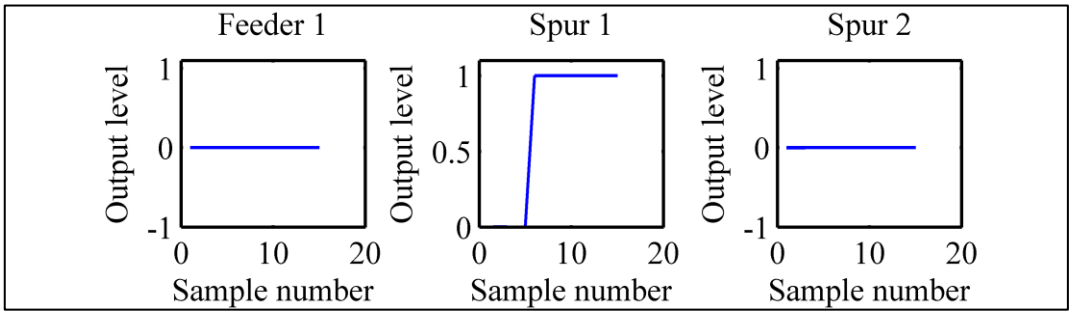

Figure 6.22: Feeder/spur classification algorithm for an AG fault at 2.5 km on Spur 1 with a fault inception angle θ =45° and a fault impedance Rf=35Ω.

Similarly, for an AG fault at 4.5 km on Spur 2 (Figure 6.23), the Spur 2 output level jumps to 1 after the occurrence of the fault.

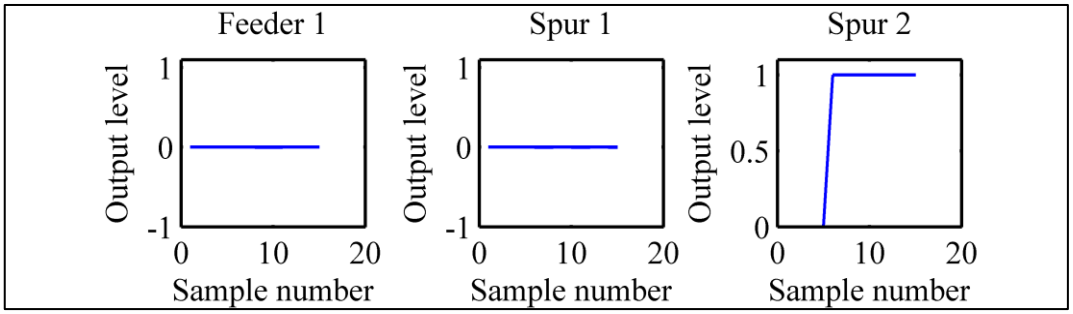

Figure 6.23: Feeder/spur classification algorithm for an AG fault at 4.5 km on Spur 2 with a fault inception angle θ =45° and a fault impedance Rf=35Ω.

The feeder/spur classification algorithms for phase to phase faults, double phase to ground faults and three phase faults have also been thoroughly tested for faults on Feeder 1, Spur 1 and Spur 2. The graphs are not displayed due to space restrictions but from the results obtained, it can be concluded that changes in the fault inception angle and the fault impedance do not affect the accuracy of the feeder/spur classification algorithms.

The ANN based fault location algorithms have only distance as output in the output layer. They have been trained to converge to the target distance. Figure 6.24 shows the output of the fault classification algorithm for an AB fault at 0.5 km on Spur 1. As it can be seen, the fault occurs at sample number 6. Prior to the fault, the estimated output distance in zero. When the fault occurs on Spur 1, the output distance jumps to 0.5 km and is maintained around that value for 2 cycles post-fault. The final value of the estimated output distance can then be calculated by taking the average of the output distances for each sample number after the fault. In this case, the average value is 0.47325 km (i.e. [0.5079 + 0.4999 + 0.4999 + 0.5 + 0.4997 + 0.5004 + 0.2250 + 0.5 + 0.4999 + 0.4998]/10).

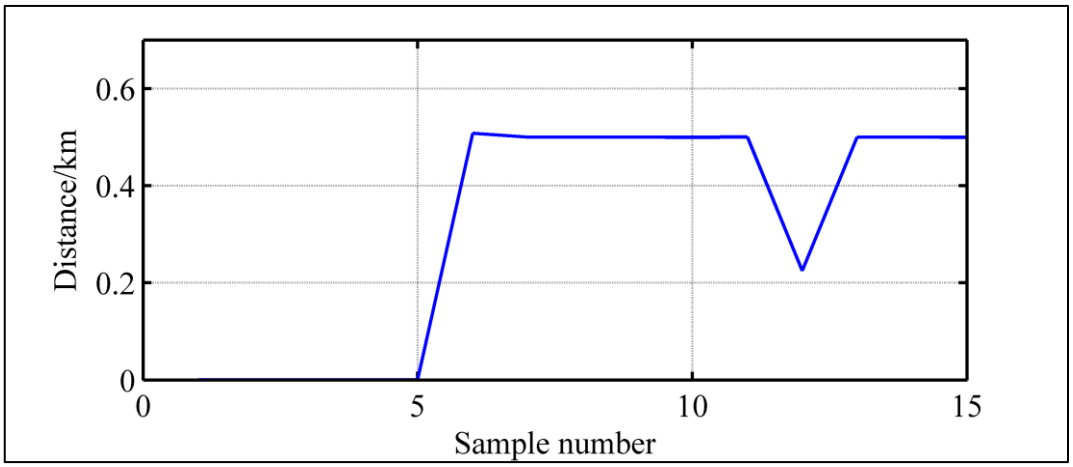

Figure 6.24: Fault location algorithm output for an AB fault at 0.5 km on Spur 1

The fault location algorithms have been tested for changes in fault inception angle and fault impedances. Figure 6.25 illustrates the percentage errors obtained in estimating the distance for an AG fault at 0.5 km (red line), 16.5 km (blue line) and 28.5 km (green line) on Feeder 1 with a fault inception angle of 45°. The X-axis shows the fault impedances and the Y-axis the percentage error. The fault

impedances were taken as 0Ω, 25Ω and 50Ω (i.e. same as for training) but also changed to 10Ω and 35Ω to verify the response of the fault location algorithm to new data. The results show that the percentage error in estimating the distance to the point of fault is less than 5% i.e. less than ± 1.5 km on Feeder 1.

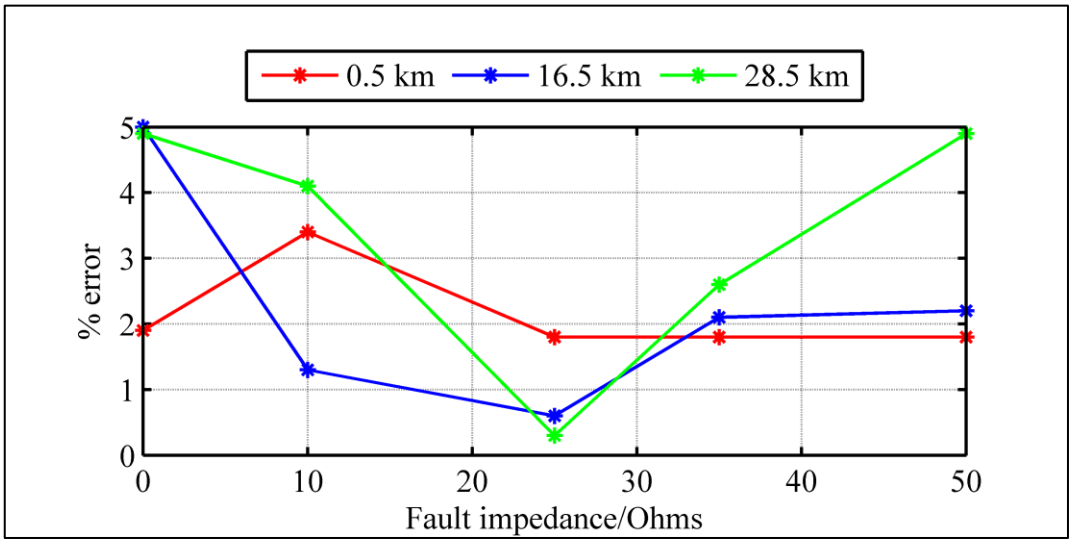

Figure 6.25: Accuracy of fault location algorithm for an AG fault for various fault impedances and at various locations on Feeder 1

Figure 6.26 gives the percentage error of the fault location algorithm for an AG fault at 2.5 km (red line) and 4.5 km (blue line) on Spur 1 for different values of fault impedances (0Ω, 10Ω, 25Ω, 35Ω and 50Ω).

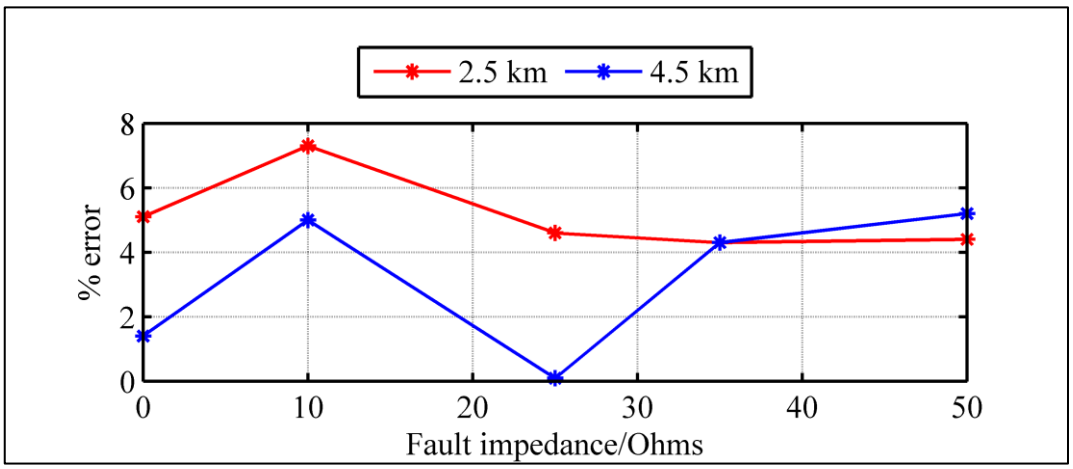

Figure 6.26: Accuracy of fault location algorithm for an AG fault for various fault impedances and at various locations on Spur 1

It can be observed that the percentage error for an AG fault on Spur 1 is less than 8% i.e. ± 480 m on Spur 1.This is an acceptable error given the short line length and thus the small change in line impedances per km.

For an ABG fault occurring at voltage minimum on Feeder 1, the percentage error for different fault impedances at various locations on Feeder 1 are shown in Figure 6.27. The fault location algorithm has a percentage error of less than 5%. The error is less than 7% for an ABG fault on Spur 1 (Figure 6.28).

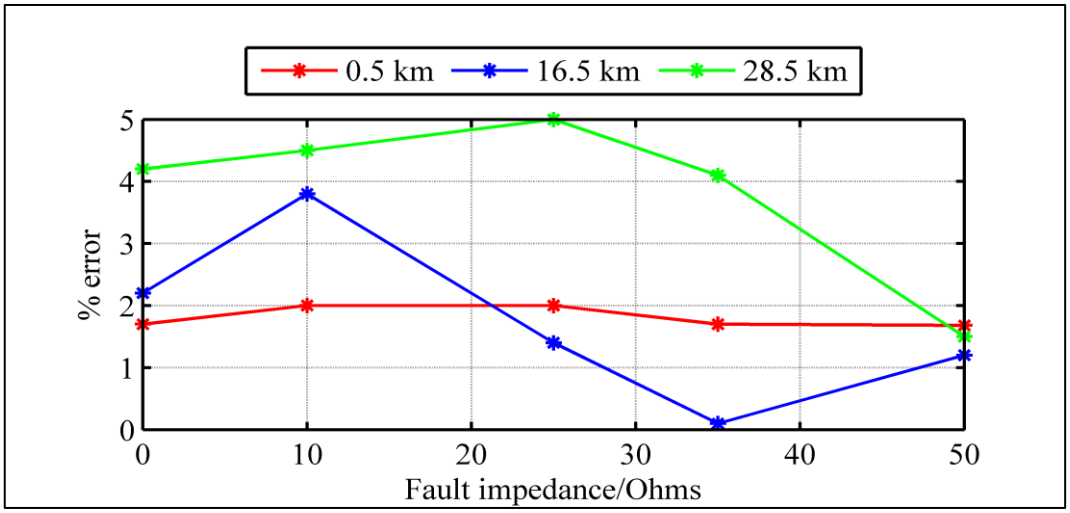

Figure 6.27: Accuracy of fault location algorithm for an ABG fault for various fault impedances and at various locations on Feeder 1

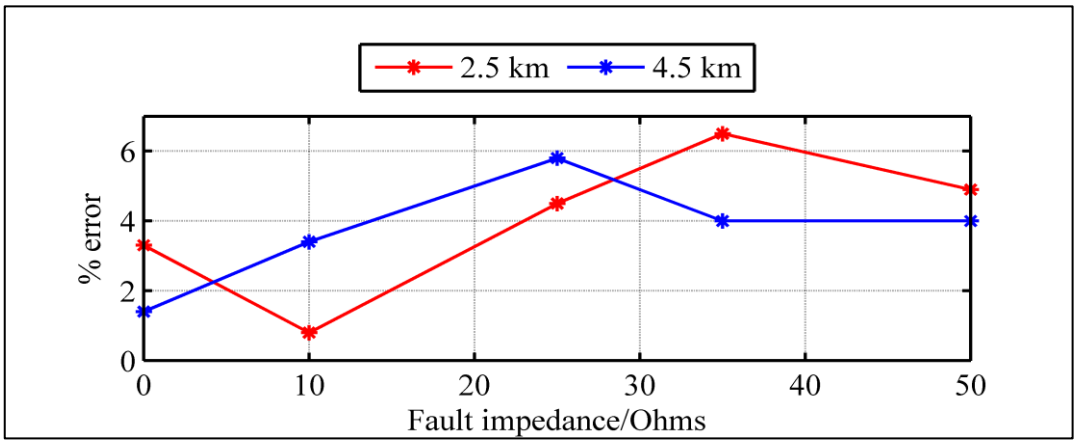

Figure 6.28: Accuracy of fault location algorithm for an ABG fault for various fault impedances and at various locations on Spur 1

Phase to phase faults and three phase faults usually do not have a path to the ground and hence the fault location algorithms have not been tested for different fault impedances. However, since the fault can occur at any point on the voltage/current waveform, some results have been shown (Table 6.3 and Table 6.4) for a fault inception angle of 45° on the A phase.

AB fault on Feeder 1		
Actual distance/km	**Estimated distance/km**	**% error**
0.5	1.0039	1.7
16.5	15.4095	3.6
28.5	29.6932	4.0
AB fault on Spur 1		
Actual distance/km	**Estimated distance/km**	**% error**
2.5	2.6138	1.9
4.5	4.3396	2.7

Table 6.3: Accuracy of fault location algorithms for an AB fault on Feeder 1 and Spur 1

For an AB fault on Feeder 1 and Spur 1, it can be seen that the estimated output distance of the ANN based fault location algorithm is close to the actual position of the fault with a small percentage error (below 5%).

ABC fault on Feeder 1		
Actual distance/km	**Estimated distance/km**	**% error**
0.5	0.9640	1.5
16.5	15.4139	3.6
28.5	27.8120	2.3
ABC fault on Spur 1		
Actual distance/km	**Estimated distance/km**	**% error**
2.5	2.8201	5.3
4.5	4.7153	3.6

Table 6.4: Accuracy of fault location algorithms for an ABC fault on Feeder 1 and Spur 1

For a three phase, ABC fault on Feeder 1, the estimation error of the fault location algorithm is below 4% and that for Spur 1 is less than 6%.

6.9 Summary

In order to deal with the presence of feeders and spurs in the distribution network, the accurate location of a fault involves three stages namely identifying the type of fault on the system, detecting the fault on the feeder or spur and eventually estimating the distance to the point of fault along the feeder or spur.

The performance analysis demonstrated that the fault classification and feeder/spur classification algorithms were able to operate as expected and their accuracies were not affected by the type of faults, the location of the fault in the network, the fault impedance and the fault inception angle.

Overall, it has been observed that for various types of faults on Feeder 1 and Spur 1, the fault location algorithms estimate the distance to the point of fault within ±1.5 km of the actual fault position on Feeder 1 (i.e. less than 5% error). Also, the estimated distance lies within ± 480 m of the actual fault position on Spur 1 (i.e. less than 8% error) for changes in fault inception angle and fault impedances.

Chapter 7: Impact of wind farm connection

7.1 Introduction

In this chapter, the impact of wind farm connection at the end of Feeder 1 is investigated (Figure 7.1). Firstly, the impact of the type of wind turbine configuration on fault current signatures is investigated and secondly, the effect of a change in the wind turbine capacity is examined. The four scenarios considered are as follows:

- Scenario 1: the integration of a 10.5 MW DFIG wind farm (i.e. 7 x 1.5 MW DFIG wind turbines)
- Scenario 2: the integration of a 10 MW PMSG wind farm (i.e. 5 x 2 MW PMSG wind turbines)
- Scenario 3: the integration of a 15 MW DFIG wind farm (i.e. 10 x 1.5 MW DFIG wind turbines)
- Scenario 4: the integration of a 16 MW PMSG wind farm (i.e. 8 x 2 MW PMSG wind turbines)

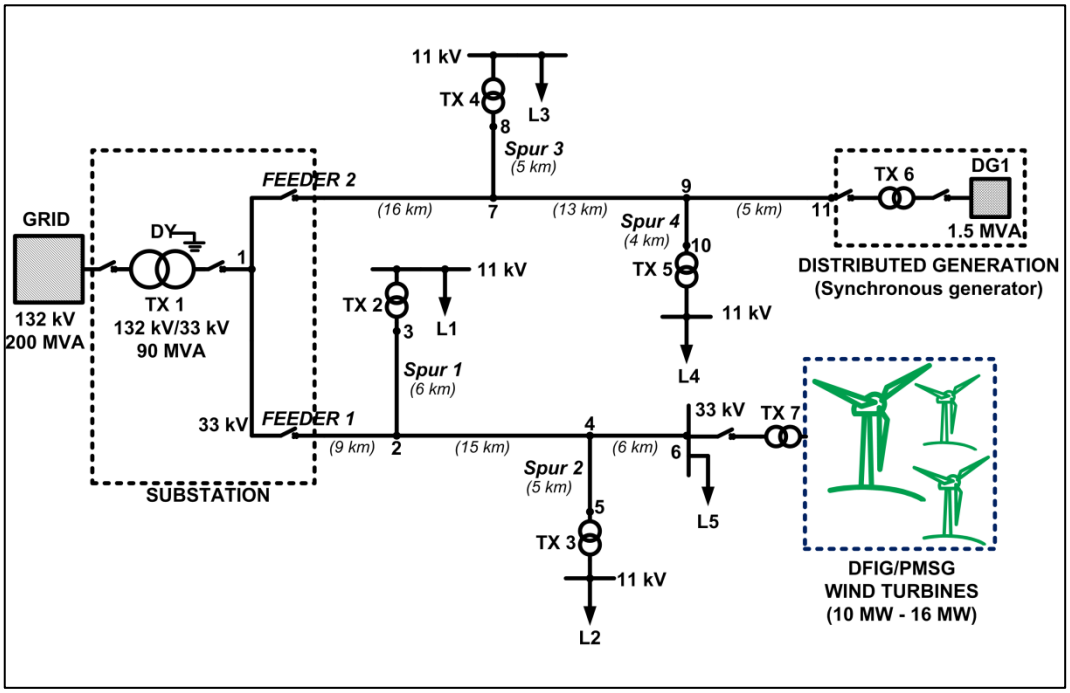

Figure 7.1: Wind turbine connections in 33 kV distribution network

7.2 Impact of wind farm type on fault current signatures

7.2.1 10.5 MW DFIG

Figure 7.2 shows the Discrete Wavelet Transform analysis of the A phase current for an A phase to ground fault at 1 km on Feeder 1 with a fault inception angle of 0° and a fault impedance of 0Ω. It compares the energies of detail 1 to detail 10 components of the A phase for a 33 kV distribution network without wind farm connection (i.e. passive network) and the same network with a 10.5 MW DFIG wind farm connection (i.e. active network) at the end of Feeder 1.

Firstly, just as in the case of a passive network, it can be seen that with a 10.5 MW DFIG wind farm connection, a spike can also be detected for high frequency components (781 Hz to 12.5 kHz) at the instant the fault occurs on the network and an oscillatory function is obtained for low frequency components (12.19 Hz to 781 Hz) after the occurrence of the fault. From Figure 7.2, it can also be observed that the amplitudes of the high frequency components in the range of 1.56 kHz to 12.5 kHz with a 10.5 MW DFIG wind farm connection are much higher than those of a passive network. However, the amplitudes of the low frequency components (12.19 Hz to 781 Hz) are almost similar for both a passive network and an active network.

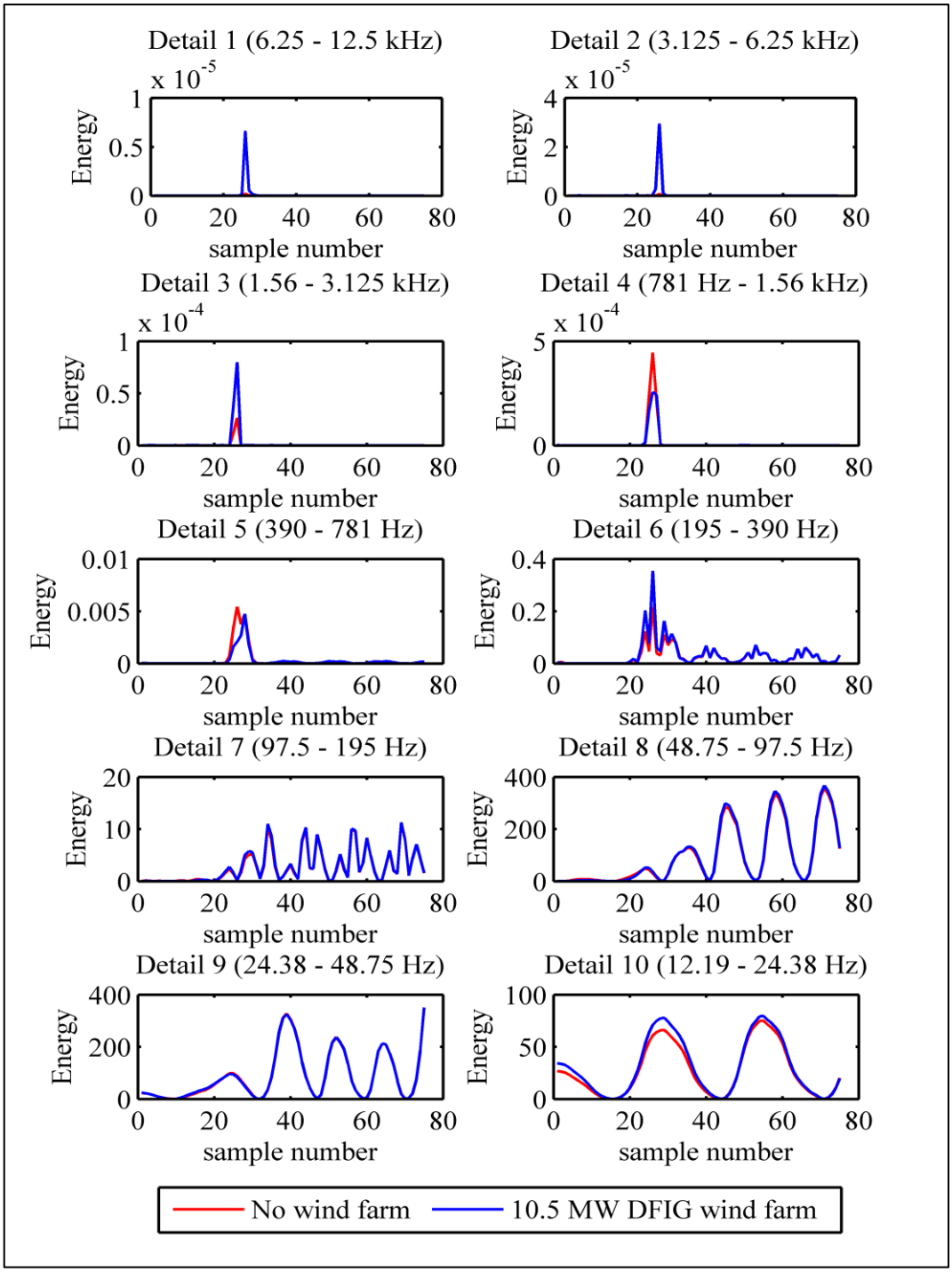

Figure 7.2: Energy comparison of the A phase for an AG fault with fault impedance Rf=0Ω and fault inception angle θ=0° at L=1 km on Feeder 1 with a 10.5 MW DFIG wind farm

For θ=0° and Rf=0Ω, but the A phase to ground fault now occurring at 15 km on Feeder 1 (Figure 7.3), the amplitudes of the high frequency components in the range of 3.125 kHz to 12.5 kHz with a 10.5 MW DFIG wind farm connection are much

lower than that of a passive network. This shows that there is a non-linear relationship between the amplitudes of the high frequency components with respect to the location of the fault on the network. However, the amplitudes of the low frequency components are almost identical in both cases.

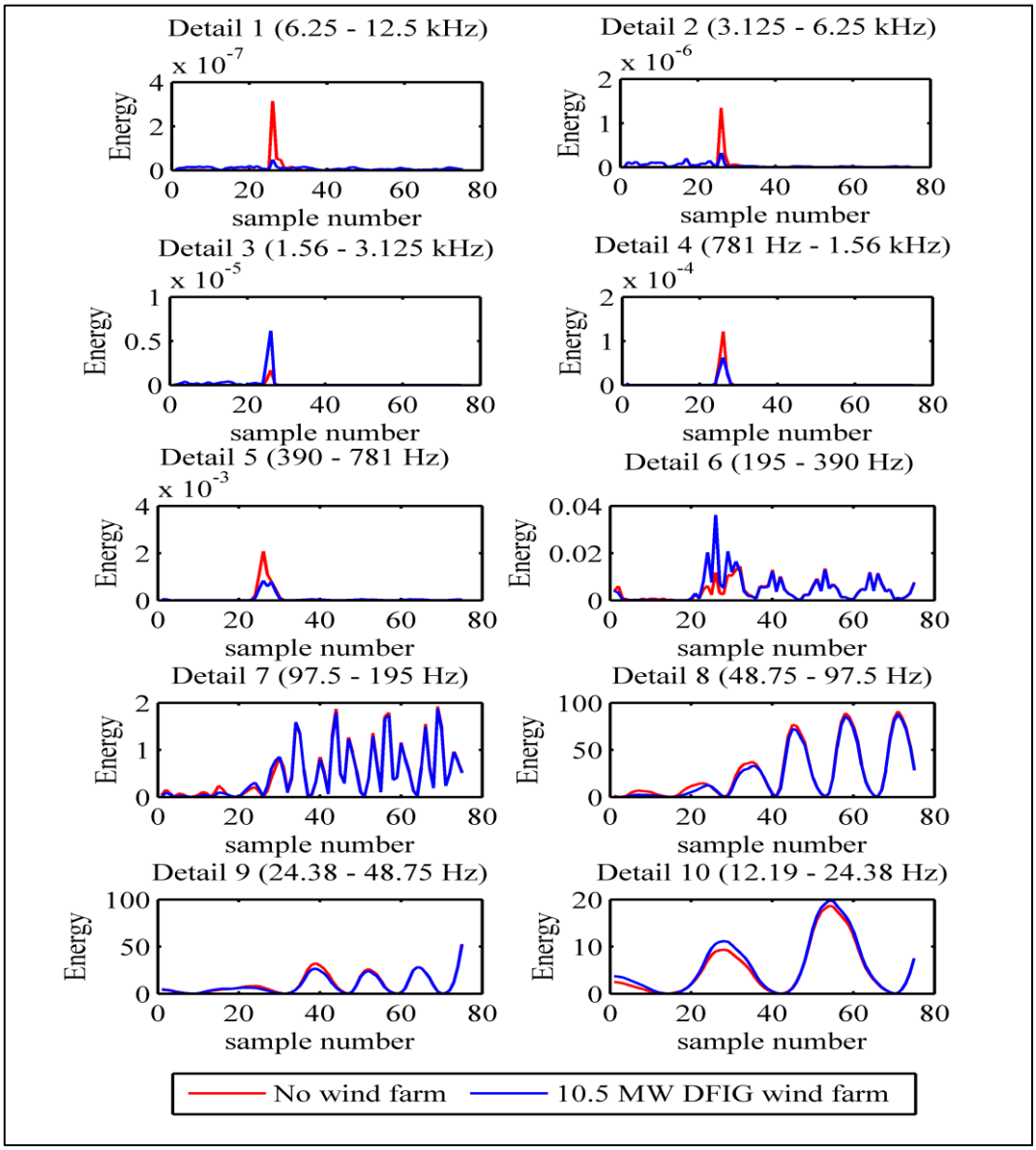

Figure 7.3: Energy comparison of the A phase for an AG fault with fault impedance Rf=0Ω and fault inception angle θ=0° at L=15 km on Feeder 1 with a 10.5 MW DFIG wind farm

With a fault inception angle of θ=90°, the non-linearity observed for the amplitudes of the high frequency components with a 10.5 MW DFIG wind farm connection with

respect to fault position is non-existent (Figure 7.4). It can clearly be observed that the amplitudes of all 10 detail components with a 10.5 MW DFIG wind farm connection are almost identical to that of a passive network as the waveforms look superimposed onto one another.

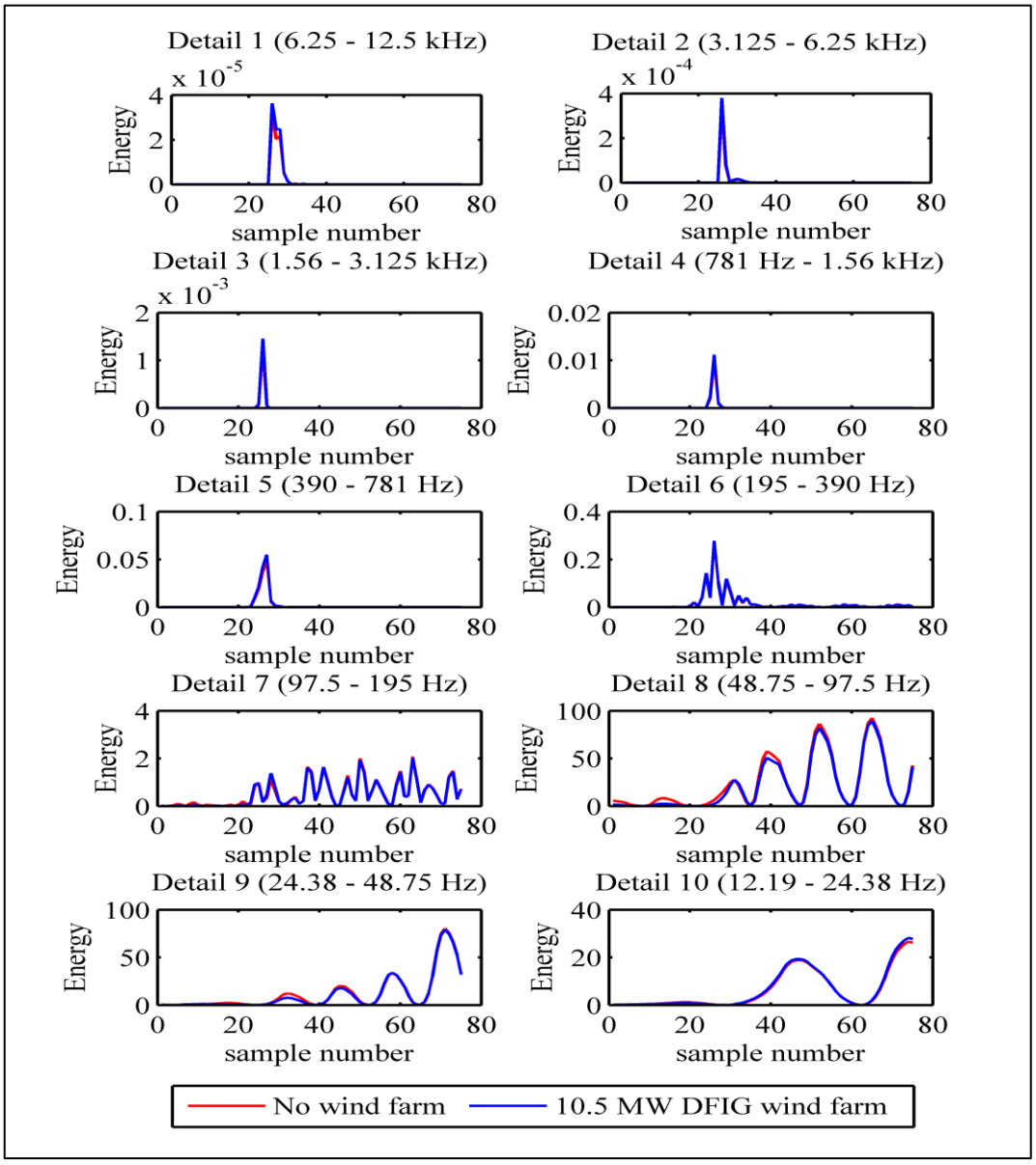

Figure 7.4: Energy comparison of the A phase for an AG fault with fault impedance Rf=0Ω and fault inception angle θ=90° at L=15 km on Feeder 1 with a 10.5 MW DFIG wind farm

For an AB, phase to phase fault (Figure 7.5), it can be seen that the energies of the high frequency and low frequency components for the faulted A phase are almost

identical in amplitudes for a fault on Feeder 1 with a 10.5 MW DFIG wind farm connection or without wind farm connection.

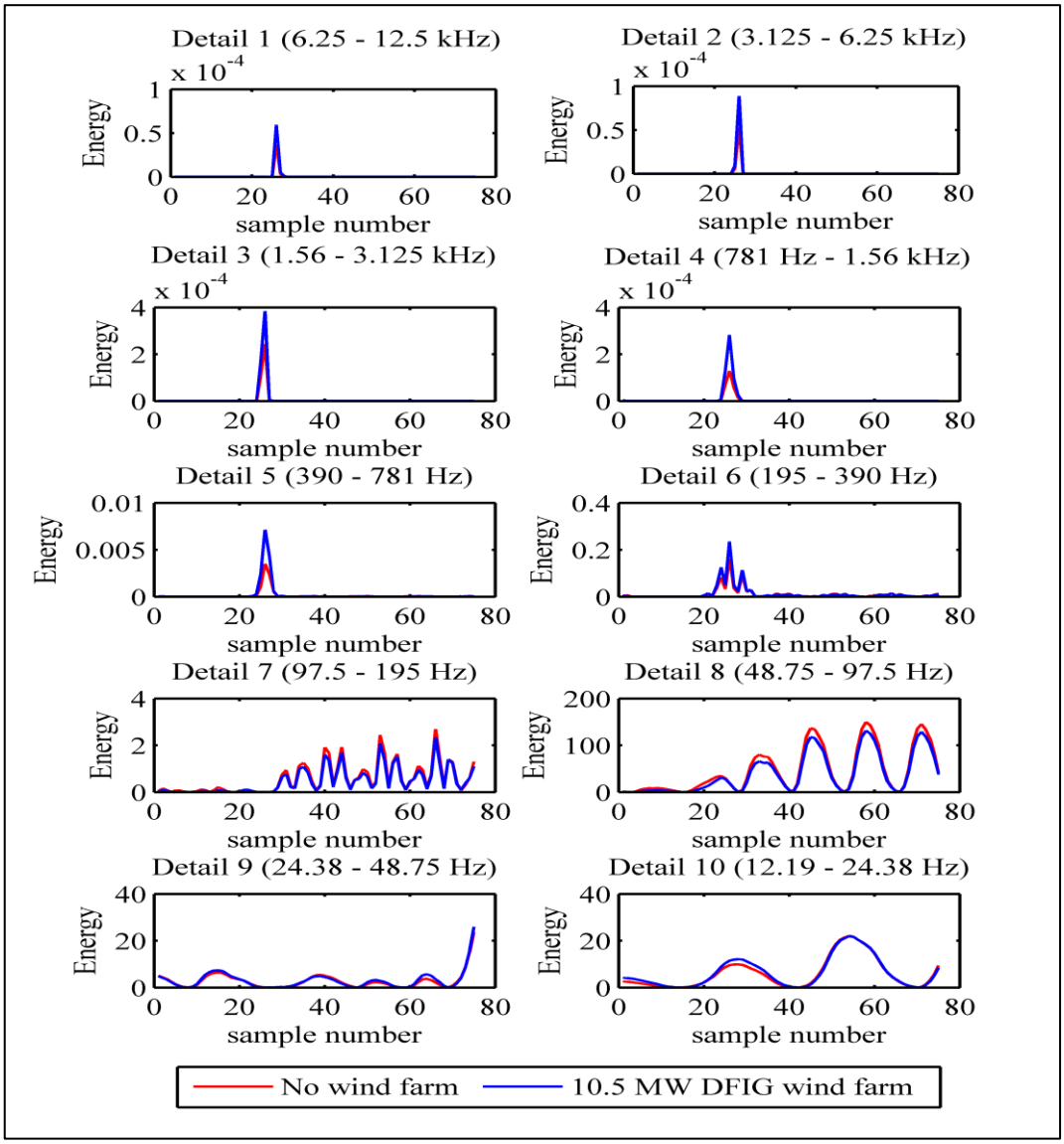

Figure 7.5: Energy comparison of the A phase for an AB fault with at L=15 km on Feeder 1 with a 10.5 MW DFIG wind farm

Figure 7.6 shows a comparison of the DWT analysis of the fault current in the B phase for an AB fault at 15 km on Feeder 1 for a passive network and an active network with 10.5 MW DFIG wind farm connection. It can be seen that for the high frequency components, the spikes at the instant of the fault inception on Feeder 1 have almost the same amplitude levels in both cases. Moreover, the energies of the low frequency components are almost identical in amplitudes.

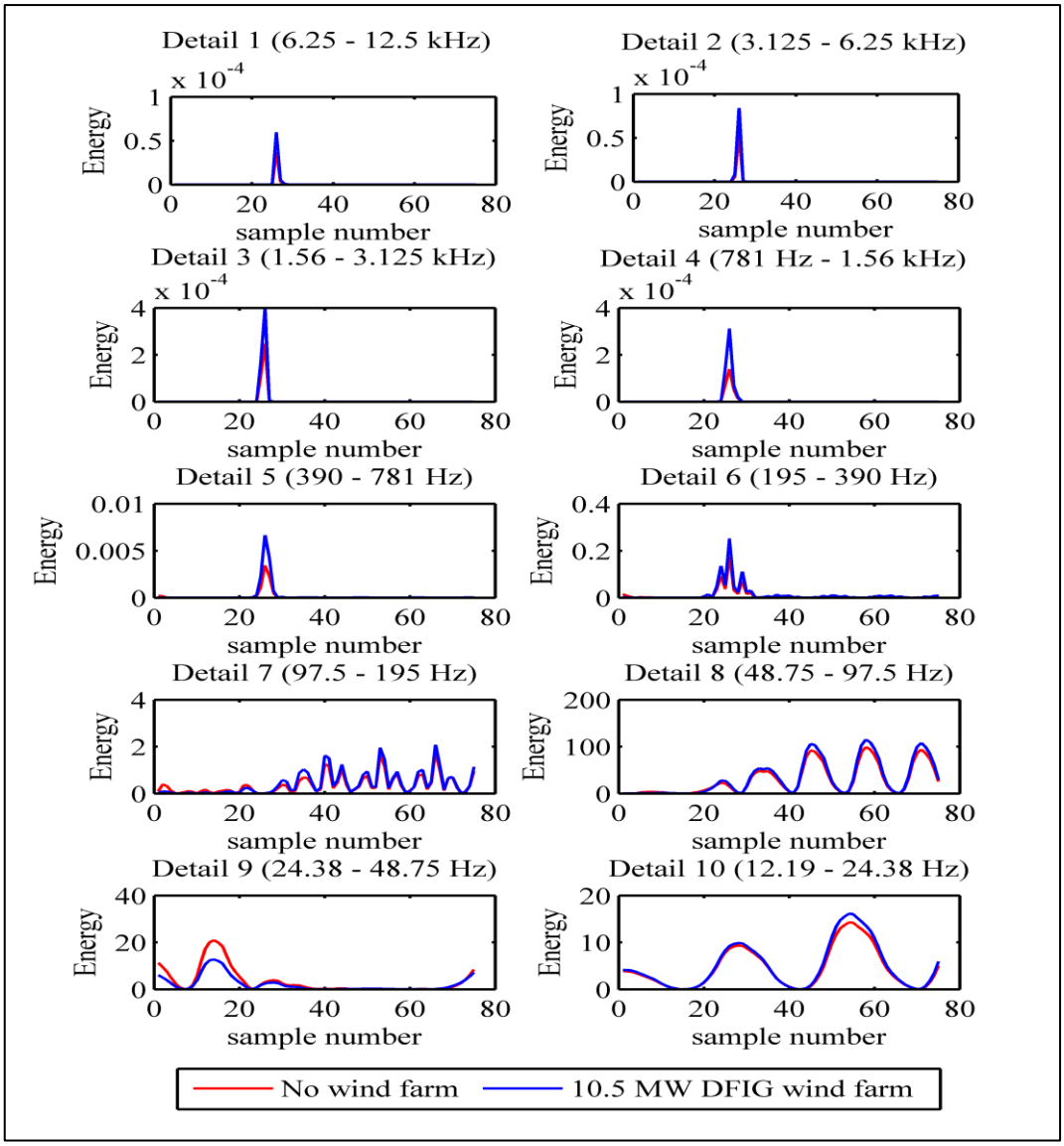

Figure 7.6: Energy comparison of the B phase for an AB fault with at L=15 km on Feeder 1 with a 10.5 MW DFIG wind farm

7.2.2 10 MW PMSG

In this section, the impact of connecting a 10 MW PMSG wind farm (5 x 2MW PMSG wind turbines) at the end of Feeder 1 on the fault current signatures is investigated. In Figure 7.7, it can be seen that for an A phase to ground fault, the amplitudes of the high frequency components in the range of 1.56 kHz to 12.5 kHz with a 10 MW PMSG wind farm connection are much higher than that in the case of a passive network. It can also be observed that the amplitudes of the low frequency components (12.19 Hz to 781 Hz) are almost similar in both cases.

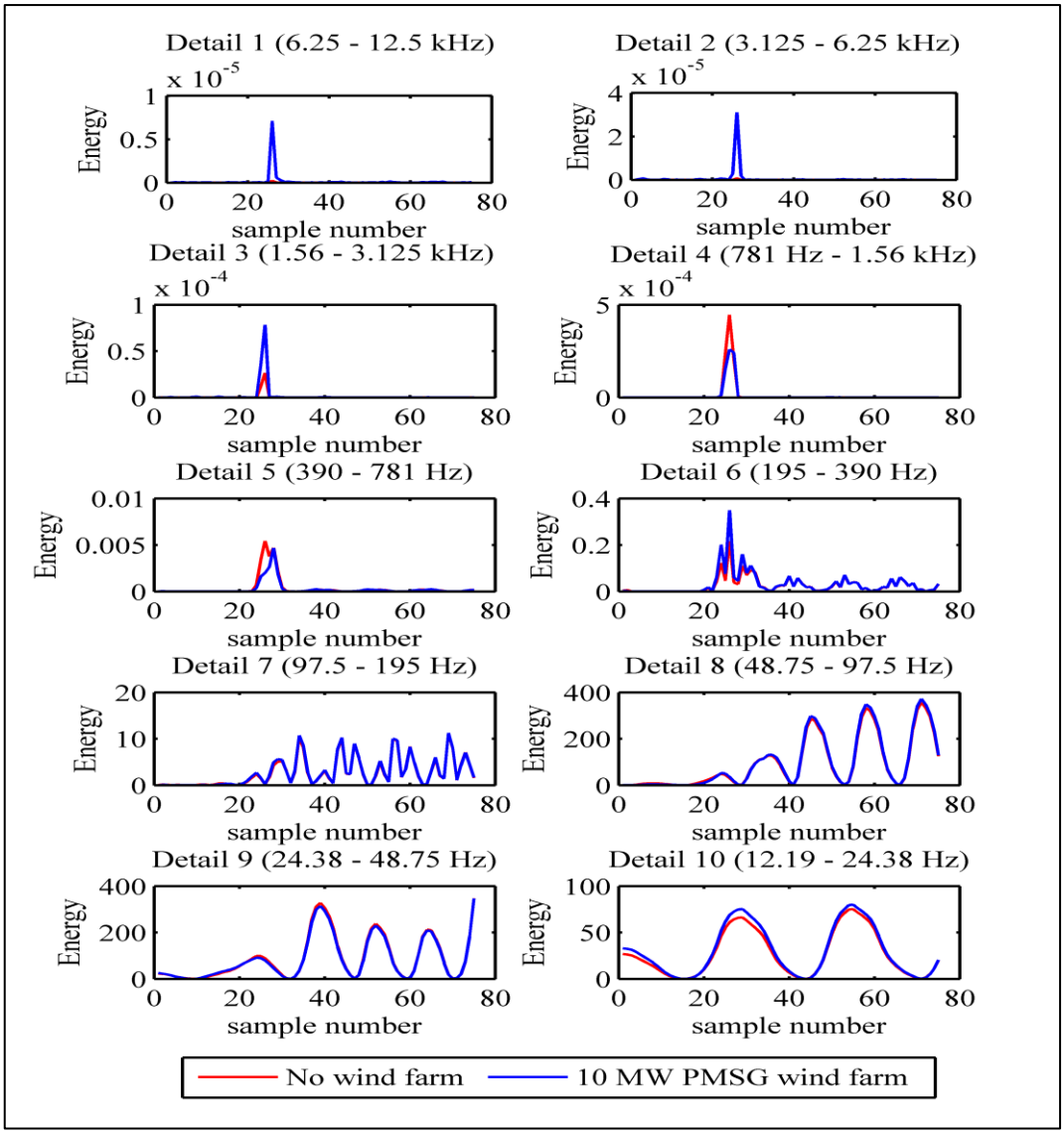

Figure 7.7: Energy comparison of the A phase for an AG fault with fault impedance Rf=0Ω and fault inception angle θ=0° at L=1 km on Feeder 1 with a 10 MW PMSG wind farm

However, for the same type of fault but with a fault inception angle of θ=90° (Figure 7.8), it can be observed the amplitudes of the high and low frequency components are the same for both a passive and an active network. After simulating different fault types with a 10 MW PMSG wind farm integration at the end of Feeder 1, it was observed that it was the high frequency components of fault currents that were mostly affected and not the low frequency components.

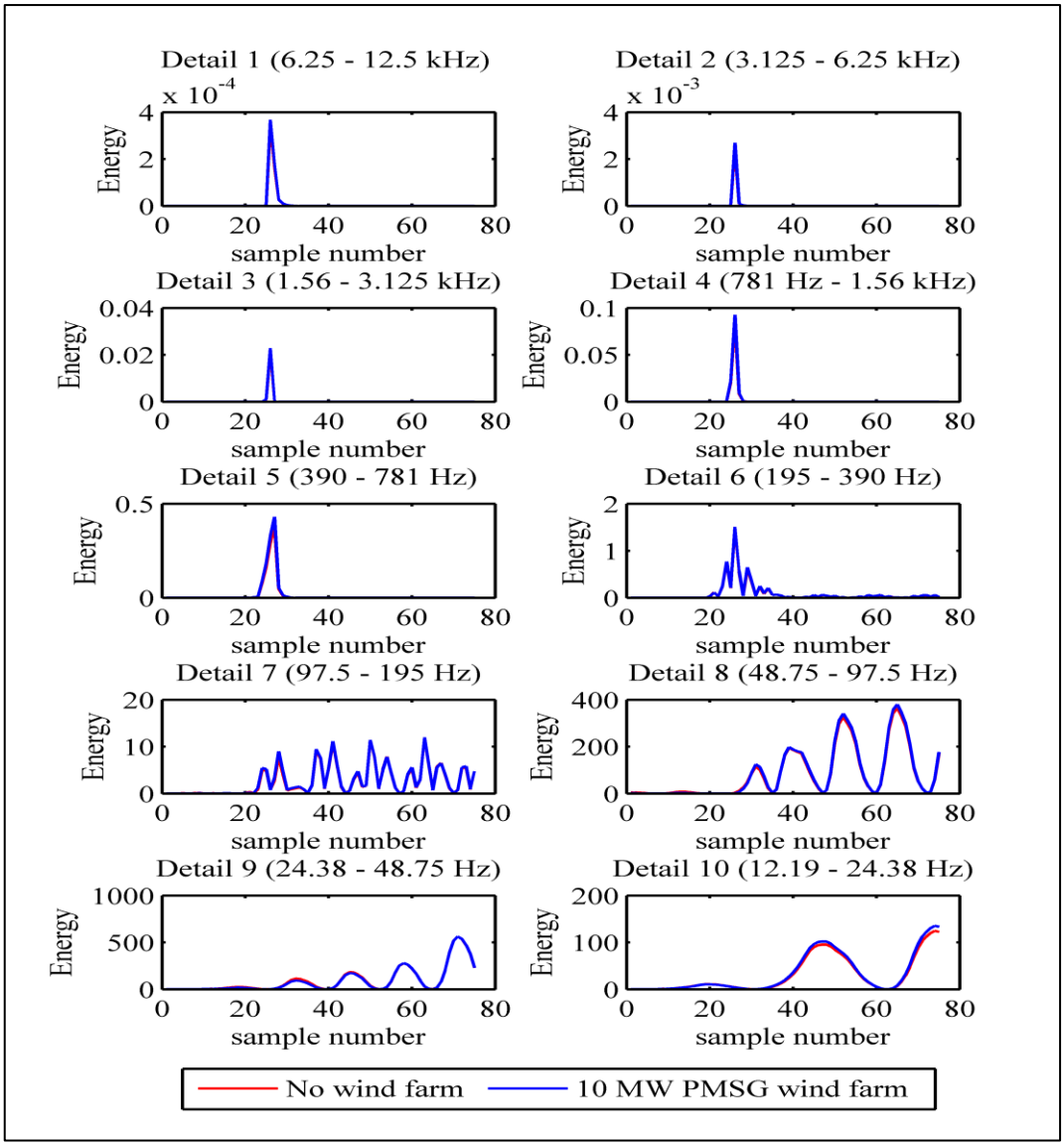

Figure 7.8: Energy comparison of the A phase for an AG fault with fault impedance Rf=0Ω and fault inception angle θ=90° at L=1 km on Feeder 1 with a 10 MW PMSG wind farm

7.2.3 Summary of effect of wind turbine type

In order to appreciate the effect of wind turbine type on the fault current signatures, it is better to have a direct comparison of the energies of the detail components between a passive network, a network with a 10.5 MW DFIG wind farm and a network with a 10 MW PMSG wind farm connection. The total energy (sum of energy amplitudes for each sample number) against distance for an A phase to ground fault has been plotted to summarise the effect of the type of wind turbine

connection in the network. From Figure 7.9, it can be observed that the total energy of the high frequency components differ by a much greater extent for different types of wind turbines. However, the total energies of the low frequency components decay exponentially with distance from the substation end and are also almost similar in amplitude. The same observation has been verified for other types of faults.

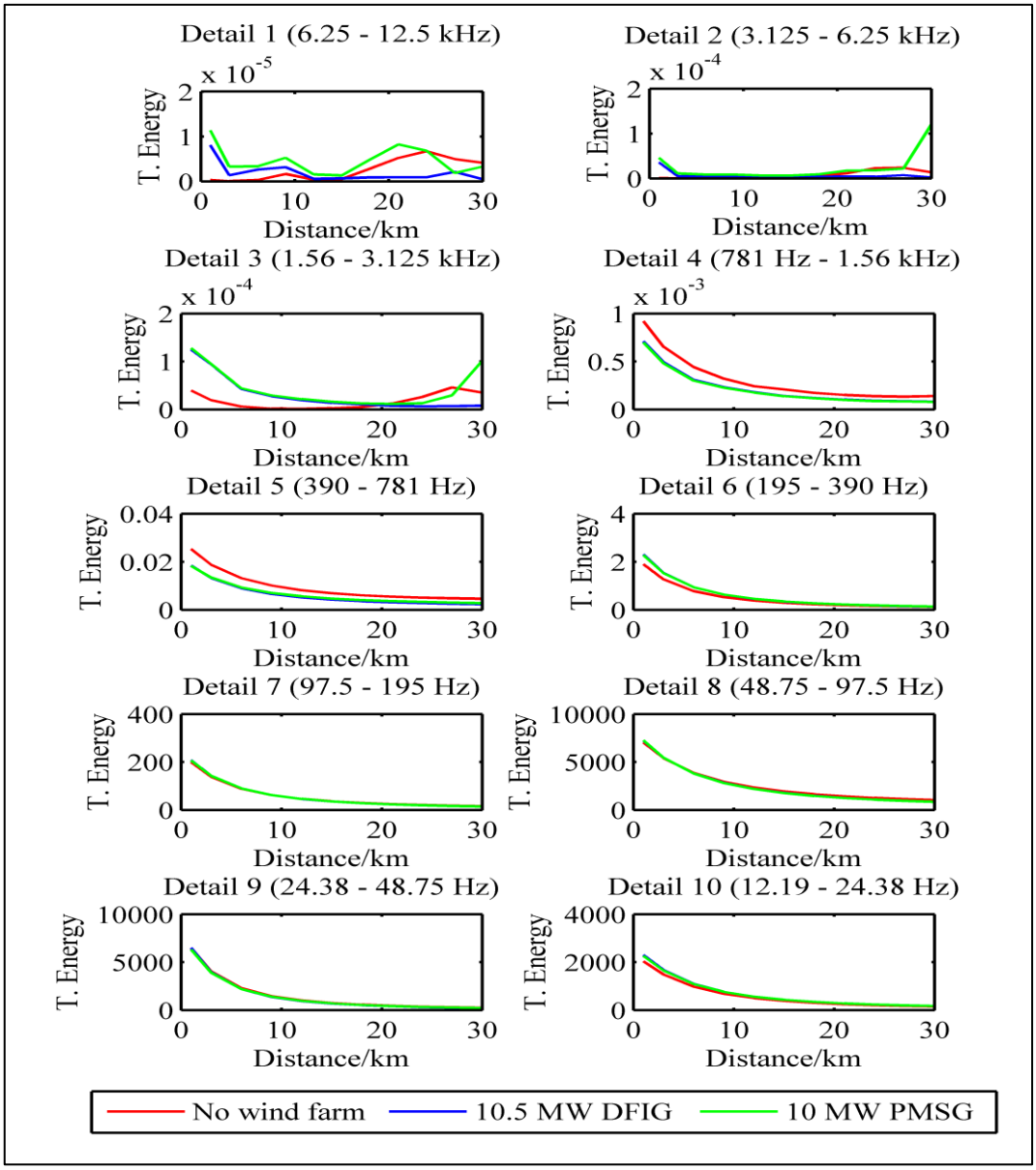

Figure 7.9: Total Energy comparison of the A phase for an AG fault with fault impedance Rf=0Ω and fault inception angle θ=0° at various locations on Feeder 1 with wind turbine types

Figure 7.10 demonstrates that total energy of the low frequency components are still almost similar in amplitude and decay exponentially with distance from the substation end for a fault inception angle of 90°. Hence, it can be concluded that the type of wind turbine affects mainly the amplitudes of the high frequency components when the power control strategies of the two different wind turbine configurations are the same.

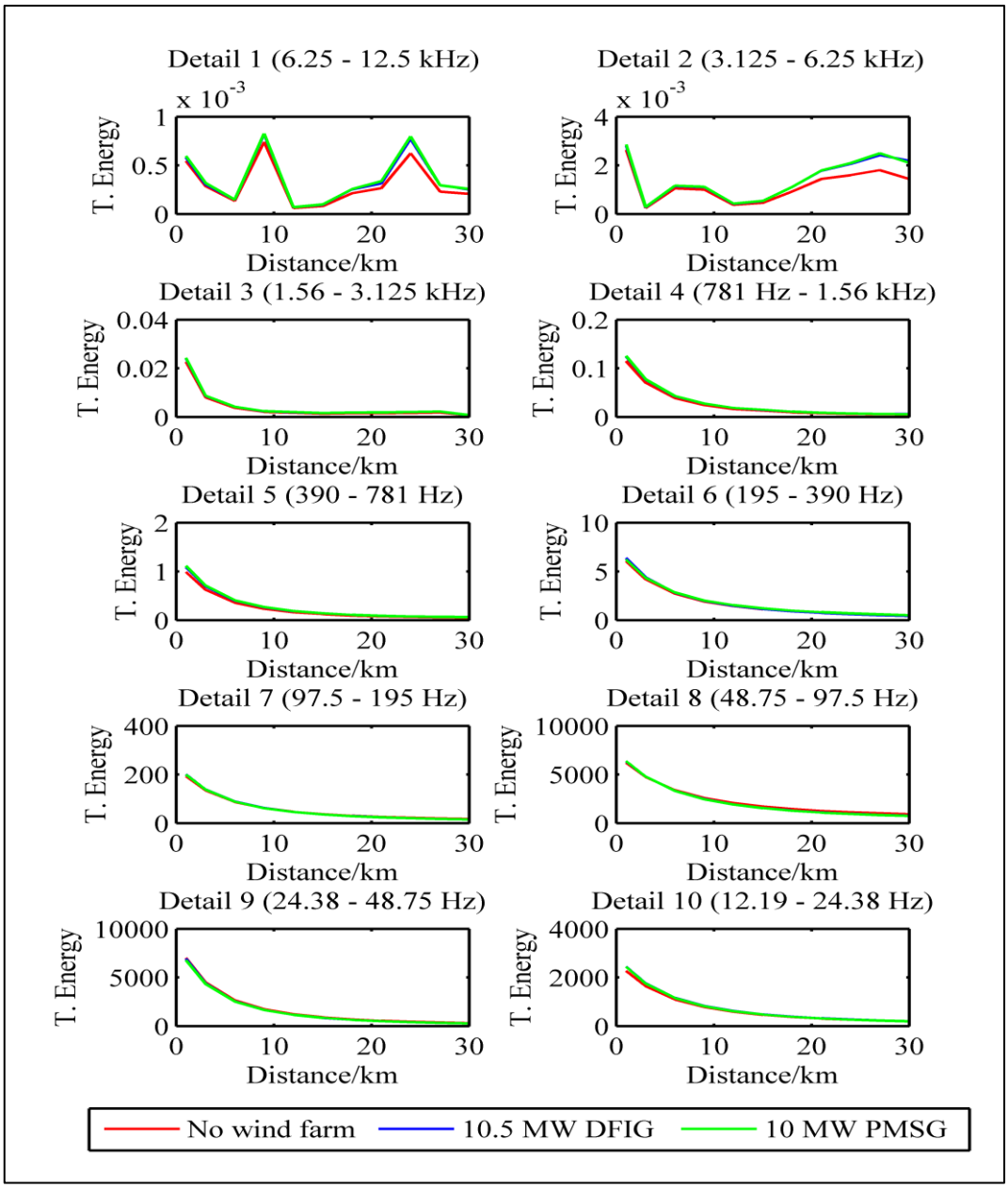

Figure 7.10: Total Energy comparison of the A phase for an AG fault with fault impedance Rf=0Ω and fault inception angle θ=90° at various locations on Feeder 1 with wind turbine types

7.3 Effect of increase in wind farm capacity on fault current signatures

In this section, the impact of an increase in wind capacity on the fault current signatures is investigated. For the DFIG wind farm, the capacity has been increased by 4.5 MW (3 additional DFIG wind turbines). Figure 7.11 shows the comparison of the total energy against distance for an A phase to ground fault occurring on a passive network, a network with a 10.5 MW DFIG wind farm connection and a network with a 15 MW DFIG wind farm connection.

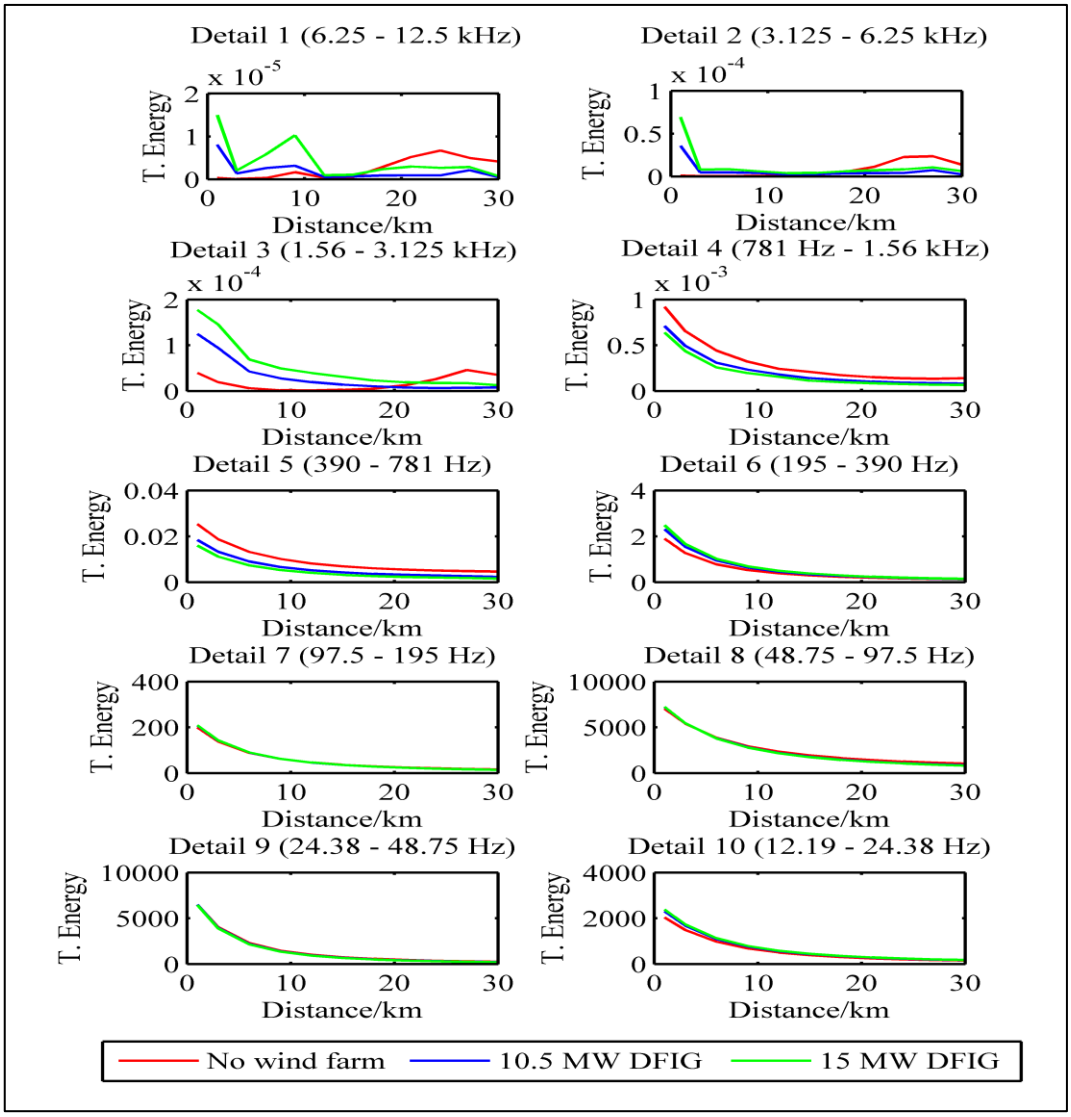

Figure 7.11: Total Energy comparison of the A phase for an AG fault with fault impedance Rf=0Ω and fault inception angle θ=0° at various locations on Feeder 1 with DFIG wind farms

It can be seen that the an increase in DFIG wind farm capacity mainly affects the amplitudes of the high frequency components whereas the amplitudes of the low frequency components decay exponentially with distance from the substation end and there is negligible differences between their amplitudes.

Figure 7.12 shows the total energies of the detail components for an A phase to ground fault at various location on Feeder 1 with an increase of 6 MW in PMSG wind farm capacity.

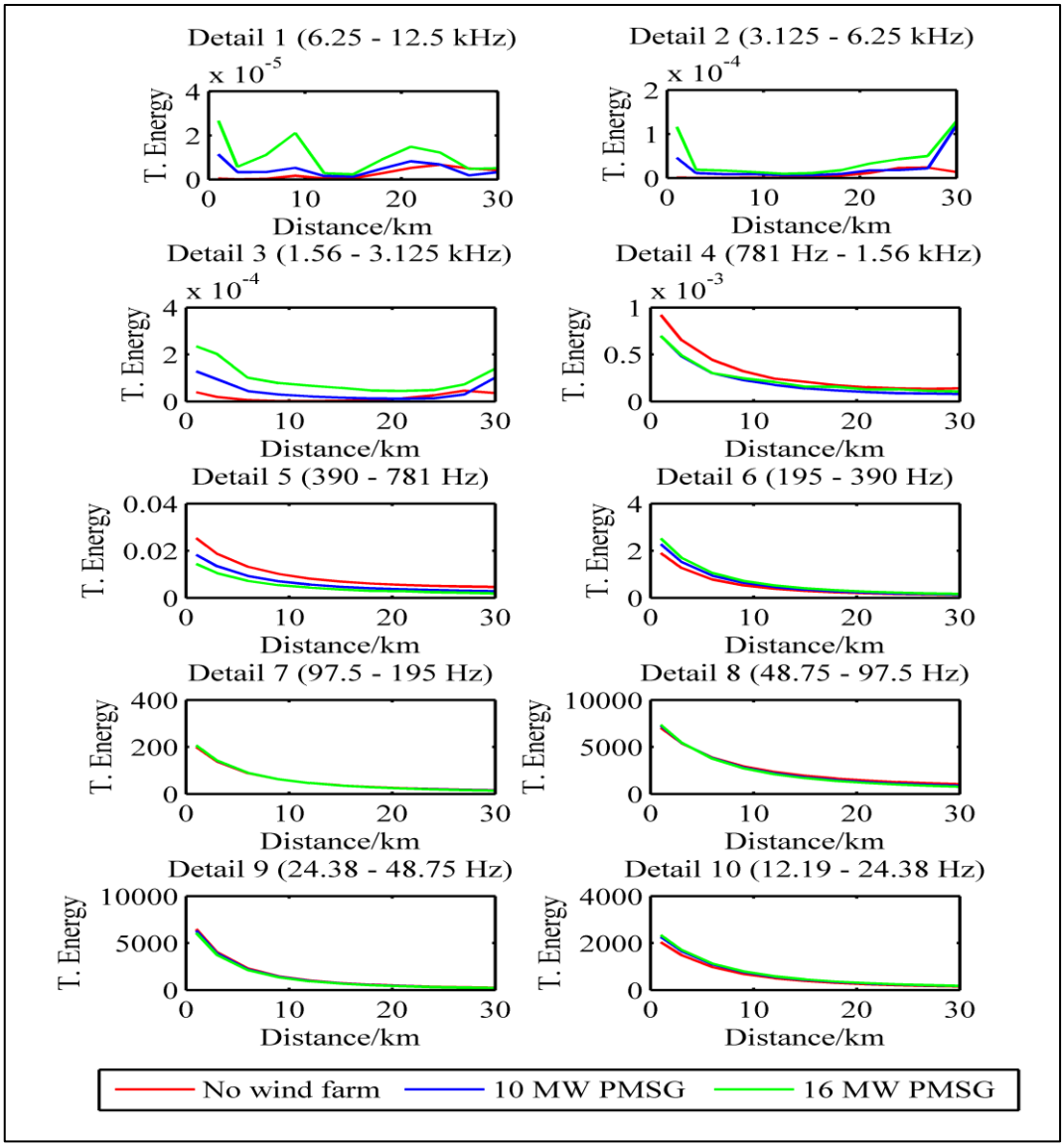

Figure 7.12: Total Energy comparison of the A phase for an AG fault with fault impedance Rf=0Ω and fault inception angle θ=0° at various locations on Feeder 1 with PMSG wind farms

The observation is similar to that of an increase in DFIG wind farm capacity since the amplitudes of the high frequency components are mainly affected by an increase in PMSG wind farm capacity whilst the total energies of the low frequency components are almost identical.

Finally, Figure 7.13 illustrates that for an A phase to ground fault at various locations on Feeder 1 with a 15 MW DFIG wind farm connection or with a 16 MW PMSG wind farm connection, the amplitudes of the low frequency components are relatively similar.

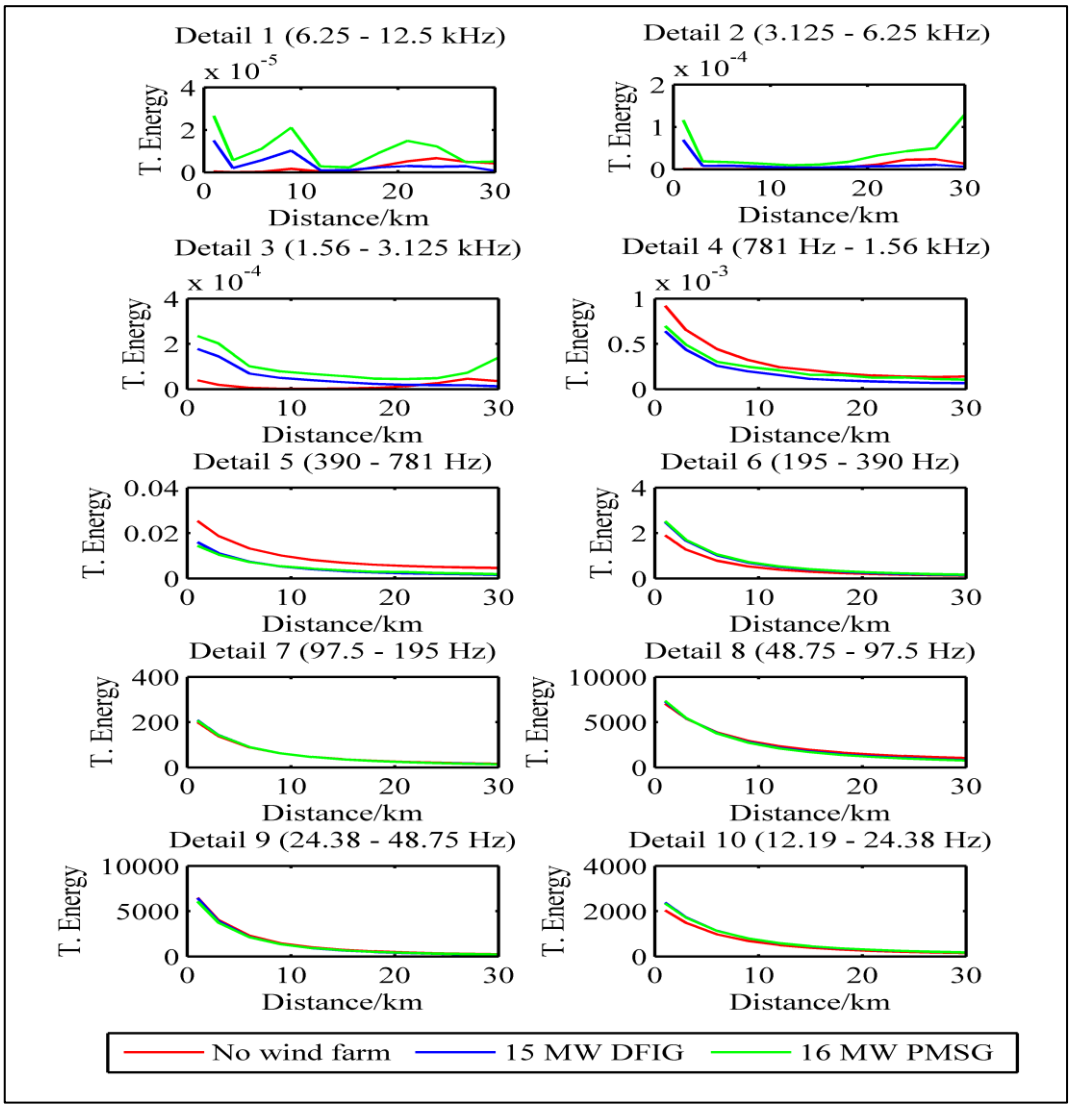

Figure 7.13: Total Energy comparison of the A phase for an AG fault with fault impedance Rf=0Ω and fault inception angle θ=0° at various locations on Feeder 1 with wind farm type

7.4 Impact of wind integration on developed algorithms

The ANN based fault classification algorithm, feeder/spur classification algorithms and fault location algorithms have all been trained using simulated data for a 33 kV distribution network without wind farm integration and simulated data for a 10.5 MW DFIG wind farm connection at the end of Feeder 1. The load connected to the network is around 20 MW and with the 10.5 MW wind farm connection, it implies that only around 50% of the load is supplied from the substation end. Thus, the amplitude of the phase currents at the substation side of Feeder 1 is much lower than the amplitude of the phase currents without wind farm connection.

In this section, the accuracies of the developed algorithms are firstly tested for different types of faults at various locations on Feeder 1 and Spur 1 with a 10.5 MW DFIG connection at the end of Feeder 1. Then, the algorithms are tested with a 10 MW PMSG wind farm connection instead of the 10.5 MW DFIG wind farm. Since the ANN based algorithms were never trained for a 10 MW PMSG wind farm connection, the results would demonstrate the robustness of the developed algorithms. Finally, the impact of an increase in the wind farm capacity on the accuracy of the ANN based algorithms is investigated.

The identification of the type of fault in the distribution network is not an issue with the type of wind turbine configuration or wind turbine capacity. It is also possible to correctly identify whether the fault lies on Feeder 1 (Figure 7.14) or Spur 1 (Figure 7.15) with a 10 MW PMSG wind farm. Moreover, an increase in wind farm capacity does not significantly affect the performance of the feeder/spur classification to correctly identify the faulted section.

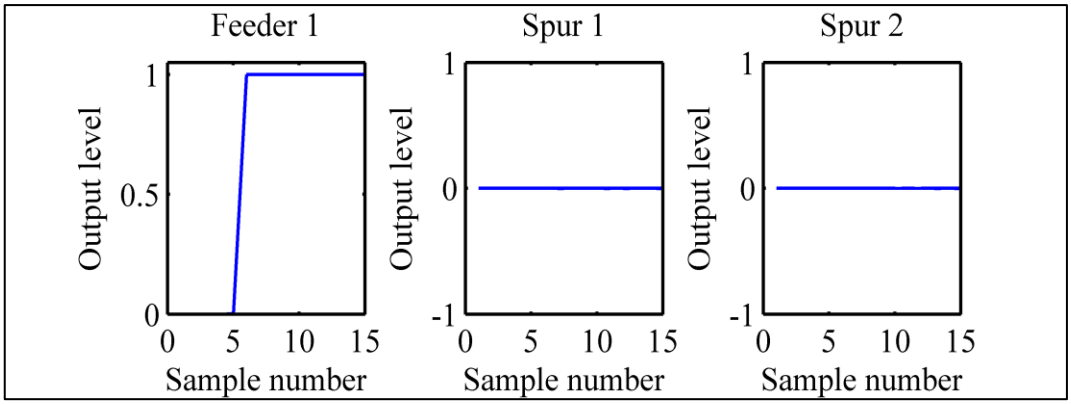

Figure 7.14: Feeder/spur classification algorithm output for an AG fault at 16.5 km on Feeder 1 with a fault inception angle of 0° and fault impedance Rf=10Ω with a 10 MW PMSG wind farm connection

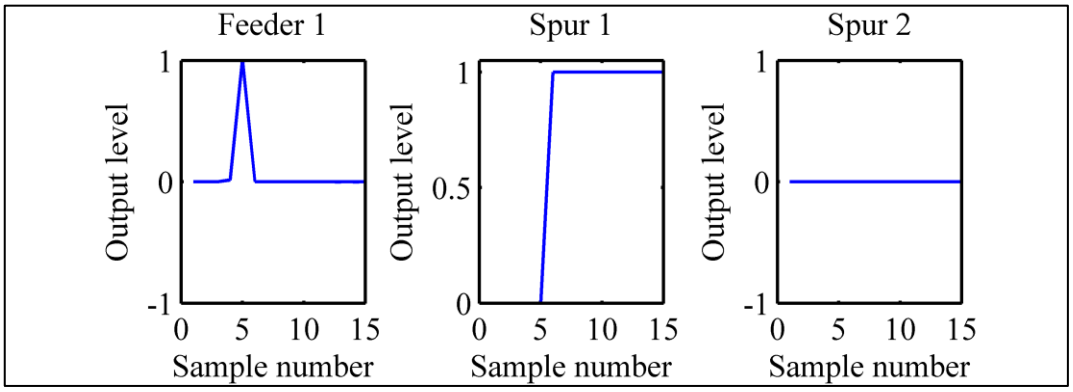

Figure 7.15: Feeder/spur classification algorithm output for an AG fault at 2.5 km on Spur 1 with a fault inception angle of 0° and fault impedance Rf=10Ω with a 10 MW PMSG wind farm connection

A comparison of accuracy of the fault location algorithm for an AG fault (Θ=0° and Rf=10Ω) at various locations on Feeder 1 with a 10.5 MW DFIG wind farm connection and a 10 MW PMSG wind farm connection is shown in Figure 7.16. The fault location algorithm was only trained with data containing information for a network without wind turbine connection and with a 10.5 MW DFIG wind farm. The results show that no significant change in accuracy can be observed when the 10.5 MW DFIG wind farm is replaced by a 10 MW PMSG. The percentage error is also less than 5% as can be seen for the case of no wind turbine connection into the system.

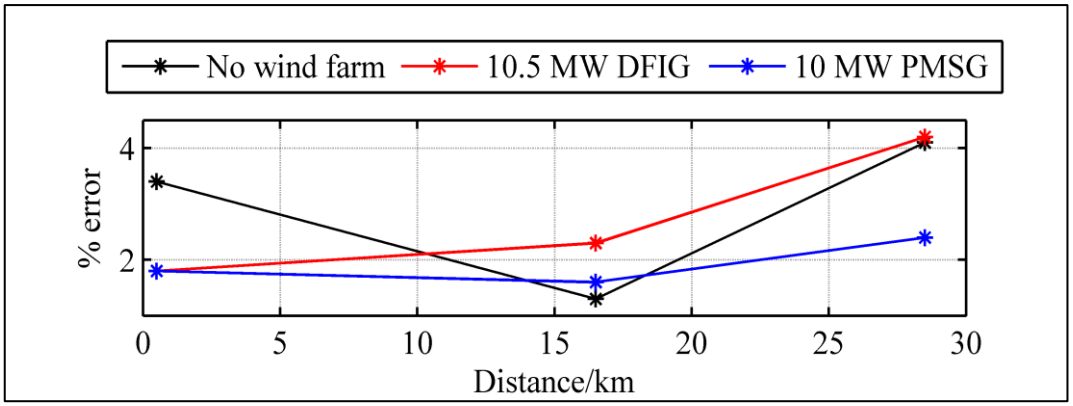

Figure 7.16: Accuracy of fault location algorithm for an AG fault on Feeder 1 with type of wind turbine configuration

The wind farm capacities have then been increased by 5 MW for the DFIG wind farm and by 6 MW for the PMSG wind farm (Figure 7.17). The fault location algorithm for the AG fault on Feeder 1 still manages to yield less than 5% error in the estimation of the distance to the fault.

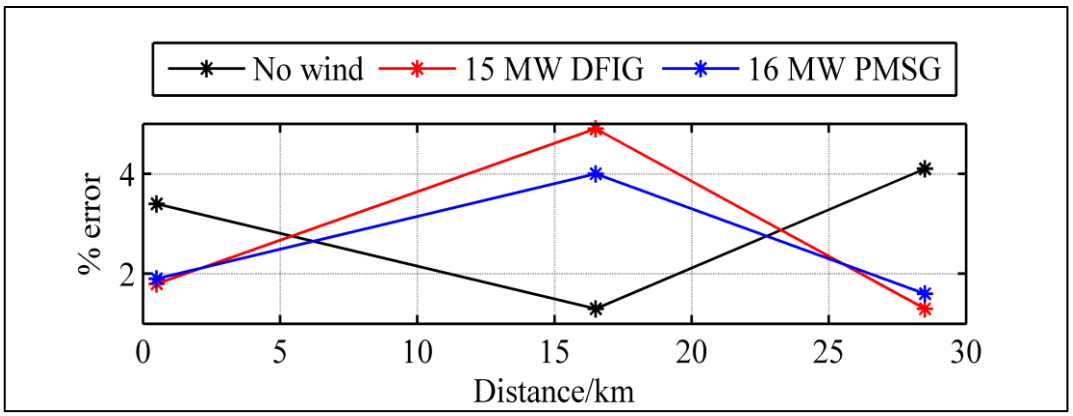

Figure 7.17: Accuracy of fault location algorithm for an AG fault on Feeder 1 with an increase in capacity of wind farm

For an AG fault (Θ=0° and Rf=10Ω) on Spur 1, the estimated distances and the percentage errors are given in Table 7.1. The percentage errors are less than 8% i.e. ± 480m of the actual fault positions on Spur 1.

Actual distance / km	No wind		10.5 MW DFIG		10 MW PMSG	
	Estimated distance /km	%error	Estimated distance /km	%error	Estimated distance /km	%error
2.5	2.2334	4.4	2.8240	5.4	2.7523	4.2
4.5	4.8141	5.2	4.8788	6.3	4.7289	3.8

Table 7.1: Accuracy of fault location algorithm for an AG fault on Spur 1 for different wind turbine configurations

However, with an increase in wind farm capacity, the percentage errors also increase for an AG fault on Spur 1 (Table 7.2). Instead of being around 8%, the percentage error has now increased to around 8.5% with the connection of a 15 MW DFIG wind farm. As compared to the case of no wind farm integration, this represents an increase of ± 30 m.

Actual distance / km	No wind		15 MW DFIG		16 MW PMSG	
	Estimated distance /km	%error	Estimated distance /km	%error	Estimated distance /km	%error
2.5	2.2334	4.4	3.0040	8.4	2.9621	7.7
4.5	4.8141	5.2	4.9744	7.9	4.9085	6.8

Table 7.2: Accuracy of fault location algorithm for an AG fault on Spur 1 for an increase in wind farm capacity

Figure 7.18 shows the accuracy of the fault location algorithm for an ABG fault on Feeder 1 for different wind turbine configurations. The maximum percentage error for an ABG fault at various locations on Feeder 1 without wind farm integration was around 5%. With the integration of a 10.5 MW DFIG wind farm or the connection of a 10 MW PMSG wind farm at the end of Feeder 1, the percentage error is still bounded to a maximum of 5%. Therefore, it can be concluded that no significant change in accuracy can be observed.

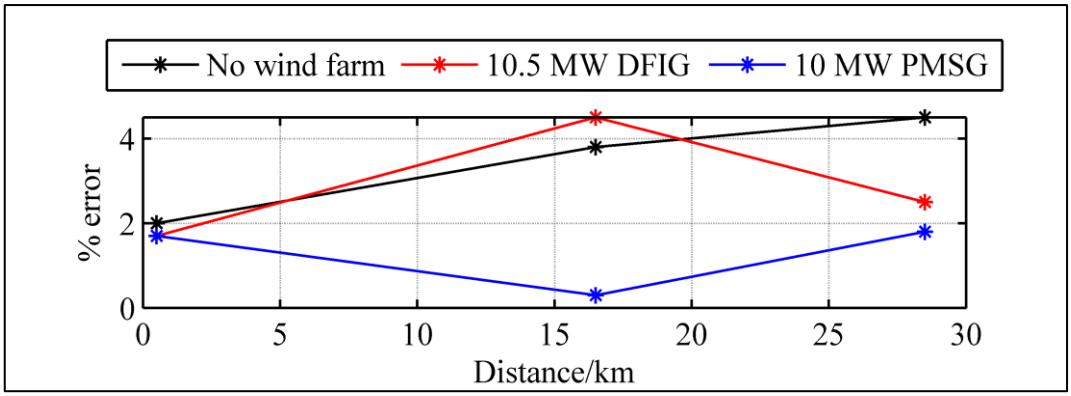

Figure 7.18: Accuracy of fault location algorithm for an ABG fault on Feeder 1 with type of wind turbine configuration

With an increase in wind farm capacity (Figure 7.19), the percentage error for the ABG fault location algorithm is still around 5% of the actual fault positions.

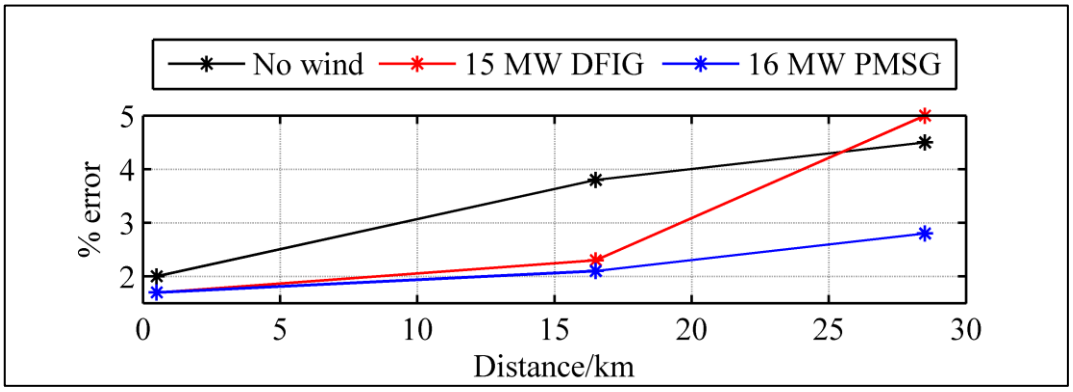

Figure 7.19: Accuracy of fault location algorithm for an ABG fault on Feeder 1 with an increase in capacity of wind farm

Table 7.3 and Table 7.4 show the effect of wind turbine type and wind turbine capacity on the fault location algorithm for an ABG fault on Spur 1. The percentage errors for an ABG fault on Spur 1 increase with an increase in wind turbine capacity. However, changing the type of wind turbine configuration does not have a considerable impact on the accuracy of the fault location algorithm.

Actual distance / km	No wind		10.5 MW DFIG		10 MW PMSG	
	Estimated distance /km	%error	Estimated distance /km	%error	Estimated distance /km	%error
2.5	2.5470	0.8	2.7463	4.1	2.8488	5.8
4.5	4.7033	3.4	4.7161	3.6	4.8960	6.6

Table 7.3: Accuracy of fault location algorithm for an ABG fault on Spur 1 for different wind turbine configurations

Actual distance / km	No wind		15 MW DFIG		16 MW PMSG	
	Estimated distance /km	%error	Estimated distance /km	%error	Estimated distance /km	%error
2.5	2.5470	0.8	2.9022	6.7	2.9550	7.6
4.5	4.7033	3.4	4.9324	7.2	4.7528	4.2

Table 7.4: Accuracy of fault location algorithm for an ABG fault on Spur 1 for an increase in wind farm capacity

For an AB fault on Feeder 1, the type of wind turbine configuration (Figure 7.20) does not affect the accuracy of the fault location algorithm and a slight increase in error can be observed for an increase in wind farm capacity (Figure 7.21), in particular for the 16 MW PMSG wind farm.

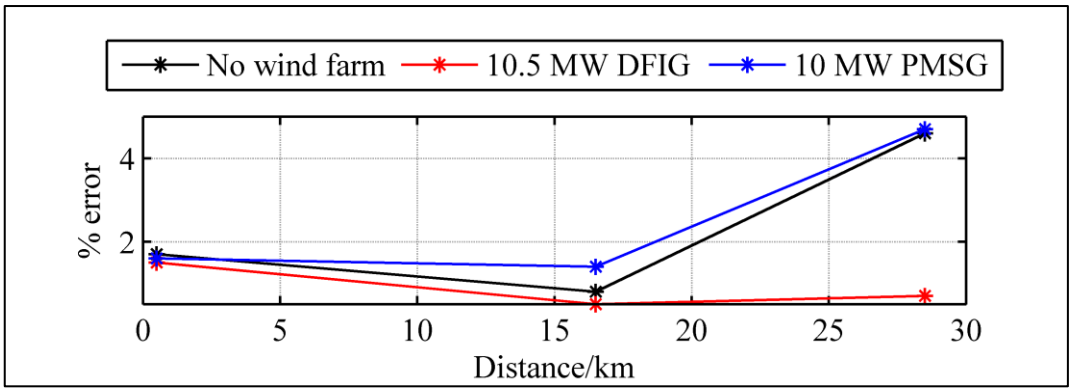

Figure 7.20: Accuracy of fault location algorithm for an AB fault on Feeder 1 with type of wind turbine configuration

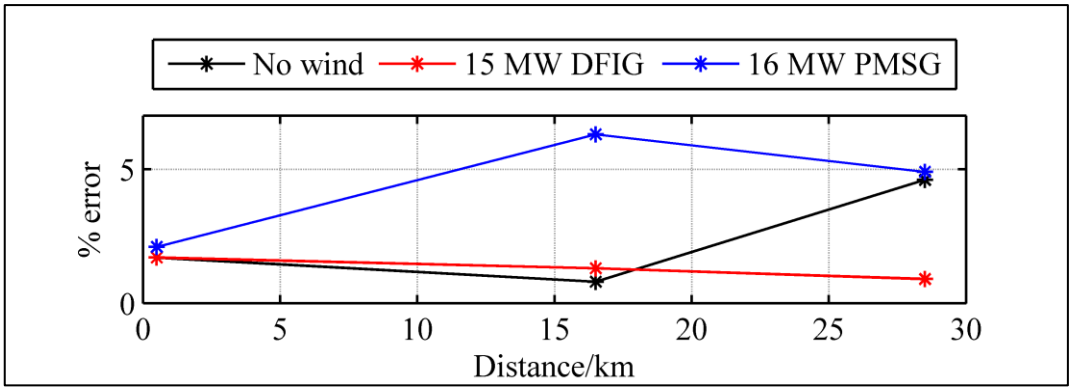

Figure 7.21: Accuracy of fault location algorithm for an AB fault on Feeder 1 with an increase in capacity of wind farm

The percentage errors for an AB fault on Spur 1 are given in Table 7.5 and Table 7.6. The maximum error (9.3%) was obtained with a 16 MW PMSG wind farm connection representing approximately an estimation error of ±558 m in the distance.

Actual distance / km	**No wind**		**10.5 MW DFIG**		**10 MW PMSG**	
	Estimated distance /km	**%error**	**Estimated distance /km**	**%error**	**Estimated distance /km**	**%error**
2.5	2.6138	1.9	2.6336	2.2	2.4307	1.2
4.5	4.3396	2.7	4.3892	1.8	4.7066	3.4

Table 7.5: Accuracy of fault location algorithm for an AB fault on Spur 1 for different wind turbine configurations

Actual distance / km	**No wind**		**15 MW DFIG**		**16 MW PMSG**	
	Estimated distance /km	**%error**	**Estimated distance /km**	**%error**	**Estimated distance /km**	**%error**
2.5	2.6138	1.9	2.3282	2.9	3.0600	9.3
4.5	4.3396	2.7	4.7755	4.6	4.3770	2.05

Table 7.6: Accuracy of fault location algorithm for an AB fault on Spur 1 for an increase in wind farm capacity

Finally, the percentage errors for an ABC fault on Feeder 1 with wind farm connection are shown in Figure 7.22 and Figure 7.23. The fault location algorithm is robust since the percentage error obtained when the 10.5 MW DFIG wind farm is replaced by the 10 MW PMSG wind farm (not part of training data) is still below 3%.

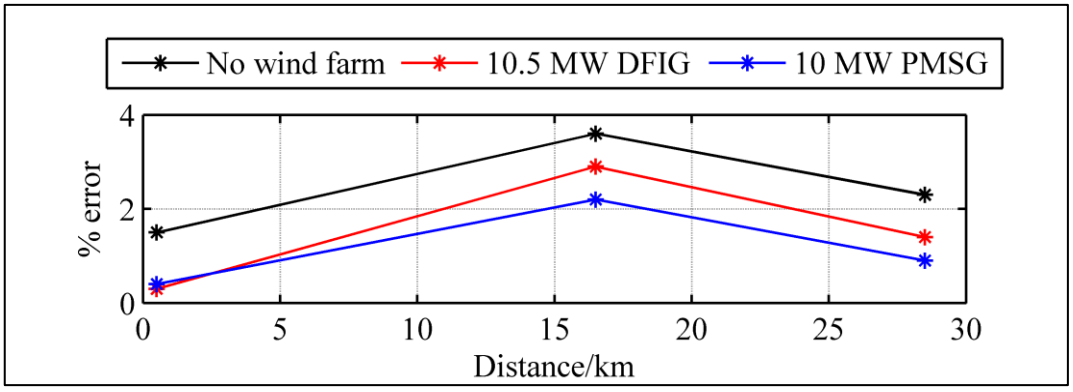

Figure 7.22: Accuracy of fault location algorithm for an ABC fault on Feeder 1 with type of wind turbine configuration

The fault location algorithm for an ABC fault on Feeder 1 with an increase in wind farm connection also demonstrates a good performance with percentage errors of less than 4%.

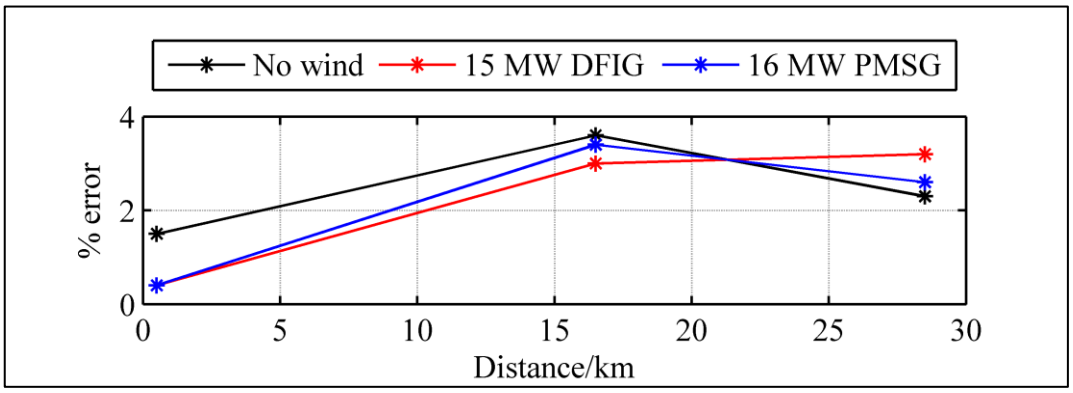

Figure 7.23: Accuracy of fault location algorithm for an ABC fault on Feeder 1 with an increase in capacity of wind farm

The percentage errors for an ABC on Spur 1 are given in Table 7.7 and Table 7.8. The accuracy of the fault location algorithm with a change in wind turbine configuration is still within the acceptable error.

Actual distance / km	No wind		10.5 MW DFIG		10 MW PMSG	
	Estimated distance /km	%error	Estimated distance /km	%error	Estimated distance /km	%error
2.5	2.8201	5.3	2.2166	4.7	2.4021	1.6
4.5	4.7153	3.6	4.6162	1.9	4.2112	4.8

Table 7.7: Accuracy of fault location algorithm for an ABC fault on Spur 1 for different wind turbine configurations

However, with an increase in wind turbine capacity, the percentage errors increase and can sometimes be higher than 8% i.e. more than ± 480 m of the actual fault location.

Actual distance / km	No wind		15 MW DFIG		16 MW PMSG	
	Estimated distance /km	%error	Estimated distance /km	%error	Estimated distance /km	%error
2.5	2.8201	5.3	3.0092	8.5	2.7952	4.9
4.5	4.7153	3.6	4.4976	0.3	4.4561	0.7

Table 7.8: Accuracy of fault location algorithm for an ABC fault on Spur 1 for an increase in wind farm capacity

7.5 Summary

The integration of wind turbines into the distribution network affects some of the features present in the fault currents measured at the substation end. It has been observed that the type of wind turbine configuration affects mainly the amplitudes of the high frequency components present in the fault current signals. On the other hand, the amplitudes of the low frequency components are relatively similar, both in the case of an active network and a passive network.

An increase in wind turbine capacity also impacts mainly on the amplitudes of the high frequency components present in the fault current waveforms; the amplitudes of the low frequency components are however almost similar.

The fault classification and location algorithms were trained with data obtained from a passive network and a network with a 10.5 MW DFIG wind turbine configuration. When the DFIG wind farm was replaced by a 10 MW PMSG wind farm, no significant change was observed in the accuracy of the developed ANN based algorithms. The feeder/spur classification algorithm correctly identified the faulted section of the network and the percentage error for the fault location algorithm was within the tolerance value of 5% for Feeder 1, and 8% for Spur 1. This proves that the developed algorithms are robust to the integration of wind turbines of the same capacity.

With an increase in wind farm capacity, the feeder/spur classification algorithm still managed to correctly identify the faulted section of the distribution network. However, the accuracy of the developed fault location algorithms were slightly affected for faults located on Feeder 1 with an increase of around 1% (i.e. around ± 300 m); and the accuracy of the fault location algorithms for faults on Spur 1 also increased by around 1.3 % (i.e. ± 78 m).

Chapter 8: Sensitivity analysis of ANN based fault classification and location algorithms

8.1 Introduction

In this section, the robustness and limitations of the developed ANN based fault classification and location algorithms are demonstrated by performing various sensitivity tests. The test data used for the feeders and spurs contains new information about faults at various locations on the feeder and spurs, not contained in the training data set.

Firstly, the network topology can change due to maintenance work on a section of the network resulting in a spur being temporarily de-energised and disconnected from the network. This change in network topology can affect the accuracy of the developed fault classification and location algorithms.

The load connected to a distribution network is not fixed. It changes with time due to some loads being switched on and off at the consumers' premises and it is also different during the summer and winter period. Therefore, the effect of a change in load on the network has to be investigated.

The ANN based fault classification and location algorithms have been trained for an overhead distribution network. In practice, distribution networks are composite networks consisting of overhead lines and underground cables. Underground cables have a higher capacitance per unit length than overhead lines and this can also affect the accurate location of a fault in the distribution network.

Finally the effects of a change in source capacity, line length and the impact of white noise on the accuracy of the developed algorithms are also investigated.

8.2 Effect of network topology

The topology of a distribution network can sometimes change due to maintenance work being carried out on part of the network or repairs being made on a faulted section after an outage. The healthy part of the system is still operational under these circumstances but the network itself now has a different topology which can affect the sensitivity of the developed fault classification and location algorithms.

In order to test the robustness of the ANN based algorithms to a change in network topology, Spur 1 on Feeder 1 in the 33 kV distribution network shown in Figure 8.1 has been disconnected from the rest of the network

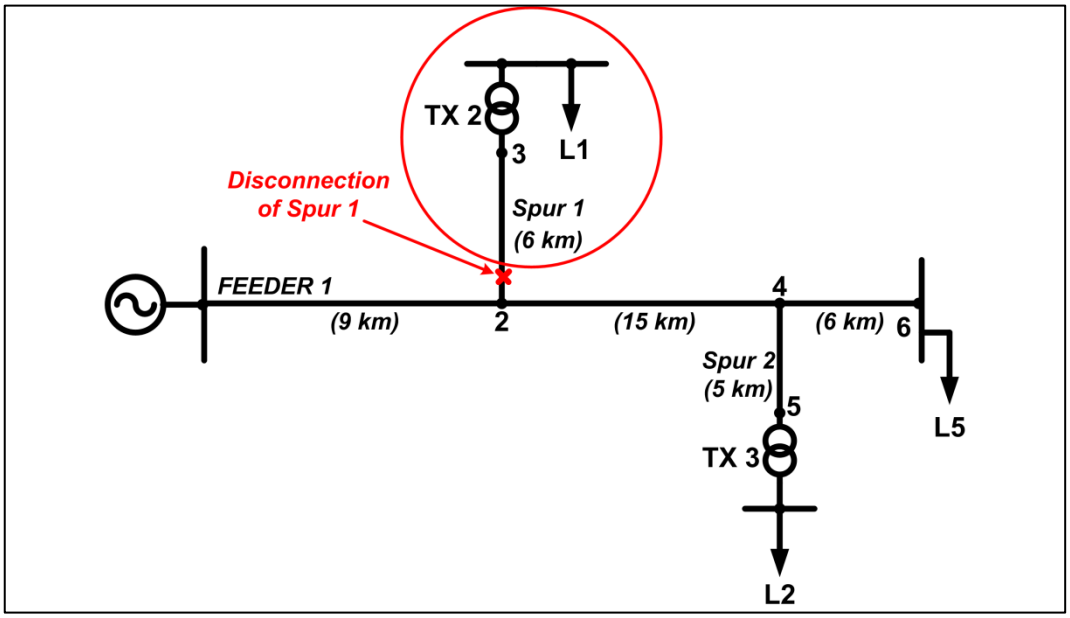

Figure 8.1: Disconnection of Spur 1 from network

The disconnection of Spur 1 from the network changes the system impedance and also results in a decrease in the total load connected to the system due to the disconnection of load L1. Firstly, the fault type classification algorithm is tested with an AG fault at 16.5 km on Feeder 1 with a fault inception angle of 90˚ and a fault impedance of 35Ω (Figure 8.2). The decision making algorithm easily determines the type of fault as an AG fault by calculating the area under each graph.

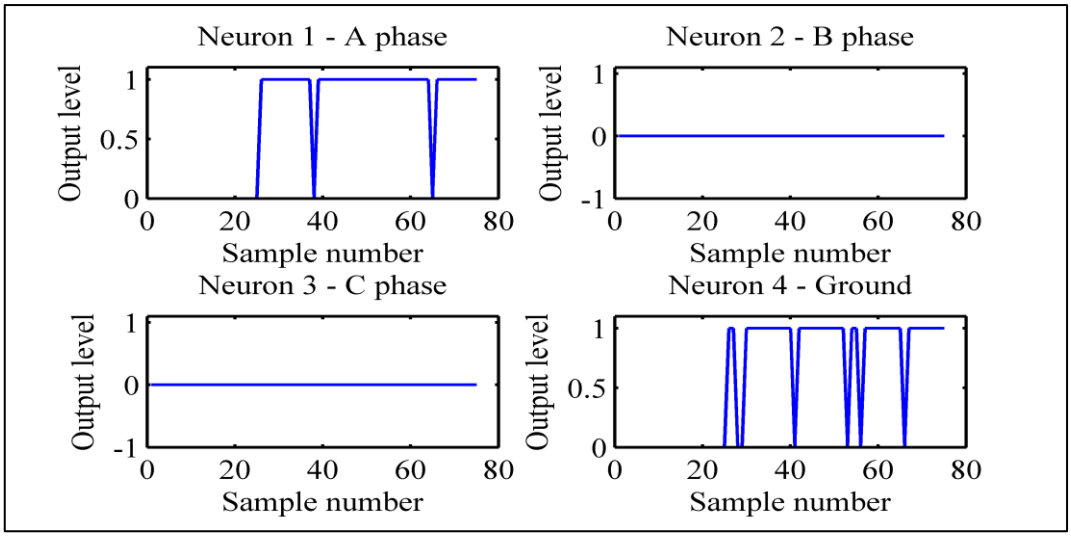

Figure 8.2: Output of fault classification algorithm for an AG fault on Feeder 1 with Spur 1 disconnected

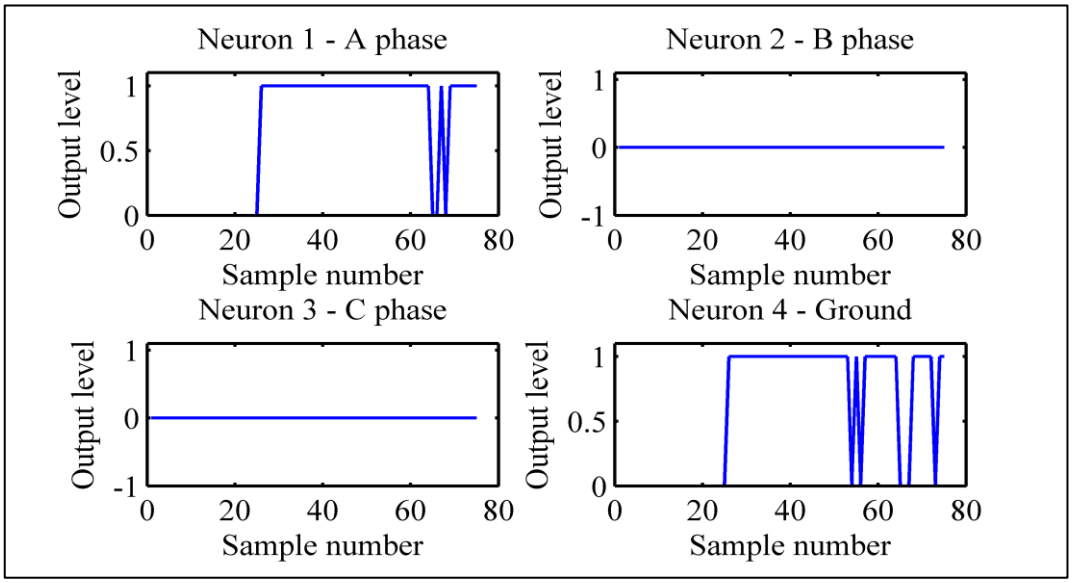

Figure 8.3: Output of fault classification algorithm for an AG fault on Spur 2 with Spur 1 disconnected

The fault classification algorithm is also successful in determining the type of fault for an AG fault at 2.5 km on Spur 2 with a fault inception angle of 90˚ and a fault impedance of 35Ω (Figure 8.3). Further experiments similarly confirmed that the fault classification algorithm was able to accurately determine the type of fault for phase to phase faults, double phase to ground faults and three phase faults on Feeder 1 and Spur 2 with Spur 1 disconnected from the network.

The next stage is to determine whether the fault lies on Feeder 1 or Spur 2. The output of the feeder/spur classification algorithm for an AG fault at 16.5 km on Feeder 1 with a fault inception angle of 90˚ and a fault impedance of 35Ω is depicted in Figure 8.4. The output of the threshold detection algorithm is unable to detect that the fault occurred on Feeder 1 and the output of the decision making algorithm interpreted the information as no fault present on the system.

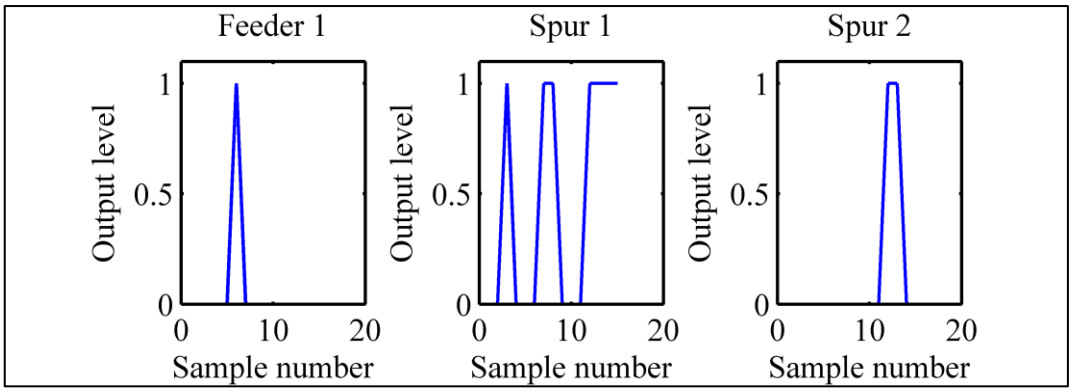

Figure 8.4: Feeder/spur classification algorithm output for an AG fault on Feeder 1 with Spur 1 disconnected

The success of accurately determining the distance to the point of fault strongly relies on first finding whether the short circuit fault occurred on the feeder or on one of the spurs. Without this classification, it is impossible to estimate the distance to the fault. Therefore, it has been verified that a change in network topology influences the performance of the developed feeder/spur classification algorithms and thus prevents the estimation of the distance to the point of fault. A possible solution to deal with a change in network topology is to have various ANN based feeder/spur classification algorithms trained for different network configurations.

8.3 Effect of change in line length

The actual length of the overhead line conductor for each phase is in general not exactly known. The length of Feeder 1 was taken as 30 km in the simulations but in practice, this length has a tolerance value. This may be due to jumpers being used to link conductors of the same phase on each side of an intermediate pole with double

cross-arm as shown in Figure 8.5. Jumpers are also used to link the conductors if part of the line section is designed to bend at a 90˚ angle.

Figure 8.5 also shows a typical connection of the primary side of a pole mounted distribution transformer to the overhead distribution network using jumpers. The line sagging in overhead distribution networks can be ignored since the span between two poles is relatively short (around 30 m) and the weight of the conductor per unit length causes negligible sag for this length of span when the conductor is properly tensioned.

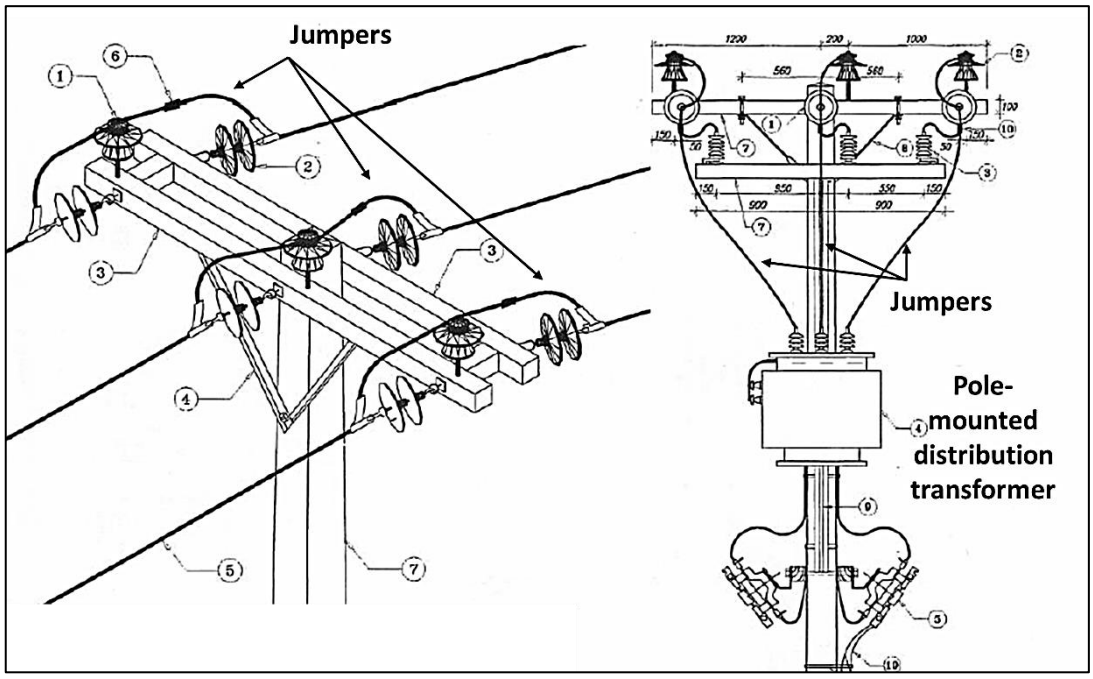

Figure 8.5: Intermediate pole connections and pole mounted transformer [105]

The robustness of the ANN based fault classification and location algorithms is tested by varying the length of Feeder 1 by ± 5% i.e. the length of Feeder 1 is changed to 28.5 km and 31.5 km in the simulations on the active distribution network (10.5 MW DFIG connected at end of Feeder 1). The already trained ANN based algorithms are then tested for different types of fault at various locations on Feeder 1. The output of the fault type classification algorithm for an ABC fault at 28.5 km on Feeder 1 with the length of Feeder 1 increased by +5% is shown in Figure 8.6.

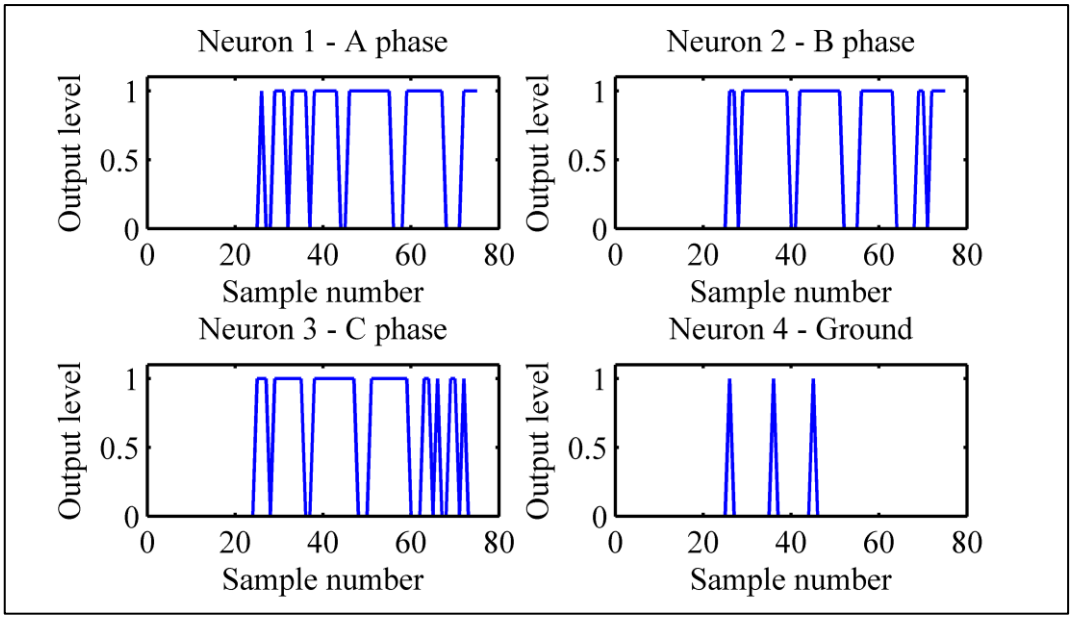

Figure 8.6: Output of fault classification algorithm for an ABC fault on Feeder 1 with an increase in length of Feeder 1 by +5%

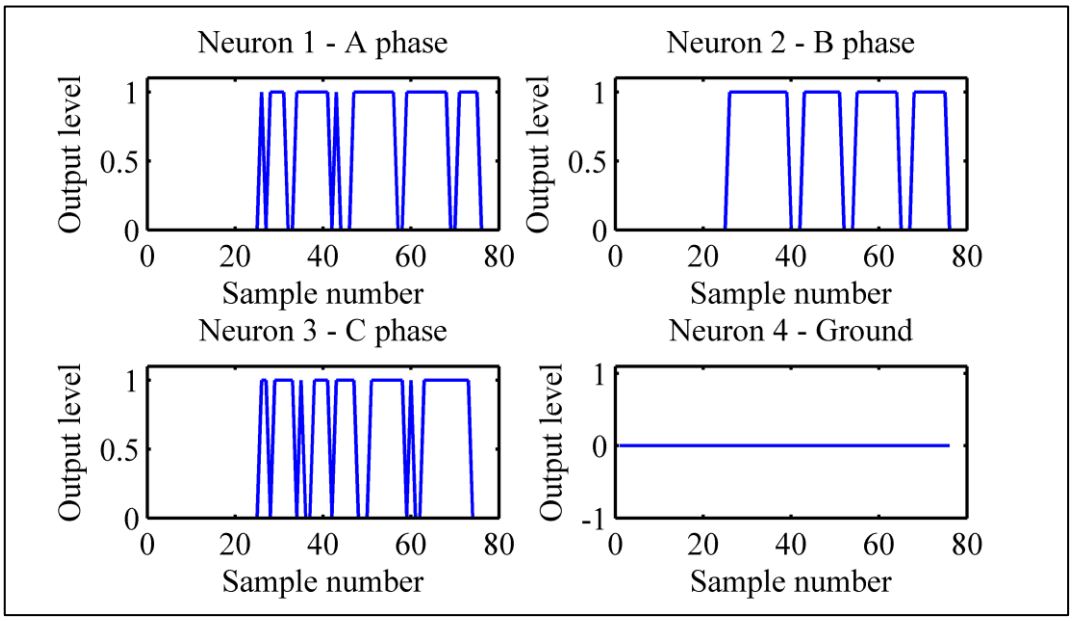

Figure 8.7: Output of fault classification algorithm for an ABC fault on Feeder 1 with a decrease in length of Feeder 1 by - 5%

It can also be observed that when the length of Feeder 1 is reduced by – 5%, i.e. actual length of Feeder 1 is now 28.5 km, the output of the fault classifier for an

ABC fault at 16.5 km on Feeder 1 remains accurate (Figure 8.7). The decision logic algorithms can clearly distinguish the short-circuit fault as a three phase fault.

The feeder/spur classification algorithms were able to correctly detect the various types of faults on Feeder 1 with a ± 5 % change in the length of Feeder 1. The output of the feeder/spur classification algorithm for an ABC fault at 28.5 km on Feeder 1 with a 5 % increase in line length is shown in Figure 8.8.

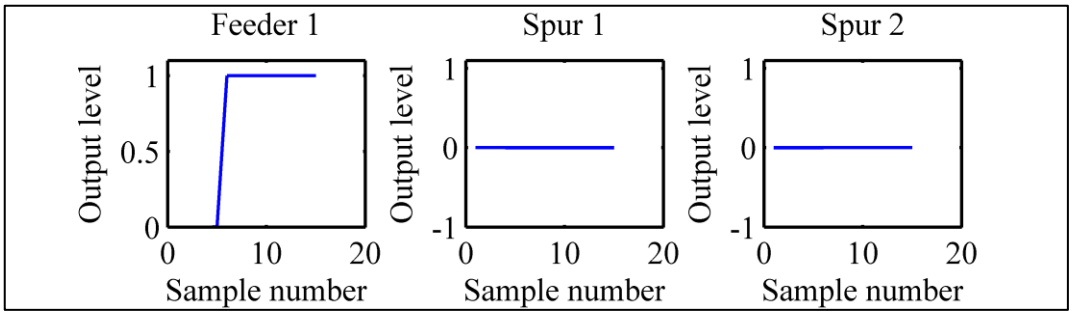

Figure 8.8: Output of feeder/spur classification algorithm for an ABC fault at 28.5 km on Feeder 1 an increase in length of Feeder 1 by +5%

The accuracies of the fault location algorithms for a single phase to ground fault, phase to phase fault, double phase to ground fault and three phase faults at various positions on Feeder 1 with a ± 5% change in the length of Feeder 1 are given in Table 8.1 to Table 8.4.

Actual distance/ km	**-5 % line length**		**+5 % line length**	
	Estimated distance/km	**%error**	**Estimated distance/km**	**%error**
0.5	1.0235	1.7	1.0377	1.8
16.5	16.3830	0.4	17.4183	3.1
28.5	29.8601	4.5	28.6986	0.7

Table 8.1: Accuracy of fault location algorithm for an AG fault on Feeder 1 for a change in length of Feeder 1

Actual distance/ km	-5 % line length		+5 % line length	
	Estimated distance/km	%error	Estimated distance/km	%error
0.5	1.0039	1.7	1.0039	1.7
16.5	19.4420	9.8	14.0645	8.2
28.5	29.9664	4.9	28.1238	1.3

Table 8.2: Accuracy of fault location algorithm for an AB fault on Feeder 1 for a change in length of Feeder 1

Actual distance/ km	-5 % line length		+5 % line length	
	Estimated distance/km	%error	Estimated distance/km	%error
0.5	1.0001	1.7	1.0010	1.7
16.5	16.1186	1.3	15.0022	5.0
28.5	28.6409	0.5	29.9228	4.7

Table 8.3: Accuracy of fault location algorithm for an ABG fault on Feeder 1 for a change in length of Feeder 1

Actual distance/ km	-5 % line length		+5 % line length	
	Estimated distance/km	%error	Estimated distance/km	%error
0.5	1.1245	2.1	1.1255	2.1
16.5	19.0654	8.9	18.9647	8.2
28.5	29.3752	2.9	29.9844	4.9

Table 8.4: Accuracy of fault location algorithm for an ABC fault on Feeder 1 for a change in length of Feeder 1

The results obtained show that the percentage error of the fault location algorithms increases with a change in the line length of Feeder 1. Previously, the accuracy of the fault location algorithms did not exceed 5% error for faults on Feeder 1. This error has now approximately doubled resulting in a ± 3 km error in estimating the distance to the point of fault due to a change in line length.

It has been observed that when the length of Feeder 1 was reduced to 28.5 km, the fault location algorithms give an over-estimate of the distance to the fault. The inaccuracies can be explained due to the change of impedance of the path to the point of fault. Although the accuracy of the fault location algorithms are affected by a change in line length, the difference between the actual line length and the simulated system would barely be around ± 1 % for a practical distribution network and the fault location algorithms would therefore still perform well.

8.4 Composite networks

The 33 kV typical UK distribution network has been modelled as an overhead line system for all feeders and spurs. In practice, part of the network may consist of underground cables. The electrical characteristics of underground cables are different from overhead conductors due to their mechanical construction. An overhead conductor is made up of a number of strands (usually of aluminium alloy) arranged in concentric layers and the arrangement of the conductor can vary depending on the current carrying capacity and the tensile strength required for the conductor (Figure 8.9).

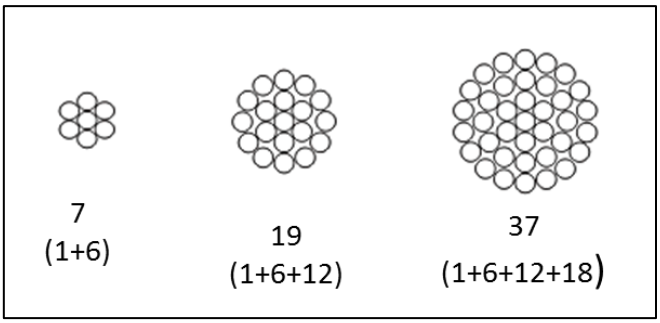

Figure 8.9: All Aluminium Alloy conductor (AAAC) arrangements

An underground cable consists of several components wrapped around a conductor (usually copper) as shown in Figure 8.10. The semiconductor screen around the copper conductor uniformly distributes the electric field lines around the conductor so that there is no concentration of electric field stress at any point around the conductor which can cause a fault on the cable. The insulation, cross-linked polyethylene, is used to insulate the conducting part from the metallic sheath which is grounded. The metallic sheath ensures that the electric field outside the cable is

zero and there is a path for zero-sequence currents to flow. A wire armour is present between the metallic sheath and the outer layer to protect the cable from any mechanical damage if the cable is directly laid in the soil.

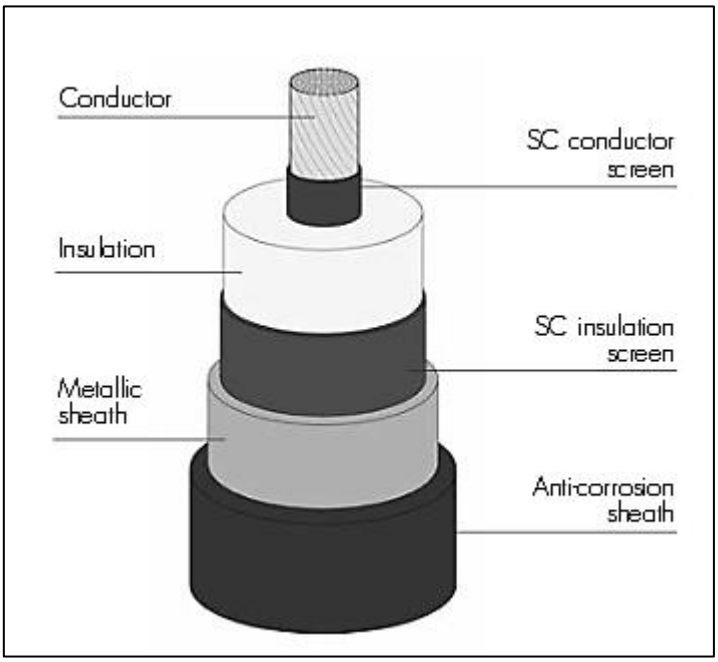

Figure 8.10: Single core underground cable components [106]

The various components affect the electrical characteristics of the underground cable. Firstly, the impedance per unit length of an underground cable is much smaller than that of an overhead line. The series inductance is much smaller but the shunt capacitance per unit length of the underground cable is much higher than that of an overhead line [107].

The performance of the ANN based fault classification and location algorithms have been tested by replacing the overhead line section 4-6 on Feeder 1 (6 km in length) by three single core 150 mm^2 underground cables. The electrical properties of a single core 150 mm^2 underground cable are given in Table 8.5 (see Appendix C for more details). In comparison to the electrical characteristics of the overhead line, the capacitance per unit length is nearly 170 times higher for the underground cable whilst its inductance per unit length is approximately half of that of the overhead line.

Electrical component	Positive sequence	Zero sequence
Resistance Ω/km	0.159	0.389
Inductance mH/km	0.47	0.233
Capacitance μF/km	0.191	0.191

Table 8.5: Electrical characteristics of 150 mm^2 single core underground cable

The type of fault that can occur in the underground cable section of the distribution network is a core to sheath fault. Therefore, an AG fault has been simulated at various positions in the underground cable with a fault inception angle of 0˚ and a fault impedance of 0Ω. Figure 8.11 depicts the output of the fault type classification algorithm for an AG fault at mid-point in the underground cable section. It is clear that the fault type can be easily determined from the output.

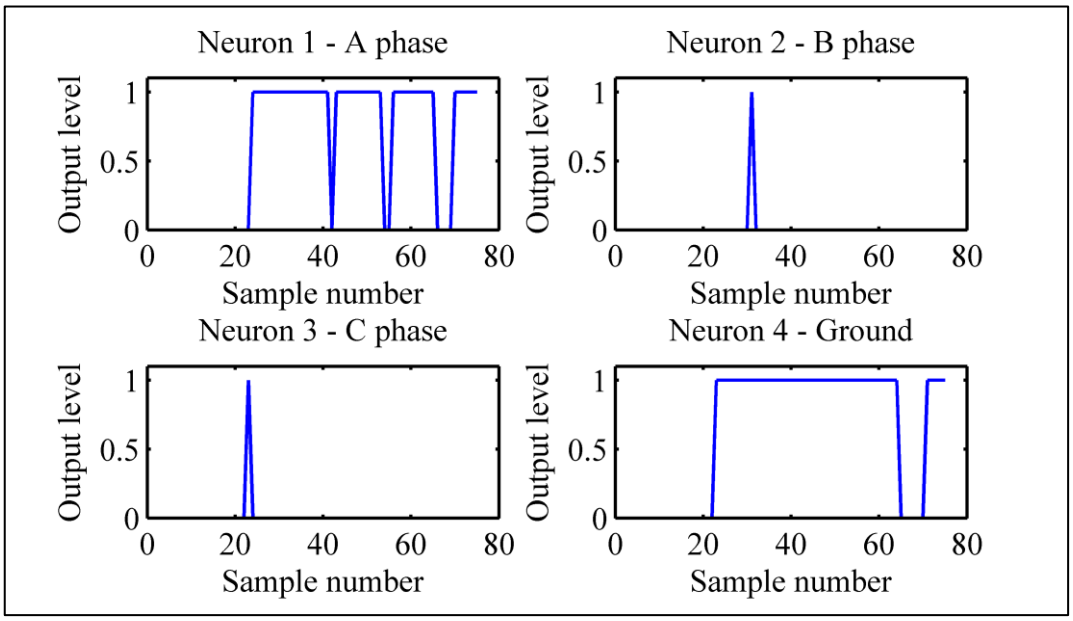

Figure 8.11: Fault classifier output for AG fault in underground cable

The feeder/spur classification algorithms are not influenced by the replacement of line section 4-6 by underground cables. The feeder/spur classification algorithm can accurately detect the fault in Feeder 1 as shown in Figure 8.12.

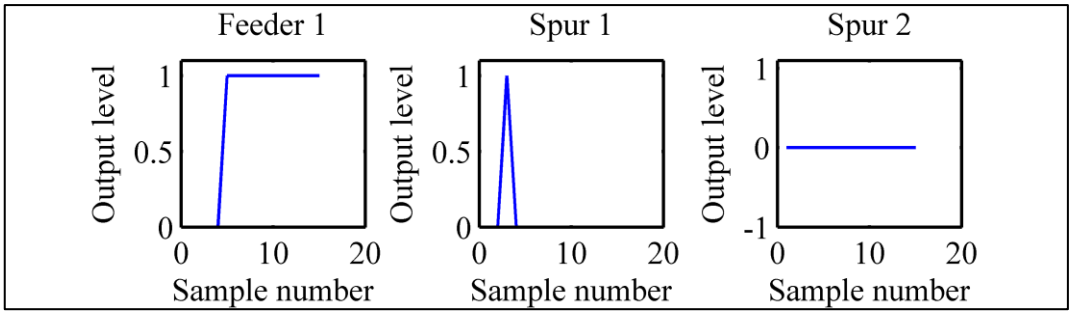

Figure 8.12: Detection of fault in Feeder 1 for AG fault in underground cable section

Table 8.6 gives the percentage errors for an AG fault at various positions in the underground cable.

Actual distance/km	Estimated distance/km	% error
25	26.5615	5.2
26	26.5197	1.7
27	26.8786	0.4
28	26.9676	3.4
29	26.8789	7.1

Table 8.6: Accuracy of fault location algorithm for an AG fault in the underground cable section of Feeder 1

It can be observed that the estimated distances are all around 26 km and the percentage error is around 7%. The accuracy of the fault location algorithm is therefore affected if part of the network is replaced by an underground cable section and a fault develops in this part of the network.

Further tests (Table 8.7 to Table 8.10) demonstrate the performance of the fault location algorithms for different types of faults in the overhead section of Feeder 1. The percentage error of the fault location algorithms is around 5 %, thus indicating that for faults occurring in the overhead line section of the network, the accuracy of the fault location algorithms is almost unchanged.

Actual distance/km	Estimated distance/km	% error
0.5	1.0081	1.7
2	2.3169	1.1
7	8.6982	5.7
13	13.2356	0.8
19	20.6457	5.5
23	21.9251	3.6

Table 8.7: Accuracy of fault location algorithm for an AG fault in the overhead line section of Feeder 1

Actual distance/km	Estimated distance/km	% error
0.5	1.0037	1.7
2	3.2210	4.0
7	7.6217	2.1
13	11.4418	5.2
19	17.8528	3.8
23	22.4876	1.7

Table 8.8: Accuracy of fault location algorithm for an AB fault in the overhead line section of Feeder 1

Actual distance/km	Estimated distance/km	% error
0.5	1.0010	1.7
2	1.1295	0.3
7	7.7799	2.6
13	11.5824	4.7
19	20.2705	4.2
23	22.4306	1.9

Table 8.9: Accuracy of fault location algorithm for an ABG fault in the overhead line section of Feeder 1

Actual distance/km	Estimated distance/km	% error
0.5	0.7364	0.8
2	1.8628	0.5
7	7.1210	0.4
13	13.1157	0.4
19	19.1784	0.6
23	22.5076	1.6

Table 8.10: Accuracy of fault location algorithm for an ABC fault in the overhead line section of Feeder 1

8.5 Effect of change in load

The load connected to a distribution network is not fixed. The variations in load are due to the fluctuating usage of electricity over the time of day. The ANN based fault classification and location algorithms have been trained for a fixed load capacity connected to the distribution network. It is therefore important to verify the extent to which the effect of a change in load can influence the accuracy of the developed algorithms. For this purpose, the load connected to Feeder 1 has been changed by ± 10%, ± 20% and ± 30%. Different types of faults have then been simulated at various locations on Feeder 1 to test the robustness of the ANN based fault classification and location algorithms.

The results confirmed that the fault type classification algorithm was able to accurately determine the type of fault on the system even with a load change of ± 30 %. Figure 8.13 shows the output of the fault classifier for an AG fault at 16.5 km on Feeder 1 with a fault inception angle of 90˚ and a fault impedance of 10 Ω for a +30 % variation in load.

The performance of the feeder/spur classification algorithms were also not affected by a change in load for different types of faults. Figure 8.14 illustrates the output of the feeder/spur classification algorithm for an ABG fault at 28.5 km on Feeder 1 with a fault inception angle of 90˚ and a fault impedance of 10 Ω for a – 30 % change in load.

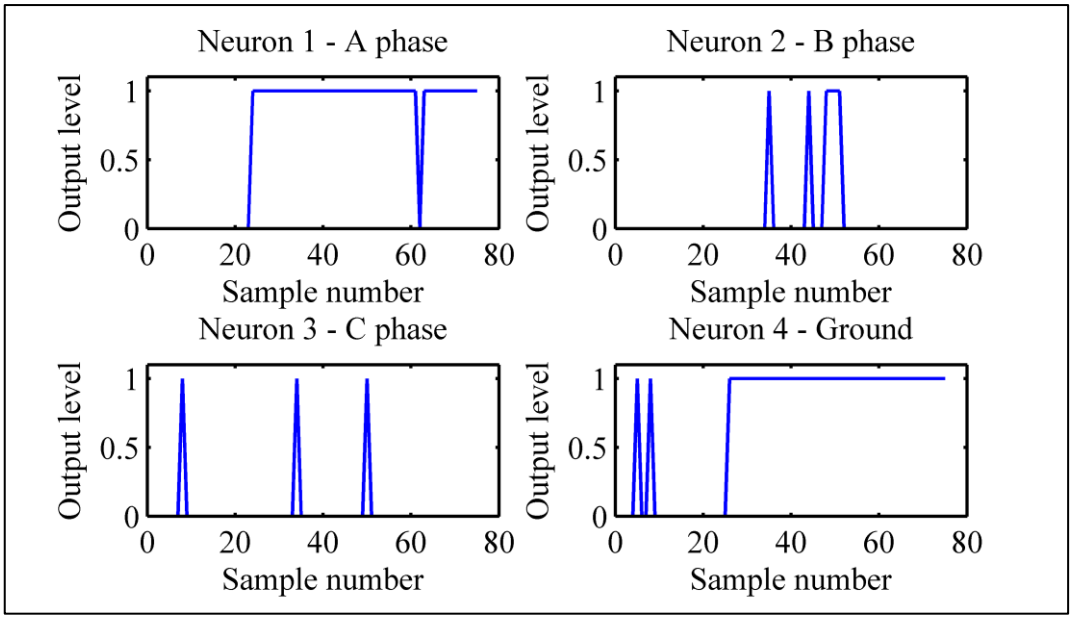

Figure 8.13: Fault type classification output for an AG fault on Feeder 1 with a 30 % increase in load

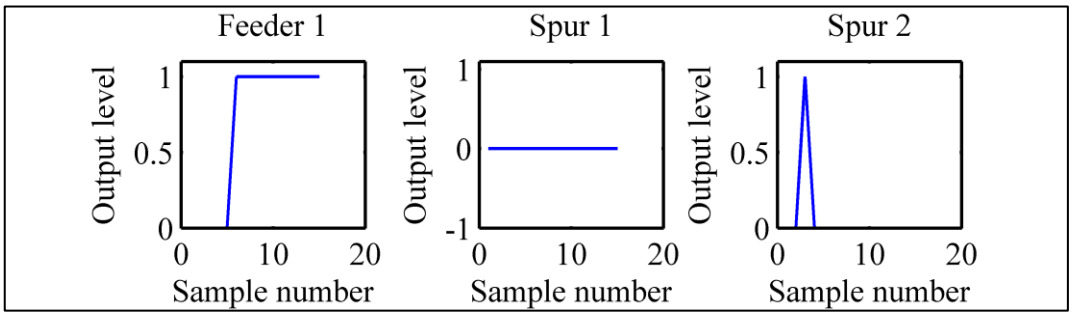

Figure 8.14: Feeder/spur classification algorithm output for an ABG fault on Feeder 1 with a 30 % decrease in load

The ANN based fault location algorithms have been tested for a change in load. Table 8.11 shows the percentage errors in distance estimation for an ABG fault on Feeder 1 with a fault inception angle of 90˚ and a fault impedance of 10 Ω for a ± 10% load variation. It can be observed that the percentage error increases for a 10 % increase in load while the algorithm is within its 5% error margin for a 10 % decrease in load. The increase in error is due to the increase in the pre-fault current and since the training data comprise of both pre-fault and post-fault information, this has an impact on the accuracy of the developed fault location algorithms.

Actual distance/ km	+10 % load		-10 % load	
	Estimated distance/km	%error	Estimated distance/km	%error
0.5	1.3461	2.8	1.0989	2.0
16.5	19.3230	9.4	15.0153	4.9
28.5	29.6605	3.9	28.1908	1.0

Table 8.11: Accuracy of fault location algorithm for an ABG fault on Feeder 1 with a ± 10% load variation

Actual distance/ km	+20 % load		-20 % load	
	Estimated distance/km	%error	Estimated distance/km	%error
0.5	1.3998	3.0	1.0411	1.8
16.5	20.8663	14.6	16.1862	1.0
28.5	29.8996	4.7	26.4834	6.7

Table 8.12: Accuracy of fault location algorithm for an ABG fault on Feeder 1 with a ± 20% load variation

Actual distance/ km	+30 % load		-30 % load	
	Estimated distance/km	%error	Estimated distance/km	%error
0.5	1.5927	3.6	1.0118	1.7
16.5	22.1883	19.0	20.0162	11.7
28.5	29.9785	4.9	25.9424	8.5

Table 8.13: Accuracy of fault location algorithm for an ABG fault on Feeder 1 with a ± 30% load variation

The accuracy of the fault location algorithm decreases with a larger variation in the load as can be observed from Table 8.12 and Table 8.13. The percentage errors for a ± 30 % change in load show a considerable impact on the accuracy of the fault location algorithm but the algorithm would still perform sufficiently well with a load variation of ±15 %.

As compared to the ANN based fault location algorithm for an ABG fault on Feeder 1, the fault location algorithm for an ABC fault on Feeder 1 behaved relatively better for a change in load of up to 30% with a percentage error of less than 5% (Table 8.14 to Table 8.16).

Actual distance/ km	**+10 % load**		**-10 % load**	
	Estimated distance/km	**%error**	**Estimated distance/km**	**%error**
0.5	0.7466	0.8	1.0989	1.0
16.5	16.5541	0.2	15.0153	1.0
28.5	28.0923	1.4	28.1908	3.1

Table 8.14: Accuracy of fault location algorithm for an ABC fault on Feeder 1 with a ± 10% load variation

Actual distance/ km	**+20 % load**		**-20 % load**	
	Estimated distance/km	**%error**	**Estimated distance/km**	**%error**
0.5	0.8187	1.1	0.7488	0.8
16.5	15.5561	3.1	16.2731	0.8
28.5	27.3910	3.7	28.0112	1.6

Table 8.15: Accuracy of fault location algorithm for an ABC fault on Feeder 1 with a ± 20% load variation

Actual distance/ km	**+30 % load**		**-30 % load**	
	Estimated distance/km	**%error**	**Estimated distance/km**	**%error**
0.5	0.8523	1.2	0.7488	0.9
16.5	15.5265	3.2	16.2731	0.6
28.5	27.2184	4.3	28.0112	2.2

Table 8.16: Accuracy of fault location algorithm for an ABC fault on Feeder 1 with a ± 30% load variation

The fault location algorithm for an ABC fault on Feeder 1 has 20 neurons in the hidden layer whereas the algorithm for an AG fault on Feeder 1 has only 16 neurons in the hidden layer. The training data set for an AG fault is larger than that for an ABC fault since it also includes training data for fault impedances of 0Ω, 25Ω and 50Ω. Therefore, the lower performance of the AG fault location algorithm can be attributed to insufficient neurons in the hidden layer. A better training performance can usually be achieved by increasing the number of neurons in the hidden layer of the Feedforward neural network. Another plausible explanation can be related to the training algorithm being stuck in a local minimum because the training was stopped before it could reach a global optimum.

8.6 Effect of source capacity

The 132 kV Grid is supplied by synchronous generators. A change in source capacity affects the behaviour of the synchronous generator during a short-circuit transient. The subtransient reactance is defined as the apparent reactance of the synchronous generator at the inception of a short-circuit fault when the machine is operating at its rated voltage under no load. It defines the short-circuit behaviour of the machine from the instant the fault occurs to a few cycles after the fault. The subtransient reactance, X_d'', is the ratio of the squared of the rms line to line voltage and the apparent short-circuit rating of the generator i.e.:

$$X_d'' = \frac{V_{L(rms)}^2}{S_{SC}} \qquad \text{Equation 8.1}$$

The variations of the subtransient reactance with a change in the short-circuit level of the 132 kV Grid are shown in Table 8.17.

% change	Short-circuit level/	X_d''/Ω
+20%	240	72.6
-20%	160	108.9
+50%	300	58.1
-50%	100	174.2

Table 8.17: Variation of subtransient reactance with source capacity

The results showed that there was no noticeable change in the accuracy of the fault type classification algorithm for various types of faults on Feeder 1 with a change in source capacity. Figure 8.15 depicts the output of the fault classifier for an AG fault at 28.5 km on Feeder 1 with a fault inception angle of 90˚ and a fault impedance of 10Ω for a -50 % in source capacity.

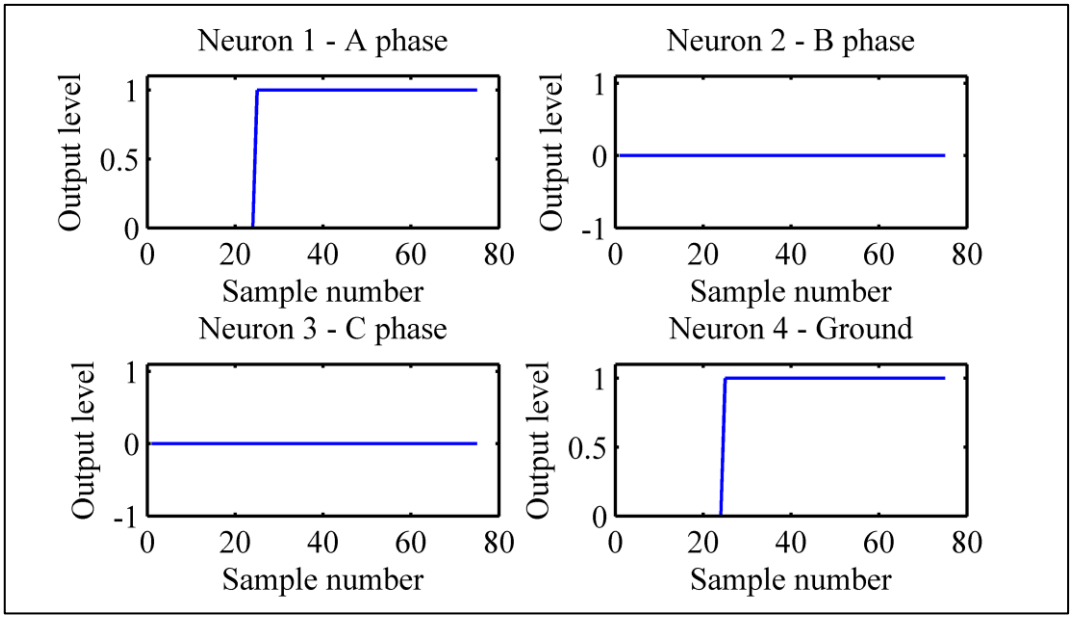

Figure 8.15: Output of fault classifier for an AG fault on Feeder 1 with a -50% change in source capacity

However, it was noticed that the accuracy of the feeder/spur classification algorithms were affected by the variation in source capacity. The algorithms were able to detect the fault on the feeder and spurs for a change of capacity of up to ± 20% only. For a higher change of ± 50%, it was no longer possible to detect whether the fault occurred on the feeder or the spurs.

Similar observations were made for the fault location algorithms. Table 8.18 gives the estimated distances at various locations on Feeder 1 for an AG fault with a fault inception angle of 90˚ and a fault impedance of 10Ω for a variation in source capacity of ± 20 %. It can be seen that the accuracy of the fault location algorithm is almost unaffected by the change in source capacity. In the case of an ABC fault (Table 8.19), the fault location algorithm demonstrates that it is robust for a change in source capacity of ± 20%.

When the source capacity was varied to ± 50% change, the estimated distances were all in the region of 30 km, thus showing that the limit of the fault location algorithms had been reached and they could no longer accurately estimate the distance to the point of fault.

Actual distance/ km	+20 % source capacity		-20 % source capacity	
	Estimated distance/km	%error	Estimated distance/km	%error
0.5	1.0000	1.7	1.0000	1.7
16.5	15.5725	3.1	18.0517	5.2
28.5	28.5307	0.1	28.2662	0.8

Table 8.18: Accuracy of fault location algorithm for an AG fault on Feeder 1 with a ± 20% variation in source capacity

Actual distance/ km	+20 % source capacity		-20 % source capacity	
	Estimated distance/km	%error	Estimated distance/km	%error
0.5	1.0100	1.7	1.0000	1.7
16.5	16.1933	1.0	16.7871	1.0
28.5	29.4384	3.1	29.7117	4.0

Table 8.19: Accuracy of fault location algorithm for an ABC fault on Feeder 1 with a ± 20% variation in source capacity

8.7 Effect of white noise

The outputs of the developed ANN based fault classification and location algorithms rely on the phase current measurements at the substation end of Feeder 1. In a real life application, measurement errors of these phase currents can occur due to unwanted random disturbances called white noise. White noise has a constant mean power per unit bandwidth at all frequencies. The signal to noise ratio can be calculated as the ratio of the signal power to the noise power i.e.:

$$Signal\ to\ noise\ ratio, SNR = \frac{P_{signal}}{P_{noise}} = \left(\frac{A_{signal}}{A_{noise}}\right)^2 \qquad \text{Equation 8.2}$$

Where A_{signal} is the root mean square value of the signal amplitude and $A_{noise}$is the root mean square value of the noise amplitude.

In decibel.

$$SNR\ dB = 10 \log_{10} \left(\frac{A_{signal}}{A_{noise}} \right)^2 \qquad \text{Equation 8.3}$$

The phase currents have been injected with additive white Gaussian noise of 40 dB and 60 dB to investigate the impact of noise on the accuracy of the developed ANN based fault classification and location algorithms as shown in Figure 8.16. As it can be seen, the amplitudes of 60 dB noise are smaller than 40 dB noise but as compared to the amplitude of the measured signal, they are both relatively negligible.

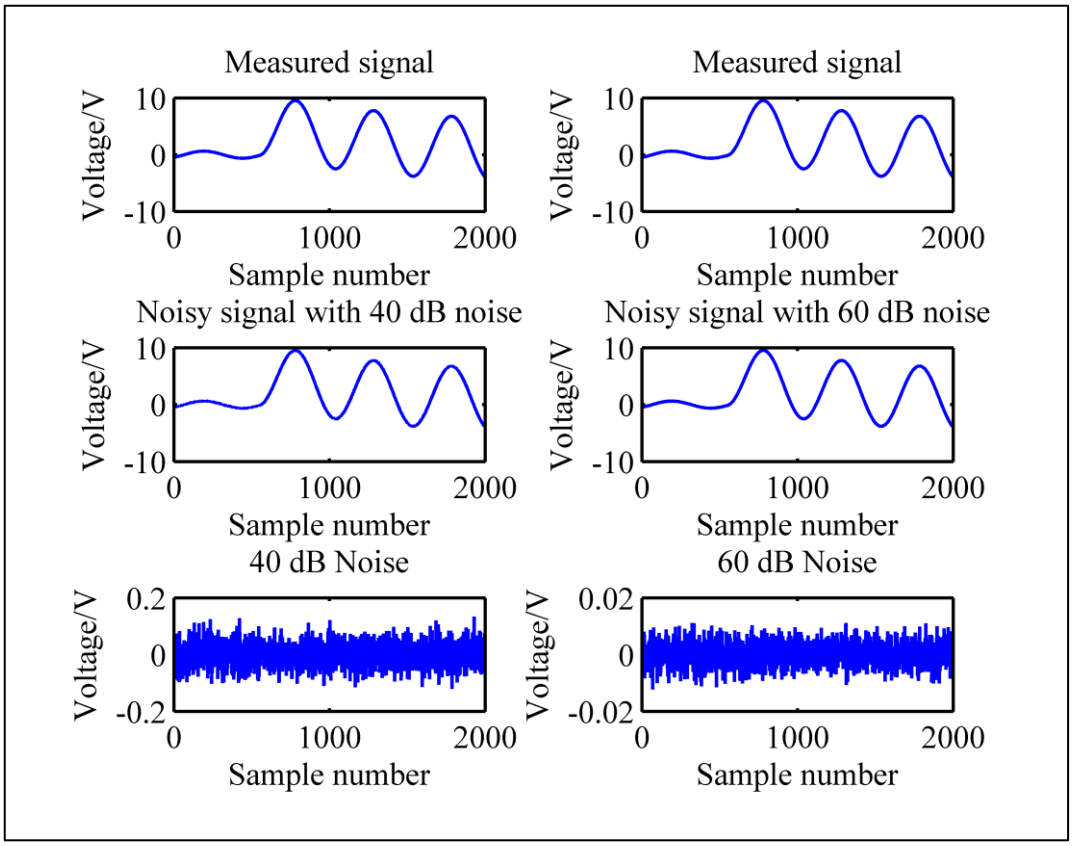

Figure 8.16: Additive white Gaussian noise injection to measured current signals after Analog to Digital conversion

The fault type classification algorithms were tested for different types of faults at various locations on Feeder 1 and Spur 1 with 40 dB and 60 dB with noise injection in the current signals. The results showed that the accuracy of the fault classification algorithm was not influenced by the white noise. Figure 8.17 illustrates the output of the fault classification algorithm for an ABC fault at 2.5 km on Spur 1 with 40 dB white Gaussian noise in the phase current signals. It was also observed that the output remains accurate even with a 60 dB noise level since the noise power at 60 dB is much less than that at 40 dB.

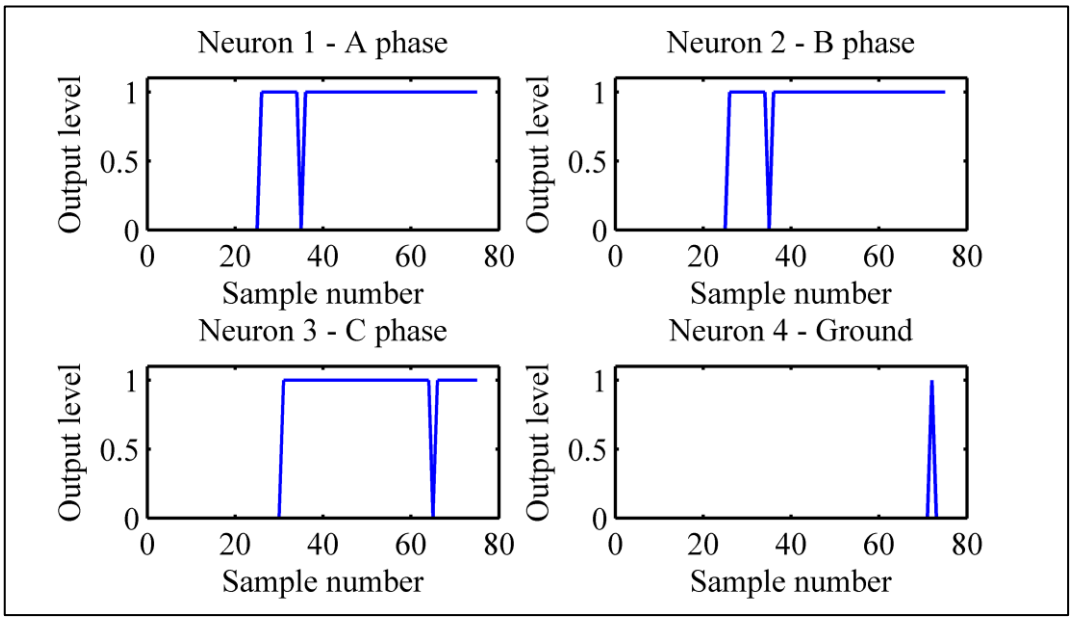

Figure 8.17: Output of fault classifier for an ABC fault at 2.5 km on Spur 1 with measured phase currents corrupted by 40 dB noise

The accuracy of the feeder/spur classification algorithms were also unaffected by the addition of white noise to the measured phase current signals. Figure 8.18 depicts the output of the feeder/spur classification algorithm for an ABC fault at 2.5 km on Spur 1 with 40 dB white noise. It can be observed that the algorithm can clearly detect the fault on Spur 1.

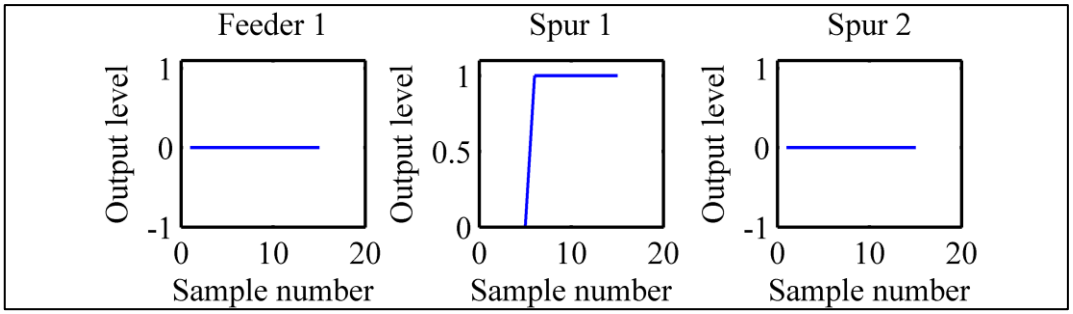

Figure 8.18: Feeder/spur classification algorithm for an ABC fault at 2.5 km on Spur 1 with 40 dB noise

The fault location algorithms were tested for different types of fault at various locations on Feeder 1 with a 40 dB white noise level in the measured phase current waveforms. Table 8.20 to Table 8.23 shows the estimated distances at various locations on Feeder 1 for different fault types.

Actual distance/km	Estimated distance/km	% error
0.5	1.1820	2.3
16.5	17.3748	2.9
28.5	29.0515	1.8

Table 8.20: Accuracy of fault location algorithm for an AG fault on Feeder 1 with 40 dB white noise

Actual distance/km	Estimated distance/km	% error
0.5	1.0001	1.7
16.5	15.8569	2.1
28.5	29.5585	3.5

Table 8.21: Accuracy of fault location algorithm for an ABG fault on Feeder 1 with 40 dB white noise

Actual distance/km	Estimated distance/km	% error
0.5	1.0039	1.7
16.5	17.2671	2.6
28.5	29.8926	4.6

Table 8.22: Accuracy of fault location algorithm for an AB fault on Feeder 1 with 40 dB white noise

Actual distance/km	Estimated distance/km	% error
0.5	1.0128	1.7
16.5	15.1379	4.5
28.5	29.9035	4.7

Table 8.23: Accuracy of fault location algorithm for an ABC fault on Feeder 1 with 40 dB white noise

The percentage errors in the estimation to the point of fault location are all below 5%, thus indicating that a white noise level of 40 dB has negligible impact on the accuracy of the ANN based fault location algorithms. A noise level of 60 dB also has a negligible impact on the estimated distances since the noise amplitudes at 60 dB are much smaller as compared to a noise level of 40 dB. Hence, it can be concluded that the fault location algorithms are robust.

8.8 Faults near boundary of Feeder 1 and Spur 1

The impedances of the overhead line sections are relatively small and the size of the intervals in the distribution network used for simulation of different types of faults on the system can have an impact on the accuracy of the feeder/spur classification algorithm to distinguish between faults near the boundary of a feeder and a spur. For homogeneous line sections, a fault on the feeder and spur just after the tap-off point will have the same impedance path as seen from the source.

In order to ascertain the robustness of the feeder/spur classification algorithms to faults near the tap-off point of a feeder and a spur, tests have been done at location A

(fault on Feeder 1) and B (fault on Spur 1) close to the junction between Feeder 1 and Spur 1 (Figure 8.19).

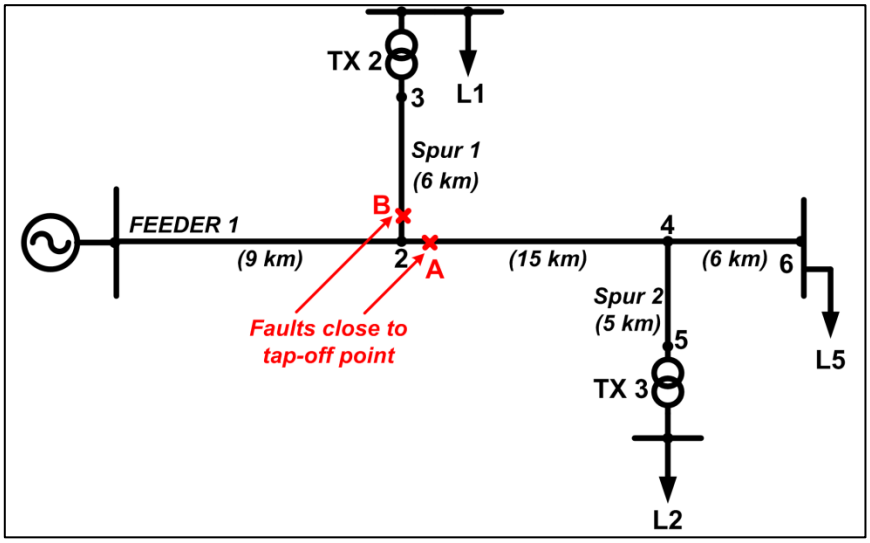

Figure 8.19: Faults near boundary of Feeder 1 and Spur 1

Single phase to ground faults and phase to phase faults were simulated at locations A and B, with both A and B placed at 30 m, 100 m and 500 m from the tap-off point of Spur 1 from Feeder 1. When A and B were placed at 30 m and 100 m from the tap-off point, the feeder/spur classification algorithms detected the faults on Feeder 1 and were unable to identify that B is actually on Spur 1.

However, when A and B were at 500 m from the junction between Feeder 1 and Spur 1, the feeder/spur classification algorithms were able to clearly differentiate between a fault on Feeder 1 and Spur 1. Figure 8.20 shows the output of the feeder/spur classification algorithm for an AB fault at 500 m on Spur 1.

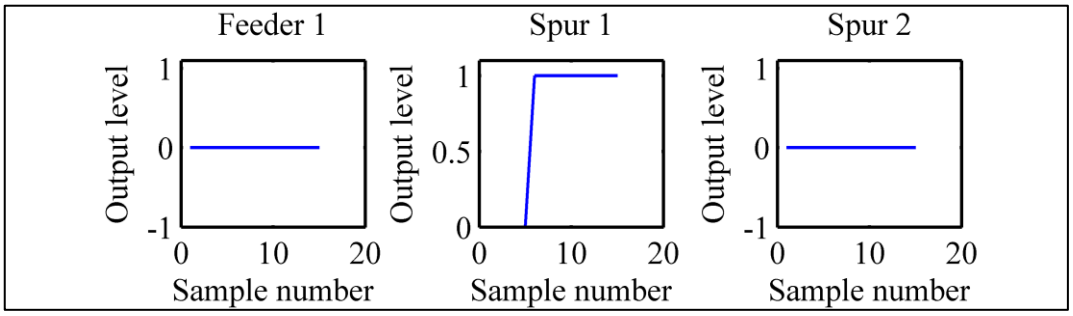

Figure 8.20: AB phase to phase fault at 500 m on spur 1

For faults exactly at the junction of Feeder 1 and Spur 1, the feeder/spur classification algorithms classify the fault as being located on Feeder 1. The accuracy of the algorithms can be improved by using a smaller distance interval, say 100 m, when populating the training data set.

8.9 Location of wind turbines

The assessment of the impact of wind turbine connections on the accuracy of the developed fault classification and location algorithms were performed by connecting a wind farm at the end of Feeder 1. It was observed that the short-circuit current with the wind farm connection was not different from that of a passive network. Analysis using the Discrete Wavelet Transform showed that mainly the amplitudes of the higher frequency components of the fault current signals were affected by the integration of wind turbine connections and overall, the fault location algorithms remained accurate.

However, the location of the wind farm connection on the distribution network can have an impact on the accuracy of the fault location algorithms. This has been investigated by relocating the 10.5 MW DFIG wind farm to the end of Spur 1 and initiating a fault at 12 km on Feeder 1, just downstream of both the source from the substation and the wind farm as shown in Figure 8.21.

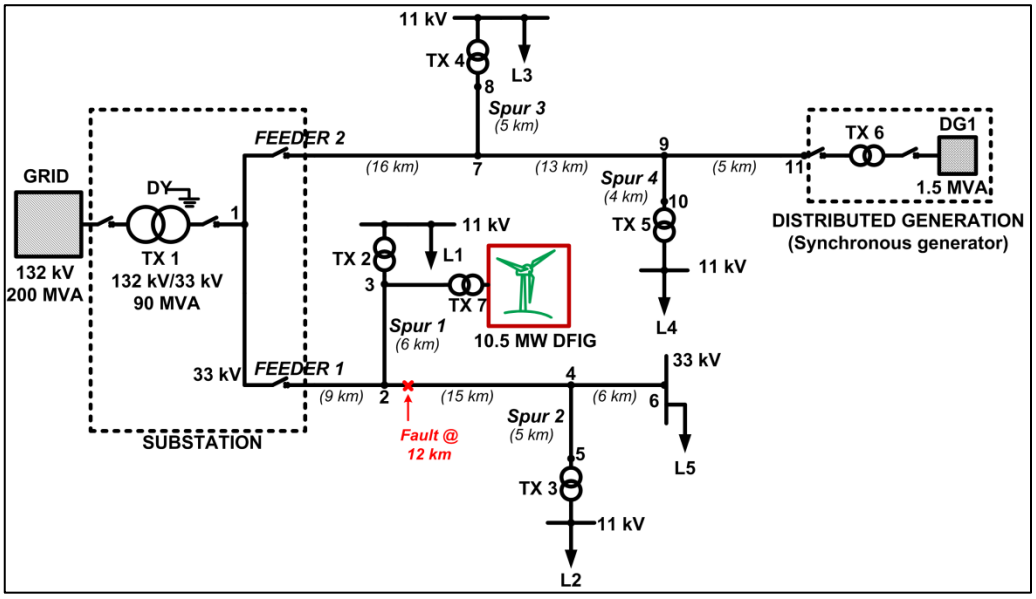

Figure 8.21: Wind farm relocated to end of Spur 1

Different types of faults (AG, AB, ABG and ABC) were simulated at 12 km on Feeder 1 and the various feeder/spur classification and fault location algorithms were tested. The accuracies of the feeder/spur classification algorithms were affected by the change in location of the wind farm and in most cases, they were unable to classify the fault as occurring on Feeder 1.

The inaccuracies can be explained by comparing the DWT analysis of the fault current for a wind farm located at the end of Feeder 1 and the wind farm relocated to the end of Spur 1. Figure 8.22 shows the DWT analysis of the A phase for an AG fault at 12 km on Feeder 1 occurring at voltage minimum with a fault impedance of 0Ω.

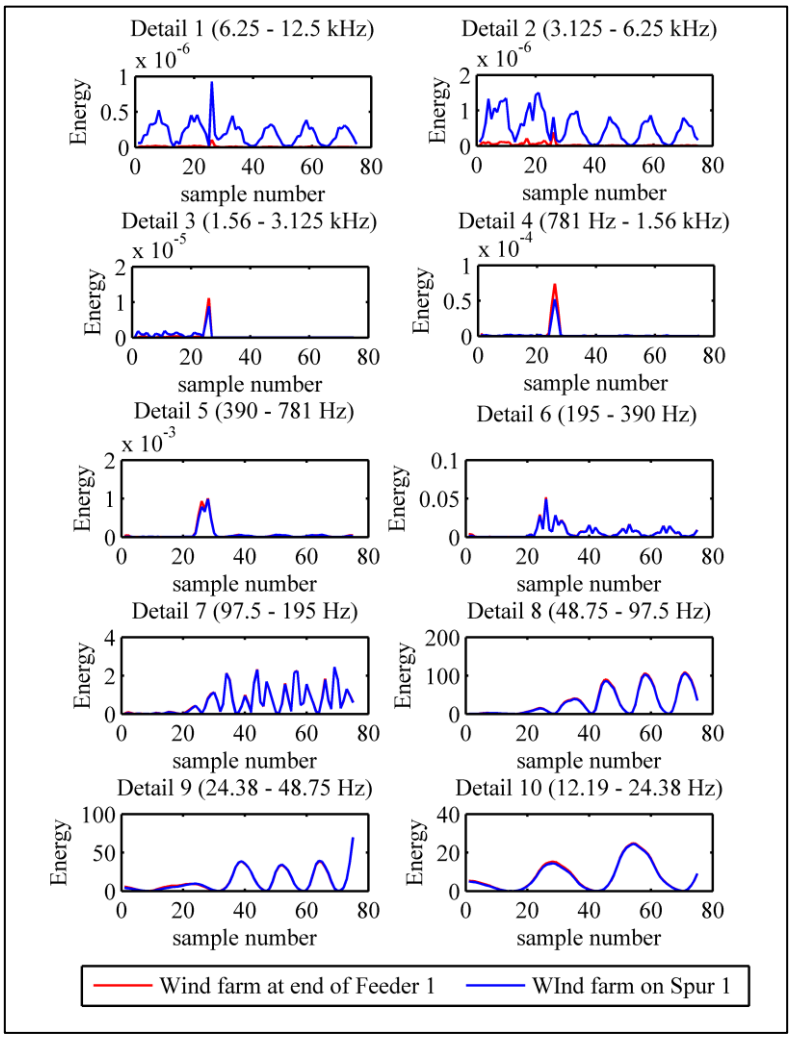

Figure 8.22: Comparison of detailed components for wind farm at different location

It can be observed that the amplitudes of the higher frequency components for the wind farm connected at the end of Spur 1 are much higher than those with the wind farm connected at the end of Feeder 1 after the point of fault inception. It can also be noted that the pre-fault energies for the high frequency components with the wind farm connected on Spur 1 are also considerably higher. The amplitudes of the lower frequencies are almost identical both pre-fault and post-fault. Therefore, it can be concluded that the location of the wind turbine has an impact on the pre-fault and post-fault amplitudes of the higher frequencies which influence the accuracy of the fault location algorithms.

8.10 Summary

In this chapter, the robustness of the developed ANN based fault classification and location algorithms have been thoroughly investigated by performing various sensitivity tests. Overall, it has been observed that the type of fault can be easily detected by the fault classification algorithm and the feeder/spur classification algorithms were able to accurately detect the faulted section of the network. The fault location algorithms were within their acceptable 5% accuracy for Feeder 1 and 8% accuracy for Spur 1 in most cases.

Chapter 9: Conclusion

9.1 Thesis summary

This thesis investigates a novel Artificial Neural Network based method of short-circuit fault location in overhead distribution networks using fault induced current transients measured at the substation end. The method is divided into three stages to ensure higher accuracy and better robustness to factors that can affect the determination of the point of fault in real systems. The first stage identifies the type of fault on the system which then initiates the second stage to detect the faulted section in the network i.e. feeder or spur. Finally the last stage computes the distance to the point of fault on the feeder/spur. A rigorous analysis of the impact of wind turbine connections through power electronic converters to the distribution network is also performed using the Discrete Wavelet Transform. Finally, a series of sensitivity tests is performed to ascertain the accuracy of the developed approach to fault location.

Outages in an electrical distribution network cause interruption of supply to the customers and thus influence the system performance indices such as the system average interruption duration index (SAIDI) and the system average interruption frequency index (SAIDI). A loss of supply entails a loss of revenue for distribution network companies and hence a loss of profit. Chapter 1 puts into context the scope of this thesis by explaining the importance of fault location in distribution networks and discussing about the current ways of detecting and clearing outages in a real system by power system engineers. It also highlights the complexities in performing accurate fault location due to the nature of distribution networks and sets out the aims of this thesis.

Chapter 2 provides a thorough review of the different types of fault location methods applied to electrical distribution networks in the past. It classifies the methods into five main categories namely knowledge based methods, impedance based methods, travelling wave techniques, signal injection and hybrid methods. The principles of operation of each technique are explained and their limitations discussed. This

chapter is essential to grasp the basic concepts of fault location applied to distribution networks and also to formulate a new approach to tackle the problem.

The impact of wind turbine connections on the accuracy of the proposed ANN based fault classification and location algorithms is an important investigation in this thesis and as such Chapter 3 introduces the basic concepts of generating electricity from the wind. Fixed speed and variable speed wind turbine technologies are briefly discussed before rapidly embarking on power control strategies to capture wind energy. Wind turbines can have various configurations and they are generally classified as Type A, Type B, Type C and Type D systems. A detailed investigation of the short-circuit current contribution of these different types of wind turbine configurations is given in comparison to synchronous generators. A market survey quickly identified that Type C (doubly-fed induction generator) and Type D (permanent magnet synchronous generator) are the preferred configurations adopted by wind turbine manufacturers. Hence, this thesis focuses exclusively on the short-circuit contribution of these two types of wind turbine configuration connected to the network through power electronic converters.

The aim of this thesis was to develop an accurate fault location algorithm for a distribution network with feeders and spurs with the integration of wind turbine connections into the system. Therefore, Chapter 4 demonstrated how a typical 33 kV distribution network with feeders and spurs was set up in the MATLAB/Simulink environment. The line parameters and transformer configurations were obtained from reports of UK distribution network companies. This network enabled different types of faults to be simulated at various locations on the feeders and spurs in order to gather enough information to develop the ANN based approach to fault location. The full-scale models of Type C (DFIG) and Type D (PMSG) wind turbines in Simulink were presented and explained. Simulations from these types of wind turbine configurations were also validated against simulation results obtained from wind turbine manufacturers. The signal conditioning stage present in all real world application before processing by a digital relay were presented and applied to the simulated phase current waveforms.

Chapter 5 briefly introduces the Discrete Fourier Transform, the Short-Time Fourier Transform and the Discrete Wavelet Transform as advanced signal processing tools for feature extraction from the simulated fault current waveforms. The limitations of the Discrete Fourier Transform and the Short-Time Fourier Transform as compared to the Discrete Wavelet Transform for feature extraction are highlighted. The Discrete Wavelet Transform has been chosen for feature extraction since it is more suitable for non-periodic waveforms (short-circuit transients are non-periodic) and offers better resolution in both the time and frequency domain. The results obtained after the analysis of the phase current signals for different types of faults using the Discrete Wavelet Transform are then presented.

The origin of the Artificial Neural Network and its suitability for fault location in distribution networks are discussed in Chapter 6. The basic principles of the artificial neuron, the building block of more complex Artificial Neural Networks, are explained. The architectures of the fault classification algorithm, the feeder/spur classification algorithms and the fault location algorithms are then presented. Since all of the ANN based algorithms are trained using supervised learning, details about the training data set, scaling of the inputs before training, the activation functions and the target outputs are given. The performance of the developed algorithms for a conventional distribution network is also verified by varying the fault position, fault inception angle and fault impedance for different types of faults.

In Chapter 7, the impact of wind turbine connections on the features present in the short-circuit fault current waveforms is investigated. The analysis is carried out for both wind turbine type (DFIG and PMSG) and an increase in wind turbine capacity. The impact of wind farm connection on the accuracy of the developed fault classification and location algorithms is also evaluated.

Finally, Chapter 8 presents the rigorous testing of the ANN based fault classification, feeder/spur classification and fault location algorithms. In a practical system, the topology of the distribution network can change due to maintenance work or an outage in part of the network and thus the importance to verify the sensitivity of the developed algorithms to such a scenario. Furthermore, the exact length of a distribution network is not known and typical distribution networks often comprise

of sections of overhead lines and underground cables which can introduce errors in detecting and locating the faults with accuracy. Other factors such as the total load connected to the network, the source capacity and the effect of white noise can also influence the performance of the developed algorithms. Therefore, it is of utmost importance to verify the extent to which the ANN based fault classification and location algorithms are affected by the above mentioned factors so as to ascertain their accuracy and substantiate their robustness.

9.2 Discussions

The fault signatures in the measured phase current signals at the substation end have been extracted using the Discrete Wavelet Transform. It has been observed that for the high frequency components (781 Hz to 12.5 kHz), a spike is detected at the point of fault inception on the faulted phase irrespective of the type of fault. The energies of the high frequency components for all three phases are zero for a pre-fault condition. The energies of the healthy phases are generally zero for the healthy phases except for single phase to ground faults and double phase to ground faults where a spike of lower energy amplitude as compared to the faulted phase/s can also be detected. This can be a result of the coupling between the phases due to the ground return path.

For low frequency components (12.19 Hz to 781 Hz), a sinusoidal disturbance is observed after the point of fault inception on the faulted phase while the energies on the healthy phases remain zero. The amplitudes of the lower frequency components are much higher than that of the high frequency components and thus they have to be scaled when used together so that the training of the ANN based algorithms are not biased towards the low frequency components. The high frequency components are suitable for fault type classification since they can detect precisely when in time the fault occurred on the system whilst all 10 detail components are suitable for feeder/spur classification and fault location.

The integration of wind farms (10.5 MW DFIG wind farm and a 10 MW PMSG wind farm) into the distribution network has an impact on the amplitudes of the high frequency components but no noticeable change can be observed in the low frequency components. In fact, it has been noted that changing the type of wind

turbine configuration whilst keeping the wind farm capacity constant only affects the amplitudes of the high frequency components. The same observation has been made for an increase in wind farm capacity of 4.5 MW for the DFIG wind farm and of 6 MW for the PMSG wind farm. In my opinion, these observations can be explained by the fact that both the Type C and Type D wind turbines export power to the distribution network through power electronic converters which employ similar power control strategies.

The fault type classification algorithm, the feeder/spur classification algorithms and the fault location algorithms have all been tested for various types of faults on the system. The fault classifier has four outputs each representing the A phase, B phase, C phase and ground G. The results obtained showed that a change in fault inception angle (Θ=45˚) and fault impedance (10Ω and 35Ω) do not affect the determination of the type of fault on the system. In fact, the accuracy of the fault type classification algorithm remains unchanged for all of the sensitivity tests performed in Chapter 8. The feeder/spur classification algorithms have three outputs each namely Feeder 1, Spur 1 and Spur 2. These algorithms are also unaffected by a change in fault inception angle and fault impedances for different types of fault on the distribution network. The same tests also demonstrated that the fault location algorithms have a percentage error of less than 5% i.e. ± 1.5 km for locating faults on Feeder 1 and a percentage error of less than 8% i.e. ± 480 m for locating faults on Spur 1. These percentage errors are acceptable given the complexities associated with electrical distribution networks and the fact that the feeder/spur classification algorithms are able to detect the fault section of the network using only phase current measurements at the substation end only is already a commendable achievement.

The ANN based fault classification and location algorithms have all been trained with data for a passive distribution network and an active distribution network with a 10.5 MW DFIG connection. New test data have been obtained by replacing the 10.5 MW DFIG wind farm with a 10 MW PMSG wind farm and simulating fault at various locations on the distribution network. The results obtained showed that the feeder/spur classification and fault location algorithms were not affected by this change in wind turbine type. The feeder/spur classification algorithms were able to detect faults on Feeder 1 and Spur 1. The estimated distances for the fault location on

Feeder 1 were still within the 5% error margin and those for Spur 1 were still within the 8% error margin. An increase in wind farm capacity does not influence the detection of the fault on the feeder or spurs but the percentage error in fault location for Feeder 1 and Spur 1 slightly increased. An increase of around 1% was observed in the fault location error of both Feeder 1 and Spur 1.

The topology of a distribution network can change mainly due to preventive maintenance being carried out on a specific section of the network or part of the network has been disconnected from the healthy section to undergo repairs due to a permanent fault. This change in network topology can lead to erratic behaviour particularly in the feeder/spur classification algorithms since they are critical to determine the fault location. In the experiment, Spur 1 was disconnected from Feeder 1 and different types of fault were simulated on Feeder 1 and Spur 2. The fault type classification algorithm was able to determine the type of fault on the system. However, the feeder/spur classification algorithms were unable to detect whether the fault occurred on Feeder 1 or Spur 2. The determination of the fault on the feeder/spur is a crucial step for the success of accurately estimating the distance to the point of fault. A possible solution to handle such situations in a real system is to train several sets of ANN based feeder/spur classification algorithms for different network configurations.

The exact length of an overhead distribution line is not known and therefore can lead to errors in estimating the distance to the point of fault. The length of the line has a tolerance value and can be more than the distance used in simulations because in a real system, jumpers are usually utilised to connect lines of the same phase together or to connect distribution transformers to the network. Sagging is not a significant issue in distribution networks since the span between poles is normally around 30 m. In order to investigate the impact of a change in line length, the length of Feeder 1 has been varied by ± 5% i.e. a change of ± 1.5 km. The feeder/spur classification algorithms were not influenced by a change in line length and were able to classify faults on Feeder 1 and Spur 1. However, the change in line length nearly doubled the percentage error for fault location in Feeder 1 thus giving a ± 3 km error in distance estimation on the feeder. In my opinion, the ± 5% change in line length is too high

for a practical system and a more reasonable change is a few hundred metres since the length of a jumper is approximately 1m.

The training data for the ANN based fault classification and location algorithms have been obtained by simulating fault on an overhead distribution line. A real system is in practice a composite network consisting of both overhead lines and underground cables. The electrical characteristics of underground cables differ from overhead lines mainly due to the mechanical construction of underground cables. As such, underground cables have a lower inductance per unit length as compared to overhead conductors but they have a significantly higher shunt capacitance than overhead lines. For this experiment, line section 4-6 on Feeder 1 was replaced by three single-core 150 mm^2 XLPE underground cables. Different types of faults were simulated in the overhead line section of Feeder 1 and the ANN based algorithms tested. The feeder/spur classification algorithms were able to detect the fault on Feeder 1 and the accuracy of the fault location algorithms remained accurate with a maximum percentage error of about 5% on Feeder 1. Single phase to ground faults (AG) were also simulated at various locations in the cable section since the type of fault that can occur in a single core underground cable is from the core to the sheath. The feeder/spur classification algorithm for an AG fault was able to detect the fault in Feeder 1. However, the percentage error increased to around 8%.

The total load connected to the distribution network depends on the time of day and therefore it is essential to test the robustness of the algorithms with a change in load. The changes in load were taken as ± 10%, ± 20% and ± 30% respectively. The performance of the feeder/spur classification algorithms were not affected by a change in load of up to 30%. The percentage errors of the fault location algorithms increased with a change in load. However, it was observed that the fault location algorithm for an ABC fault was relatively not affected for a change in load. At closer inspection, the ANN fault location algorithm for an ABC fault has more neurons in the hidden layer as compared to that for an ABG fault. Therefore, a lower performance of the fault location algorithm for an ABG fault can be attributed to the fact that insufficient neurons are present in the hidden layer. Moreover, the training performance of the ABC fault location algorithm was better than the ABG algorithm which indicates the possibility that the training algorithm for the ABG fault was

stopped too early when it was stuck in a local minimum and had not yet reached its global minimum.

The source capacity can have an impact on the accuracy of the ANN based fault classification and location algorithms. A change in source capacity affects the subtransient reactance of a synchronous generator and the subtransient reactance defines the behaviour of the short-circuit transient for a few cycles after the fault inception. The results obtained showed that the accuracy of the feeder/spur classification algorithms and the fault location algorithms were not affected by a change of source capacity of up to ± 20 % i.e. a ± 40 MVA change. However, a change of ± 50% in source capacity caused the mal-operation of the feeder/spur classification algorithms and the fault location algorithms.

In real life applications, white noise present in the external environment can corrupt the measurements of the input signals and thus influence the accuracy of the ANN based fault classification and location algorithms. White Gaussian noise of 40 dB and 60 dB has been added to the measured current signals at the substation to evaluate their impact on the developed algorithms. It has been observed that the amplitudes of the white noise as compared to the measured signals are relatively insignificant and the accuracy of the ANN based fault classification, feeder/spur classification and fault location algorithms are unaffected by a white noise level of 40 dB (noise power for 40 dB is more significant than 60 dB).

Faults close to the boundary of the feeder and the spur can cause errors in determining the location of the fault and the developed fault location algorithms are only capable of differentiating between a fault on the feeder or spur if the fault is located at 500 m from the tap-off point. The accuracy can be improved by simulating faults at shorter intervals on the feeder and re-training the algorithms.

Overall, it has been confirmed that ANN based fault location in a distribution network with feeders and spurs using current signals measured only at the substation end is indeed possible. The type of wind turbine configuration and wind turbine capacity affect only the high frequency components in the fault current signal. The range of sensitivity tests demonstrate that the accuracies of the fault type classifier,

the feeder/spur classification algorithms and the fault location algorithms are mildly influenced by various system parameters thus substantiating the fact that these algorithms are robust and can be deployed in practical systems. However, the system topology can have a significant impact on the performance of the feeder/spur classification algorithms for which a set of ANN algorithms for different network topologies have been suggested as a possible solution.

9.3 Major contributions

Fault location in a distribution network is a difficult task due to the presence of feeders and spurs, the small impedances of the line sections and the non-homogeneity of the lines. The load current flowing through the conductors also changes with time of day and the season of the year and this also adds to the complexity of the whole fault location process. Several techniques of fault location such as impedance based methods, travelling wave methods and Artificial Intelligence methods, have been applied to distribution networks in the past and their major drawback is their inability to differentiate between a short-circuit fault on the feeder and a spur. My proposed method ensures that it is possible to distinguish between a fault on the feeder or the spur.

The proposed method relies on the extraction of distinct features i.e. a set of data that characterise a particular type of short-circuit fault at a given location, using the Discrete Wavelet Transform and then use this training set of data to train a series of Artificial Neural Network algorithms to determine the location of the fault in the feeder or spur. The Discrete Wavelet Transform is applied to a window of the measured fault current signal, i.e. 1 cycle pre-fault and 2 cycles post-fault, to extract the spectral energies of the frequency components present in the fault current waveform during the fault. Other methods such as the impedance based methods use only the fundamental frequency component of the current and voltage and as such discard all important information contained at other frequencies that can characterise a fault.

The fault location process has been divided into three stages to prevent the occurrence of multiple fault positions. Instead of estimating the distance to the point of fault and then trying to eliminate some of the possible fault locations, the proposed

method firstly identifies the type of short-circuit fault on the system before enabling the desired feeder/spur classification algorithm. This ensures that the faulted section of the network (feeder or spur) is correctly identified prior to estimating the distance to the point of fault.

Nowadays, more and more renewable generation plants are integrated into distribution networks and it is important to test any fault location technique for inaccuracies that can arise due to the active nature of the network. In the literature review, it was noted that most researchers model a doubly-fed induction generator wind turbine or a permanent magnet synchronous generator wind turbine by a voltage source behind a subtransient reactance. Although this is an appropriate representation of a synchronous generator for most short-circuit fault studies, the DFIG or PMSG wind turbine systems behave more like a controlled current source due to the power electronic converters. Hence, in this thesis, detailed models (complete model of power electronic circuits) of both the DFIG and PMSG wind farms have been used to analyse the impact of wind turbine integration on the accuracy of the fault location algorithms.

In the literature review, it was also noted that, in general, researchers only test their fault location algorithms for changes in fault inception angle, fault impedance and source capacity before claiming the robustness of their proposed methods. In practice, a lot more tests have to be carried out to ascertain the robustness of the fault location method and therefore, a wider range of tests were carried out to assess the proposed method developed in this thesis. The practicality of the proposed fault location method was investigated by considering the effect of a change in network topology, the presence of overhead lines and underground cables, a load change, faults close to the boundary between a feeder and spur and last but not the least, the location of the wind farm in the distribution network.

Overall, the major contributions of this thesis address most, if not all, of the short-comings of previous methods and the proposed method has been carefully developed to overcome any issues that can occur when the fault location algorithm is deployed in a real distribution network.

9.4 Future works

In this thesis, it has been verified that an ANN based approach to fault location in distribution networks using only current signals measured at the substation end is achievable, given the inputs to the ANN algorithms are correctly selected and the algorithms trained properly. Although it has been demonstrated that the proposed method works on this particular network configuration, it was observed that network topology can hinder the operation of the feeder/spur classification algorithm and thus jeopardise the whole process of accurate fault location. Therefore, further tests need to be performed to assess the robustness of the developed algorithms before they can be commercially viable.

Perhaps, the first task is to train another set of feeder/spur classification algorithms for different network configurations such as loss of Spur 1, loss of Spur 2 and loss of both spurs. These algorithms can then be tested to verify their robustness for different types of faults on the system. The typical UK 33 kV distribution network consisted of only 2 spurs connected per feeder. The system was relatively simple but yet complete and practically accurate to develop and test the proposed solution. It is therefore desirable to apply the proposed fault location approach to a larger system consisting of more spurs per feeder to further assess the performance of the ANN based fault classification, feeder/spur classification and fault location algorithms. Also, it will be interesting to verify the performance of the feeder/spur classification algorithm for a scenario where two spurs tap-off at the same point on the feeder and for the algorithm to work, a smaller distance interval, say 100 m, may be considered where simulating short-circuit faults for training.

In the proposed method, it is assumed that relays at substations are capable of storing high resolution data during fault transients but not all substations are equipped with microprocessor relays that have an event recording function. This can be an added cost to utilities wanting to implement the fault location algorithms onto their system. Also, microprocessor relays for feeder protection usually employ a sampling rate of up to 80 samples per 50 Hz cycle and the proposed method relies on a high sampling frequency of 500 samples per cycle. Some protection relay manufacturers, like SEL, offer digital fault recording capability with a sampling frequency of 8 kHz [108] and

therefore it is recommended to investigate the development of fault location algorithms with a sampling frequency of up to 8 kHz.

The window length used for feature extraction was made up of 1 cycle pre-fault and 2 cycles post-fault. The pre-fault current values are usually affected by a change in load or wind turbine connection and as such influence the accuracy of the fault location algorithms. It is therefore recommended to develop new fault location algorithms based on features extracted over a window length of 1 cycle post-fault. This can improve the robustness of the fault location algorithms to changes in load and wind farm connections. The digital fault recording functionality of microprocessor based relays are also often triggered after fault inception and choosing 1 cycle post-fault will improve the practicality of the method. Also, since it was observed that the integration of wind farms, irrespective of location in the network, mainly influences the high frequency components (1.56 kHz to 12.5 kHz), future fault location algorithms may be trained with only the lower frequencies since their amplitudes are only slightly affected by changes in system parameters.

Unfortunately, this PhD project was not funded by industry and it was a major challenge to acquire information about practical systems. A fair amount of time was spent to set up an accurate model of a 33 kV distribution network and to find appropriate wind turbine models for short-circuit studies. The ultimate test is now to identify part of a real 33 kV distribution network with wind farm connections and develop ANN based fault classification and location algorithms for that network. The overcurrent relay at the substation end must have a fault recording capability so that the short-circuit transients can be downloaded from the relay and run through the developed ANN algorithms to ascertain their robustness for a real system.

References

1. Lehtonen, M., *Novel techniques for Fault Location in Distribution Networks*, in *IEEE Power Quality and Supply Reliability Conference 2008*. 2008. p. 199-204.
2. Mirzaei, M., et al., *Review of fault location methods for distribution power system.* Australian Journal of Basic and Applied Sciences, 2009. **3**(3): p. 2670-2676.
3. European Commission, *Renewable energy targets by 2020*. 25 September 2012]; Available from: http://ec.europa.eu/energy/renewables/targets_en.htm.
4. legislation.gov.uk. *Climate Change Act 2008*. 25 September 2012]; Available from: http://www.legislation.gov.uk/ukpga/2008/27/contents.
5. European Wind Energy Association, *Building a stable future*. 2013.
6. RenewableUK. *Hive Five! Momentous month for onshore wind*. 25 September 2012]; Available from: http://www.renewableuk.com/en/news/press-releases.cfm/2012-09-21-high-five-momentous-month-for-onshore-wind.
7. RenewableUK, *Wind Energy in the UK: State of the industry report 2013*. 2013.
8. RenewableUK. *New record high: 22% of UK electricity from wind*. 2014; Available from: http://www.renewableuk.com/en/news/press-releases.cfm/18-08-14-new-record-high-22-of-uk-electricity-from-wind.
9. DECC. *Why is onshore wind an important part of the UK energy mix?* 25 September 2012]; Available from: http://www.decc.gov.uk/en/content/cms/meeting_energy/wind/onshore/delivering/why_onshore/why_onshore.aspx.
10. Eickhoff, F., E. Handschin, and W. Hoffmann, *Knowledge based alarm handling and fault location in distribution networks*, in *IEEE Transactions on Power Systems*. 1992.
11. Jarventausta, P., P. Verho, and J. Patanen, *Using Fuzzy sets to model the uncertainty in the fault location process of distribution networks*, in *IEEE Transactions on Power Delivery*. 1994.
12. Saha, M., et al., *Review of fault location techniques for distribution systems.* Power Systems and Communications Infrastructures for the future, Beijing, 2002.
13. Mora, J.J., J.C. Bedoya, and J. Melendez, *Extensive events database development using ATP and Matlab to fault location in power distribution systems*, in *IEEE Transmission and Distribution Conference and Exposition*. 2006: Latin America.
14. Chen-Fu, C., C. Shi-Lin, and L. Yih-Shin, *Using Bayesian network for fault location on distribution feeder.* Power Delivery, IEEE Transactions on, 2002. **17**(3): p. 785-793.

15. Jun, Z., D.L. Lubkeman, and A.A. Girgis, *Automated fault location and diagnosis on electric power distribution feeders.* Power Delivery, IEEE Transactions on, 1997. **12**(2): p. 801-809.

16. Mokhlis, H. and H. Li, *Non-linear representation of voltage sag profiles for fault location in distribution networks.* International Journal of Electrical Power & Energy Systems, 2011. **33**(1): p. 124-130.

17. Senger, E.C., et al., *Automated fault location system for primary distribution networks.* Power Delivery, IEEE Transactions on, 2005. **20**(2): p. 1332-1340.

18. Mora-Flòrez, J., J. Meléndez, and G. Carrillo-Caicedo, *Comparison of impedance based fault location methods for power distribution systems.* Electric Power Systems Research, 2008. **78**(4): p. 657-666.

19. Das, S., et al., *Impedance-Based Fault Location in Transmission Networks: Theory and Application.* Access, IEEE, 2014. **2**: p. 537-557.

20. Vahamaki, O., et al., *A new technique for short circuit fault location in distribution networks*, in *18th International Conference on Electricity Distribution CIRED*. 2005: Turin.

21. Girgis, A.A., C.M. Fallon, and D.L. Lubkeman, *A fault location technique for rural distribution feeders.* Industry Applications, IEEE Transactions on, 1993. **29**(6): p. 1170-1175.

22. Yuan, L., *Generalized Fault-Location Methods for Overhead Electric Distribution Systems.* Power Delivery, IEEE Transactions on, 2011. **26**(1): p. 53-64.

23. Nouri, H. and M.M. Alamuti, *Comprehensive Distribution Network Fault Location Using the Distributed Parameter Model.* Power Delivery, IEEE Transactions on, 2011. **26**(4): p. 2154-2162.

24. Hänninen, S. and M. Lehtonen, *Characteristics of earth faults in electrical distribution networks with high impedance earthing.* Electric Power Systems Research, 1998. **44**(3): p. 155-161.

25. Keng-Yu, L., et al., *Energy variance criterion and threshold tuning scheme for high impedance fault detection.* Power Delivery, IEEE Transactions on, 1999. **14**(3): p. 810-817.

26. Alamuti, M.M., et al., *Intermittent Fault Location in Distribution Feeders.* Power Delivery, IEEE Transactions on, 2012. **27**(1): p. 96-103.

27. Myeon-Song, C., et al., *A new fault location algorithm using direct circuit analysis for distribution systems.* Power Delivery, IEEE Transactions on, 2004. **19**(1): p. 35-41.

28. Filomena, A.D., et al., *Fault location for underground distribution feeders: An extended impedance-based formulation with capacitive current compensation.* International Journal of Electrical Power & Energy Systems, 2009. **31**(9): p. 489-496.

29. Junyu, H. and P.A. Crossley. *Fault location on a mixed overhead and underground transmission feeder using a multiple-zone quadrilateral impedance relay and a double-ended travelling wave fault locator*. in

Developments in Power System Protection (DPSP 2014), 12th IET International Conference on. 2014.

30. Yanfeng, G. and A. Guzman, *Integrated Fault Location System for Power Distribution Feeders.* Industry Applications, IEEE Transactions on, 2013. **49**(3): p. 1071-1078.
31. Dommel, H.W. and J.M. Michels, *High speed relaying using traveling wave transient analysis*, in *IEEE PES Winter Power Meeting*. 1978: New York. p. 1-7.
32. Borghetti, A., et al., *Continuous-Wavelet Transform for Fault Location in Distribution Power Networks: Definition of Mother Wavelets Inferred From Fault Originated Transients.* Power Systems, IEEE Transactions on, 2008. **23**(2): p. 380-388.
33. Bo, Z.Q., et al. *Accurate fault location and protection scheme for power cable using fault generated high frequency voltage transients*. in *Electrotechnical Conference, 1996. MELECON '96., 8th Mediterranean*. 1996.
34. Bo, Z.Q., G. Weller, and M.A. Redfern, *Accurate fault location technique for distribution system using fault-generated high-frequency transient voltage signals.* Generation, Transmission and Distribution, IEE Proceedings-, 1999. **146**(1): p. 73-79.
35. Borghetti, A., et al., *Integrated Use of Time-Frequency Wavelet Decompositions for Fault Location in Distribution Networks: Theory and Experimental Validation.* Power Delivery, IEEE Transactions on, 2010. **25**(4): p. 3139-3146.
36. Magnago, F.H. and A. Abur, *Fault location using wavelets.* Power Delivery, IEEE Transactions on, 1998. **13**(4): p. 1475-1480.
37. Zimath, S.L., et al. *Traveling wave fault location applied to high impedance events*. in *Developments in Power System Protection (DPSP 2014), 12th IET International Conference on*. 2014.
38. Dwivedi, A. and Y. Xinghuo. *Fault location in radial distribution lines using travelling waves and network theory*. in *Industrial Electronics (ISIE), 2011 IEEE International Symposium on*. 2011.
39. Magnago, F.H. and A. Abur. *A new fault location technique for radial distribution systems based on high frequency signals*. in *Power Engineering Society Summer Meeting, 1999. IEEE*. 1999.
40. Tang, J., et al. *Fault location in distribution networks using Prony analysis*. in *Advanced Power System Automation and Protection (APAP), 2011 International Conference on*. 2011.
41. Tang, J., et al. *Fault location in distribution networks base on the use of wavelet packet analysis*. in *Electric Utility Deregulation and Restructuring and Power Technologies (DRPT), 2011 4th International Conference on*. 2011.

42. Buigues, G., et al., *Signal injection techniques for fault location in distribution networks,* in *International Conference on Renewable Energies and Power Quality*. 2012: Spain.

43. Navaneethan, S., et al., *Automatic fault location for underground low voltage distribution networks.* Power Delivery, IEEE Transactions on, 2001. **16**(2): p. 346-351.

44. Bhowmik, P.S., P. Purkait, and K. Bhattacharya. *A Novel Wavelet Transform and Neural Network Based Transmission Line Fault Analysis Method*. in *Developments in Power System Protection, 2008. DPSP 2008. IET 9th International Conference on*. 2008.

45. Raval, P.D., *ANN based classification and location of faults in EHV transmission line,* in *Proceedings of the International Multiconference of Engineers and Computer Scientists*. 2008: Hong Kong.

46. Sahoo, S., et al., *A computational intelligence approach for fault location in transmission lines,* in *International Conference on Power Electronics, Drives and Energy Systems (PEDES)*. 2010: India. p. 1-6.

47. Sanaye-Pasand, M. and H. Khorashadi-Zadeh, *Transmission line fault detection and phase selection using ANN,* in *International Conference on Power System Transients IPST 2003*. 2003: New Orleans USA. p. 1-6.

48. Butler, K.L. and J.A. Momoh. *A neural net based approach for fault diagnosis in distribution networks*. in *Power Engineering Society Winter Meeting, 2000. IEEE*. 2000.

49. Butler, K.L., J.A. Momoh, and D.J. Sobajic, *Field studies using a neural-net-based approach for fault diagnosis in distribution networks.* Generation, Transmission and Distribution, IEE Proceedings-, 1997. **144**(5): p. 429-436.

50. Mora-Florez, J., V. Barrera-Nuez, and G. Carrillo-Caicedo, *Fault Location in Power Distribution Systems Using a Learning Algorithm for Multivariable Data Analysis.* Power Delivery, IEEE Transactions on, 2007. **22**(3): p. 1715-1721.

51. Thukaram, D., H.P. Khincha, and H.P. Vijaynarasimha, *Artificial neural network and support vector Machine approach for locating faults in radial distribution systems.* Power Delivery, IEEE Transactions on, 2005. **20**(2): p. 710-721.

52. Thukaram, D., U.J. Shenoy, and H. Ashageetha. *Neural network approach for fault location in unbalanced distribution networks with limited measurements*. in *Power India Conference, 2006 IEEE*. 2006.

53. Khorashadi-Zadeh, H. and M.R. Aghaebrahimi, *A novel approach to fault classification and fault location for medium voltage cables based on artificial neural network.* International Journal of Information and Mathematical Sciences, 2006. **2**(2).

54. Javadian, S.A.M., et al. *Determining fault's type and accurate location in distribution systems with DG using MLP Neural networks*. in *Clean Electrical Power, 2009 International Conference on*. 2009.

55. Zayandehroodi, H., et al. *Determining exact fault location in a distribution network in presence of DGs using RBF neural networks*. in *Information Reuse and Integration (IRI), 2011 IEEE International Conference on*. 2011.

56. Zayandehroodi, H., et al. *Performance comparison of MLP and RBF neural networks for fault location in distribution networks with DGs*. in *Power and Energy (PECon), 2010 IEEE International Conference on*. 2010.

57. DECC, *The UK Renewable Energy Strategy*. 2009 15th July 2009; Available from: https://www.gov.uk/government/publications/the-uk-renewable-energy-strategy.

58. DECC, *UK energy statistics*. 2014 27th March 2014; Available from: https://www.gov.uk/government/news/uk-energy-statistics-statistical-press-release-march-2014.

59. DECC, *Energy trends section 6: Renewables*. 2014 13th November 2014 18th November 2014]; Available from: https://www.gov.uk/government/statistics/energy-trends-section-6-renewables.

60. RenewableUK, *Wind Energy in the UK: State of industry report 2014*. 2014 12th November 2014 18th November 2014]; Available from: http://www.renewableuk.com/en/publications/index.cfm/state-of-industry-report-2014.

61. Nixon, N. *Timeline: The history of wind power*. 2008 2008 18th November 2014]; Available from: http://www.theguardian.com/environment/2008/oct/17/wind-power-renewable-energy.

62. Masters, G.M., *Renewable and Efficient Electric Power Systems*. 2004, John Wiley & Sons Inc: New Jersey.

63. Ackermann, T., ed. *Wind power in power systems*. 2nd ed., ed. T. Ackermann. 2012, John Wiley & Sons Ltd.

64. Gasch, R. and J. Twele, *Wind Power Plants: Fundamentals, Design, Construction and Operation*. 2nd ed. 2012, Berlin: Springer.

65. Walling, R.A. and M.L. Reichard. *Short circuit behavior of wind turbine generators*. in *Protective Relay Engineers, 2009 62nd Annual Conference for*. 2009.

66. Martinez, J., et al. *Short circuit signatures from different wind turbine generator types*. in *Power Systems Conference and Exposition (PSCE), 2011 IEEE/PES*. 2011.

67. Gevorgian, V., M. Singh, and E. Muljadi. *Symmetrical and unsymmetrical fault currents of a wind power plant*. in *Power and Energy Society General Meeting, 2012 IEEE*. 2012.

68. Das, S. and S. Santoso. *Effect of wind speed variation on the short-circuit contribution of a wind turbine*. in *Power and Energy Society General Meeting, 2012 IEEE*. 2012.

69. British Standard, *BS EN 60909-0:2001 Short-circuit currents in three-phase a.c. systems*, in *Part 0: Calculation of currents*. 2001.

70. Morcos, M. and J.C. Gomez. *Distributed generation: Short circuit current supplied for induction generators*. in *Transmission and Distribution Conference and Exposition: Latin America, 2008 IEEE/PES*. 2008.

71. Muljadi, E., et al. *Different Factors Affecting Short Circuit Behavior of a Wind Power Plant*. in *Industry Applications Society Annual Meeting (IAS), 2010 IEEE*. 2010.

72. Walling, R.A., E. Gursoy, and B. English. *Current contributions from Type 3 and Type 4 wind turbine generators during faults*. in *Power and Energy Society General Meeting, 2011 IEEE*. 2011.

73. Gao, X., et al. *Fault current contributions of doubly fed induction generator wind turbines under different control strategies*. in *Advanced Power System Automation and Protection (APAP), 2011 International Conference on*. 2011.

74. Morren, J. and S.W.H. de Haan, *Short-Circuit Current of Wind Turbines With Doubly Fed Induction Generator.* Energy Conversion, IEEE Transactions on, 2007. **22**(1): p. 174-180.

75. Grigsby, L.L., *Power Systems*. 3rd ed. 2012: CRC Press.

76. Nelson, R.J. *Short-circuit contributions of full converter wind turbines*. in *Transmission and Distribution Conference and Exposition (T&D), 2012 IEEE PES*. 2012.

77. Llorente Iglesias, R., R. Lacal Arantegui, and M. Aguado Alonso, *Power electronics evolution in wind turbines—A market-based analysis.* Renewable and Sustainable Energy Reviews, 2011. **15**(9): p. 4982-4993.

78. Siemens. *Onshore wind power solutions*. 2014 18th November 2014]; Available from: http://www.energy.siemens.com/hq/en/renewable-energy/wind-power/onshore.htm#content=Turbines.

79. Nordex. *Wind turbines*. 2014 18th November 2014]; Available from: http://www.nordex-online.com/en/products-services/wind-turbines.html.

80. Vestas. *Turbines*. 2014 18th November 2014]; Available from: http://www.vestas.com/en/products_and_services/turbines.

81. SP Distribution Ltd, *Distribution Long Term Development Statement*. 2013.

82. Western Power Distribution, *Long Term Development Statement for Western Power Distribution (South West) plc's Electricity Distribution System*. 2011.

83. MathWorks. *Wind Farm - DFIG Detailed Model*. 2015 [cited 2015 21st May]; Available from: http://uk.mathworks.com/help /physmod/sps/examples/wind-farm-dfig-detailed-model.html.

84. MATLAB, *Universal bridge*. 2014.

85. Fletcher, J. and J. Yang, *Introduction to Doubly-fed Induction Generator for Wind Power Applications, Paths to sustainable energy*. 2010, InTech.

86. Clark, K., N.W. Miller, and J.J. Sanchez-Gasca, *Modeling of GE wind turbine-generators for grid studies*. 2010, General Electric International, Inc.

87. MathWorks. *Wind Farm - Synchronous Generator and Full Scale Converter (Type 4) Detailed Model*. 2015 [cited 2015 21st May]; Available from:

http://uk.mathworks.com/help/physmod/sps/examples/wind-farm-synchronous-generator-and-full-scale-converter-type-4-detailed-model.html.

88. Mohan, N., T.M. Undeland, and W.P. Robbins, *Power Electronics: Converters, Applications and Design*. 2003: John Wiley & Sons.

89. Sachdev, M.S. and R. Das, *Understanding microprocessor-based technology applied to relaying.* IEEE Power System Relaying Committee, 2004.

90. Brahma, S.M., P.L. De Leon, and R.G. Kavasseri, *Investigating the option of removing the antialiasing filter from digital relays.* Power Delivery, IEEE Transactions on, 2009. **24**(4): p. 1864-1868.

91. Ukil, A., *Intelligent systems and signal processing in power engineering*. 2007: Springer.

92. Rebizant, W., J. Szafran, and A. Wiszniewski, *Digital signal processing in power system protection and control*. 2011: Springer.

93. Chul Hwan, K. and A. Raj, *Wavelet transforms in power systems. I. General introduction to the wavelet transforms.* Power Engineering Journal, 2000. **14**(2): p. 81-87.

94. Robertson, D.C., et al., *Wavelets and electromagnetic power system transients.* Power Delivery, IEEE Transactions on, 1996. **11**(2): p. 1050-1058.

95. Ruqiang, Y. and R.X. Gao, *Tutorial 21 wavelet transform: a mathematical tool for non-stationary signal processing in measurement science part 2 in a series of tutorials in instrumentation and measurement.* Instrumentation & Measurement Magazine, IEEE, 2009. **12**(5): p. 35-44.

96. MATLAB, *Introduction to Walet Families*. 2014.

97. Chul Hwan, K. and R. Aggarwal, *Wavelet transforms in power systems. II. Examples of application to actual power system transients.* Power Engineering Journal, 2001. **15**(4): p. 193-202.

98. Aggarwal, R. and S. Yonghua, *Artificial neural networks in power systems. I. General introduction to neural computing.* Power Engineering Journal, 1997. **11**(3): p. 129-134.

99. Bose, B.K., *Modern power electronics and AC drives*. 2001: Prentice Hall.

100. Aggarwal, R. and S. Yonghua, *Artificial neural networks in power systems. III. Examples of applications in power systems.* Power Engineering Journal, 1998. **12**(6): p. 279-287.

101. Leonard, P., *Neural Networks*. 2014, University of Bath.

102. Aggarwal, R. and S. Yonghua, *Artificial neural networks in power systems. II. Types of artificial neural networks.* Power Engineering Journal, 1998. **12**(1): p. 41-47.

103. Engelbrecht, A.P., *Computational Intelligence, An Introduction*. 2007: John Wiley & Sons.

104. Leonard, P., *Supervised training for multi-layer networks*. 2014, University of Bath.

105. CEB, *Construction manual, Standard drawings*. n.d.

106. Nexans, *6-36Kv Medium Voltage Underground Power Cables*. n.d.

107. Zhihan, X. and T.S. Sidhu, *Fault Location Method Based on Single-End Measurements for Underground Cables.* Power Delivery, IEEE Transactions on, 2011. **26**(4): p. 2845-2854.

108. SEL. *Distribution Protection*. 2015 [cited 2015 25th May]; Available from: https://www.selinc.com/distributionprotection/.

Appendix A

The 33 kV distribution network model can be validated by performing a three-phase short-circuit fault calculation at a certain point in the network. The simplified short-circuit calculations provide a good approximation that can be used to verify whether simulated short-circuit currents match the theory.

A three-phase short-circuit fault has been simulated at 5 km on Feeder 1 (Figure A.1) without any load and DG connected to the system and the peak phase current is around 5100 A (Figure A.2).

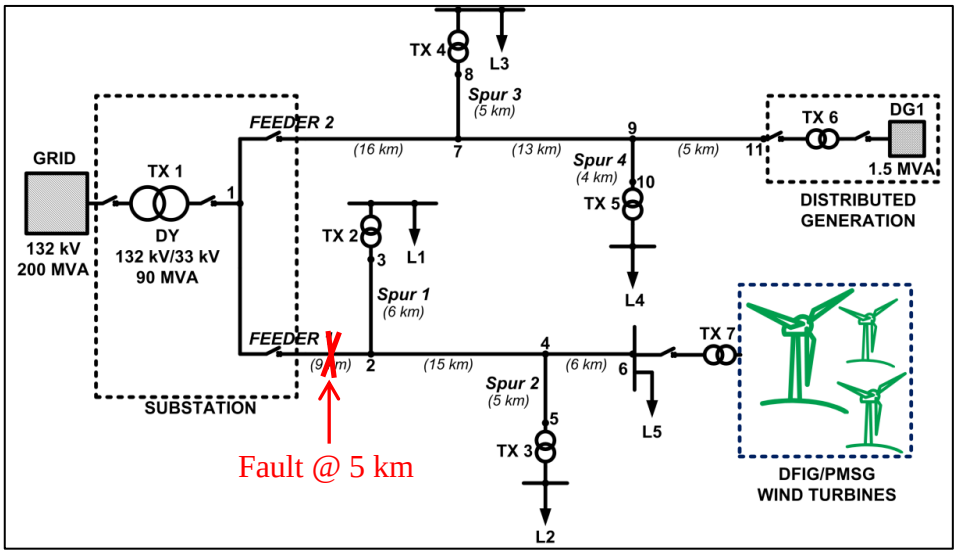

Figure A.1: Three-phase short-circuit at 5 km on Feeder 1

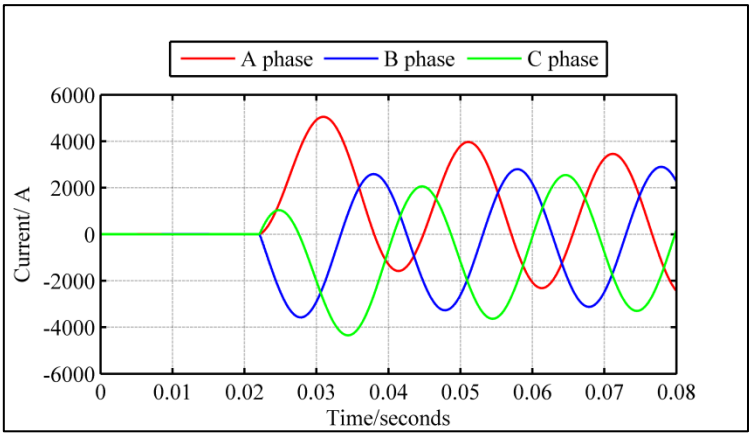

Figure A.2: Three-phase fault current waveforms at 5 km on Feeder 1

Basic assumptions made before short-circuit calculations:

- The three-phase short-circuit fault is assumed to occur simultaneously on all phases.
- Neglect resistances of electrical components.
- Neglect load currents.
- Neglect all line capacitances.
- No significant change in voltages and short-circuit impedances during the three-phase short-circuit fault.

Grid:

V_B= 132 kV, S_B= 200 MVA and $X'' = j0.35\ pu$

Transformer:

S_B = 90 MVA and X = j0.1 pu

Assuming a common base of 200 MVA,

$$X_T = j0.1 \times \left(\frac{200}{90}\right) = j0.222\ pu$$

Line:

V_B = 33 kV, S_B= 200 MVA

$$Z_B = \frac{V_B^2}{S_B} \qquad I_B = \frac{S_B}{\sqrt{3}V_B}$$

$X_1 = j2\pi fL_1$ = j0.39 Ω/km

At 5 km down Feeder 1,

$$X_{L(pu)} = 5 \times j0.39 \times \frac{S_B}{V_B^2}$$

$$X_{L(pu)} = j0.358$$

Simplified impedance diagram to point of fault:

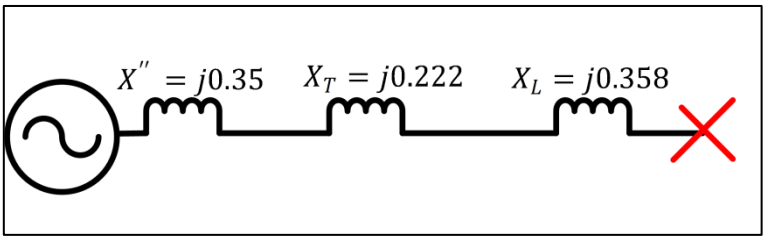

Figure A.3: Impedance to fault

$X_{total} = X'' + X_T + X_L$ = j0.93

$$Short - circuit\ current, I_{S.C} = \frac{E}{X_{total}} = \frac{1}{j0.93} = -j1.075 \text{ pu}$$

Therefore,

$$|I_{S.C}| = 1.075 \times I_B = 1.075 \times \frac{200 \times 10^6}{\sqrt{3} \times 33000} = 3761.5\ A$$

Peak short-circuit current,

$$\text{Peak } |I_{S.C}| = \sqrt{2} \times 3761.5 = 5319.5\ A$$

Since the calculated value is close to the simulated fault current value, it can be concluded that the 33 kV distribution network model has a reasonably good level of accuracy.

Appendix B

Main program for extraction of data from simulations:

```
%Extracting data from mat files

n=33; %number of files in the folder
phase_current=ones(2001,3*n);
i=1;
for f=1:n
    filename=sprintf('a%d.mat',f);
    load(filename)
    phase_current(:,i)=Iabc(:,1);
    phase_current(:,i+1)=Iabc(:,2);
    phase_current(:,i+2)=Iabc(:,3);
    i=i+3;
end

sample=phase_current(1:2000,:);

%butterworth filter for antialiasing filtering
[b,a]=butter(3,0.8);
ifiltered=filter(b,a,sample);

%16 bit ADC, bipolar 10 V
iscale=(ifiltered/8000)*10;
iquantized=floor(iscale*2^15)*1/2^15+1/2^16;

%%
%discrete wavelet transform at 10 levels

[E1,E2,E3,E4,E5,E6,E7,E8,E9,E10]=dwavelett(iquantized);
%reducing number of input data by selecting one cycle prefault and 2
cycles
%post fault

[EW1,EW2,EW3,EW4,EW5,EW6,EW7,EW8,EW9,EW10]=datareduction1(E1,E2,E3,E
4,E5,E6,E7,E8,E9,E10);
%%
%feature extraction
[F1,F2,F3,F4,F5,F6,F7,F8,F9,F10]=ftraction2(EW1,EW2,EW3,EW4,EW5,EW6,
EW7,EW8,EW9,EW10);
%%
%regrouping
[FA,FB,FC]=regrouping3(F1,F2,F3,F4,F5,F6,F7,F8,F9,F10);
```

General format for the threshold detection algorithm:

```
% Threshold detector algorithm
[r,c]=size(out);
out_threshold=zeros(r,c);
for i=1:c
    for j=1:r
        if (out(j,i)>0.7)
            out_threshold(j,i)=1;
        else
            out_threshold(j,i)=0;
        end
    end
end
```

Decision logic algorithm for feeder/spur classification:

```
% Decision logic algorithm

d=c/15;
decision=zeros(r,d);

for i=1:r
    a=1; b=15;

    for j=1:d
        Z=out_threshold(i,a:b);
        area=trapz(Z);
        if(area>6)
            decision(i,j)=1;
        else
            decision(i,j)=0;
        end
        a=b+1;
        b=a+14;
    end
end
```

Appendix C

19/33kV Single Core Screened & PVC Sheathed

Copper Conductors, up to 10kA Fault Level

Nominal conductor area	Nominal conductor diameter	Nominal insulation thickness	Nominal diameter over insulation	Nominal screen area on each core	Number and nominal diameter of screen wires	Nominal diameter over wire screen	Nominal overall diameter	Approx. mass	Product code	Max. pulling tension	Min. bending radius		Nominal duct diameter	
											During pulling	Set in position		
mm²	mm	mm	mm	mm²	no/mm	mm	mm	kg/100m		kN	mm	mm	mm	mm
50	8.0	8.0	25.5	48.7	34/1.35	29.8	34.3	170	XNHP19AA001	3.5	620	410	63	100
70	9.6	8.0	27.1	68.7	48/1.35	31.4	36.1	215	XNHP20AA001	4.9	650	430	63	100
95	11.5	8.0	29.0	68.7	48/1.35	33.3	38.0	245	XNHP22AA001	6.7	680	460	65	150
120	13.1	8.0	30.6	68.7	48/1.35	34.9	39.8	280	XNHP23AA001	8.4	720	480	65	150
150	14.5	8.0	32.0	68.7	48/1.35	36.5	41.4	310	XNHP24AA001	11	750	500	65	150
185	16.1	8.0	33.6	68.7	48/1.35	38.1	43.2	345	XNHP25AA001	13	780	520	65	150
240	18.5	8.0	36.0	68.7	48/1.35	40.5	45.9	410	XNHP26AA001	17	830	550	65	150
300	20.7	8.0	38.4	68.7	48/1.35	42.9	48.4	475	XNHP27AA001	21	870	580	80	150
400	23.6	8.0	41.3	68.7	48/1.35	45.8	51.5	575	XNHP28AA001	28	930	620	80	150
500	26.5	8.0	44.2	68.7	48/1.35	48.7	54.9	685	XNHP30AA001	35	990	660	80	200
630	29.9	8.0	47.9	68.7	48/1.35	52.4	58.8	815	XNHP32AA001	44	1060	710	100	200
800	35.9	8.0	54.0	68.7	48/1.35	58.5	65.3	1020	XNHP33AA001	56	1180	780	100	200
1000	40.2	8.0	59.5	68.7	48/1.35	64.0	71.0	1220	XNHP34AA001	70	1280	850	125	200
1200	43.8	8.0	63.5	68.7	48/1.35	68.0	75.2	1420	XNHP50AA001	84	1350	900	125	200

Current Ratings

Nominal conductor area	Continuous current-carrying capacity, A												Fault current carrying capacity for 1 second	
	In air					In ground			In underground ducts					
mm²	Solid Bond	Solid Bond	Solid Bond	Solid Bond	Solid Bond	Solid Bond	Solid Bond	Solid Bond	Solid Bond	Solid Bond	Solid Bond	Solid Bond	Cond. kA	Screen kA
50	224	250	210	221	160	208	209	205	187	186	185	174	7.15	7.22
70	276	306	259	273	202	251	249	249	223	219	223	216	10.0	10.1
95	333	369	315	332	242	297	292	297	265	258	267	258	13.6	10.1
120	381	420	361	381	276	335	327	336	296	287	300	292	17.1	10.2
150	429	469	407	430	308	372	359	375	327	313	333	325	21.4	10.2
185	485	527	463	490	348	414	397	421	362	343	372	366	26.4	10.2
240	563	605	542	574	402	471	444	485	408	382	425	420	34.3	10.2
300	634	674	616	653	452	521	485	542	446	413	471	469	42.9	10.2
400	719	756	706	750	533	579	531	610	492	449	526	547	57.2	10.2
500	807	837	803	854	600	637	574	682	539	484	585	611	71.5	10.2
630	902	924	911	969	672	697	619	759	576	513	635	680	90.0	10.2
800	1012	1026	1036	1103	748	756	664	838	630	552	705	748	114	10.2
1000	1160	1131	1219	1300	888	845	713	966	661	578	749	880	143	10.2
1200	1252	1204	1337	1426	963	896	745	1043	698	603	801	948	171	10.2

Electrical Characteristics

Nominal conductor area	Maximum Conductor DC resistance at 20°C	Cond. AC resistance at 50Hz and 90°C		Inductive reactance at 50Hz and 90°C			Insulation resistance at 20°C	Conductor to screen capacitance	Charging current per phase	Dielectric loss per phase	Maximum dielectric stress	Screen DC resistance at 20°C	Zero sequence resistance at 20°C	Zero seq. react. at 50Hz
		Trefoil or flat touching	Flat spaced	Trefoil touching	Flat touching	Flat spaced								
mm²	Ohm/km	Ohm/km	Ohm/km	Ohm/km	Ohm/km	Ohm/km	MegOhm.km	μF/km	A/km	W/km	kV/mm	Ohm/km	Ohm/km	Ohm/km
50	0.387	0.494	0.494	0.163	0.178	0.224	18000	0.133	0.796	60.5	4.05	0.372	0.759	0.0999
70	0.268	0.342	0.342	0.154	0.169	0.215	16000	0.148	0.883	67.1	3.82	0.263	0.531	0.0919
95	0.193	0.247	0.247	0.143	0.158	0.204	15000	0.165	0.984	74.8	3.61	0.263	0.457	0.0817
120	0.153	0.195	0.195	0.137	0.153	0.198	14000	0.179	1.07	81.1	3.48	0.263	0.416	0.0767
150	0.124	0.159	0.159	0.133	0.148	0.194	13000	0.191	1.14	86.8	3.38	0.264	0.389	0.0731
185	0.0991	0.127	0.127	0.129	0.144	0.190	12000	0.205	1.23	93.2	3.29	0.264	0.364	0.0693
240	0.0754	0.0976	0.0972	0.124	0.139	0.185	11000	0.227	1.35	103	3.17	0.263	0.340	0.0645
300	0.0601	0.0786	0.0779	0.120	0.135	0.181	9800	0.247	1.48	112	3.09	0.264	0.325	0.0612
400	0.0470	0.0625	0.0616	0.115	0.130	0.176	8900	0.272	1.62	123	3.00	0.263	0.312	0.0564
500	0.0366	0.0499	0.0487	0.111	0.126	0.172	8100	0.297	1.77	135	2.93	0.263	0.302	0.0531
630	0.0283	0.0403	0.0387	0.108	0.123	0.169	7300	0.329	1.96	149	2.86	0.263	0.294	0.0504
800	0.0221	0.0336	0.0315	0.102	0.117	0.163	6300	0.381	2.27	173	2.78	0.263	0.289	0.0452
1000	0.0182	0.0245	0.0240	0.100	0.115	0.161	5600	0.427	2.55	194	2.72	0.263	0.282	0.0441
1200	0.0150	0.0207	0.0201	0.0984	0.114	0.159	5200	0.461	2.75	209	2.68	0.263	0.279	0.0426

Related publications

1. Lout, K. and Aggarwal, R.K., 2014. Performance analysis of a novel AI based approach to fault classification and location in an active distribution network with type 3 and type 4 wind turbine connections. In: 12th IET International Conference on Developments in Power System Protection, DPSP 2014, 2014-03-31 - 2014-04-03, Copenhagen.

2. Lout, K. and Aggarwal, R. K., 2013. Current transients based phase selection and fault location in active distribution networks with spurs using artificial intelligence. In: 2013 IEEE Power and Energy Society General Meeting (PES 2013), 2013-07-21 - 2013-07-25, Vancouver.

3. Lout, K. and Aggarwal, R.K., 2012. A feedforward Artificial Neural Network approach to fault classification and location on a 132kV transmission line using current signals only. In: Proceedings of the Universities Power Engineering Conference. IEEE.